FORGE

Fate Of Repository Gases

European Commission FP7

FORGE Milestone D4.24-R Summary report: Experiments and modelling of excavation damage zone (EDZ) behaviour in argillaceous and crystalline rocks (Work Package 4)

FORGE Report D4.24-R

	Name	Organisation	Signature	Date
Compiled	Jon Harrington	BGS		13-02-14
Verified	Richard Shaw	BGS		13-02-14
Approved	Richard Shaw	BGS		13-02-14

Euratom 7th Framework Programme Project: FORGE

EURATOM

FORGE
Fate Of Repository Gases
European Commission FP7

FORGE Milestone D4.24-R

Summary report: Experiments and modelling of excavation damage zone (EDZ) behaviour in argillaceous and crystalline rocks (Work Package 4)[1]

December 2013

Work Package leader: Jon Harrington

Authored by:

Belgium	Geert Volckaert[2], Elke Jacops, Norbert Maes & Lou Areias (SCK-CEN)
(Ulg)	Robert Charlier, Collin Frédéric, Pierre Gerard[3] Severine Levasseur & Jean-Pol Radu
Czech Republic	Jiří Svoboda (CTU)
France	Sylvie Granet (EDF)
Spain	Jordi Alcoverro, Diego Arnedo, Sebastia Olivella & Eduardo Alonso (UPC)
Switzerland	Paul Marschall, Irina Gaus & Jörg Rüedi (Nagra)
United Kingdom	Rob Cuss, Shanvas Sathar[4], Jon Harrington & David Noy (BGS)

Edited by:	Jon Harrington	Date: 13.02.2014
Checked by:	Bill Lanyon	Date: 19.09.2013
Approved by:	Richard Shaw	Date: 13.01.2014
EC Project Officer:		Date:

Euratom 7th Framework project: FORGE 2013

[1] Harrington, J., Volckaert, G., Jacobs, E., Maes, N., L.Areias, Charlier, R., Frédéric, C., Gerard, P., Radu, J-P., Svoboda, J., Granet, S., Alcoverro, J., Arnedo, D., Olivella, S., Alonso, E., Marschall, P., Gaus, I, Rüedi, J., Cuss, R., Sathar, S. and Noy, D. *Summary report: Experiments and modelling of excavation damage zone (EDZ) behaviour in argillaceous and crystalline rocks (Work Package 4)*, EC FORGE Project Report D4.24-R, 2013.
[2] Now (FANC-AFCN)
[3] Now Univeristé Libre de Bruxelles
[4] Now Durham University

Fate of repository gases (FORGE)

The multiple barrier concept is the cornerstone of all proposed schemes for underground disposal of radioactive wastes. The concept invokes a series of barriers, both engineered and natural, between the waste and the surface. Achieving this concept is the primary objective of all disposal programmes, from site appraisal and characterisation to repository design and construction. However, the performance of the repository as a whole (waste, buffer, engineering disturbed zone, host rock), and in particular its gas transport properties, are still poorly understood. Issues still to be adequately examined that relate to understanding basic processes include: dilational versus visco-capillary flow mechanisms; long-term integrity of seals, in particular gas flow along contacts; role of the EDZ as a conduit for preferential flow; laboratory to field up-scaling. Understanding gas generation and migration is thus vital in the quantitative assessment of repositories and is the focus of the research in this integrated, multi-disciplinary project. The FORGE project is a pan-European project with links to international radioactive waste management organisations, regulators and academia, specifically designed to tackle the key research issues associated with the generation and movement of repository gasses. Of particular importance are the long-term performance of bentonite buffers, plastic clays, indurated mudrocks and crystalline formations. Further experimental data are required to reduce uncertainty relating to the quantitative treatment of gas in performance assessment. FORGE will address these issues through a series of laboratory and field-scale experiments, including the development of new methods for up-scaling allowing the optimisation of concepts through detailed scenario analysis. The FORGE partners are committed to training and CPD through a broad portfolio of training opportunities and initiatives which form a significant part of the project.

Further details on the FORGE project and its outcomes can be accessed at www.FORGEproject.org.

Contact details:

EC FORGE Work Package 4 Leader: J.F. Harrington
Organisation: British Geological Survey
Tel: +44 (115) 9363133 Fax: +44 (115) 9363200
email: jfha@BGS.ac.uk
web address: http://www.bgs.ac.uk/
Address: British Geological Survey, Keyworth, Nottingham NG12 5GG.

Acknowledgements

This report is a product of Work Package 4 of the FORGE project.

All participating organisations and personnel are thanked for their scientific input at meetings and for delivery of associated text that is collectively presented in this report.

The European Commission is acknowledged for its funding of this pan-European project.

Contents

Acknowledgements ii

Contents ii

FIGURES iii

TABLES viii

Executive summary ix

1. Introduction 1

2. Laboratory Experiments 2
   - 2.1 Effect of stress field and mechanical deformation (BGS) 2
   - 2.2 verification of critical stress theory applied to repository concepts (BGS) 20
   - 2.3 Gas-driven radionuclide movement in EDZ (SCK) 34

3. In-situ experiments 42
   - 3.1 Gas transport in EDZ at Mont Terri (Nagra) 42
   - 3.2 Gas transport in EDZ - in situ experiment in Boom Clay (SCK) 48
   - 3.3 Gas transport in crystalline rock (CTU) 58

4. Modelling 69
   - 4.1 Gas migration in Opalinus (UPC) 69
   - 4.2 Gas migration in Opalinus Clay and Callovo-Oxfordian claystone (EDF) 80
   - 4.3 Gas migration in Opalinus/COX (ULg) 91

5. Discussion 105
   - 5.1 Gas diffusion 105
   - 5.2 Two-phase flow (WP4) 106
   - 5.3 Pathway dilatancy 107
   - 5.4 Gas fracturing 108
   - 5.5 Role of interfaces 108
   - 5.6 Spatial upscaling 109

6. Conclusions 110

7. References 111

FIGURES

Figure 1 Description of four main processes of gas movement in clays (after Marschall et al., 2005). 2

Figure 2 The critical state model of soil mechanics, showing the relationship of the tension line (TL), normal consolidation line (NCL) and critical state line (CSL). These lines bound the Hvorslev and Roscoe surfaces in the *p′* - *q′* space. 3

Figure 3 The Stress Path Permeameter (SPP): a) schematic; b) photo of the end platen showing the injection filter and guard ring arrangement. 5

Figure 4 Results for test SPP_COx-1; a). stress path; b). strain; c). time-dependent radial and axial displacement observed for each stage; d). time-dependent radial displacement for each step against time of step; and e). guard-ring porewater pressure…….7

Figure 5 Post-test observations of SPP_COx-1; a). photograph of the test sample clearly showing the main fracture surface; b). circumference of the final sample…….8

Figure 6 Data for the complete test history of test SPP_COx-2; a) pressure history; b) sample strain….. 9

Figure 7 Data for the hydraulic testing stage of the test history; a). pressure history; b). sample strain; and c). flow data. 10

Figure 8 Data for the gas testing stage of the test history up until the attainment of near-steady-state flow; a). pressure history; b). radial and axial displacement; c). sample strain; and d). flow data.....11

Figure 9 Four stage model of onset of gas flow and experimental observations of processes occurring. Refer to text for detailed explanation. 13

Figure 10 A general model for advective gas flow in Callovo-Oxfordian claystone; a). gas starts to enter the sample; b). a dendritic pattern of gas pathways forms, slowly propagating through the sample; c). gas migration reaches the back-pressure end of the sample…….14

Figure 11 Summary of main events during onset and shut-off of gas flow; a). deformation; b). volumetric strain measured using two different methods; c). injection and back-pressure flow; d). pressure history; e). detail of pressure at injection guard ring; and f) detail of pressure at back-pressure guard ring. 16

Figure 12 Summary of main events during the lowering of back-pressure; a). volumetric strain; b). injection and back-pressure flow; c). pressure history; d). detail of pressure at back-pressure guard ring; and e). cumulative flow during the stages of lowering back-pressure. 17

Figure 13 Observations of sample SPP_COx-2 after testing; a). back-pressure end of the sample; b). observations of de-gassing during heating in glycerol; c). length-wise fracture seen in the sample; and d). detail of the mode-I fracture seen in the sample after testing…. 18

Figure 14 Critical stress hypothesis (adopted from Barton *et al.*, 1995; Jaeger *et al.*, 2007; Rogers, 2003). The three-dimensional Mohr diagram represents the shear stress and normal stress acting along a fracture in response to the *in situ* stress field. The open circles represent fractures experiencing state of stress above the failure criterion and therefore subject to shear failure. The closed circles represent fractures whose stress state is insufficient to induce shear failure and hence stable. 21

Figure 15 Schematic of the Angled Shear Rig (ASR).....23

Figure 16 Example of hysteresis seen in water flow during a loading/unloading experiment on a 30° slip-plane. 25

Figure 17 Example of loading-unloading cycle seen during a gas injection test on a 30° slip-plane. 25

Figure 18 Fracture width recorded during a loading-unloading experiment…….26

Figure 19 Shear displacement caused as the result of loading-unloading…….27

Figure 20 The hysteresis observed in horizontal stress during loading-unloading experiments; a) water injection; b) gas injection. 28

Figure 21 The variation of the ratio of horizontal stress : vertical stress seen during loading-unloading experiments; a) water injection; b) gas injection. The arrows indicate horizontal stress to vertical stress ratios during unloading which are greater than the initial values and indicates an enhancement in flow rate. 28

Figure 22 Comparing results for water and gas injection during loading and unloading experiments; a) horizontal stress; b) flow response. 28

Figure 23 Results from ASR_Tau06_30gGI showing different gas breakthrough indicating fault-valve behaviour. a) Flow rate versus time plot showing the gas injection rates used in different stages (indicated as numerals) of the experiment. b) Vertical stress versus time showing the vertical stress applied to the slip plane. c) Gas injection pressure versus time plot showing the evolution of injection pressure before and after each breakthrough event. d) The variations in fracture width during various gas injection stage…….30

Figure 24 Repeatability of gas injection tests; a) pressure response, b) flow results…….31

Figure 25 Gas injection pressure variation with discontinuity orientation. Grey data points represent the recorded gas entry pressure from each individual test; the blue data represents the average for each orientation; the dashed line is the polynomial fit of the data. 31

Figure 26 Comparison of results from the two methods used to determine gas entry pressure. Both methods show that gas entry pressure alters with fracture orientation, with entry pressure determined from STP flow into the fracture predicting higher pressures…..32

Figure 27 Photo showing the escape of gas into from the slip-plane…….33

Figure 28 Example of pressure recorded on the slip-plane. A low pressure of less than 20 kPa is observed. Little variation is seen, with no correlation with other data identified……34

Figure 29 Basic concept of the tests to study gas driven tracer transport in disturbed Boom Clay. 35

Figure 30 Basic concept of the tests to study gas driven tracer transport in the interface Boom Clay – Bentonite. Blue = NaI saturated Boom Clay core. Yellow = half Boom Clay core. Pink = half bentonite core. 35

Figure 31 Iodine concentration in breakthrough samples (log-scale) vs. time of breakthrough for all experiments.....37

Figure 32 Role of time of sealing (1 night vs. 1 week) on the degree of desaturation (% of NaI saturated pore water that was transported during gas breakthrough – calculation based on measured concentration of I) for samples oriented parallel (left) and perpendicular (right) to the bedding plane. 37

Figure 33 Left: location of the gas pathway during breakthrough vs. degree of desaturation (% of NaI saturated pore water that was transported during gas breakthrough – calculation based on measured concentration I). Right: schematic view of interface clay fracture-cell. 38

Figure 34 Observation of gas bubbles during the dismantling of experiments 2011/1-1 (left) and experiment 2011/3-1(right). 38

Figure 35 Role of orientation wrt. bedding plane for disturbed clay samples sealed 1 week (left) and 1 night (right) (desaturation is % of NaI saturated pore water that was transported during gas breakthrough – calculation based on measured concentration I). 39

Figure 36 Desaturation (% of NaI saturated pore water that was transported during gas breakthrough – calculation based on measured concentration I) in combined Boom Clay/Bentonite cores (4 different samples). 40

Figure 37 Location and layout of HG-A a) location at the Mont Terri Laboratory; b) Schematic drawing of the Microtunnel and the site instrumentation. Colour coding refers to the steel liner (red), the seal section (green) and the backfilled test section (orange).....43

Figure 38 Microtunnel stress, pore pressure, water content and flowrate measurements from start of saturation. 44

Figure 39 a) Linear and b) log-log plots of delta pressure from GI1-3.....45

Figure 40 Microtunnel stress, pore pressure, water content and flowrate measurements during gas injection. 45

Figure 41 Sealing Index during water injection. Periods of reduced Megapacker pressure (low effective stress) are marked. 46

Figure 42 EDZ schematic (from Marschall et al. 2008) with stages of gas injection: a) EDZ structure, b) storage & dissolution, c) storage & leakage, d) breakdown and gas flow into the EDZ.....48

Figure 43 EDZ The URF in Mol showing the location of the Forge packer system installation. 49

Figure 44 Layout [bottom] and overview [top] of packer system and multi-filter monitoring boreholes. 50

Figure 45 Layout Packer performance curve under confinement. 51

Figure 46 Detection and injection filters installed at Intervals 1, 2 and 3 of the packers [top] and one of the multi-filter monitoring boreholes showing minipacker and seven of the eight monitoring piezometer locations [bottom]. 51

Figure 47 Custom-made twin drill head used to drill large diameter borehole for installation of the packers. 53

Figure 48 Evolution of inflation pressure of packers. 55

Figure 49 Evolution of pore water pressures in monitoring piezometer 1.....55

Figure 50 Evolution of pore water pressures in monitoring piezometer 2.....56

Figure 51 Planned future in-situ gas test set-up. 57

Figure 52 Experimental equipment.....60

Figure 53 Example of CHIT tests in undisturbed rock 62

Figure 54 Example of CFIT test in disturbed rock with maximum flow rate…….62

Figure 55 Results of the intrinsic permeability and gas conductivity testing of individual borehole sections 65

Figure 56 Dependence of intrinsic permeability (gas tests) on distance from the gallery……66

Figure 57 Dependence of intrinsic permeability on injection pressure (gas and water injection tests) 66

Figure 58 Dependence of intrinsic permeability (water injection tests) on injection pressure……67

Figure 59 Dependence of intrinsic permeability (gas CFIT tests) on injection pressure……68

Figure 60 Real and modelled tunnel excavation rates.....72

Figure 61 Modelled region and system of coordinates. 72

Figure 62 Boundary conditions: a) mechanical ($\sigma_1 = 6.5\ \mathrm{MPa}$, $\sigma_2 = 4.5\ \mathrm{MPa}$, $\sigma_3 = 2.5\ \mathrm{MPa}$ compression is positive); b) hydraulic (upper face $p_l = 1.95\ \mathrm{MPa}$, lower face $p_l = 2.05\ \mathrm{MPa}$) 72

Figure 63 Evolutions of liquid pressure at the isolated intervals in boreholes HG-A2 (above the tunnel) and HG-A3 (at the left of the tunnel), that are subparallel to the tunnel; a) measured by the installed sensors, Marschall et al. (2006); b) computed using the model. Note that the same colours are used for corresponding evolutions in a) and b), but time and pressure scales used on b) double those used on a).....73

Figure 64 Evolution of the liquid phase pressure at 8 points on the vertical plane at y = 7 m and 0.5 m from the tunnel wall; a) location of points; b) computed evolutions…….73

Figure 65 a) damage zones around de HG-A tunnel, Marschall et al. (2008); b) porosity distributions on a 10 m × 10 m square zone around the tunnel on a vertical plane at y = 7 m at 107 days (left) and 217days (right) 74

Figure 66 Liquid pressure distribution (in MPa) on a plane orthogonal to the Opalinus clay bedding planes and passing through the tunnel axis at several times: a) 100.29 days; b) 107 days; and c) 217 days.....74

Figure 67 Evolution of the crack aperture (left axis) and of the intrinsic permeability (right axis, in logarithmic scale) as a function of volumetric deformation with the parameters used in the calculations (circles indicate the initial state, at $\varepsilon = 0$). 75

Figure 68 Measured input evolutions and model polygonal approximations: a) megapacker pressure; b) liquid volume injection rate; and c) gas volume injection rate…….76

Figure 69 a) Geometry around the megapacker section and system of coordinates; b) modelled region and materials: (undamaged) Opalinus clay (green), EDZ (blue) and gravel (pink). The tunnel axis is the axisymmetry axis. 76

Figure 70 Boundary conditions: a) mechanical (u_y are and u_r are the components of the displacement; t_y are and t_r are the components of the (total) traction); b) hydraulic (j_w are and j_a are mass rates of species water and species air).....77

Figure 71 a) Evolution of the measured liquid phase pressure (dark blue), computed liquid phase pressure (light blue) and gas phase pressure (red) in the EDZ; b) evolution of the computed intrinsic permeability in the EDZ, close to the test section…….77

Figure 72 Transformation of 2D axisymmetric boundary conditions into 1D boundary conditions and body terms. The 1D domain represents the EDZ in front of the megapacker, which is bounded to the left by the test section and to the right by the liner section…….78

Figure 73 Results of the 2D axisymmetric model at day 900 (hydraulic tests) on the zone around the megapacker half close to the test section: a) displacements (radial); b) strains (plane strain); and c) volume flow of liquid phase (axial on EDZ, zero on Opalinus clay)…….78

Figure 74 Results of the 1D simplified model (EDZ zone close to the test section): a) measured (red) and computed (blue) evolution of fluid pressure in the test section; b) computed evolution of intrinsic permeability in the EDZ. 79

Figure 75: Experimental results. (a) on the left: The water pressure in triple packer HG-A02 and HG-A03. (b) on the right: 3D laser scan of the HG-A micro-tunnel with a tachymeter. Pictures ext from Marshall et al (2006). 82

Figure 76 – PGZ1 experiment configuration 83

Figure 77 – Water pressure and gas fluxes in PGZ1201 (a) and Water pressure in PGZ1202 (b) 84

Figure 78 : time steps of excavation 84

Figure 79 : 3D geometry Figure 80 : 3D mesh 85

Figure 81 : Boundary conditions 85

Figure 82 : Pressure on HG-A3 for the first 10 days.....85

Figure 83: Pressure on HG-A3 for 45 weeks 85

Figure 84 : Pressure on HG-A2 for 45 weeks.....86

Figure 85 – 2D axisymmetrical geometry 86

Figure 86 – Plastic deformation on Lh 87

Figure 87 – Configuration and hypothesis of BDZ model 87

Figure 88 –injection chamber Interval 2 (or PRE02) 88

Figure 89 – Liquid pressure evolution in interval 2: goal of initial saturation 89

Figure 90 – Gas Pressure at several times along L_h.....89

Figure 91 – Liquid Saturation at several times along L_h.....89

Figure 92 – Gas/liquid ratio of Nitrogen at several times along L_h.....89

Figure 93 – Gas pressure evolution in interval 2 : goal of BDZ 90

Figure 94 – Gas pressure evolution in interval 2: goal of relative permeability in host rock……91

Figure 95: Transformation of the global axis $(\underline{E}_1, \underline{E}_2, \underline{E}_3)$ into anisotropic axes $(\underline{e}_1, \underline{e}_2, \underline{e}_3)$ …….92

Figure 96: Schematic view of the cohesion evolution as a function of the angle between the normal vector to bedding plane and the direction of major principal stress…….94

Figure 97: Evolution of fracture aperture with strains (a) in a potentially fractured rock and (b) in an initially fractured rock.....96

Figure 98: Water pressure and suction fields after ventilation phase....97

Figure 99: Water pressure and displacement evolutions with time.....98

Figure 100: Damage observed in situ in HGA microtunnel.....98

Figure 101: Influence (a) of the initial degree of saturation in the injection interval and (b) of the presence of an excavated damaged zone around the borehole on the numerical results of the gas pressures in the injection interval 99

Figure 102: (a) Influence of the gas relative permeability function of the undisturbed host rock on the numerical results of the gas pressures in the injection interval and (b) Gas permeability vs. Degree of saturation relationship tested 100

Figure 103: Time evolution of pore pressures in the injection interval – Comparisons between experimental and 3D numerical results 100

Figure 104: Gas flows profiles at different gas injection peak – 1D modelling……101

Figure 105: Pre-existing fracture and distribution of the degree of saturation, gas permeability and gas pressure at different increasing gas injection stages.....103

Figure 106: Gas outflow: comparison between experimental and numerical results (a) with two-phase flow model and (b) with embedded fracture model with and without considering the evolution of air entry pressure.....103

Figure 107: Gas outflow: comparison between experimental and numerical results with embedded fracture model (a) without and (b) with considering the maximal opening threshold strain ε1 (ε0=6.4 10^{-4} - ε1=4.9 10^{-4} – Pr,0=5 MPa – λ=6700)……104

Figure 108: (a) New pre-existing fracture geometry and (b) Gas outflow: comparison between experimental and numerical results with embedded fracture model for this new geometry (ε0=6.4 10^{-4} - ε1=4.9 10^{-4} – Pr,0=4MPa – λ=7000 for increasing stages and λ=4200 for decreasing stages) 104

TABLES

Table 1 Dimensions and basic properties of the Callovo-Oxfordian claystone test material from pre-test measurements of water content from off-cut material adjacent to the core. An assumed specific gravity for the mineral phases of 2.70 Mg.m-3 (Zhang *et al.* 2007) was used. 5

Table 2 Summary of experimental history for test SPP_COx-1. 6

Table 3 Summary of experimental test history.....10

Table 4 Dimensions and basic properties of the Callovo-Oxfordian claystone test material (sample SPP_COx-2). The data from pre-test measurements of water content from off-cut material adjacent to the core, data for final post-test measurement are directly from the test sample. An assumed specific gravity for the mineral phases of 2.70 $Mg.m^{-3}$ (Zhang *et al.* 2007) was used in these calculations. 19

Table 5 HG-A experiment chronology. 44

Table 6 - Hydro-mechanical parameters for Argilite and Chamber.....86

Executive summary

This report summarises work undertaken within Work Package (WP) 4 of the FORGE (Fate Of Repository GasEs) Project, examining the impact of tunnel and deposition hole construction on the hydromechanical and transport behaviour of host rock. The WP is split into three components; (i) laboratory scale measurements; (ii) field scale measurements; (iii) numerical modelling. The WP was comprised of eight institutions located in six European countries. Salient results from these activities are summarised in the proceeding chapters, with data and outputs from this WP used across the FORGE project in the development and validation of process models aimed repository performance assessment. Outputs from this study have also been integrated into the state-of-the-art summary report prepared by WP1 (Norris et al., 2013).

1. Introduction

Construction of any underground opening results in a re-distribution of the local stress field. At depth it is possible to remove mass from the system (e.g. tunnelling), but it is not possible to remove the stress. Therefore the rock surrounding the opening has to accommodate the load that was originally borne by the removed rock, leading to a localised stress concentration. In most geological setting, rocks at depth are at a point of limiting equilibrium (Engelder, 1992), i.e. they are at a stress state just short of failure. Therefore, any stress re-distribution is likely to result in localised deformation and possible failure of the host rock.

Failure is usually observed in the form of a complex fracture network, which is heterogeneous in distribution around a circular tunnel opening because of the anisotrpic stress distribution. The orientation of stress with respect to the fracture network is known to be important. The complex heterogeneous stress trajectory and heterogeneous fracture network results in a broad range of stresses and stress directions acting on the open fracture network. During the open stage of the repository, stress will slowly alter as shear movements occur along the fractures, as well as other time-dependent phenomena. As the repository is back filled, the stress field is further altered as the backfill settles and changes volume due to resaturation. Therefore, a complex and wide ranging stress regime and stress history will result. As such, there is a need to understand the roles of the stress tensor, the stress path and associated mechanical deformation in determining permeability changes affecting the sealing efficiency of the host rock. The work package was split into three main areas, laboratory, field and numerical simulation. The objectives of this integrated work package are:

1. perform laboratory scale experiments to: (a) provide data to test, develop and validate theoretical frameworks and predictive tools to analyse the effects of the stress tensor, the stress path and associated mechanical deformation in determining permeability changes affecting the water and gas sealing efficiency of the host-rock following repository closure, (b) examine the role of the stress tensor orientation with fracture orientation and examine the conditions under which fractures become conductive, (c) examine possible radionuclide movement in an artificially damaged plastic clay formation (Boom Clay) supported by X-ray tomographic techniques (a technique successfully applied in the SELFRAC Project), (d) examine the permeability evolution of the seal plug/host rock interface supported by X-ray tomographic imaging of test cores
2. perform field-scale experiments to: (a) provide a comprehensive insight into the hydro-mechanical behaviour of a fractured EDZ in an indurated mudrock formation (Opalinus Clay) in transporting gas along the backfilled tunnels and seals; (b) examine EDZ-sealing, radionuclide (Radionuclide) migration and gas movement in a plastic clay formation (Boom Clay) simulating the expected sequence of phenomena in a medium-level waste (MLW) repository that could lead to gas-driven radionuclide transport; (c) investigate the hydro-mechanical behaviour of the EDZ in a disturbed crystalline rock formation (granite) and its role in the movement of repository gases; (d) examine issues of up-scaling from laboratory to field-scale experiments
3. Undertake detailed numerical modelling of laboratory and field scale experiments with particular emphasis placed on the assessment and application of constitutive models to describe hydraulic and gas flow properties in a clay-based EDZ. This will be facilitated through the development of strong interactive links between modeling and experimental teams.

The following chapters of this report detail the laboratory, field and numerical studies undertaken to examine issues of gas flow, at different scales, in the EDZ surrounding a GDF.

2. Laboratory Experiments

2.1 EFFECT OF STRESS FIELD AND MECHANICAL DEFORMATION (BGS)

In a geological disposal facility (GDF) for radioactive waste, corrosion of metallic materials under anoxic conditions combined with the radioactive decay of the waste and the radiolysis of water, will lead to the formation of hydrogen. A full understanding of the migration behaviour of this gas is of fundamental importance to the development of the GDF. If the rate of gas production exceeds the rate of gas diffusion within the pores of the barrier or host rock, a discrete gas phase will form (Weetjens & Sillen, 2006; Ortiz *et al*., 2002; Wikramaratna *et al*., 1993). If this occurs, capillary restrictions (Aziz & Settari, 1979) on the movement of gas will result in the build-up of pressure to a critical value when pressure becomes sufficiently large for it to enter the surrounding material and move through advective processes.

To accurately predict the movement of gas through argillaceous materials (Neretnieks, 1984; Kreis, 1991; Askarieh *et al*., 2000; Ekeroth *et al*., 2006; Smart *et al*., 2006), it is first necessary to define the correct conceptual model that best represents the empirical data. In a clay-based GDF four primary phenomenological models can be defined to describe gas flow as proposed by Marschall *et al*. (2005; Figure 1):

1. Gas movement by solution and/or diffusion governed by Henry's and Fick's Laws respectively within interstitial fluids along prevailing hydraulic gradients;
2. Gas flow in the original porosity of the fabric governed by a generalised form of Darcy's Law, commonly referred to visco-capillary (or 2-phase) flow;
3. Gas flow along localised dilatant pathways (micro-fissuring), which may or may not interact with the continuum stress field, the permeability of which is dependent on an interplay between local gas pressure and the effective stress state; and
4. Gas flow along macro fractures similar in form to those observed in hydrofracture activities during reservoir stimulation, where fracture initiation occurs when the gas pressure exceeds the sum of the minor principle stress and tensile strength.

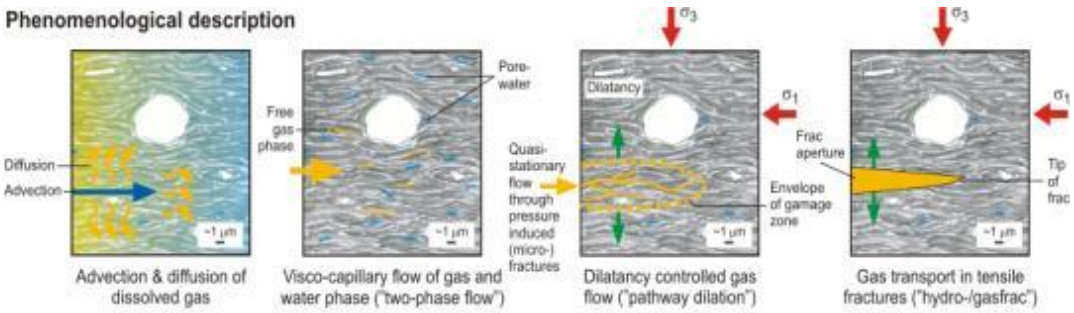

Figure 1 Description of four main processes of gas movement in clays (after Marschall et al., 2005).

To investigate which mechanism(s) control the advective movement of gas, an experimental programme was devised to carefully examine the volumetric deformation of Callovo-Oxfordian claystone (COx). The exact mechanisms controlling gas entry, flow and pathway sealing in clay-rich media are not fully understood and the "memory" of such pathways could impair barrier performance.

Under certain stress conditions, mudrock deformation will result in dilation (net volume increase) or contraction (net volume decrease). The boundary between these conditions is referred to as the dilatancy boundary and this plots as a point in the mean stress (p) versus

deviatoric stress (q) space (see Figure 2), or a line when specific volume (v) is used as a third axis. Critical state mechanics (Roscoe *et al*., 1958; Figure 2) shows that complex deformation can be described by a series of yield surfaces in the $p' - q' - v$ parametric space. The critical state approach has been shown to be effective in soils (Roscoe & Burland, 1968; Schofield & Wroth, 1968).

There are many examples within the literature of studies on soils and clays that demonstrate the validity of critical state theory and the use of the Cam-clay derived models; including: Adams & Wulfsohn (1997), Byerlee (1967), Cotecchia & Chandler (2000), Cuss & Rutter (2003), Cuss (1999); Diaz-Rodriguez *et al.* (1992), Hudson & Harrison (1997), Kirby & O'Sullivan (1997), Kirby (1994), Maâtouk *et al.* (1995), Maltman (1994), Mitchell (1970), Ohnaka (1973), Petley (1999), Schofield (1998), Tavenas & Leroueil (1977), Wheeler & Sivakumar (1995), Wong *et al*. (1997), Zhu & Wong (1997[a,b]).

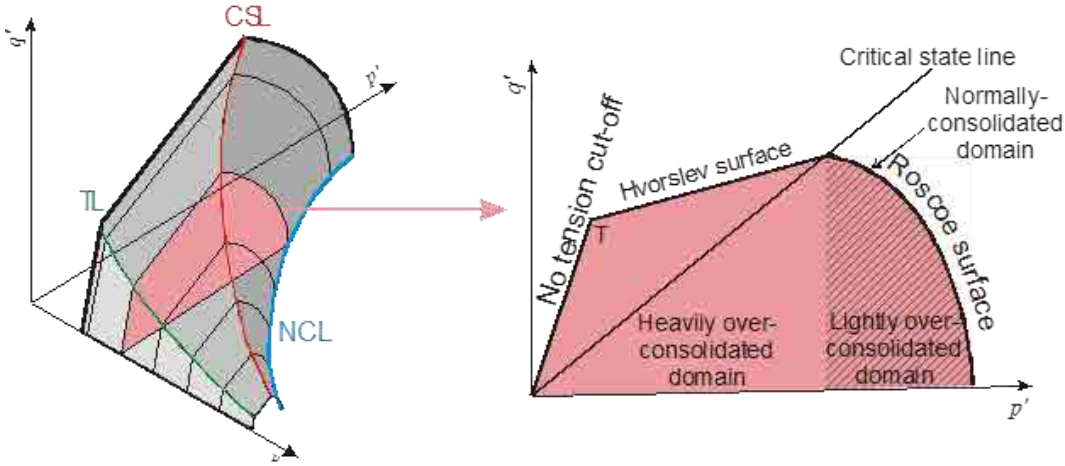

Figure 2 The critical state model of soil mechanics, showing the relationship of the tension line (TL), normal consolidation line (NCL) and critical state line (CSL). These lines bound the Hvorslev and Roscoe surfaces in the *p'* - *q'* space.

The relationship between effective stress and permeability for different rock types has been widely reported (e.g. Zoback and Byerlee 1975; Walsh and Brace 1984; Morrow *et al.*, 1984; David *et al.*, 1994; Dewhurst *et al*., 1999[a]; Dewhurst *et al*., 1999[b]; Katsube, 2000; Katsube *et al*., 1996[a]; Katsube *et al*., 1996[b]; Kwon *et al*., 2001; Neuzil *et al*., 1984). However, few studies have been conducted looking at changes in transport properties as samples are taken along a stress path through to failure. Calibration of the critical state model can be undertaken by taking samples of COx along predefined stress paths extending to the yield surfaces while measuring the resulting changes in permeability (both aqueous and gaseous).

Objectives

The main output of the research is an enhanced process understating in Engineering Disturbed Zone (EDZ) mudrock environments, through the critical examination and subsequent validity of key geomechanical relationships applied to mudrock deformation and its role in the temporal evolution of permeability during the operational and post closure repository phases.

The original objective of the experimental programme was to examine the impact of changing effective stress (e.g. caused by the construction of a disposal/storage facility) and its effect on the sealing characteristics of the Callovo-Oxfordian (COx) claystone. As such, there is a need to understand the roles of the stress tensor, the stress path and associated mechanical deformation in determining permeability changes affecting the sealing efficiency of the claystone. A secondary objective of the experimental programme was to determine the

volumetric deformation observed during the onset of gas flow and to discriminate between flow mechanisms.

Two experiments were conducted. The first test, SPP_COx-1, aimed to define the bulk volumetric deformation of a sample during progression along a stress path through to ultimate failure. Unforeseen was the strong observed time-dependent deformation caused by changes of boundary condition. This meant that mechanical tests had to have long test stages in order to allow the COx to fully equilibrate to the boundary conditions. The second test conducted, SPP_COx-2 was a gas entry experiment, which had a much greater gas entry pressure than had been anticipated. This proved problematic as a gas pressure close to confining pressure results in little scope to alter the stress path and as a result a stress-path leading to failure could not be achieved. Prior to altering the stress field, flow in the sample stopped and the conductive pathways self-sealed; this too was unexpected. Therefore metrology limited the ability of the study to fully achieve the primary aims and as a result the secondary aim of the study became the focus of investigation.

Callovo-Oxfordian claystone (COx)

The composition of the Callovo-Oxfordian claystone (150-160 Ma) can be divided in to three main constituents; clay, silt and carbonate. Wenk *et al.* (2008) reports these constituents (at the Bure site) as follows; clay 25-55 wt%, 23-44% carbonates and 20-31% silt (essentially quartz + feldspar). Clay minerals are reported to include illite and illite-smectite with subordinate kaolinite and chlorite. In the upper half of the formation the illite-smectite is disordered and contains 50-70% smectite interlayers, whilst in the lower half the illite-smectite is ordered (R=1 type) with lower contents (20-40%) of smectite interlayers (Wenk *et al.*, 2008). Beds can contain common organic matter.

Two test samples were prepared when required. The preserved T1-cell core barrels were cut to approximately 100mm length using a dry-cut diamond encrusted bladed saw. For test sample SPP_COx-1 a 56mm diameter sample was produced by a combination of dry core-drilling (with gas flushing and vacuum removal of fines) and diamond slicing. The ends of the sample were ground flat and parallel to minimise “end-effects” during testing. Sample SPP_COx-2 was produced using a modified methodology. A 100m section of complete core was placed in a lathe and slowly trimmed down to a diameter of 56mm to get a good even surface finish and the sample ends were lathed flat and parallel. Sample off-cuts were used to determine the geotechnical properties of the starting material; Table 1 summarises the parameters of the test material.

Experimental set-up

The bespoke Stress-Path Permeameter (SPP, Figure 3) was designed and used to investigate water and gas (helium) flow in COx. The SPP is an evolution of the elastimeter apparatus that has been shown to perform well (Horseman *et al.*, 2005) and was specifically designed to resolve very small volumetric (axial and radial) strains potentially associated with the onset of gas flow. The SPP comprises 6 main components:

1) The specimen, surrounded by a modified flexible Hoek sleeve and main pressure vessel body.

2) Three “dash pots” that are mounted along the radial mid-plane of the sample which directly measure the radial strain of the sample. The dash pots are pressure balanced in order to reduce the force imposed upon the sample and to make sure the push-rods are not simply pushed out of the pressure vessel.

3) An axial load system comprising of an Enerpac single acting hydraulic ram pressurised by an ISCO-500 series D syringe pump. This is connected via an axial strain jig to a Global Digital Systems optical encoder for measuring linear displacement accurate to 0.003 mm. Miniature load cells are located at the piston ends to measure stress at the sample ends.

4) A confining pressure system using an ISCO-500 series D syringe pump and glycerol confining medium allowing radial strain measurements to be calculated through volume change.

5) A pore pressure system comprising two ISCO-100 series D syringe pumps to create pore fluid pressure and monitor back pressure. The injection media can be either water or gas (usually Helium).

6) A state-of-the-art custom designed data acquisition system facilitating the remote monitoring and control of all experimental parameters, with data recorded every 2 minutes throughout the test programme.

	Units	Value	Value
Sample reference		SPP_CoX-1	SPP_COx-2
Location		Bure URL, France	Bure URL, France
Borehole / drill core		OHZ1201 / EST30340	OHZ1201 / EST30341
Core direction		Parallel to bedding	Parallel to bedding
Average length	mm	76.63 ± 0.02	82.45 ± 0.03
Average diameter	mm	55.50 ± 0.01	55.85 ± 0.04
Volume	m^3	1.854×10^{-4}	2.020×10^{-4}
Average weight	g	455.6	495.02
Density	$g.cc^{-1}$	2.458	2.451
Grain density	$g.cc^{-1}$	2.7	2.7
Moisture weight	g	24.6	28.7
Moisture content	%	5.7	6.2
Dry weight	g	431	466
Dry density	$g.cc^{-1}$	2.33	2.31
Void ratio		0.166	0.174
Porosity	%	14.2	14.8
Saturation	%	93	96

Table 1 Dimensions and basic properties of the Callovo-Oxfordian claystone test material from pre-test measurements of water content from off-cut material adjacent to the core. An assumed specific gravity for the mineral phases of 2.70 Mg.m-3 (Zhang *et al.* 2007) was used.

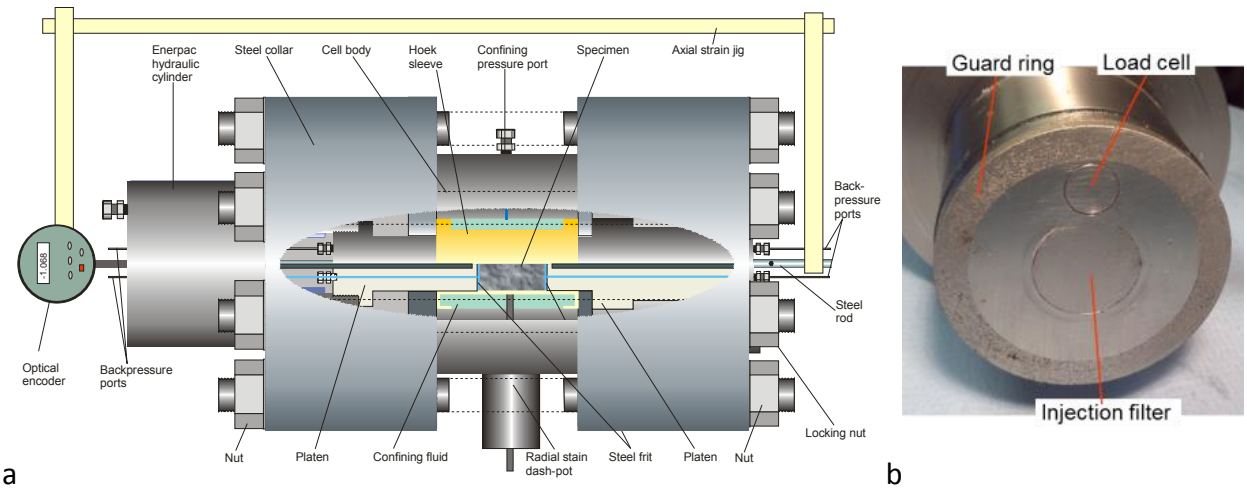

a b

Figure 3 The Stress Path Permeameter (SPP): a) schematic; b) photo of the end platen showing the injection filter and guard ring arrangement.

A cylindrical rock specimen was positioned between two stainless steel platens and jacketed in a flexible Hoek sleeve to exclude the confining fluid. The inlet and outlet zones for water flow to and from the specimen are provided by stainless-steel discs, nominally 20 mm in diameter and 3 mm depth. Guard rings (Figure 3b) of 6mm thickness and 2 mm depth are located on the outer diameter of the platens, allowing pore pressure to be measured in two locations on the faces of the sample.

The stainless steel load platens are in direct contact with the sample transmitting the axial force generated by the Enerpac ram directly to the specimen. Each platen has two ports facilitating flushing of the system and the removal of residual air prior to testing. Retaining collars and axial tie-rods lock the system components together to provide a rigid test rig; these were pre-tensioned at 300 Nm.

The experimental rig was completed by a number of pressure sensors and thermocouples. For water flow experiments a chemically balanced synthetic pore fluid similar to that found at Bure was manufactured at BGS with the following composition: 227 $mg.l^{-1}$ Ca^{2+}, 125 $mg.l^{-1}$ Mg^{2+}, 1012 $mg.l^{-1}$ Na^{+}, 35.7 $mg.l^{-1}$ K^{+}, 1266 $mg.l^{-1}$ SO_4^{2-}, 4.59 $mg.l^{-1}$ Si, 9.83 $mg.l^{-1}$ SiO_2, 13.5 $mg.l^{-1}$ Sr, 423 $mg.l^{-1}$ total S, and 0.941 $mg.l^{-1}$ total Fe.

Test SPP_COx-1 (mechanical deformation)

The first test (SPP_COx-1) was a relatively quick test in order to confirm the location of the Hoek-Brown failure envelope. The stress level at which failure occurred would be important in the following gas experiment (SPP_COx-2), which would follow the same stress path but with five detailed steps designed to observe the changes in permeability during deformation.

The sample was loaded into the SPP on the 5th May 2010. Considerable care was taken in order to achieve loading conditions equivalent to in situ conditions; confining pressure = 11.5 MPa, axial load = 12.5 MPa and pore-water pressure = 4.5 MPa (see Table 2).

Step	Confining pressure (MPa)	Pore Pressure (MPa)	Axial load (MPa)	Differential load (MPa)	Differential stress Q (MPa)	Effective mean stress P' (MPa)	Start time (day)	End time (day)
Swell	11.5	4.5	12.5	1.0	1.0	7.33	0	15.1
1	12.5	4.5	13.0	0.5	0.5	8.17	15.1	17.9
2	12.0	4.5	13.5	1.5	1.5	8.00	17.9	22.1
3	11.5	4.5	14.0	2.5	2.5	7.83	22.1	26.9
4	11.0	4.5	14.5	3.5	3.5	7.67	26.9	35.1
5	10.5	4.5	15.0	4.5	4.5	7.50	35.1	41
6	10.0	4.5	15.5	5.5	5.5	7.33	41.0	15.9
7	9.5	4.5	16.0	6.5	6.5	7.17	45.9	50.1
8	9.0	4.5	16.5	7.5	7.5	7.00	50.1	60.9
9	8.5	4.5	17.0	8.5	8.5	6.83	60.9	67.9
10	8.0	4.5	17.5	9.5	9.5	6.67	67.9	73.9
11	7.5	4.5	18.0	10.5	10.5	6.50	73.9	80.9
12	7.0	4.5	18.5	11.5	11.5	6.33	80.9	88.0
13	6.5	4.5	19.0	12.5	12.5	6.17	88.0	94.9
14	6.0	4.5	19.5	13.5	13.5	6.00	94.9	101.9
15	5.5	4.5	20.0	14.5	14.5	5.83	101.9	108.9
16	5.0	4.5	20.5	15.5	15.5	5.67	108.9	123.2

Table 2 Summary of experimental history for test SPP_COx-1.

Figure 4 shows the results of test SPP_COx-1, with considerable time-dependent deformation observed. During the initial stage of the test the sample swelled and the apparatus successfully measured this deformation. During the successive stages the sample deformed quickly to the

change in stress state but showed considerable time-dependent creep during all stages of the test. As the test progressed the amount of creep observed increased (Figure 4c,d). However, during each step equilibrium had not been achieved so this may be superposition of deformation from stage to stage. This hypothesis is strengthened by the observations of stages three and seven (Figure 4d), which were prolonged stages and were followed in successive steps by a decrease in time dependent deformation. A certain component of the observed creep is caused by pore pressure, which due to the low permeability of the sample takes time to homogenise within the sample, i.e. is the result of drainage. A secondary component of creep is caused by the time-dependent deformation (true creep) of the clay minerals.

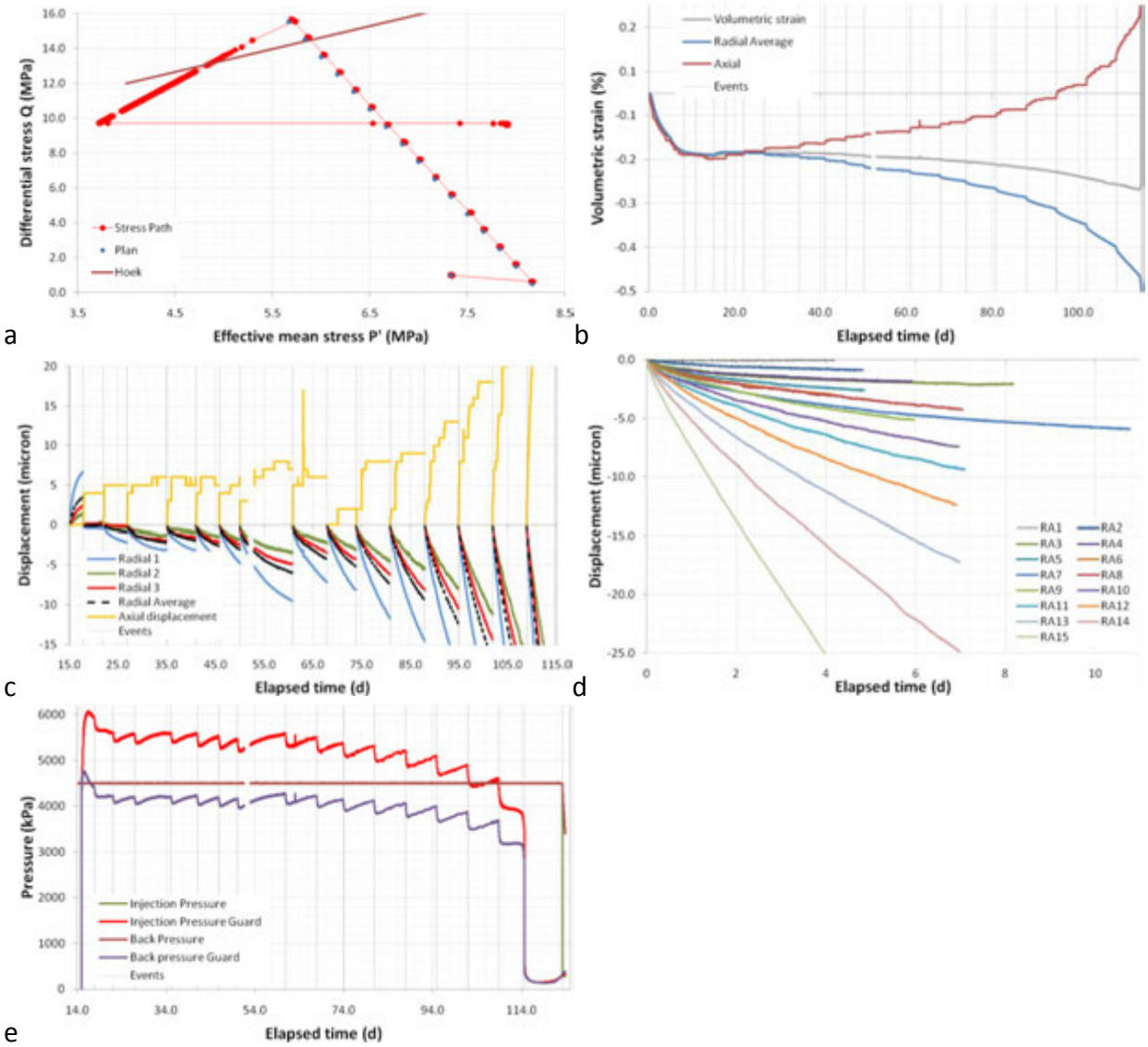

Figure 4 Results for test SPP_COx-1; a). stress path; b). strain; c). time-dependent radial and axial displacement observed for each stage; d). time-dependent radial displacement for each step against time of step; and e). guard-ring porewater pressure.

There are several implications of the observed creep. For experimental studies it means that each stage of testing has to be conducted to the point of equilibrium. This greatly lengthens the time each step has to be conducted. The observed creep also places a question as to whether deformation in COx is rate-dependent, as seen in Kimmeridge caly (Swan *et al.*, 1989). The time-dependency suggests that heterogeneous pore pressure distributions are created in

deforming samples and that failure may result at different stress levels. Therefore a test conducted quickly may predict a weaker strength than one conducted slowly. This suggests that care should be taken when comparing data from different sources that have used different apparatus, different sized samples, drained or undrained conditions etc. This may explain why failure occurred at a stress-state higher than that predicted for COx by the Hoek-Brown failure criterion. It is also noted that sample failure occurred 5.5 days into a constant stress-state step (static boundary condition).

The time-dependent nature of deformation observed and possible rate-dependency of deformation also means that experimental data may not be applicable for all applications. For instance, tunnelling results in a rapid change in stress where the COx is unable to sufficiently drain. Convergence post-closure is a much longer process where drainage can be accommodated. Therefore long-term experiments may over-predict the strength and gas entry pressure for tests representative of stress-paths created during tunnelling and short-term experiments will under-predict strength and gas entry pressure for post-closure scenarios.

The observed behaviour of pore pressure at the guard rings is complex (Figure 4e). For all stress steps the pore pressure initially drops and within two days reaches a minimum. During each step the axial load is increased and the confining pressure is lowered. It is likely that the pore pressure response is showing that dilation is occurring which is causing fluid to flow away from the corners of the sample where the guard rings are located. Once the pressure minimum has been reached, in all but one of the steps the pressure begins to rise. This suggests that the deformation at first results in pore-pressure moving away from the sample corners and that with time it is drawn back to the corners. This could either be the fluid expelled from the corners returning or pore fluid from the injection point flowing into the now lower-pressure zone. In the early stages of the test (stage 1-7) it was observed that pore pressure generally returned to that seen at the start of the stage. In later stages it was observed that full pressure recovery was not achieved and over time the pore pressure at the guard-rings reduced. This may be the result of conducting each step for insufficiently time, but may also be indicative of permanent damage and/or dilation occurring to the sample. The observations at the guard ring show that pore pressure distribution within the sample is complex.

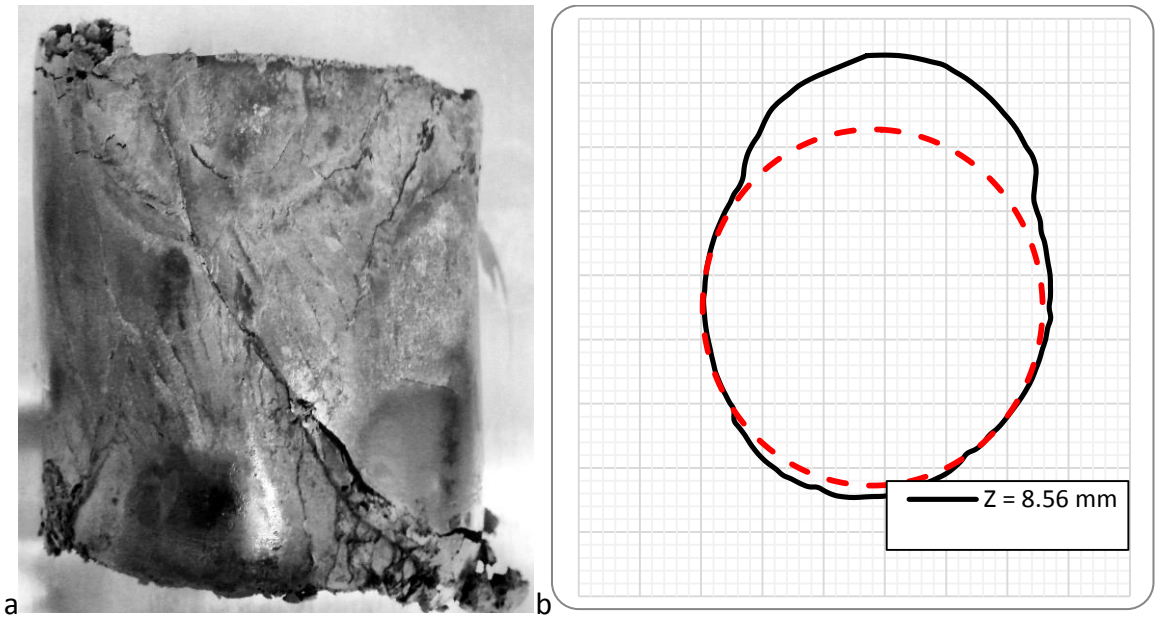

Figure 5 Post-test observations of SPP_COx-1; a). photograph of the test sample clearly showing the main fracture surface; b). circumference of the final sample.

Considerable anisotropy was observed in radial deformation (ε_{rad}); $\varepsilon_{rad1} > \varepsilon_{rad3} > \varepsilon_{rad2}$. This anisotropy will have influenced the formation of the fault in the sample; however the orientation of the fracture was not recorded with respect to the orientation of Radial 1-3. The anisotropy observed may be the result of the sample being oriented parallel to bedding and differences in deformation of the layers seen within COx.

The final test sample showed considerable deformation, with SPP_COx-1 failing following the formation of a fracture/fault oriented approximately 30° to the length of the sample (Figure 5). It is observed that this fracture appears to intersect both corners of the sample and this may be the result of edge effects created by friction acting along the ends of the sample between rock and steel platten. A series of fractures parallel to the main fracture could be seen, as well as a series of conjugate fractures.

Test SPP_COx-2 (gas transport)

Test SPP_COx-2 lasted a total of 566 days, with Figure 6 showing the test result data for the complete test history and Table 3 summarising the test stages. The three stages of the test can be seen (initial swelling stage, hydraulic testing, gas injection testing). The gas injection testing can be further split into stages of (i) gas flow initiation, (ii) gas flow shut-off, (iii) attempted gas flow re-initiation by raising injection pressure, and (iv) attempted gas flow re-initiation by lowering back pressure.

The first stage of testing imposed stress conditions similar to *in situ* conditions for borehole OHZ1201 (σ_1 = 13 MPa, σ_2 = σ_3 =12.5 MPa, P_p = 4.5 MPa) and observed swelling for 21 days. Chemically balanced water was injected at both ends of the sample in order to re-establish full sample saturation, minimise air content of pipework & pore network, and to minimise chemically driven swelling of the sample. During the resaturation stage, the inlet/outlet and guard rings were used to hydrate the sample and ensured that the air content of all pipework and pressure transducers was negligible. During initial pressurization ~ 0.11 % volumetric strain was observed and during the swelling stage 0.12 % dilational volumetric strain was recorded.

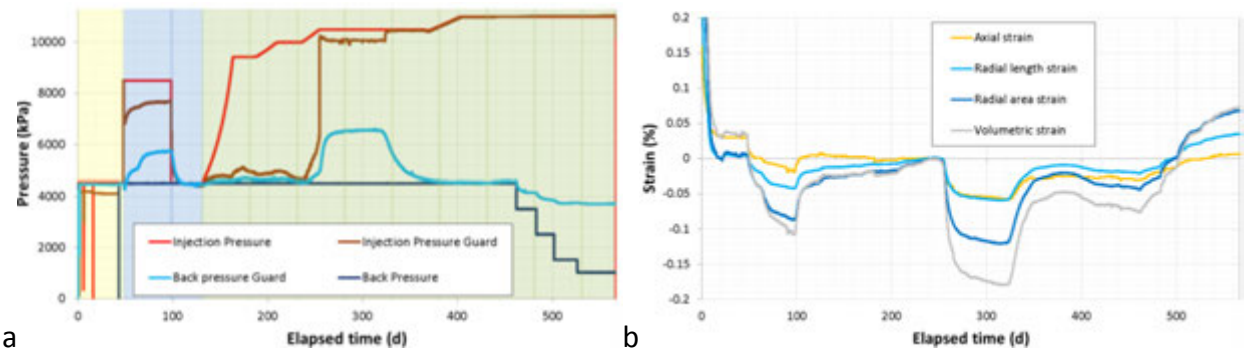

Figure 6 Data for the complete test history of test SPP_COx-2; a) pressure history; b) sample strain.

Stage	Description	Axial stress (MPa)	Confining stress (MPa)	Injection pore pressure (MPa)	Back pore-pressure (MPa)	Test time at start (days)	Length of stage (days)
1	Saturation and swelling	12.5	11.5	4.5	4.5	0.1	21.7
2	Equilibration	13.0	12.5	4.5	4.5	21.8	26.1
3a	Hydraulic testing	13.0	12.5	8.5	4.5	47.9	50.1
3b	Hydraulic testing	13.0	12.5	4.5	4.5	98.0	29
4a	Gas injection ramp	13.0	12.5	4.5–9.5	4.5	127.0	35.3
4b	Gas injection at constant pressure	13.0	12.5	9.5	4.5	162.3	25.5
4c	Gas injection ramp	13.0	12.5	9.5–10.0	4.5	187.8	22.2
4d	Gas injection at constant pressure	13.0	12.5	10.0	4.5	210.0	26.1
4e	Gas injection ramp	13.0	12.5	10.0–10.5	4.5	236.1	18.9
4f	Gas injection at constant pressure	13.0	12.5	10.5	4.5	255.0	~65
4g	Gas shut-off	13.0	12.5	10.5	4.5	~320	~49
4h	Gas injection ramp	13.0	12.5	10.5–11.0	4.5	368.8	34.3
4i	Gas injection at constant pressure	13.0	12.5	11.0	4.5	403.1	58.8
4j	Lowering of back pressure step 1	13.0	12.5	11.0	3.5	461.9	21.1
4k	Lowering of back pressure step 2	13.0	12.5	11.0	2.5	483.0	18.8
4l	Lowering of back pressure step 3	13.0	12.5	11.0	1.5	501.8	24.2
4m	Lowering of back pressure step 4	13.0	12.5	11.0	1.0	526.0	40.8
End	Test end	0	0	0	0	566.8	/

Table 3 Summary of experimental test history.

A two-stage constant head test was conducted; pore pressure was raised to 8.5 MPa and the guard-rings were isolated. Both injection (IGR) and back-pressure (BGR) end guard rings showed an initial decrease in pore pressure, which within a couple of days started to recover in

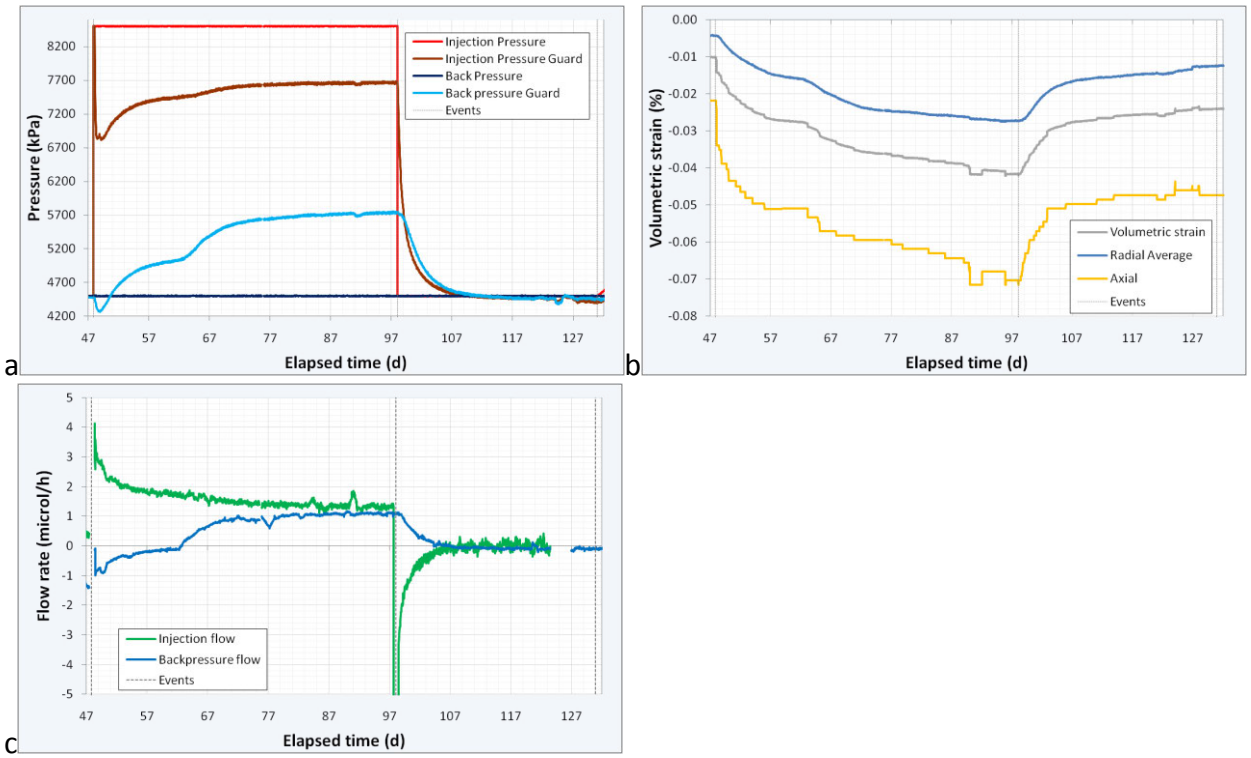

Figure 7 Data for the hydraulic testing stage of the test history; a). pressure history; b). sample strain; and c). flow data.

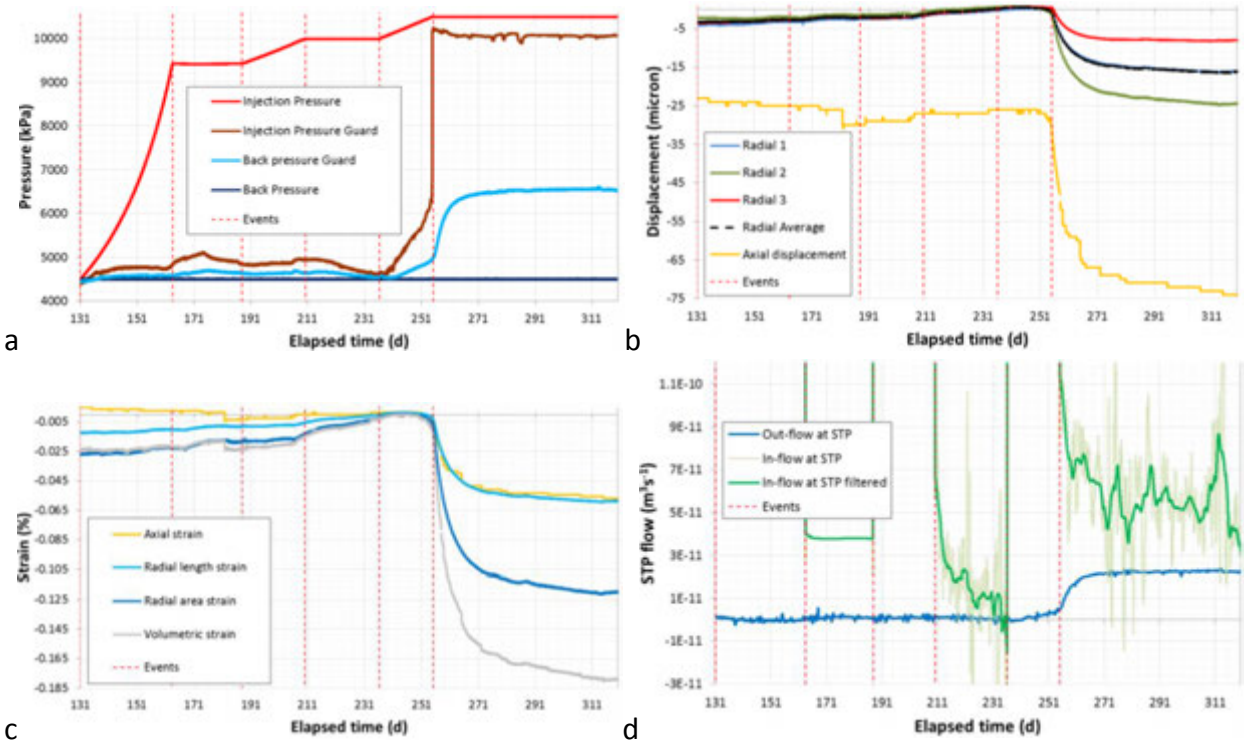

Figure 8 Data for the gas testing stage of the test history up until the attainment of near-steady-state flow; a). pressure history; b). radial and axial displacement; c). sample strain; and d). flow data.

pressure and equilibrated. The IGR pressure stabilised approximately 1 MPa below the injection pressure, whereas BGR was approximately 0.5 MPa above back pressure. Flow data shows that in the first 7 days of the hydraulic test there was no flow at the back-pressure end of the sample. On Day 62 the backpressure flow started to increase, reaching a steady state of approximately 1 µl.hr^{-1} by Day 87. At the onset of flow out of the sample the bulk sample volume increased, resulting in an additional 0.015 % volumetric strain (~ 30 µl). The onset of flow resulted in IGR and BGR changing at both sample ends with BGR having a larger increase of ~0.7 MPa. Injection pore pressure was lowered to 4.5 MPa on Day 98. Over the remaining 32 days of the low pressure constant head hydraulic test stage the strain was only partially recovered. This was accompanied by the slow decrease in IGR and BGR; IGR decreased much slower than BGR. During this test stage an additional 0.014 % of dilational strain occurred.

Gas testing started on Day 131 with gas entry achieved after three constant-flow ramp stages. During the increase in gas pressure from 4.5 MPa to 9.5 MPa volumetric strain was negligible and essentially iso-volumetric. Small amounts of volumetric strain (0.02 %, contraction) was seen by the time of gas entry; therefore gas pressure resulted in only localised changes in pore pressure close to the injection port as confirmed by the small changes in IGR pressure.

A four stage conceptual model has been developed in order to describe all features observed in COx during the initiation of gas flow (Figure 9).

Stage 1 of gas migration (Figure 9a)**:** At about Day 220 gas started to enter the sample at a gas pressure of 10 MPa. Gas migrated as far as the load-cell, where it was identified as an anomalous reading. It is probable that gas migrated along a single bedding layer of the parallel to bedding oriented COx sample. Gas propagation was along dilatant pathways that exploited the pore network of the material. The pathways can be visualised as “ruptures” in the pore

network. Around each pathway the fabric would have compressed, which may have led to localised movement of water away from the pathways.

Stage 2 of gas migration (Figure 9b)**:** Gas propagation throughout the sample was migrating further and had reached the corner of the sample, as seen by the onset of pressure rise at the guard ring. The geometry of the SPP apparatus had gas injected horizontally at one end of the sample. Therefore, when gas reached the injection guard-ring it displaced water from the guard-ring into the sample until the guardring was saturated with gas (slug flow). Early in the gas migration water was being displaced into the sample, resulting in small amounts of swelling. This stage was identified by a slow increase in IGR. The start of the stage occurred at Day 237.32 with a second anomalous reading in the injection-end load cell signifying the movement of gas. Pressure in the guard-ring started to increase at Day 238.55. A day later at Day 239.8 the first indiciation of radial deformation was recorded at the mid-plane.

Stage 3 of gas migration (Figure 9c)**:** A large increase in pore pressure at IGR occurred at Day 238.55 and was likely to be the result of a major conductive feature being formed in the sample. As this propagated through the sample it resulted in an acceleration of dilatant deformation. The acceleration of midplane deformation began 32 days after the first indication of gas migration. Radial 2 was the first to show accelerated deformation, followed 0.7 days later by Radial 1 and a further 0.4 days later by Radial 3. Axial deformation did not start to accelerate until 11 days after Radial 2. If the observed radial deformation was derived from water displaced from the guard-ring it would be expected that axial deformation would have reacted first. Therefore the observed dilatancy cannot be attributed completely to swelling. Stage 3 also shows the onset of out-flow from the sample and therefore must indicate gas movement. Although the experimental geometry is likely to result in slug flow, the majority of observed deformation was caused by the dilatant propagation of gas along pathways.

Stage 4 of gas migration (Figure 9d)**:** Gas had propagated through the sample as far as the back-pressure end. The onset of gas reaching BGR at Day 273 indicated that gas was now moving throughout the entire length of the sample. During this stage the sample continued to dilate, which suggests that the number of gas pathways was increasing.

The observed events show that gas reached the injection guard-ring at Day 238.55, dilatancy was first seen at the mid-plane at Day 239.8 and the back-pressure guard ring started to increase at Day 240.5. This means that the pressure pulse propagated at a rate of approximately 37.6 mm/day or 1.6 mm/hr. This is interpreted as being a hydro-mechanical response and is created by a change in effective stress as gas started to propagates into the sample.

The acceleration of strain at the mid-plane occurred at approximately Day 255, whereas pressure at the back-pressure guard ring initiated at Day 240.5 (nearly 15 days previous). This suggests that the back-pressure response was a hydromechanical response, whereas the accelerated dilatation was one of gas movement. The pressure increase in the injection pressure guard-ring was unstable and this was indicative of gas propagation, whereas the pressure increase at the back-pressure guard ring was gradual and suggests that this response was not indicative of gas and was the result of hydromechanical coupling. Gas is inferred as reaching the back-pressure end at Day 273. The acceleration of dilation caused by the propagation of dilatant gas pathways at the midplane and the inferred onset of gas reaching the back-pressure end give a gas propagartion rate of approximately 100 microns/hour. This means that per annum gas may have moved 0.85 m.

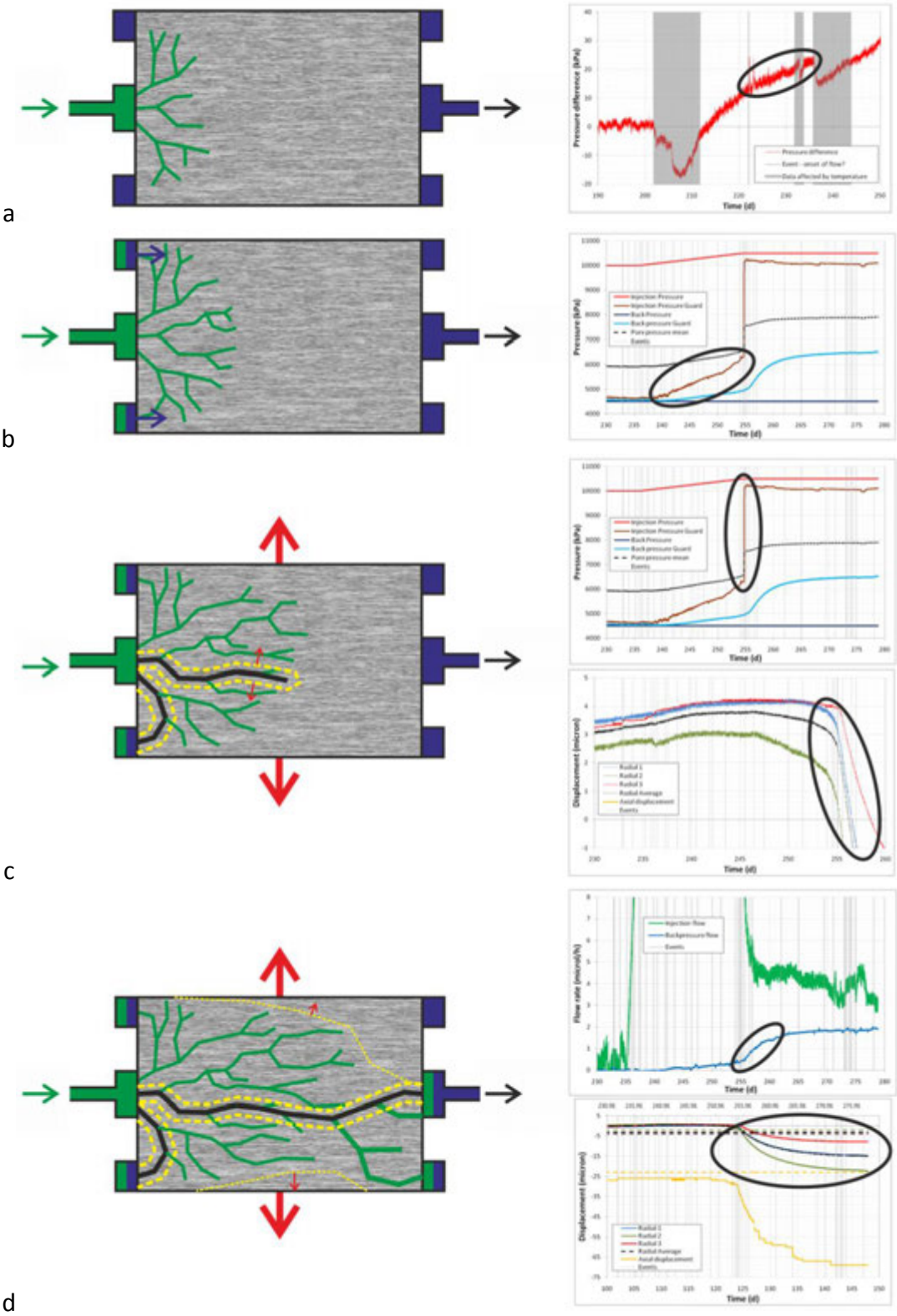

Figure 9 Four stage model of onset of gas flow and experimental observations of processes occurring. Refer to text for detailed explanation.

The interpretation has three components; 1) a response caused by the expulsion of water from the injection guard ring due to the geometry of the test set-up and the resultant swelling; 2) a hydro-mechanical response as a result of the change of pore pressure from ambient (4.5 MPa) to the injection gas pressure (10 MPa); 3) a dilatant response as gas propagates through the sample. It is challenging to decouple all three components fully. However, taking all observations into consideration and comparing with observations from other tests at BGS and elsewhere (Harrington *et al*. 2012, Cuss *et al*., 2013, Angeli *et al*., 2009; Autio *et al*., 2006; Gallé

& Tanai, 1998; Harington & Horseman, 1997, 1999; Harrington et al., 2009, 2012 (a), 2012 (b); Horseman *et al*., 1996, 1999, 2004; Ortiz *et al*., 1996, 2002) a three stage model has been proposed for gas flow in COx:

Stage 1: Gas begins to enter the sample at the gas entry pressure along dilatant pathways that exploit the pore network; the pathways can be visualised as "ruptures" in the pore network. As a result of the dilation of the pathways, the fabric surrounding the pathway compresses, which may lead to localised movement of water away from the pathway.

Stage 2: The dendritic network of dilatant pathways propagates further and as a result dilatant deformation and pore-fluid out-flow is observed.

Stage 3: Gas propagation reaches the out-flow of the sample, with gas moving throughout the entire length of the sample. During this stage the sample continues to dilate as the number of gas pathways increases. Stage 3 sees the formation of a major conductive feature connecting both ends of the sample.

The observed dilatant (net volume increase) strain could be interpreted as resultant from a change in effective stress. The injection of gas raised pore pressure from 4.5 MPa to the gas injection pressure (approximately 10.5 MPa). Assuming that the entire pore network of the sample experienced this 6 MPa change in pore pressure, the sample strain would be 78 µl. This is much less (~20 %) of the total sample deformation recorded of 360 µl. However, the experimental set-up measures pore pressure at four locations (injection, injection guard-ring, back-pressure and back-pressure guard ring) and this showed that the bulk sample did not undergo a 6 MPa increase in pore pressure. A mean pore pressure of 7.9 MPa was observed which gives a change in average pore pressure of just 3.4 MPa. This would give an elastic deformation of just 40 µl. Therefore the full deformation seen by the sample cannot be explained by elastic deformation of the sample in response to pore pressure changes.

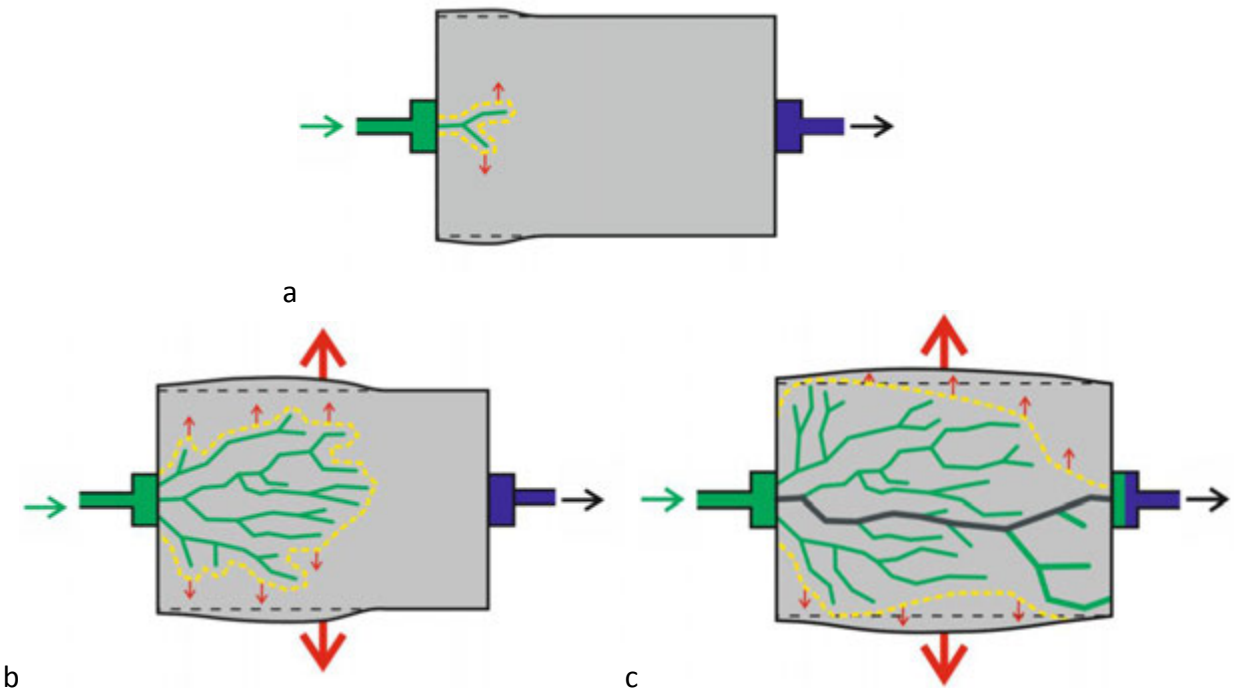

Figure 10 A general model for advective gas flow in Callovo-Oxfordian claystone; a). gas starts to enter the sample; b). a dendritic pattern of gas pathways forms, slowly propagating through the sample; c). gas migration reaches the back-pressure end of the sample.

The recording of pore pressure at four locations shows that pore pressure distribution within the test sample is complex. The guard ring and pressure port are separated by 12 mm and significantly different pressures were observed; at the injection end of the sample 5.3 MPa difference was noted. This demonstrates that pore pressure increase is highly localised and COx is able to sustain considerable pressure gradients over small distances.

Flow shut-off

Prior to achieving steady-state flow and equilibration of volumetric strain the outflow from the sample unexpectedly shut-off (Figure 11). Flow at the injection end of the sample increased and peaked at approximately Day 311 and this may have been the driver for the reduction in out-flow from the sample that begin around Day 320. The reduction in out-flow corresponded with a change in radial strain (contraction of the sample), a reduction in in-flow, and a reduction in pressure in the back-pressure guard ring. A few days following the reduction in out-flow the injection-end guard ring pressure increased to approximately equal the injection pressure; this event corresponds with a short-lived peak in in-flow. This is likely to be the formation of a major conductive pathway between the injection port and the guard ring. Mode-I (pull-apart) type fractures were seen in the sample at the end of the test. Although these would explain the connectivity between the guard-ring and injection port other evidence does not support the formation of a fracture at this time; namely the lack of dilatant deformation seen at the radial mid-plane. There is evidence of multiple pathways forming through the sample and these may have been the cause of the increase in pressure in the guard-ring.

Gas leakage from the experimental apparatus can be discounted as a cause of shut-off; either through the seal between jacket and loading plattens or by diffusion through the Hoek-sleeve. The decommissioning of the test did observe a “frothy” nature to the confining glycerol that may indicate that gas was entering the confining system. However, close examination of all behaviour means that gas leakage can be discounted as the cause of shut-off. At the start of flow reduction it can be seen that in-flow increased, meaning it is possible a fracture or conductive pathway formed at this time at the injection end of the sample. However, following this event, flow at the injection end reduced to a condition of no-flow. If shut-off was the result of gas leakage from the apparatus it would be expected that in-flow would have increased. It would then be expected that the pressure in the conductive pathways would reduce as gas was lost and this could result in the closure of the formed dilated pathways. The reduction in in-flow does not support this hypothesis, nor does the retention of high pressure in the injection guard-ring. The change in confining system volume suggests that no significant gas volume was added to this part of the experimental system. Therefore, although gas leakage from the system cannot be ruled out, it is unlikely to be the cause of shut-off.

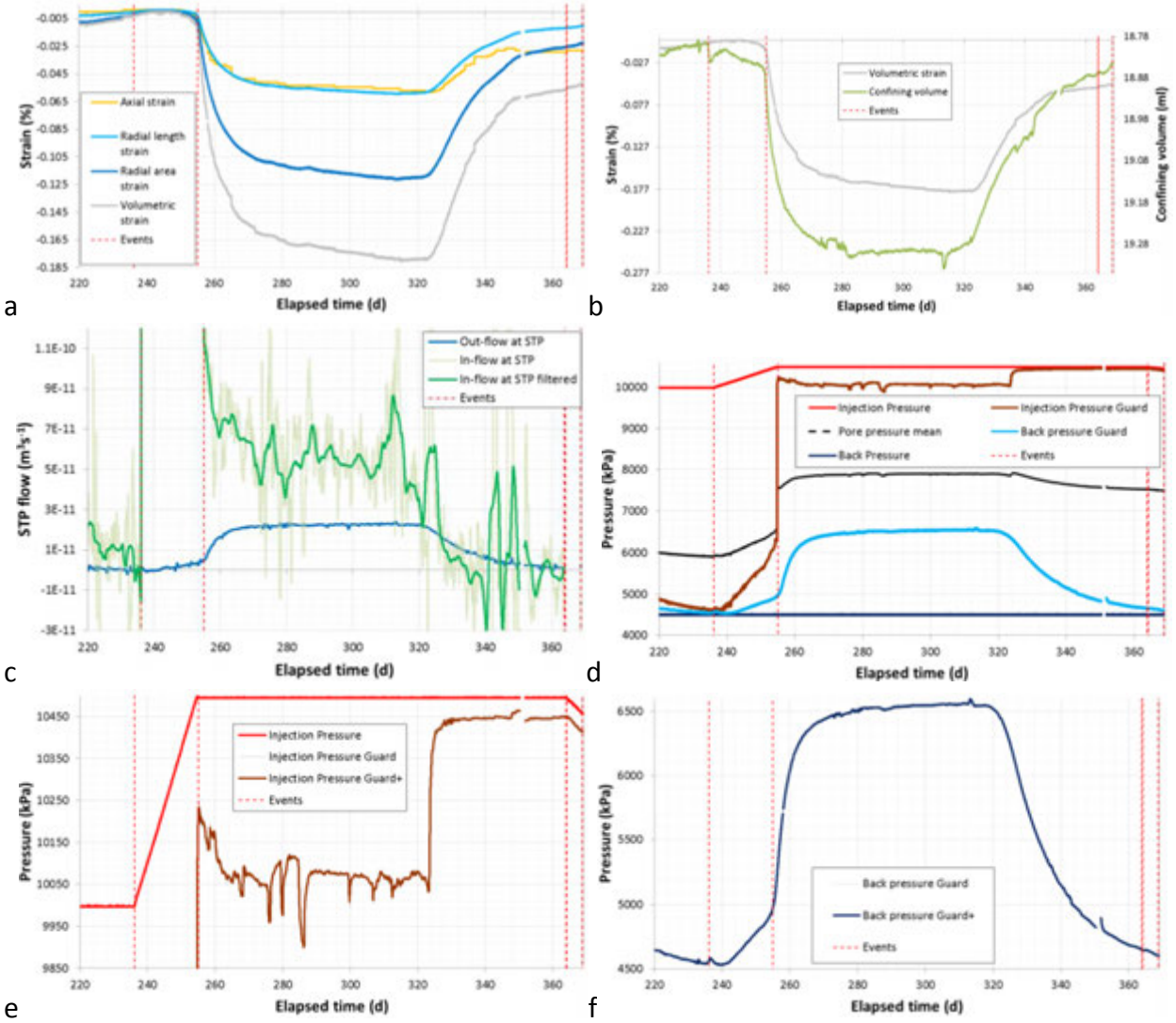

Figure 11 Summary of main events during onset and shut-off of gas flow; a). deformation; b). volumetric strain measured using two different methods; c). injection and back-pressure flow; d). pressure history; e). detail of pressure at injection guard ring; and f) detail of pressure at back-pressure guard ring.

By the end of full flow shut-off the sample had recovered radial strain and back-pressure guard ring pressure was similar to back-pressure (Figure 11a,f). A degree of permanent deformation was noted (Figure 11a,b) and this is likely to correspond with gas trapped within the sample.

The raising of the injection gas pressure did not result in re-establishing flow. Therefore, the cause of self-sealing was effective and the sample sustained higher gas pressures without flow. This suggests that some form of localised consolidation occurred near to the injection port.

The cause of shut-off is therefore unknown. Mode-I type fractures may have been the cause of the shut-off by lowering gas pressure within the conductive pathways resulting in their closure; although the in-flow and out-flow do not support this hypothesis.

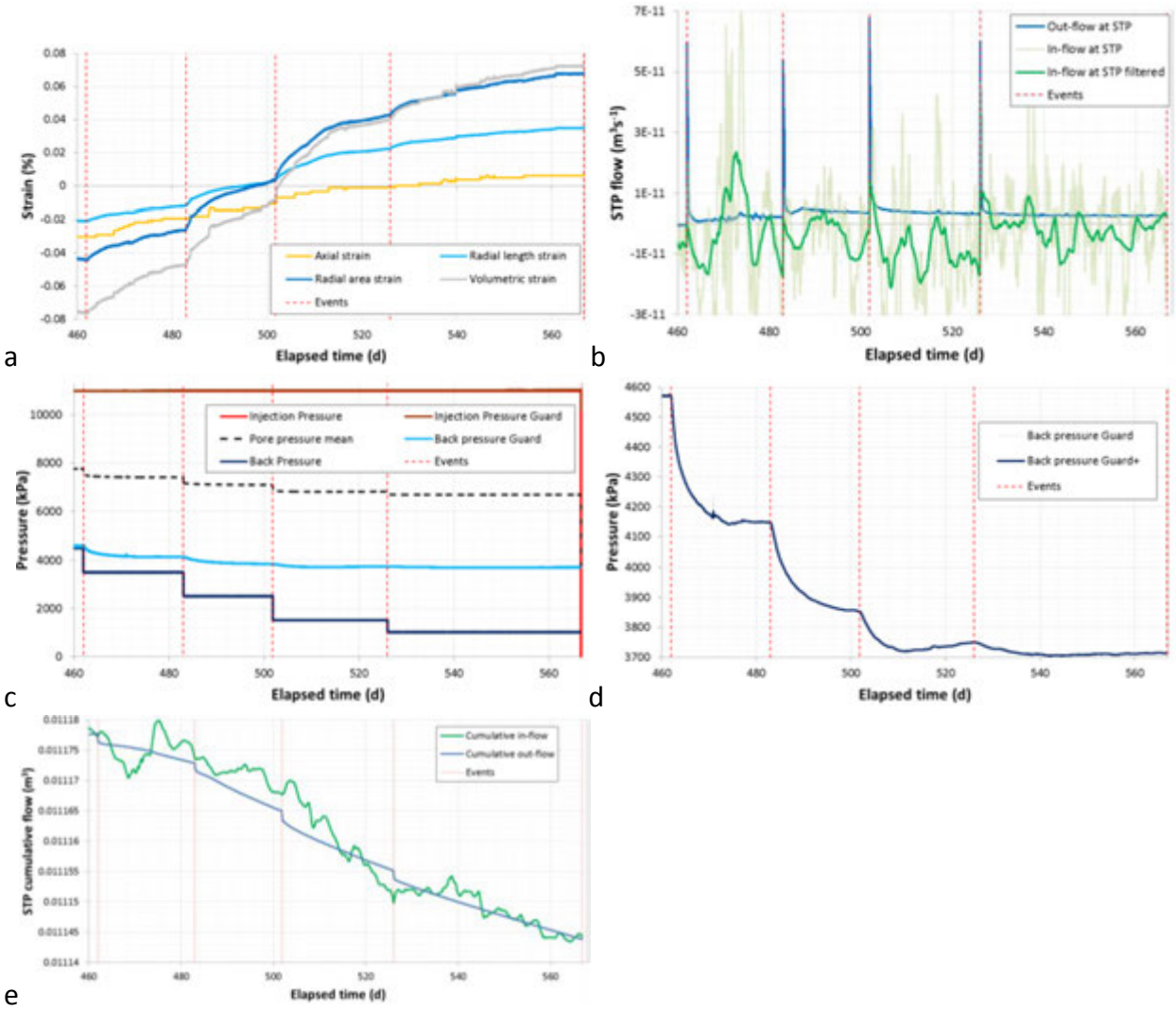

Figure 12 Summary of main events during the lowering of back-pressure; a). volumetric strain; b). injection and back-pressure flow; c). pressure history; d). detail of pressure at back-pressure guard ring; and e). cumulative flow during the stages of lowering back-pressure.

In order to re-initiate gas flow, the back-pressure was lowered in steps from 4.5 MPa to 1 MPa. This increased effective stress and the gas gradient along the length of the sample. However, this did not result in flow through the sample and merely resulted in draining the sample; leading to compaction. As seen with test SPP_COx-1, large samples of COx have considerable time dependent deformation that is a combination of material creep and drainage. Therefore outflow was the result of this considerable time-dependent feature. Out-flow from both ends of the sample were remarkably similar showing that it was the result of drainage and not related to gas flow through the sample.

The experimental setup is not able to determine the phase of the outflow, be it gas or water. The final saturation of the sample was determined to be indistinguishable from 100% (Table 4). Therefore it is likely that out-flow was the expulsion of gas, and possibly free water, from the sample as a result of bulk compaction. The final saturation of the sample demonstrates that even after prolonged periods of gas flow through the COx no measureable desaturation occurred.

A reduction in back-pressure resulted in bulk sample volume reduction; consolidation increased gas entry pressure. During the shut-off stage a reduction in BGR was the first recorded event. It is possible that this lowering of pressure resulted in localised consolidation and that this caused the flow to shut-off. The cause of the reduction in BGR pressure has been suggested to have

been the formation of a conductive micro-fracture linking the guard-ring with the pressure port. It may be possible that the formation of the fracture/conductive pathway ultimately resulted in the closure of flow through the sample due to the localised nature of the flow paths and their inherent instability being strongly linked with the consolidation of the sample.

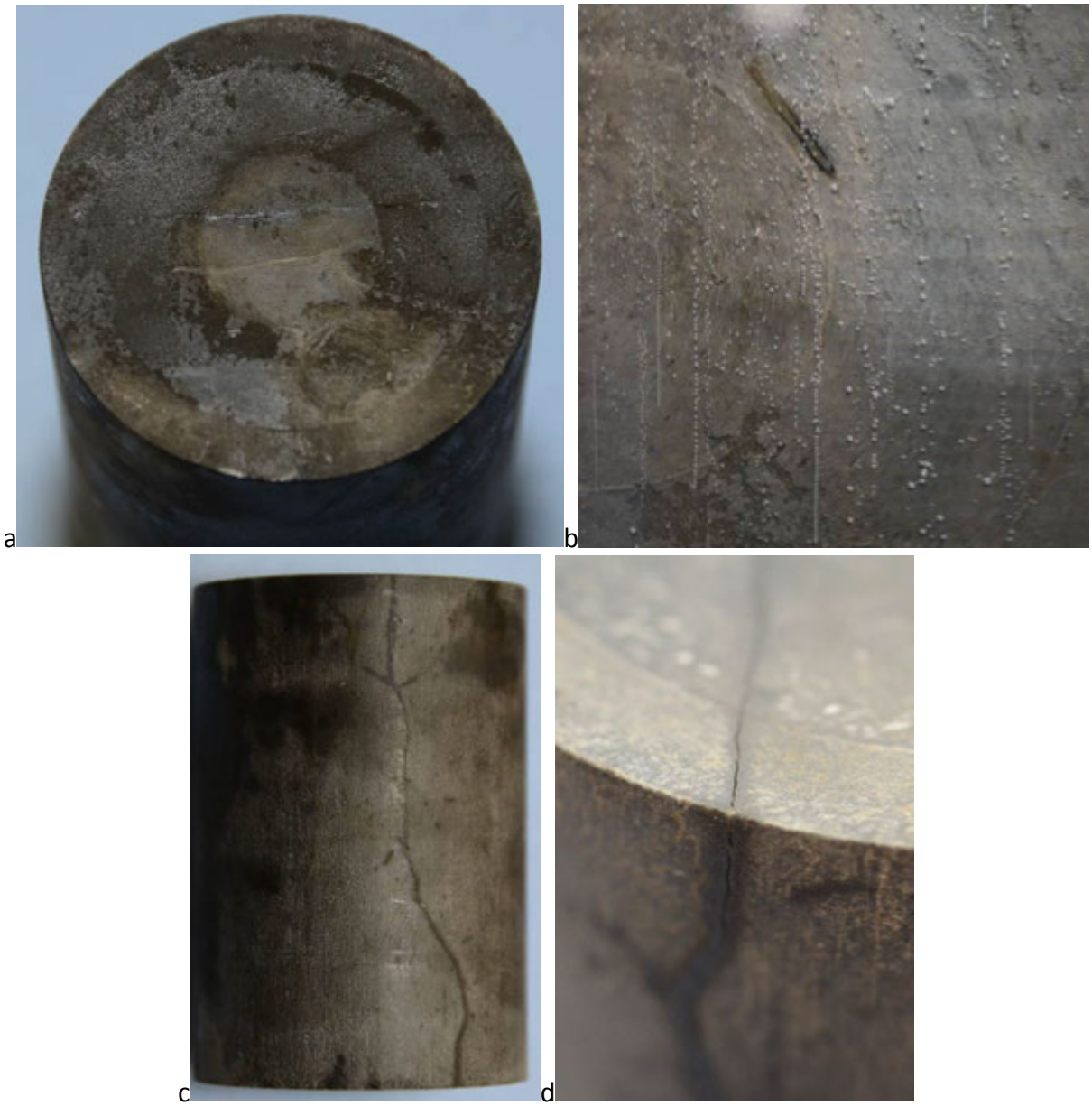

Figure 13 Observations of sample SPP_COx-2 after testing; a). back-pressure end of the sample; b). observations of de-gassing during heating in glycerol; c). length-wise fracture seen in the sample; and d). detail of the mode-I fracture seen in the sample after testing.

Considerable care was taken to slowly lower stress on the sample before extraction. Prior to sample removal a number of fractures were seen. Figure 13 shows the post-test sample. A number of fractures had formed and some ran the full length of the sample. The fractures were not planar and in places were made up of a number of intersecting fractures. Close examination (Figure 13d) showed Mode I (opening) fracturing with little evidence of shear movement; resembling a fabric tear. These fractures could potentially have been formed as trapped pressurised gas within the sample expanded during de-pressurisation of the sample.

The sample was placed within a bath of glycerol and slowly heated (Figure 13b). The majority of escaping bubbles were from the sample ends; with a lot more gas at the injection end, with little gas from the back-pressure end. This showed that significantly more gas pathways were formed at the injection end of the sample and only a few of these propagated as far as the back pressure end. Gas was seen to escape the sample from a number (10s) of locations. It was evident that the size of the bubbles varied, with a few (<5) locations having bubble significantly larger in size.

The sample was oven dried in order to establish the final sample saturation (Table 4), which was indistinguishable from 100 %. This indicates that the propagation of gas did not result in sample desaturation.

	Units	Value	Value	Change
Time of measurement		Before gas testing	After gas testing	
Average length	Mm	82.45 ± 0.03	82.57 ± 0.03	+ 0.12
Average diameter	Mm	55.85 ± 0.04	55.95 ± 0.08	+0.1
Volume	m^3	2.020×10^{-4}	2.030×10^{-4}	$+0.01 \times 10^{-4}$
Average weight	G	495.02	497.69	+ 2.67
Density	$g.cc^{-1}$	2.451	2.452	+ 0.001
Grain density	$g.cc^{-1}$	2.7	2.7	/
Moisture weight	g	28.7	32.6	+ 3.9
Moisture content	%	6.2	7.0	+ 0.8
Dry weight	g	466	465	- 1
Dry density	$g.cc^{-1}$	2.31	2.29	- 0.02
Void ratio		0.174	0.183	+ 0.009
Porosity	%	14.8	15.5	+ 0.7
Saturation	%	96	100	+ 4

Table 4 Dimensions and basic properties of the Callovo-Oxfordian claystone test material (sample SPP_COx-2). The data from pre-test measurements of water content from off-cut material adjacent to the core, data for final post-test measurement are directly from the test sample. An assumed specific gravity for the mineral phases of 2.70 $Mg.m^{-3}$ (Zhang *et al.* 2007) was used in these calculations.

Major conclusions

- COx shows considerable time-dependency in drainage and deformation.
- Test SPP_COx-2 showed a high gas entry pressure of 10.5 MPa.
- Considerable dilation was observed as gas propagated through the test sample, the magnitude of which could not be described by elastic deformation as a result of changes in effective stress. Anisotropy was noted and a three stage model of gas propagation in COx proposed.
- At a time when steady-state flow was approaching, i.e. a small difference between in-flow and out-flow, out-flow from the sample slowly shut-off. The origin of the shut-off was not definitively established, but corresponds with establishment of connection between the injection filter and guard rings.
- Shut-off and time-dependent radial deformation show that gas flow is unstable and constantly evolving, even when end-to-end flow was established in the sample. The flow paths became unstable and shut-off.
- An increase in gas pressure and reduction in back-pressure did not re-establish flow, showing that the shut-off was an effective self-sealing feature.

- Lowering of back pressure resulted in the sample compacting and slowly draining. Consolidation would increase gas entry pressure and it was not un-expected that this stage of the test did not re-establish flow.
- The test sample was seen to include a number of fractures. The exact timing of their formation is undetermined and it is likely that these formed during the de-pressurisation of the sample and the expansion of the trapped gas bubbles, which did not have sufficient time to escape. The fractures were mode-I and appeared as fabric ruptures.
- No discernible de-saturation was seen in the final test sample.

2.2 VERIFICATION OF CRITICAL STRESS THEORY APPLIED TO REPOSITORY CONCEPTS (BGS)

Discontinuities (fracture, faults, joints, interfaces, etc) play a pivotal role in controlling the movement of water and gas around an underground disposal facility (GDF) for radioactive waste. According to the current concepts, high level and long lived radioactive waste and spent fuel are intended to be stored/disposed of in a GDF within a stable geological formations (host rock) at depth (usually ~50-800 meters) beneath the ground surface. Hence, the radioactive waste is securely isolated and contained. At depth the rock mass may be a naturally fractured environment, such is the case for a GDF in crystalline rock, and the excavation of the GDF galleries is recognised to induce additional fractures (Bossart *et al.*, 2002; Rutqvist *et al.*, 2009). Therefore, all current concepts of disposal, be these in argillaceous, crystalline or salt rocks, will have a multitude of discontinuities as part of the engineered environment within the EDZ. Depending on the *in situ* stress conditions, preferential pathways may form along any, or all, of these discontinuities.

Fluids, such as gases and water, are expected to play a role in the transport of radionuclides away from the GDF. The conductivity of fluids through discontinuities (fractures, faults, joints etc) is understood to be controlled, in part, by the interplay of their orientation and stress tensor direction (Barton *et al.*, 1995; Finkbeiner *et al.*, 1997). Other factors such as clay content, fabric, and fracture connectivity also play a role in controlling fluid conductivity. Around the GDF there are two distinct zones with differing discontinuity orientation, discontinuity densities, and fluid flow properties; (a) the enginnering disturbed zone (EDZ) where an intricate range of discontinuity (fracture) orientations are present in a complex localised-stress field, and (b) the far field zone where discontinuous (pre-fractured/faulted) host rock may be present.

It has been proposed that discontinuities that are oriented parallel to the maximum horizontal stress orientation (σ_H) experience the lowest normal stresses acting across them and therefore will undergo the least amount of closure and will thus be the most permeable (Heffer & Lean, 1993). This is based on the assumption that discontinuities experiencing the least amount of stress will offer minimum resistance to flow and therefore will have relatively high permeability. However, observations by Laubach *et al.* (2004) on a number of sedimentary basins in the western United States using core permeability, stress measurements, and fluid flow datasets showed that at a depth of >3 km, the open discontinuities were not aligned parallel to σ_H as previously understood. Hence, *in situ* stress orientations cannot be realistically used as an indicator for predicting fluid flow in fractured rocks.

Barton *et al.* (1995) proposed that discontinuities whose state of stress are close to the failure criterion are more likely to be conductive because of the localised failure as a consequence of the large shear component acting along the discontinuity surface. Such features are termed “critically stressed” and are oriented approximately 30 degrees to σ_H (Rogers, 2003; Rogers & Evans, 2002). In order to apply the critical stress theory to the study of flow, the *in situ* stress

field acting along all discontinuities in a volume of rock can be resolved into shear and normal stress components. When the magnitude and direction of the stress field has been constrained, the shear stress (τ) and normal stress (σ_n) acting on a discontinuity can be expressed by (Jaeger *et al.*, 2007):

$$\tau = \beta_{11}\beta_{21}\sigma_1 + \beta_{12}\beta_{22}\sigma_2 + \beta_{13}\beta_{23}\sigma_3 \qquad \text{and} \quad \sigma_n = \beta_{11}{}^2\sigma_1 + \beta_{12}{}^2\sigma_2 + \beta_{13}{}^2\sigma_3$$

where, β_{ij} = directional cosines between the discontinuity and the stress tensor, σ_1, σ_2, and σ_3 = magnitude of the maximum, intermediate, and minimum principal stresses respectively.

When the shear stress and normal stress on the discontinuities are plotted with respect to the *in situ* stress field in a Mohr space, the faults and fractures that are scattered above the Mohr-Coulomb failure criterion are termed critically stressed and hence expected to be conductive (Figure 14). Critically stressed discontinuities are expected to be present amongst the numerous complex fracture networks within and around the EDZ and in the far field around the GDF.

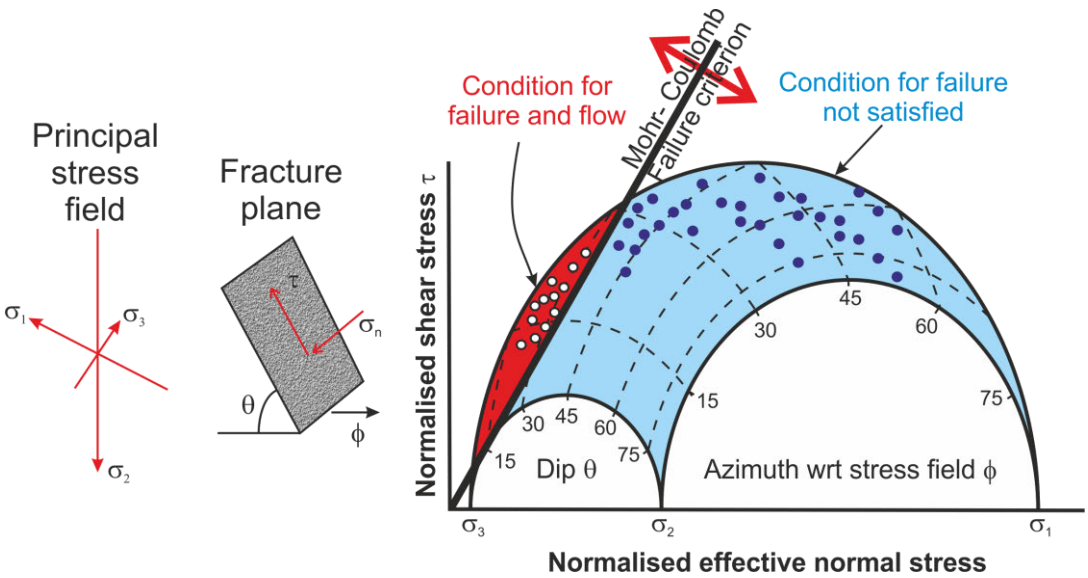

Figure 14 Critical stress hypothesis (adopted from Barton *et al.*, 1995; Jaeger *et al.*, 2007; Rogers, 2003). The three-dimensional Mohr diagram represents the shear stress and normal stress acting along a fracture in response to the *in situ* stress field. The open circles represent fractures experiencing state of stress above the failure criterion and therefore subject to shear failure. The closed circles represent fractures whose stress state is insufficient to induce shear failure and hence stable.

2.2.1 Objectives

Whilst there is considerable field evidence for the applicability of the critical stress approach from many sedimentary basins worldwide, the theory has been found to be lacking in describing the flow regime in the Sellafield area, UK (Reeves 2002). This study explained the discrepancy by considering the tectonic history of the region. Sellafield has undergone uplift and the stress acting on the faulted bedrock is now lower than at the time of their formation. Therefore, this study showed that the flow regime of discontinuities is more complex than the critical state approach would predict.

The objective of this experimental programme was to examine the relationship between the stress tensor direction and discontinuity orientation, as well as examining the conditions under which discontinuities became conductive. This experimental study aimed to verify the critical

stress theory, which could be used to understand the reasons why some fractures in the EDZ are conductive and hence aid performance assessment. Specific objectives were:

(i) perform and interpret small scale experiments to investigate relationship between the stress tensor direction and fracture orientations, as well as examining the conditions under which fractures became conductive,

(ii) provide high-quality experimental data to test/verify the critical stress theory in relation to repository condition for the first time.

Previous work at BGS on fracture transmissivity in Opalinus clay (Cuss *et al.*, 2011) designed an effective apparatus and showed that flow is a complex, focused, transient property that is dependent upon normal stress, shear displacement, fracture topology, fluid composition, and swelling characteristics of the material. The current experimental programme aimed to extend this knowledge by investigating the influence of discontinuity orientation. The programme was not proscribed and investigation of other factors influencing flow were explored. However, some elements of discontinuity flow were only "identified" and will require follow-up work in order to describe fully their influence.

2.2.2 Experimental set-up

All experiments were performed using the bespoke Angled Shear Rig (ASR, Figure 15) designed and built at the British Geological Survey. Experiments conducted on Opalinus clay (Cuss *et al.*, 2011) have shown that fracture topology is a key parameter in controlling fluid flow along fractures. In order to reduce the number of variables required to fully understand discontinuity flow, a "generic" discontinuity was investigated. The ASR comprised of two stainless steel blocks with a clay gouge of saturated kaolinite (gravimetric water content of 80%) of 60mm × 60 mm × 50 µm sandwiched between them. This allowed the pure mechanical influence of discontinuity orientation to be investigated in a simplified system. Results are applicable to clay-rich and crystalline disposal concepts in the numerous discontinuities seen.

The ASR comprised 6 main components:

1. Rigid frame that had been designed to deform as little as possible during the experiment;
2. Vertical load system comprising an Enerpac hydraulic ram that was controlled using an ISCO 260D syringe pump, a rigid loading frame and an upper thrust block (up to 20 MPa vertical stress, 72 kN force);
3. Shear force actuator designed to drive horizontal movement as slow as 14 microns a day at a constant rate (equivalent to 1 mm in 69 days);
4. Pore pressure system comprised of an ISCO 500D syringe pump that could deliver either water or gas through the centre of the top block directly to the fracture surface;
5. A state-of-the-art custom designed data acquisition system using National Instruments LabVIEW™ software facilitating the remote monitoring and control of all experimental parameters.
6. The experimental slip plane assembly consisted of precision machined 316 stainless steel top and bottom blocks with dip of 0°, 15°, 30°, and 45° forming a fault/slip plane. The top block was connected to the vertical loading mechanism by means of a swivel mechanism which was engaged to the shoulders on either side of the top block.

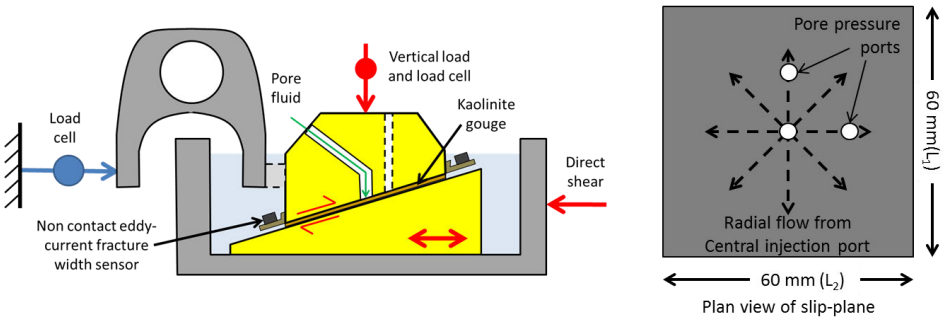

Figure 15 Schematic of the Angled Shear Rig (ASR).

Unlike standard direct shear experiments, the top and bottom blocks could be oriented at different angles to the vertical load/horizontal displacement. Experiments were conducted on horizontal blocks and angles of 15, 30, and 45 degrees. Vertical load was applied using a servo controlled Teledyne ISCO-260D syringe pump pressurising an Enerpac single acting hydraulic ram connected to a rigid loading frame. The Enerpac ram had a stroke of 105 mm, which meant that the ram could easily accommodate the vertical displacement of the top block as it rode up the fracture surface at constant normal load. Pore fluid (water or helium) was introduced through the centre of the top block by means of a Teledyne ISCO 500D syringe pump connected in series to a gas-water interface vessel. Pore pressure transducers, attached to ports which were positioned orthogonally to each other at 15 mm from the central pore fluid inlet allowed measurement of pore pressures within the slip plane (see Figure 15). The shear-force actuator was comprised of an ISCO 500 series D syringe pump, which was modified by mounting horizontally. The ISCO pump was designed to push a syringe through a barrel to deliver pressure. In the current setup, the barrel had been removed and the drive-train directly connected to the sample assembly, itself mounted on a low friction bearing. Horizontal (shear) load was measured using a load cell fitted laterally to the top-block.

The upper and lower thrust blocks of the apparatus were made out of stainless steel with a contact area of 60 mm × 60 mm. The lower thrust block was longer than the top one so that the contact area was maintained constant throughout the test. Vertical travel of the thrust block (giving gouge dilation) was measured by a high precision non-contact capacitance displacement transducer, which had a full range of ± 0.5 mm and an accuracy of 0.06 µm. Following early testing, it was necessary to add two high precision Eddy current non-contact displacement transducers to either end of the top thrust block in order to record gouge thickness directly and to determine non-parallel alignment of the two thrust blocks. These submersible devices had a full range of ± 1 mm and an accuracy of 0.2 µm. Lateral movement was measured using a high precision linear variable differential transformer (LVDT), which had a full range of ± 25 mm and an accuracy of 0.5 µm

The complete experimental programme conducted 48 separate experiments. All experimental results are described in detail in Cuss *et al.* (2013). Two main types of experiment were conducted: 1). Loading-unloading tests, where fracture flow was monitored at constant injection pressure as vertical load was increased in steps to a given level and then reduced back to the starting stress state; 2). Gas breakthrough experiments, where gas injection pressure was increased in a pressure ramp at constant vertical load. These were conducted with and without active shear. In additional, a number of other experiments were conducted. The main conclusions from this study are summarised below:

1. Loading-unloading tests:

a. During a loading (vertical stress) and unloading cycle considerable hysteresis in flow was observed signifying the importance of stress history on fracture flow.
b. For the case of gas injection the change in flow is chaotic at low vertical loads, whereas for water injection the flow reduces smoothly with increased vertical load.
c. Hysteresis in horizontal stress observed during unloading demonstrates the importance of the ratio between horizontal stress and vertical stress and its control on flow.
d. Differences have been observed between injection fluids (water and helium), especially the hysteresis observed in flow. For water injection flow is only partially recovered during unloading, whereas for gas enhanced flow is seen at low vertical loads.

2. Gas breakthrough experiments:

a. During gas breakthrough experiments episodic flow/fault valve behaviour was seen with a decrease in subsequent peak pressures and the form of the pressure response was different during subsequent breakthrough events.
b. Repeat gas injection testing has shown a consistent gas entry pressure but considerably different, non-repeatable, gas peak pressures.
c. Differences in gas entry pressure are seen dependent on the orientation of the fracture.
d. Active shear reduces the gas entry pressure, which is contrary to observations seen in Opalinus clay.

3. General observations:

a. The results show that the flow of fluids through clay filled fractures is non-uniform and occurs via localised preferential pathways.
b. The pressure recorded within the slip-plane showed a negligible fracture pressure and did not vary much in all tests.

Each finding is discussed in more detail below.

2.2.3 Loading-unloading tests

A total of 17 loading-unloading experiments were conducted, all on a 30° slip-plane. Nine tests were conducted without a permeant in order to understand the behaviour of the kaolinite gouge whilst loading/unloading, five tests were conducted with water as the injection fluid, whilst three gas flow experiments were conducted.

Figure 16 shows the results of flow achieved for two tests conducted injecting water into a 30° discontinuity during loading from 0.2/0.1 to 2.6 MPa (vertical load) and unloading from 2.6 to 0.2 MPa. As can be seen, the starting flow rate of the two tests are different by nearly a factor of 5. Both tests were setup in identical ways using the same pre-mixed weight of kaolinite and deionised water. This difference may derive from variations of gouge thickness and as a result the experimental system was modified in order to measure the starting gouge thickness.

As vertical load was increased in steps, the flow along the slip plane could be seen to steadily reduce. In both expereiments, although starting from dissimilar flow rates, both achieved a flow rate of approximately 6 µl/h by 2.6 MPa vertical load. On unloading, this flowrate did not significantly alter until a vertical load of approximately 0.75 MPa. Therefore it can be noted that the “memory” of the maximum load experienced was retained. This illustrates the importance of stress history on predicting flow along discontinuities and has been used to explain the non-applicability of the critical stress approach in its simple form at the Sellafield site in the UK (Sathar *et al.*, 2012).

All loading-unloading experiments showed marked hysteresis in flow. During a loading (vertical stress) and unloading cycle considerable hysteresis in flow was observed signifying the importance of stress history on fracture flow. For the case of gas injection (Figure 17) the change in flow was chaotic at low vertical loads, whereas for water injection the flow reduced smoothly with increased vertical load.

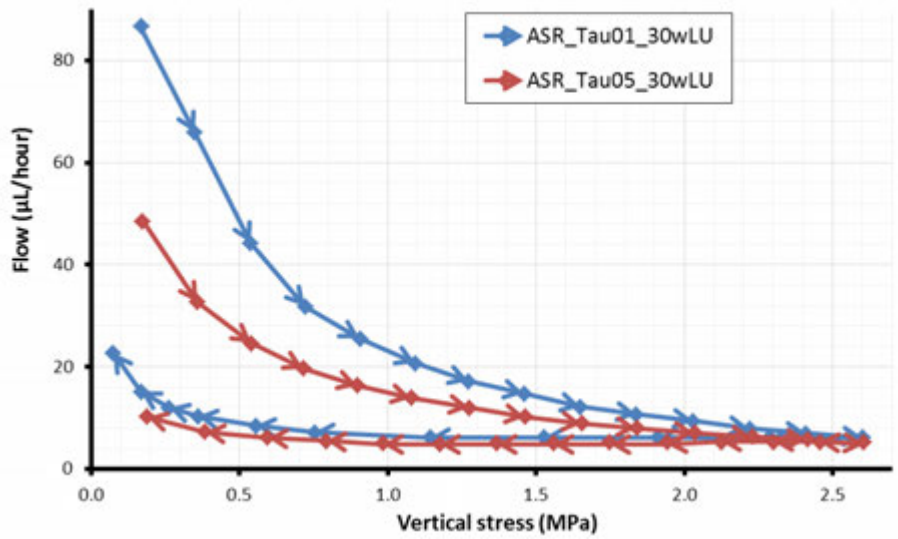

Figure 16 Example of hysteresis seen in water flow during a loading/unloading experiment on a 30° slip-plane.

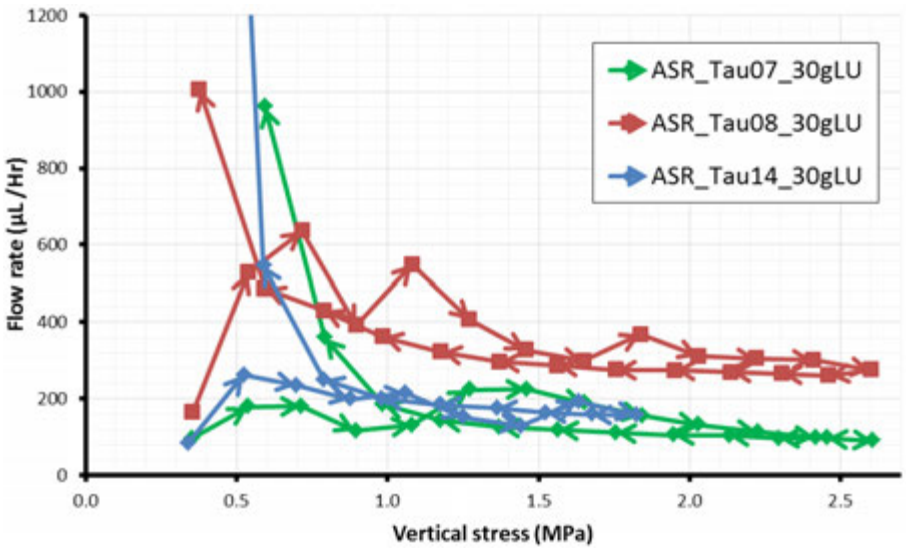

Figure 17 Example of loading-unloading cycle seen during a gas injection test on a 30° slip-plane.

Figure 17 shows the results for three loading-unloading experiments with gas as the injection medium. Considerable difference was seen between the loading and unloading cycles. On loading the progression of flow was chaotic. In all three tests, once vertical load was increased from the starting value of approximately 0.3 to 0.5 MPa flow increased. All three tests showed that increased vertical load resulted in episodes of increasing and decreasing flow. This could possibly be explained by 3 possible mechanisms:

1. Gas flow was highly sensitive to water content of the gouge and the duration of the experiment meant that full drainage was not possible;

2. The gougue was not remaining even in thickness along the complete length, i.e. increased load was resulting in a wedge shaped gouge;
3. Shear movement was occuring along the 30° slope as vertical load was increased and there was some form of stick-slip, which meant that the movement was uneven between steps.

It is difficult to rule out scenario (1) as this was not investigated fully. However, wide variation in flow rates have not been observed, which suggests that a fairly homogenous paste of gouge had been created and that subtle, localised changes in saturation (caused by uneven drainage) was unlikely to be the main cause of this effect.

The second scenario (2) is not supported by the measurement of the gouge thickness during experimentation, as seen in Figure 18. Even reduction in gouge thickness was observed, with more chaotic variations in thickness seen during unloading. This is contrary to the flow data, where chaotic flow is seen during loading and even variation seen during unloading. Therefore this effect is unlikely to be caused by uneven thicknesses of gouge.

The third scenario (3) is also not supported by experimental observations. Figure 19 shows that there is shear movement as a result of only increasing vertical load. However, this increased relatively evenly and suggests that changes in vertical load have resulted in the gouge moving evenly.

Observations of localised flow (see 3a) suggests that gas exploited sub-micronscale features within the clay, similar to features observed in bentonite (WP3). The exact cause of the chaotic behaviour has not been determined due to the macro-scale of measurement and the likely microscopic origin of this behaviour. However, the chaotic behaviour was repeatable and suggests that gas flow predictions of transmissivity are problematic. The “even” reduction in flow on unloading supports the “memory” effect of the clay introduced in the previous section.

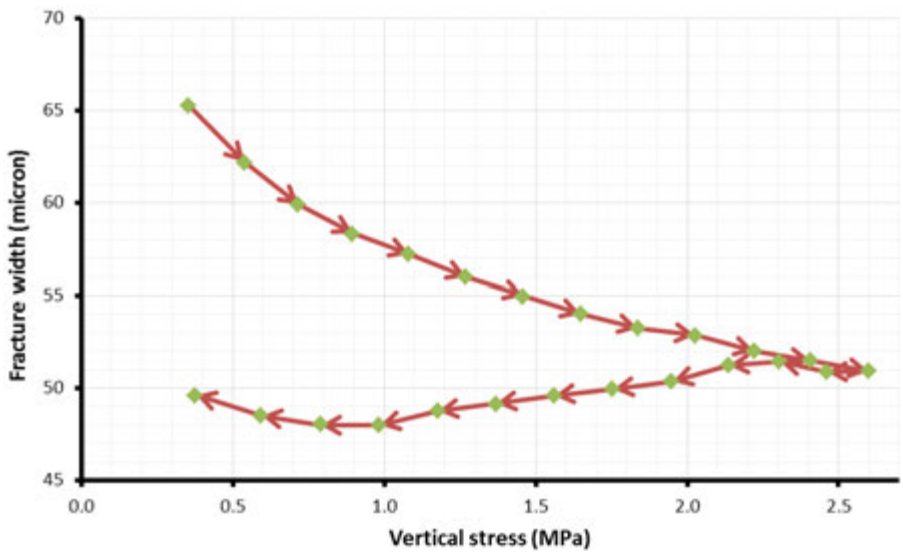

Figure 18 Fracture width recorded during a loading-unloading experiment.

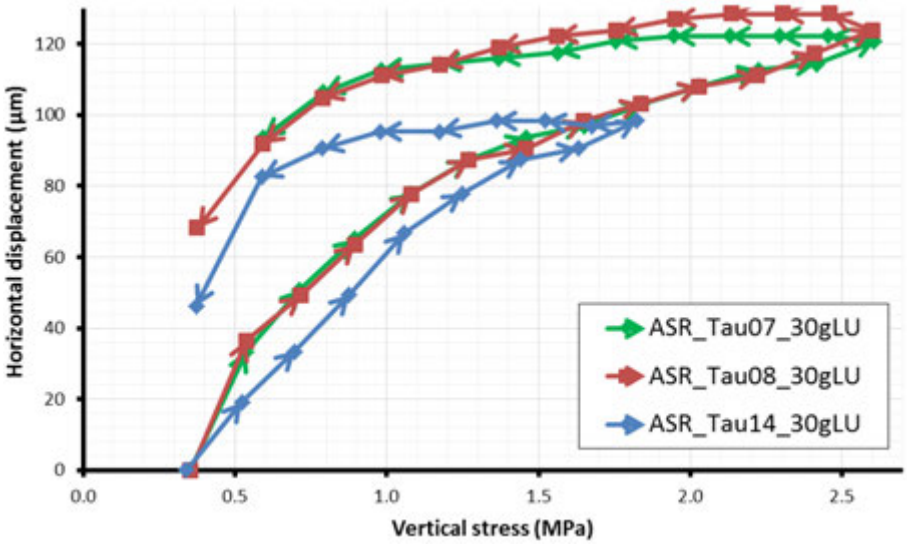

Figure 19 Shear displacement caused as the result of loading-unloading.

Hysteresis in horizontal stress observed during unloading demonstrates the importance of the ratio between horizontal stress and vertical stress and its control on flow.

Figure 20 shows that considerable hysteresis was also observed in horizontal stress during loading-unloading experiments for both water and gas injection. The repeatability of the results shows that free movement of the gouge was achieved. The hysteresis in horizontal stress during unloading may be attributed to the cohesive strength of the kaolinite clay gouge. Figure 21 shows how the ratio of horizontal stress to vertical stress varied during the experiment. Here, subtle variation between water and gas injection experiments was seen during unloading once the ratio exceeded unity. Significant gas flow rate increase occurred when the horizontal stress to vertical stress ratio increased above unity during unloading.

Zoback *et al.* (1985) and Brudy *et al.* (1997) have shown that the ratio of shear stress to normal stress is crucial in controlling permeability and in the movement of gas through fractures. The close relationship between fracture flow and the horizontal stress to vertical stress ratio during the unloading stages in the present experiments also points towards its significance in understanding the flow of fluid through discontinuities. In the case of a fractured rock formation undergoing uplift stress relaxation is likely to result in a high horizontal stress to normal stress ratio.

Understanding the horizontal stress to normal stress ratio is important in predicting the flow properties of discontinuities. Features experiencing horizontal stress to normal stress ratios are expected to be more conductive. High horizontal stress to normal stress scenarios are likely to be more prevalent in regions experiencing stress relaxation due to structural uplift or removal of the overburden. Again, this highlights that an understanding of the stress history of a discontinuity is essential to effectively predict the present fluid flow properties of those features.

Differences have been observed between injection fluids (water and helium), especially the hysteresis observed in flow. For water injection flow is only partially recovered during unloading (see Figure 22a), whereas for gas enhanced flow is seen at low vertical loads (see Figure 22b).

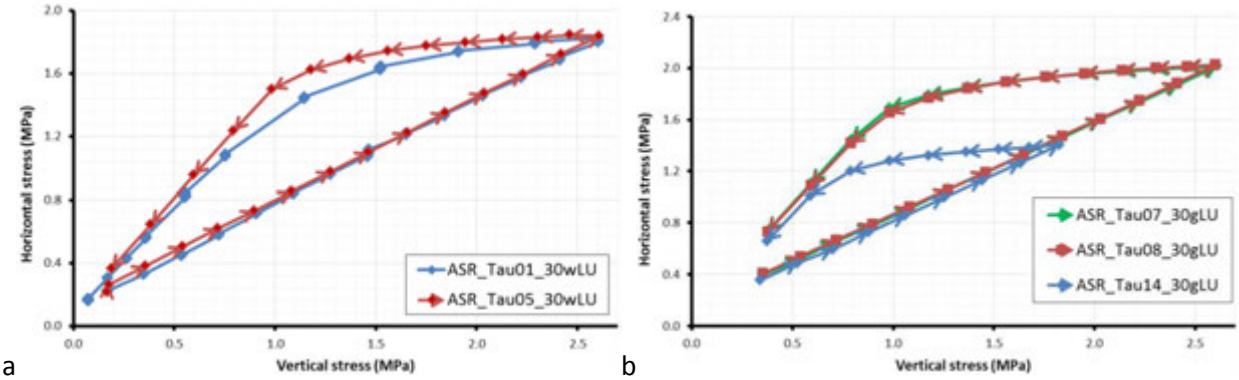

Figure 20 The hysteresis observed in horizontal stress during loading-unloading experiments; a) water injection; b) gas injection.

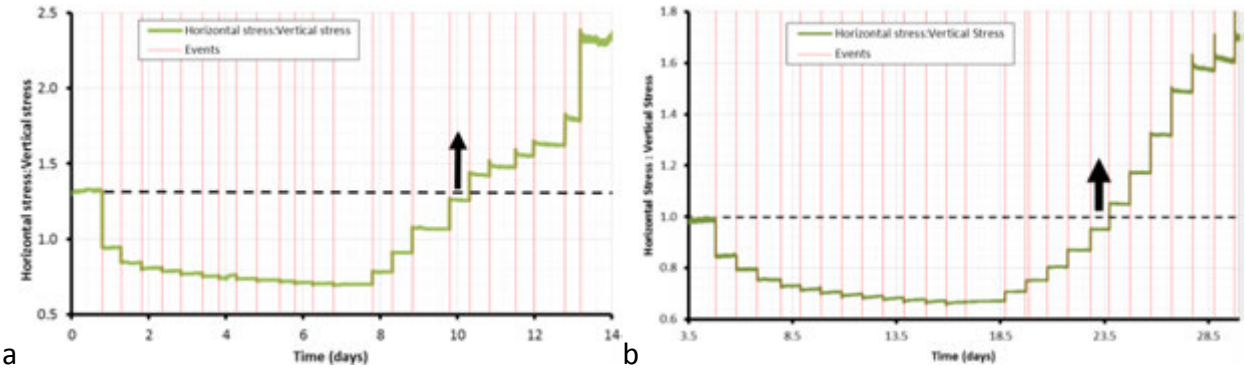

Figure 21 The variation of the ratio of horizontal stress : vertical stress seen during loading-unloading experiments; a) water injection; b) gas injection. The arrows indicate horizontal stress to vertical stress ratios during unloading which are greater than the initial values and indicates an enhancement in flow rate.

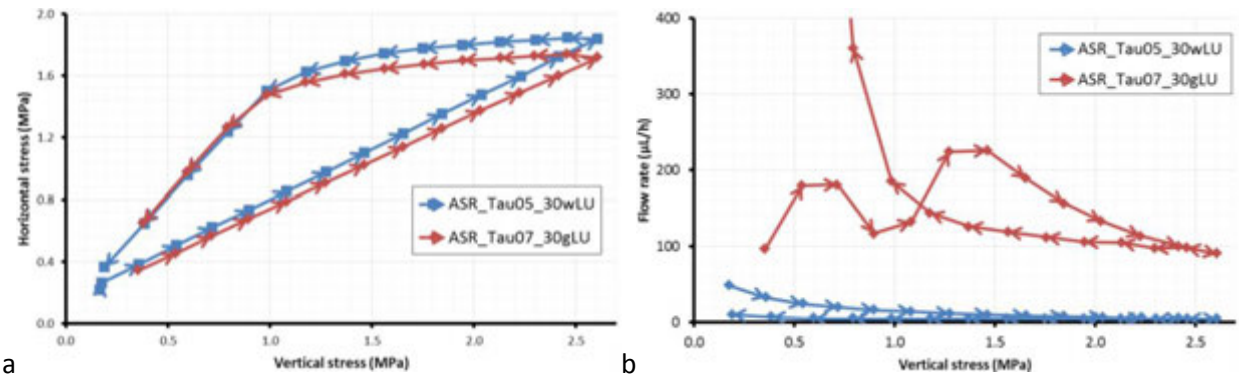

Figure 22 Comparing results for water and gas injection during loading and unloading experiments; a) horizontal stress; b) flow response.

Figure 22a shows a comparison of the horizontal stress response during a loading-unloading experiment conducted using water and gas as the injection medium. There is agreement between the data recorded, which demonstrates that the gouge mechanically behaves the same way if water or gas is injected into a saturated kaolinite gouge. The similarities suggest that the gouge is neither hydrated by water injection (as it is already fully saturated), nor is it desaturated by gas injection.

However, considerable differences were seen in flow behaviour. For water injection, a pore pressure of 1 MPa was sufficient to initiate flow, whereas a gas pressure in excess of 3.5 MPa was required to initiate flow. This results in much lower flow rates observed in water injection tests, as seen in Figure 22b. The differences suggest that the governing physics controlling gas movement is dissimilar to that controlling water movement.

As previously introduced, there was also considerable difference in the progression of flow during the loading cycle. At low normal loads this behaviour was chaotic in gas injection, whereas it was smooth for water injection. By 1.5 MPa vertical load the two behaviours were similar, both decaying evenly with increasing vertical load.

Differences were also seen during the unloading cycle. Both injection fluids showed a similar initial response with considerable hysteresis seen and the slow recovery of flow. Dissimilarity was seen as normal load reduced below approximately 1 MPa. For the case of water injection, flow was always only partially recovered. For gas injection, at low vertical loads flow increased to high levels much greater than that recorded at the corresponding vertical load on the loading cycle. The enhanced flow became catastrophic and at low vertical loads all gas in the gas reservoir was expelled through the slip-plane. Such catastrophic failure during water injection was not seen. This may in part be due to the expansion of gas as it propagated along the slip-plane as pressure reduced.

2.2.4 Gas breakthrough experiments:

A total of 26 gas breakthrough experiments were conducted on 0°, 15°, 30°, and 45° discontinuities; both with and without active shear. All tests were conducted in an identical manner with a known starting volume of 200 ml of helium at 4 MPa and a pressure ramp created by constant flow displacement of the ISCO syringe pump by 700µl/h.

During gas breakthrough experiments episodic flow/fault valve behaviour was seen with a decrease in subsequent peak pressures and the form of the pressure response was different during subsequent breakthrough events.

A single test was conducted (ASR_Tau06) for a prolonged gas injection ramp to see if there was repeat gas entry. A total of seven steps were conducted, as seen in Figure 23. The exact detail of this particular test was complicated due to the need to refill the gas reservoir several times and is described in detail in Cuss et al. (2013). However, general observations are introduced below.

It could be seen that the first gas breakthrough at 0.2 MPa normal load resulted in the sudden catastrophic loss of gas pressure at 3.2 MPa as the gas reservoir was emptied through the slip-plane. Vertical load was increased to 1.85 MPa to see if a secondary breakthrough could be initiated following fracture sealing due to increased load. This resulted in a distinct peak in gas pressure at 1.9 MPa, which was followed by a decay to 1.2 MPa and then slow recovery of gas pressure to another breakthrough at 1.6 MPa. Pressure dropped to 0.5 MPa and again recovered to another breakthrough event at about 1 MPa. This partial breakthrough was followed by pressure recovery to a plateau of 1.1 MPa. Vertical load was increased to 2.25 MPa and a fifth breakthrough was initiated at 1.8 MPa.

The form of the breakthrough event changed during the experiment. The first event was a catastrophic total loss of pressure. The second event was a peak and trough, similar in form to that seen during gas injection in bentonite (WP3). The third event was a sudden drop in pressure by 1 MPa, and the fourth event could be described as the system reaching equilibrium and the attainment of a plateau.

These observations suggest that “fault-valve behaviour” has been demonstrated in the laboratory and the magnitude of subsequent break-through events reduced (at constant vertical load) and the “form” of the breakthrough events changed with each successive feature. It also demonstrated that an increase in vertical load resulted in a degree of self-sealing, although the “memory” of previous breakthrough events may still be apparent.

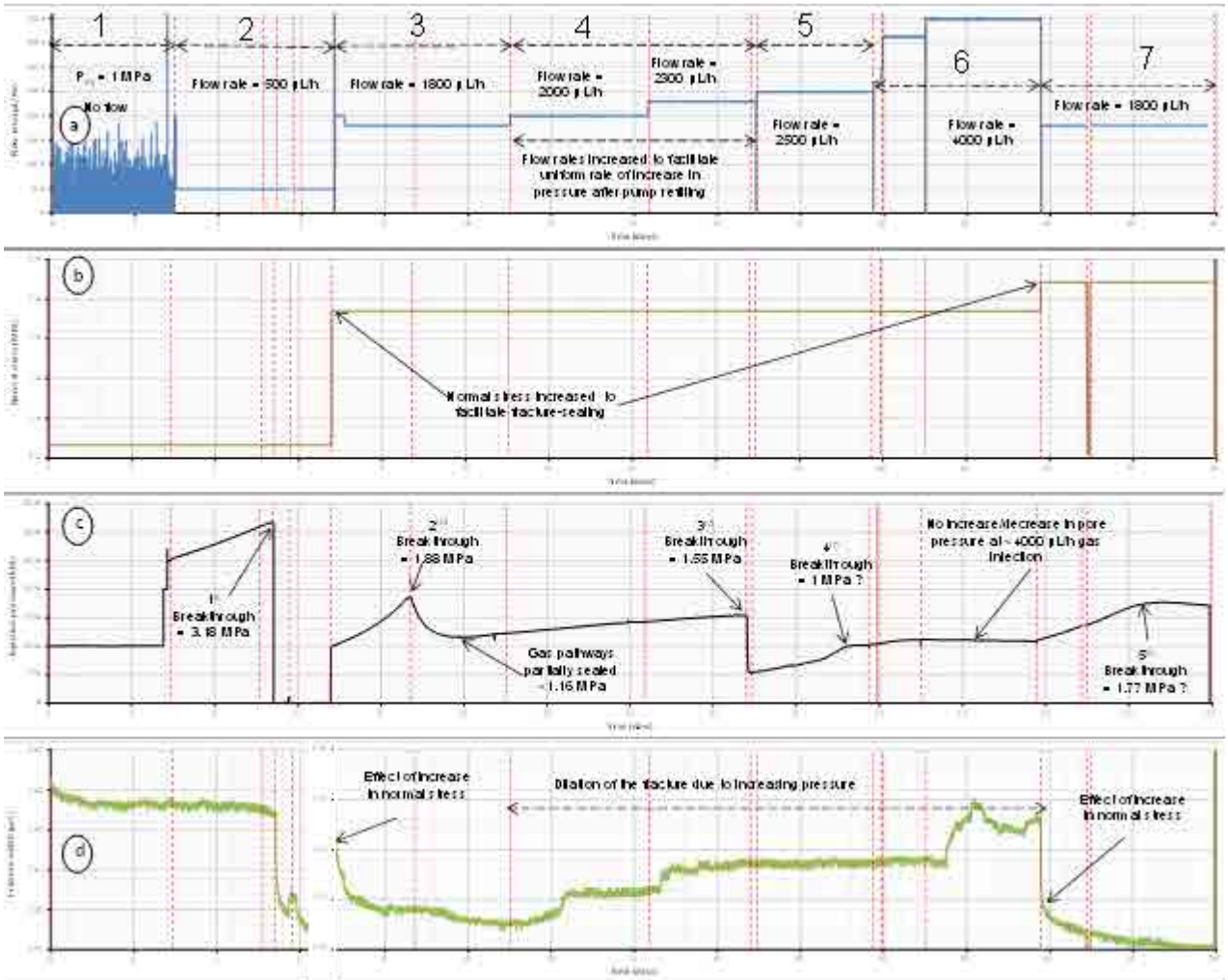

Figure 23 Results from ASR_Tau06_30gGI showing different gas breakthrough indicating fault-valve behaviour. a) Flow rate versus time plot showing the gas injection rates used in different stages (indicated as numerals) of the experiment. b) Vertical stress versus time showing the vertical stress applied to the slip plane. c) Gas injection pressure versus time plot showing the evolution of injection pressure before and after each breakthrough event. d) The variations in fracture width during various gas injection stages.

Repeat gas injection testing has shown a consistent gas entry pressure but considerably different, non-repeatable, gas peak pressures. Figure 24 shows an example of the repeatability of experimental results for four tests conducted on a discontinuity oriented at 30°. As seen in the plots, three of the tests show relatively similar results, with test ASR_Tau07 showing anomalous results.

Gas entry pressure has been determined by comparing the gas pressure recorded with that predicted at the given pressure (Figure 24b). Three tests show similar gas entry of approximately 8 MPa, with test ASR_Tau07 showing an anomalously low entry pressure of 5.5

MPa. This suggests that test ASR_Tau07 has had gas entry at a much lower pressure for an unknown reason. Similar anomalously low gas entry pressures were seen on other orientations, suggesting that gas was able to exploit a "defect" of some form at a low pressure and the experiment was unable to be perfectly reproducible.

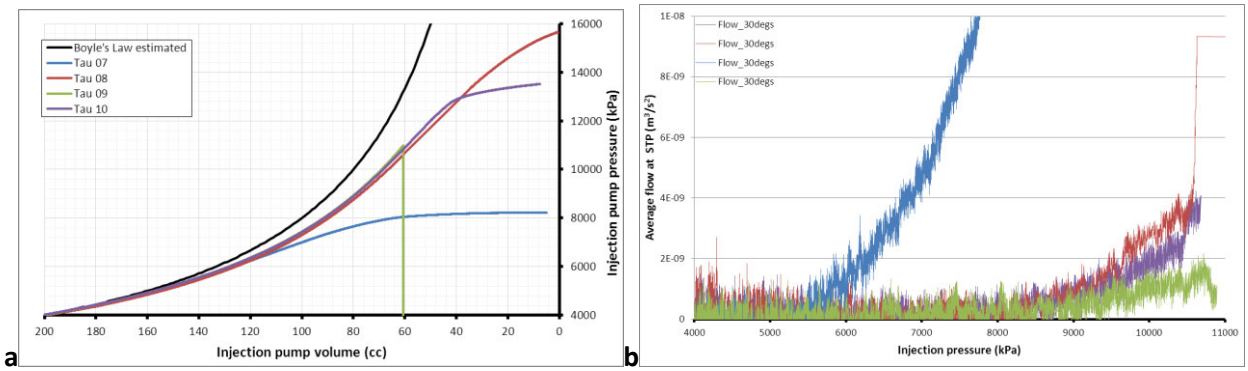

Figure 24 Repeatability of gas injection tests; a) pressure response, b) flow results.

Whilst three of the four tests show a similar gas entry pressure, these tests showed considerably different peak pressures of 10.8, 13.5, and 15.5 MPa (test ASR_Tau07 achieved a peak pressure of only 8.2 MPa). One test catastrophically broke-through at 10.8 MPa.

These observations suggest that the physical control on gas entry is repeatable, although in the presence of any form of imperfection gas was able to enter at lower pressures. Once gas started to move within the slip-plane the progression of pressure was less predictable and depended on whether the evolving gas network located an exit from the system. Similar results were seen for all discontinuity orientations.

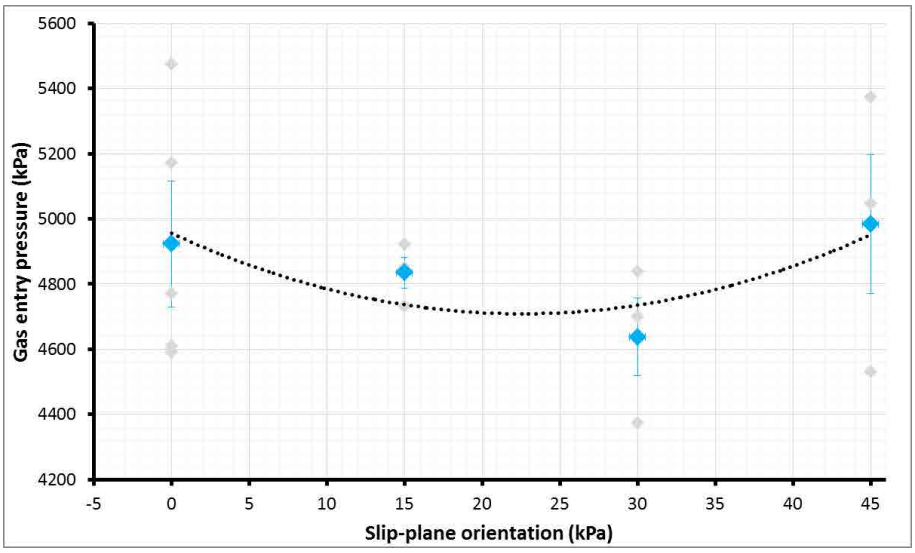

Figure 25 Gas injection pressure variation with discontinuity orientation. Grey data points represent the recorded gas entry pressure from each individual test; the blue data represents the average for each orientation; the dashed line is the polynomial fit of the data.

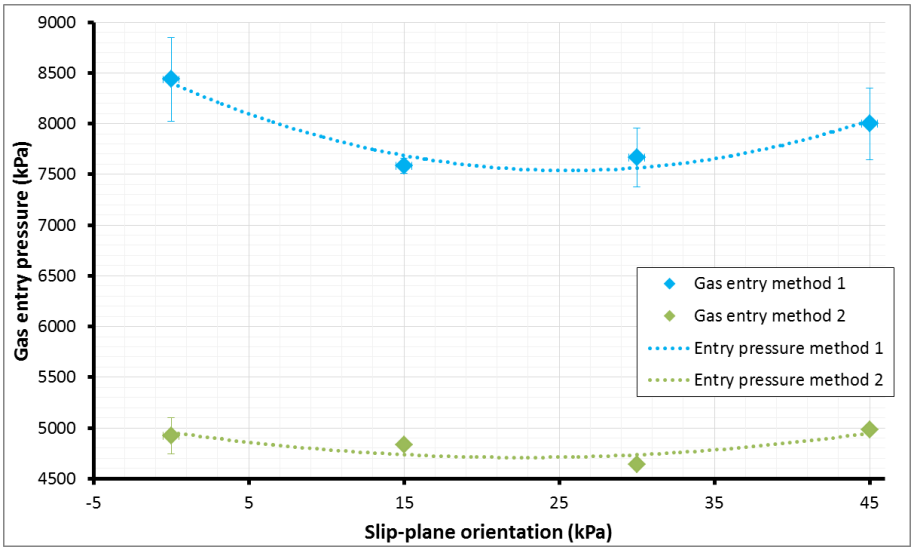

Figure 26 Comparison of results from the two methods used to determine gas entry pressure. Both methods show that gas entry pressure alters with fracture orientation, with entry pressure determined from STP flow into the fracture predicting higher pressures.

Differences in gas entry pressure were seen dependent on the orientation of the fracture. Two methods were used for determining gas entry pressure. In the first method the gas pressure was compared with the predicted pressure from the ideal gas law. In the second method the STP flow into the slip-plane was determined. Although some tests had shown anomalously low gas entry pressures, Figure 25 shows a general variation of gas entry pressure with discontinuity orientation. Figure 26 compares the results achieved from the two methods to determine gas entry pressure.

For the method determined from the ideal gas law the highest gas entry pressure was seen on a flat and 45° slip-plane with an entry pressure of approximately 5 MPa. The lowest gas entry pressure was recorded at 30° of 4.6 MPa. Generally, the results suggest that the lowest gas entry pressure would be observed at 20 to 25°. However, the variation in gas entry pressure is minor and a constant gas entry pressure could be fitted to the data in Figure 25.

For the method determined from STP flow into the slip-plane the highest gas entry pressure was seen on a flat slip-plane with an entry pressure of approximately 8.4 MPa. The lowest gas entry pressure was recorded at 15° of 7.6 MPa. Similarly, the results suggest that the lowest gas entry pressure would be observed at 25°. The variation in gas entry pressure seen is significant and represents a 1 MPa.

All tests have been conducted at identical vertical loads. As discontinuity orientation varied, the load acting normal to the slip-plane would vary. Taking this geometrical effect into account, the variation seen in gas entry pressure is more complex than a simple stress rotation about the slip-plane.

The experimental study has demonstrated a variation in fracture transmissivity with discontinuity orientation, demonstrating that the critical stress theory is applicable in the absence of stress relaxation.

2.2.5 General observations

The results show that the flow of fluids through clay filled fractures is non-uniform and occurs via localised preferential pathways.

Three tests were conducted and recorded using time-lapse photography to observe the escape of gas from the slip-plane into the bath of the apparatus. All three of these experiments showed that a small, isolated stream of bubbles escaped from a single location (see Figure 27). In all tests a single stream of bubble was created, i.e. a single pathway and a second pathway either had not formed or did not reach the edge of the slip-plane. In all tests the frequency of escaping bubles increased with time, as did the size of the bubbles.

Fracture width data were inconsistent in recording dilation events at the onset of gas flow. However, some tests clearly showed dilation. This observation combined with the isolated single bubble stream show that gas propagated by means of a dilatant process.

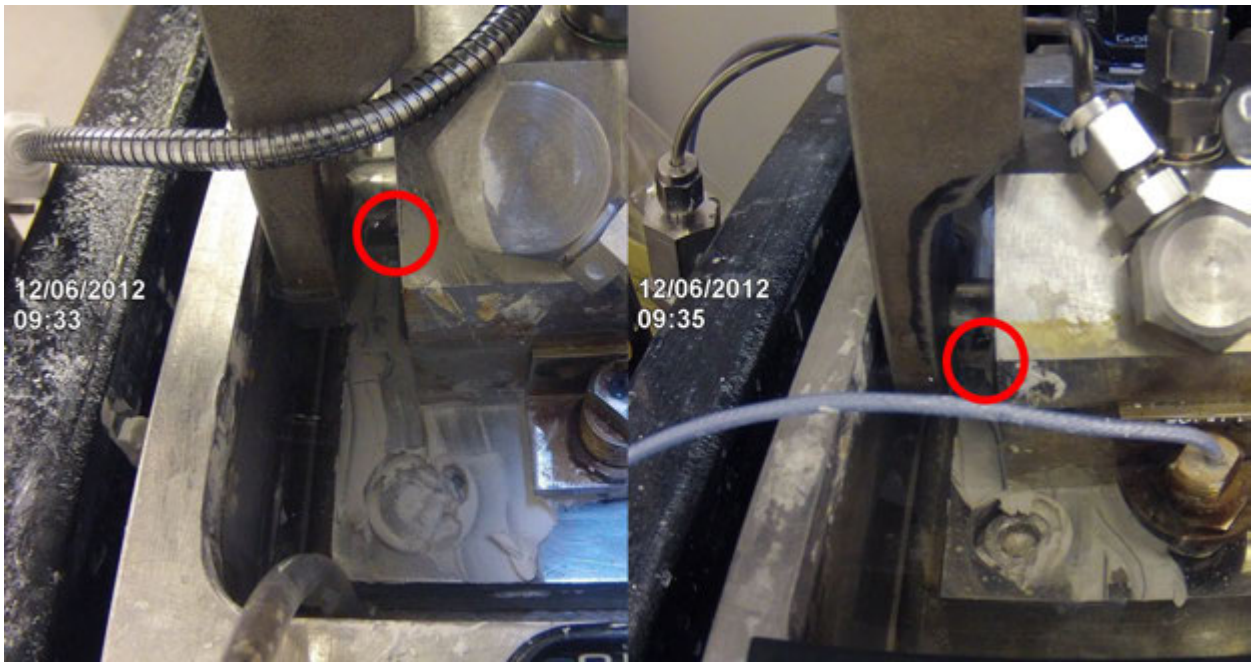

Figure 27 Photo showing the escape of gas into from the slip-plane.

The pressure recorded within the slip-plane showed a negligible fracture pressure and did not vary much in all tests.

In all tests, the two pressure ports located within the slip-plane registered pressure less than 50 kPa, effectively close to zero (see Figure 28). Little variation was seen, although some changes occurred during loading-unloading experiments as a result of consolidation. However, no evidence of elevated gas pressures were seen during any experiment. This strengthens the observation of localised dilatant pathways as opposed to a distributed radial migration of gas.

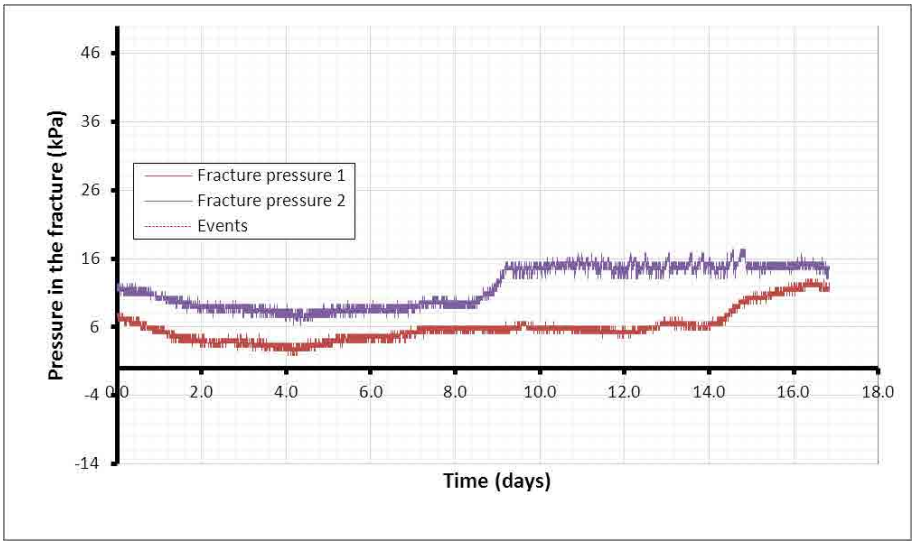

Figure 28 Example of pressure recorded on the slip-plane. A low pressure of less than 20 kPa is observed. Little variation is seen, with no correlation with other data identified.

2.3 GAS-DRIVEN RADIONUCLIDE MOVEMENT IN EDZ (SCK)

2.3.1 Scope and objectives

The main mechanisms by which gas will be generated in deep geological repositories are: anaerobic corrosion of metals in wastes and packaging; radiolysis of water and organic materials in the packages, and microbial degradation of various organic wastes. Corrosion and radiolysis yield mainly hydrogen while microbial degradation leads to among others methane and carbon dioxide.

The gas generated in the near field of a geological repository in clay will dissolve in the ground water and is transported away from the repository by diffusion as dissolved species. However if the gas generation rate is larger than the capacity for diffusive transport of dissolved gas, the pore water will get oversaturated and a free gas phase will be formed, leading to a gas pressure build-up. The gas production rate for some waste types and packages, especially ILLWs, is expected to be significantly higher than the diffusive flux (although marred by large uncertainties). Hence, one of our research objectives is to improve the understanding of gas transport modes through the EBS and clay when the capacity for transport of dissolved gasses is exceeded. Indeed, the processes by which gasses are transported in porous media with a low hydraulic conductivity like clays are still poorly understood: 2-phase flow, pathway dilatation (µ-fracturing), fracturing…? Of particular importance for long-term radiological safety is the question whether the aforementioned gas transport modes are accompanied by displacement of significant amounts of pore water which could contain radionuclides depending on the timing of the "breakthrough event". (FORGE D4.17 §1.2)

The work performed within FORGE WP4 and described in D4.17 tried to answer the question "to what extent can a gas pressure build-up enhance the radionuclide and contaminants transport in a clay hostrock and the EBS". More particular, we focussed on the transfer through localised paths developing along specific discontinuities, such as fissures in the EDZ and interfaces between the EBS components and the host rock.

2.3.2 Short description/overview of executed experiments

2.3.2.1 Method

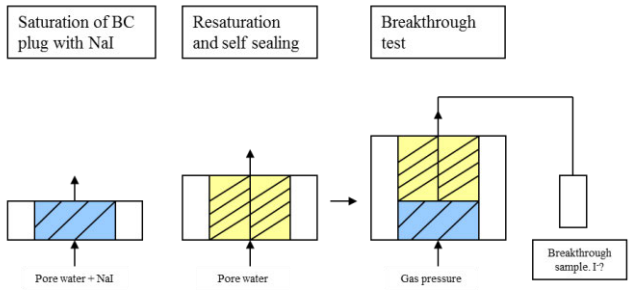

Figure 29 Basic concept of the tests to study gas driven tracer transport in disturbed Boom Clay.

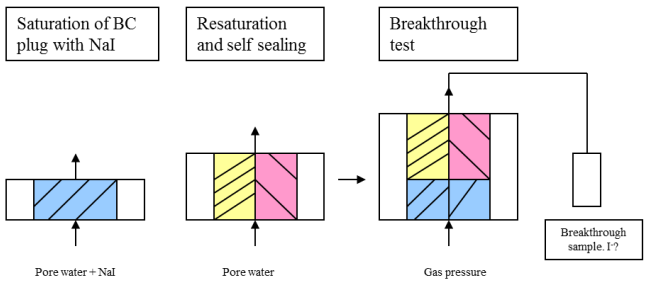

Figure 30 Basic concept of the tests to study gas driven tracer transport in the interface Boom Clay – Bentonite. Blue = NaI saturated Boom Clay core. Yellow = half Boom Clay core. Pink = half bentonite core.

To demonstrate the effect of a gas breakthrough on the transport of radionuclides, an anionic tracer is used.

So first, a small Boom Clay (BC) core (Ø 38 mm) is saturated with the anionic tracer (iodide [I^-], 0.01 mol/l NaI in Boom Clay natural pore water). Iodide (I^-) is chosen because its transport is not retarded under normal Boom Clay conditions: the sorption to clay minerals is negligible and it does not react with natural organic matter. The used iodine concentration is more than 1000x higher than the natural iodine concentration in Boom Clay pore water (~5 10^{-6} mol/l) (De Craen *et al*., 2004).

Second, for the experiments on disturbed Boom Clay (Figure 29) a larger core (38 mm high) is cut with a knife in 2 half cylinders, recombined and resaturated with natural pore water for different time periods ranging from one night to one week. During the SELFRAC project (Van Geet *et al*., 2008), the artificially created fracture was hardly visible after 16h, and after 20h the fracture was even no longer visible. So sealing of fractures goes very fast.

For the experiments with bentonite (Figure 30), the saturated bentonite cores (Volclay KWK, dry density 1.6 g/cm³) and the Boom Clay cores are halved, and both pieces are combined and resaturated with natural pore water during 1 week.

In the next step, the disturbed resaturated core or combined bentonite-Boom clay core is put on top of the NaI-conditioned core in a polycarbonate permeameter cell and confined (constant volume) between 2 porous stainless steel filters. The upper filter is filled with natural clay water which has a low average background concentration of iodide ~5 10^{-6} mol/l (De Craen *et al.*, 2004).

Finally a gas pressure (helium) is imposed at the bottom of the cell, and stepwise increased until gas breakthrough occurs. When gas breakthrough occurs, water can be expelled. Therefore, the water at the outflow, expelled after gas breakthrough, is analysed (with ICP-MS) for iodine enrichment. An enrichment in iodine concentration after breakthrough can be seen as an indicator for gas driven tracer transport.

The entire test is conducted in a temperature controlled room, at a constant temperature of 21°C (± 2°C).

A more detailed description of the used method can be found in FORGE D4.17 §2.1 and 2.3.

As the diffusion of iodide is unretarded it cannot be neglected when experiments last longer than 4 days. Transport calculations have shown that already after 3.5 days the concentration of diffused iodide is at the same level as the natural iodide concentration in Boom Clay water. So gas breakthrough should occur within 4 days to allow a determination of gas induced water (contaminated with tracer) displacement. In this case, a water displacement of only 0.002 ml is sufficient to double the I concentration in the pore water. So this is in fact the detection limit for gas induced water displacement of these experiments. (Jacops *et al.*, 2013) FORGE D4.17 §2.3.3

2.3.2.2 Experimental configurations

Experiments have been performed on undisturbed Boom Clay (no artificial fissure), disturbed Boom Clay (artificially fissured) and combined Boom Clay – bentonite cores. Disturbed Boom Clay samples were cut in 2 half cylinders and resealed for different time periods: 4 hours, 1 night or 1 week.

To investigate the effect of the artificial fissure, the NaI saturated cores were also cut in half for some experiments.To investigate the effect of the orientation of the bedding plane, we used both Boom Clay cores sampled perpendicular and parallel to the bedding plane.

An overview of all experimental configurations with only Boom Clay samples is given in FORGE D4.17 §2.3.4. Next to the experiments with Boom Clay, we also performed 4 experiments with combined Boom Clay – bentonite cores.

2.3.3 Discussion of results

2.3.3.1 General overview of the results

For every experiment the I concentration in the breakthrough sample vs. time of sampling is measured and plotted in Figure 31. The background concentration accounts for the concentration of I which is naturally present in Boom Clay pore water and the concentration of I that has diffused from the 0.01 mol/l NaI saturated Boom Clay core through an undisturbed (pore water saturated) Boom Clay core of 38 mm high. The results are presented in Figure 31.

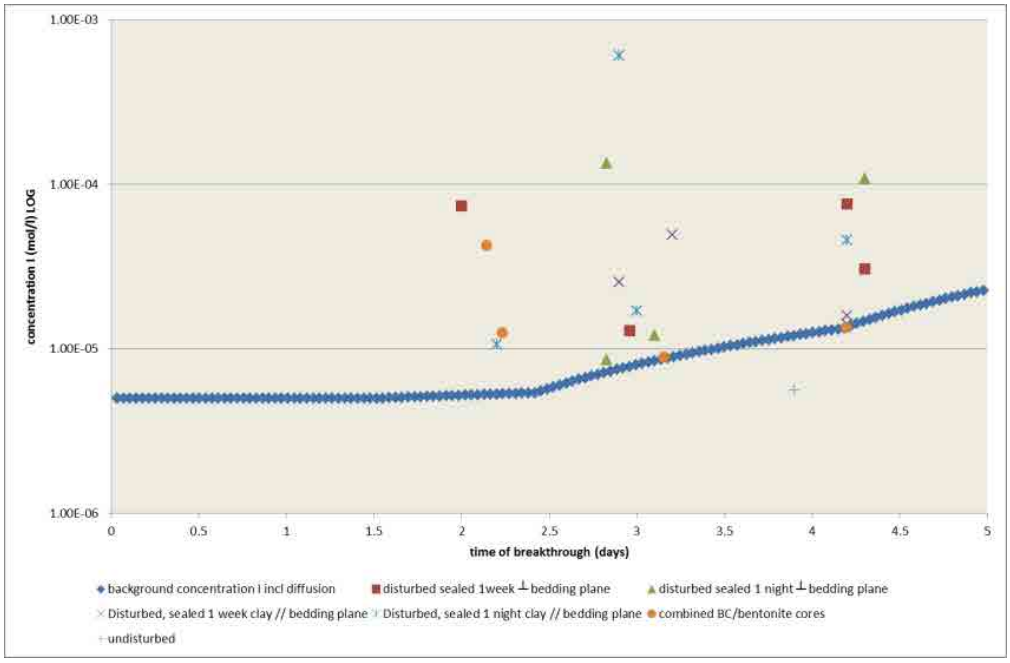

Figure 31 Iodine concentration in breakthrough samples (log-scale) vs. time of breakthrough for all experiments.

Based on the I-analyses of the pore water, and by taking into account the unretarded diffusion of I and the background concentration of I in Boom Clay pore water, we calculated the concentration of I in the water sample that is solely related to transport during gas breakthrough. Based on this value, we calculated the amount of pore water of the NaI-saturated core that was transported. This can be recalculated as a degree of desaturation of the NaI saturated plug.

In general, the measured concentration of I is rather low (< 10^{-4} mol/l I), and consequently the degree of desaturation of the bottom (NaI saturated) plug is also low (< 0.5%). A detailed table with all experimental results can be found in FORGE D4.17 §3.1

2.3.3.2 Comparison between different experimental configurations

Role of sealing

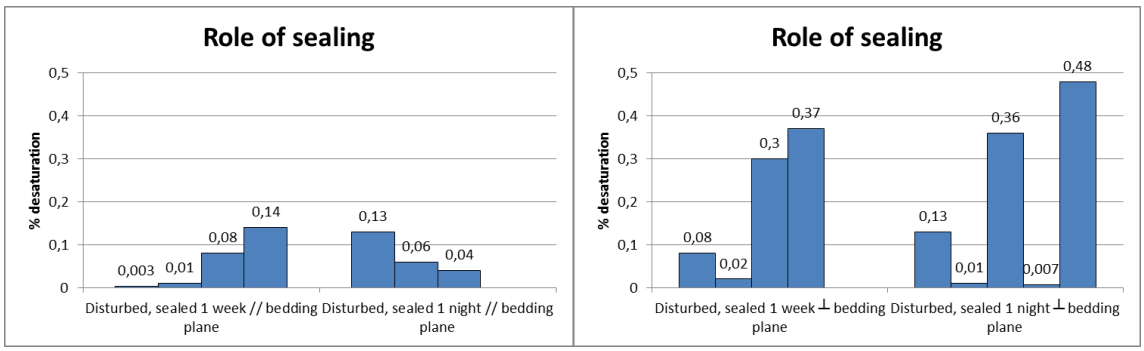

Figure 32 Role of time of sealing (1 night vs. 1 week) on the degree of desaturation (% of NaI saturated pore water that was transported during gas breakthrough – calculation based on measured concentration of I) for samples oriented parallel (left) and perpendicular (right) to the bedding plane.

From Figure 32, we observe no significant difference between sealing for 1 night or sealing for 1 week. Even after 1 night of sealing, the degree of desaturation is already low (< 0.5%). So the sealing process can be considered as a fast process.

In experiments with fissured and (re)sealed Boom Clay cores, breakthrough occurs often at the interface fissure – cell (see Figure 33, left). At this location, some "clay" material is missing (see Figure 33 right) due to the artificial fracturing (in fact cutting) and consequently it's a weak part of the core and thus a preferential path for gas.

If we want to investigate solely the role of fissures in gas-induced tracer transport, we have to use another set-up in which a confining pressure can be used to exclude gas transport along the wall. In addition, such a set-up would also allow comparing, for instance, the breakthrough and the confinement pressure. One could expect that when breakthrough occurs along the interface clay – cell, more I is transported compared to breakthrough through the clay sample. Our experimental results (see Figure 33), seem to support this hypothesis.

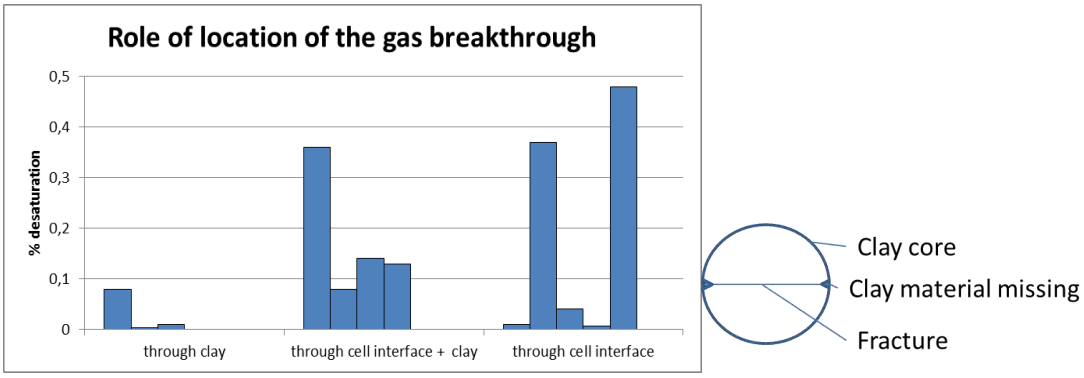

Figure 33 Left: location of the gas pathway during breakthrough vs. degree of desaturation (% of NaI saturated pore water that was transported during gas breakthrough – calculation based on measured concentration I). Right: schematic view of interface clay fracture-cell.

Based on these experiments we can state that gas moves through the weakest path which was in most cases the interface fracture – cell. In at least 10 out of 19 experiments, we observed gas breakthrough pathways at the interface clay/fracture – cell (see Figure 34 left). In only 3 experiments out of 19, we observed gas breakthrough pathways going only through the clay core. In some experiments, we observed both (see Figure 34 right).

More detailed information can be found in FORGE D4.17 §3.2.1.

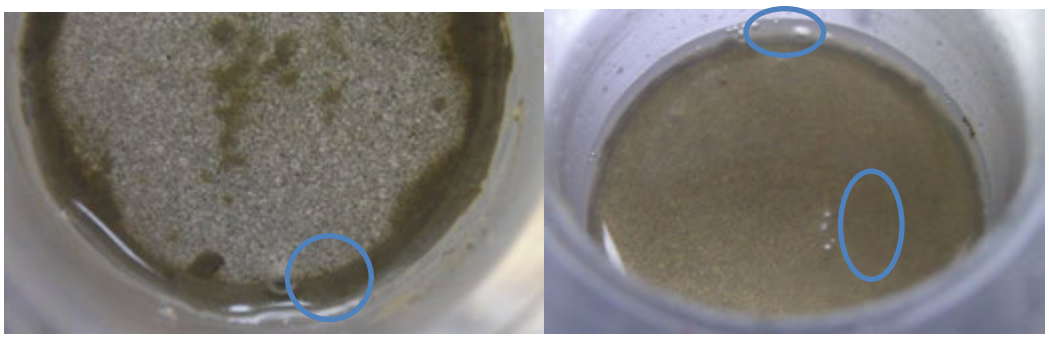

Figure 34 Observation of gas bubbles during the dismantling of experiments 2011/1-1 (left) and experiment 2011/3-1(right).

Role of orientation with respect to bedding plane

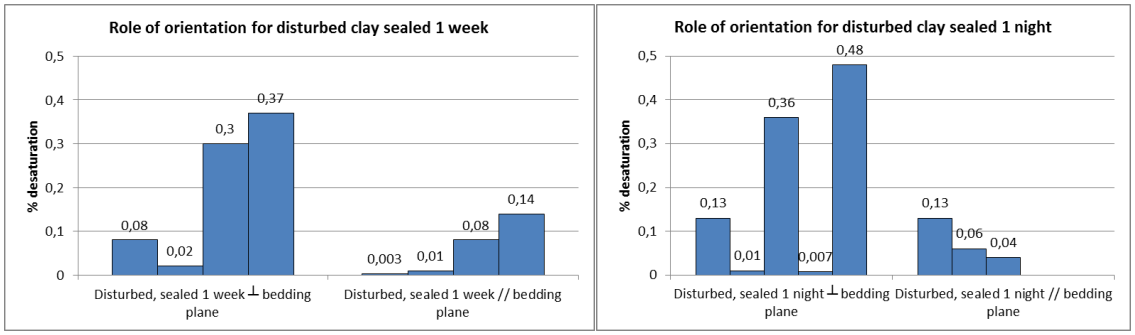

Figure 35 Role of orientation wrt. bedding plane for disturbed clay samples sealed 1 week (left) and 1 night (right) (desaturation is % of NaI saturated pore water that was transported during gas breakthrough – calculation based on measured concentration I).

When looking at the role of orientation wrt. bedding plane (Figure 35), it seems that more water is expelled from samples with an orientation perpendicular to the bedding plane. So the average degree of desaturation (hence tracer transported by gas) is less for samples // to the bedding plane. This observation could be explained by the structure of clay: clay minerals are plates oriented parallel to bedding and when swelling occurs e.g. due to unloading or after fissuring this swelling will be mainly in the direction orthogonal to bedding. Thus fissures parallel to bedding close faster and better than fissures that are orthogonal to bedding.

But we can state that if the clay core can seal properly, the amount of water transported during gas breakthrough is low. However, due to the selected experimental set-up and the selected experimental procedure, we have no objective data on the sealing status of the clay cores so it is difficult to prove a relation between orientation of the clay sample, time of sealing and degree of desaturation.

Another aspect that cannot be neglected is the reproducibility of the fractures. Fractures are created by cutting clay with a knife. This "cutting" will be a combination of shear and smearing and are totally different compared to tensile fractures. The "cutting" can "turn" the clay plates, leading to much more disturbances compared to a tensile fracture. Moreover, the cutting is not reproducible: every fracture is different, leading to other smaller fractures in the neighbourhood and different apertures of the fracture. This variability may play a larger role during the gas breakthrough process than time of sealing or orientation.

More detailed information can be found in FORGE D4.17 §3.2.2.

Role of materials

The presence of an interface Boom Clay / Bentonite does not lead to more tracer transport, compared to fractured (sealed and unsealed) Boom Clay (see Figure 36).

It is mainly the interface between the Boom Clay/Bentonite core and the wall of the cell which act as a preferential path. If we want to investigate solely the role of the interface Boom Clay / bentonite as a pathway in gas-inducted tracer transport, we would have to use another set-up in which a confining pressure can be used to exclude gas transport along the wall.

More detailed information can be found in FORGE D4.17 §3.2.3.

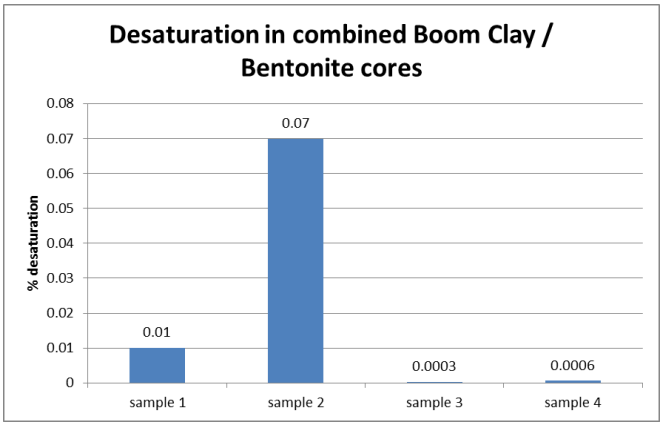

Figure 36 Desaturation (% of NaI saturated pore water that was transported during gas breakthrough – calculation based on measured concentration I) in combined Boom Clay/Bentonite cores (4 different samples).

2.3.3.3 Discussion

During many of the experiments we performed, we observed that interfaces play an important role in the gas-induced tracer transport. They often act as a preferential pathway. Our most important interface was the interface between the clay sample and the wall of the permeameter cell. Especially when samples are fractured and some clay material is missing at the intersection of the fracture edge with the core cylindrical surface, then the interface Boom Clay core –cell at the level of the fracture is rather weak and acts as a gas conducting pathway. If gas starts to accumulate in a repository, this suggests that the gas might more easily escape along the interface of natural and engineered barriers than that it would escape through the host rock.

The experiments are also strongly influenced by the lack of reproducibility of the fracture. As discussed in previous paragraphs, creating fractures by cutting the clay causes much more disturbance compared to the tensile fracture that could occur in-situ and this disturbance is not reproducible.

In previous breakthrough tests performed in the 1990's on undisturbed Boom Clay, a mean decrease in saturation less than 2% was reported (MEGAS project, Volckaert *et al.*, 1994). Based on the results of the experiments on undisturbed and disturbed Boom Clay and combined bentonite – Boom Clay cores, the amount of I that was transported and consequently the degree of desaturation due to gas breakthrough was very low (< 0.5%).

If we have a look at the amount of gas transported during breakthrough compared to the amount of tracer that was transported during this gas breakthrough, we get following results: in experiment 2010/4-1, 200.5 ml gas (STP) was blown through the clay and it transported only 0.77 µl contaminated water. In experiment 2011/3-3, 1291 ml gas (STP) was blown through the clay and it transported only 7.64 µl contaminated water. So despite the large amount of gas transported, only very small amounts of contaminated water were transported. This points rather to "pathway dilation" and not to visco-capillary 2-phase flow.

During the experiments, we made a lot of observations on the gas flow during the gas breakthrough event and these observations allow us to draw some conclusions regarding flow mechanisms. During the breakthrough experiments, gas flow was very unstable. It could suddenly stop, start again, increase or decrease while the gas pressure was constant. Also when we observed the surface of the clay core in a dismantled cell, we could observe gas bubbles escaping at one location, and the next moment we observed gas bubbles escaping at another

location or it suddenly stopped. So based on these observations, we can state that gas flow was very unstable – rather indicating another flow mechanism than visco-capillary 2-phase-flow.

2.3.4 Conclusion

The goal of this research was to answer the following question: "to what extent can a gas pressure build-up enhance the radionuclide and contaminants transport in a clay host rock?" Based on the obtained results, we can state that the transport of radionuclides and contaminants due to a gas breakthrough is indeed possible but seems very limited.

The effect of different parameters (orientation of the samples wrt. bedding plane, time of sealing of the fractures and porous medium type) on the degree of desaturation was investigated, but we did not find a clear relationship. In our opinion, other aspects like the reproducibility of the fracture, the stress-state of the sample and the presence of interfaces (Boom Clay-cell, bentonite-cell) have a stronger influence on the experimental results.

To get a better hold on the process, it could be interesting to perform some additional experiments in an adapted set-up, with control of the total stress (tri-axial cell), using a confining pressure to avoid breakthrough along the wall and making use of samples with a more realistic (shear or tensile) fracture.

Concerning the gas flow mechanisms, the observations of laboratory gas tests on BC samples indicate more and more that gas dissipation through dilation pathways is more likely than development of plane-type fractures. Of course this observation is stress and scale dependent. However, direct characterisation of the dilation pathway is with the current experiments very difficult to apply. More evidence needs to be collected to prove pathway dilation at relevant scales.

Concerning the stability of gas pathways we believe that created gas pathways are not stable in time. When we performed gas breakthrough experiments on disturbed (fissured) and undisturbed Boom Clay, the flow after breakthrough was never stable. We observed all kinds of flow patterns, even stopping and resuming of flow (Jacops *et al*., 2013). Probably opening and closing of pathways is related to gas pressure and stress inside the sample. Our experiments were not designed to examine this into detail as it was not our goal of the experiments. Moreover, Boom Clay is plastic and pathways can easily and quickly seal. (Van Geet *et al*., 2008).

Concerning interfaces, we can conclude that they played an important role in our experiments as gas mainly escaped at the interface sample – cell. However, this phenomenon is stress-related but our experiments were not equipped with for instance, strain gauges so conclusions on the stress state of the sample cannot be drawn.

Experiments performed within FORGE WP's 4 & 5 (Jacops *et al*., 2012) demonstrated that radionuclides can indeed be transported during gas breakthrough, but it is considered limited as the amount of displaced water is less than 0.5% of the "contaminated" water volume. The volume of water displaced is also very low (3 orders of magnitude) compared to the volume of gas transported upon breakthrough. We do not expect that gas induced transport will have a significant effect on RN migration at repository scale.

3. In-situ experiments

3.1 GAS TRANSPORT IN EDZ AT MONT TERRI (NAGRA)

3.1.1 Scope and objectives

The experiment ("Gas path through host rock and along seal sections / HG-A") as part of the Mont Terri research programme was designed as a long-term water & gas injection experiment in a backfilled microtunnel, to investigate both water/gas leak-off rates and gas release paths from a sealed tunnel section in an ultra-low permeability host rock (Opalinus Clay). The aims of the HG-A experiment are to:

- Provide evidence for barrier function of the Opalinus Clay on the tunnel scale (scale effects in rock permeability);
- Investigate self-sealing of the EDZ after tunnel closure (mechanical self-sealing in response to packer inflation and pore pressure changes);
- Provide evidence for gas transport capacity of Opalinus Clay (intact host rock and EDZ).

The experiment combines field investigations with extensive hydro-mechanical instrumentation in and around the HG-A microtunnel with geotechnical laboratory studies on core samples and extensive modelling activities for the validation of coupled hydro-mechanical models. Further details on the experiment are found in FORGE deliverable D4-16.

3.1.2 Description of the experiment

The HG-A experiment is located in the southern part of the Mont Terri Rock Laboratory off Gallery 04 (see Figure 37). The 1m diameter, 13m long microtunnel was excavated during February 2005 using a steel auger from a niche in Gallery 04. The microtunnel was excavated parallel to bedding strike and bedding parallel features run along the tunnel replicating the expected relationship between bedding and emplacement tunnel orientation in a deep repository, where bedding is expected to be flat-lying and emplacement tunnels to be sub-horizontal. Excavation was monitored by a borehole array containing piezometers and deformation gauges (clino-chain and chain deflectometers). The borehole array was subsequently augmented with additional piezometer boreholes and borehole stressmeters (Fig. Figure 37b).

The first 6m of the microtunnel was lined with a steel casing immediately after excavation to stabilize the opening. The gap behind the liner was then cement-grouted, but not sealed. The purpose-built hydraulic megapacker (diameter 940mm and sealing section length 3000mm) was installed in 2006. The sealing section was located at 6-9m with a 1m grouted zone containing the non-sealing part of the packer and retaining wall from 9-10m. The final 3m of the microtunnel from 10-13m forms the test section which was instrumented and backfilled prior to packer emplacement.

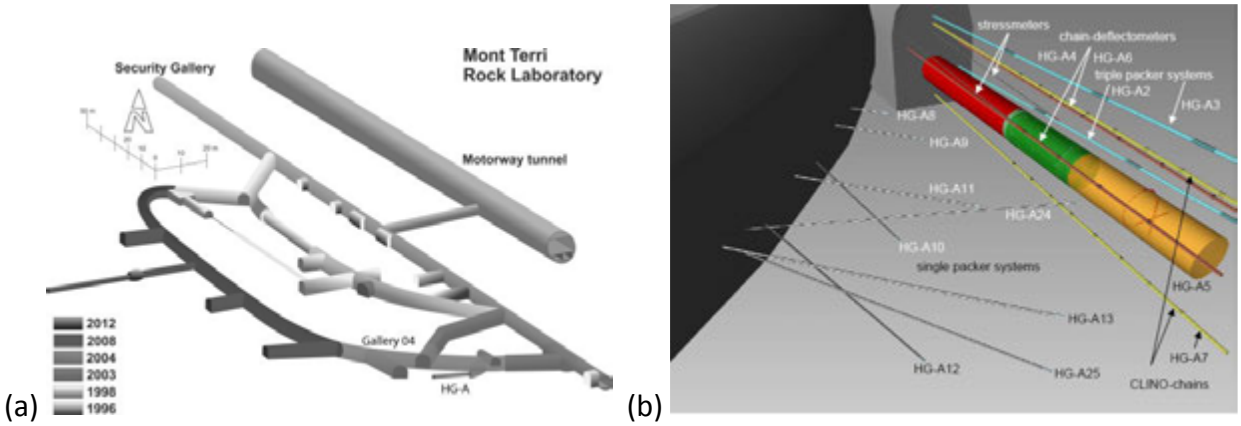

Figure 37 Location and layout of HG-A a) location at the Mont Terri Laboratory; b) Schematic drawing of the Microtunnel and the site instrumentation. Colour coding refers to the steel liner (red), the seal section (green) and the backfilled test section (orange).

The test section was instrumented with piezometers, extensometers, strain-gauges and Time Domain Reflectometers (TDRs) to measure pressure, deformation and water content. After instrumentation the test section was ventilated for about 3 months and then backfilled with sand behind a retaining wall.

The seal section was instrumented with piezometers, total pressure cells and TDRs prior to the installation of the megapacker. Following the installation of the megapacker the volume between the retaining wall and the megapacker was filled with a cement grout. Overall, a total of more than 100 sensors were placed in the geosphere, test and sealing sections.

3.1.3 Chronology of the experiment and results

An overall chronology of the HG-A experiment from excavation to the current day (November 2012) is given in Table 5. Saturation of the test section and surrounding rock was started in November 2006 following emplacement of the megapacker (June 2006) and subsequent grouting of the section between the megapacker and Test Section. A variety of saturation tests were performed using a synthetic pore water until January 2008 when a long-term multi-rate hydraulic test was initiated. This test continued until February 2010 and involved a series of constant rate injection steps. During the test the injection rate declined from ~10 ml/min to 0.1 ml/min (144 ml/day). Figure 38 displays an overview of the available long-term monitoring data in terms of microtunnel stress, pore pressure, water content and flowrate measurements from start of saturation.

The gas injection phase included three separate Nitrogen gas injections (GI1-3). After each gas injection, following a shut-in period, water was extracted from the test section and depressurized to remove trapped gas (gas-water exchange). The degassed water was then re-injected into the test section. This procedure provided a well-defined initial gas saturation in the test section pore water for the subsequent gas injection. During gas injection a low constant rate (~0.02 ml/min) water injection was maintained into the test section.

Figure 39 shows a comparison between the test section pressures in GI1 GI2 and GI3. Inspection of the log-log plots (Figure 39b) shows a roughly linear behaviour for the first 20 days prior to the subsequent breakdown in GI2 and GI3. In GI1 pressure is held constant and no breakdown was observed.

Start	End	Activity
17/02/2005	25/02/2005	Excavation of Micro-tunnel and installation of liner 0-6m
25/02/2005	29/06/2006	Tunnel open instrumentation and backfill of test section
29/06/2006	29/06/2006	Megapacker emplacement
29/06/2006	21/11/2006	Tunnel closed grouting between Megapacker & backfill
21/11/2006	23/01/2008	Saturation Tests
23/01/2008	15/02/2010	Long Term Multirate Hydraulic test
15/02/2010	21/04/2010	GI1 -initial flow 20 mln/min, switch to constant pressure 1200kPa
21/04/2010	01/06/2010	GI1 Recovery and gas/water exchange
01/06/2010	28/10/2010	GI2 - 10 mln/min constant rate
28/10/2010	29/03/2011	GI2 Recovery and gas/water exchange
29/03/2011	16/09/2011	GI3 - 20 mln/min constant rate
16/09/2011	30/09/2011	GI3 Recovery and gas/water exchange
30/09/2011	Ongoing	Post-Gas Hydraulic test: constant rate injection

Table 5 HG-A experiment chronology.

Gas pressure during GI1 was limited to 1200 kPa, significantly below the minimum stress, to avoid coupled mechanical effects. After an initial 20 mlN/min injection when pressure rose quickly, the injection rate was reduced to about 10 mlN/min to maintain roughly constant test section pressure.

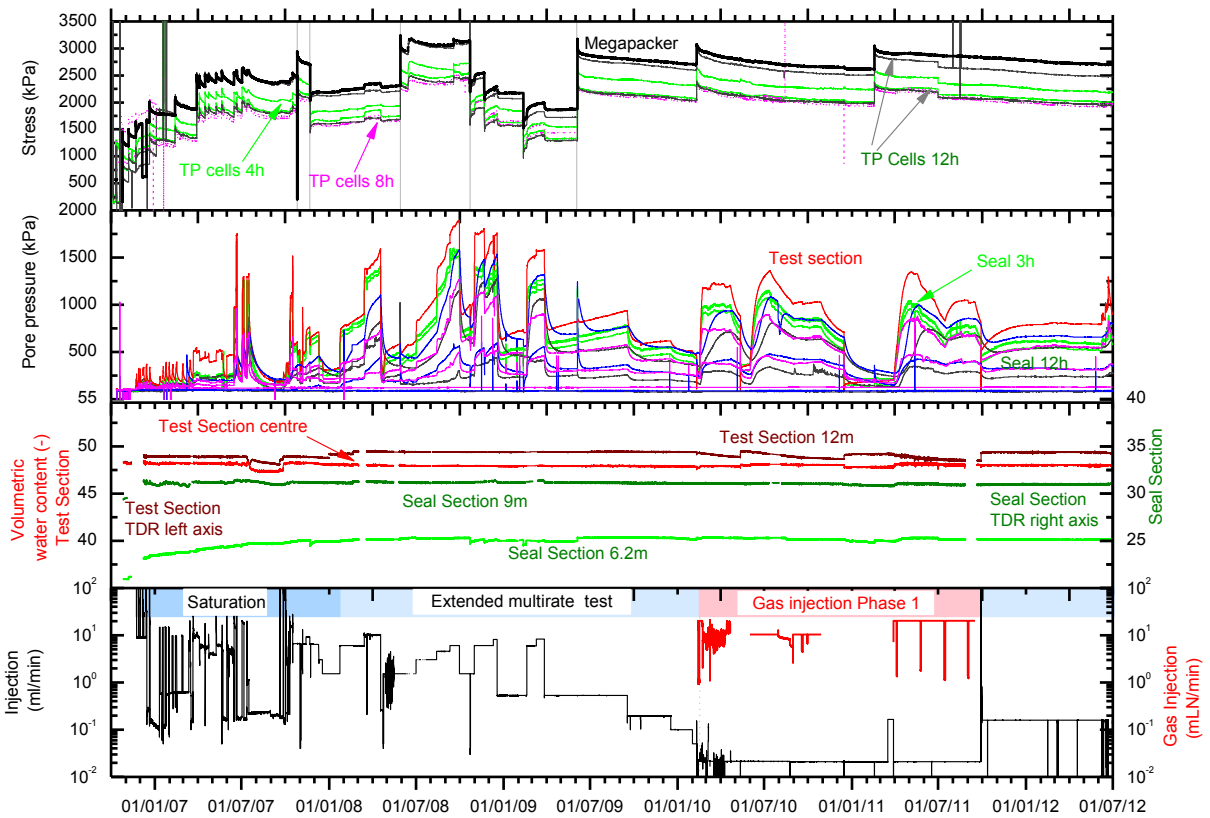

Figure 38 Microtunnel stress, pore pressure, water content and flowrate measurements from start of saturation.

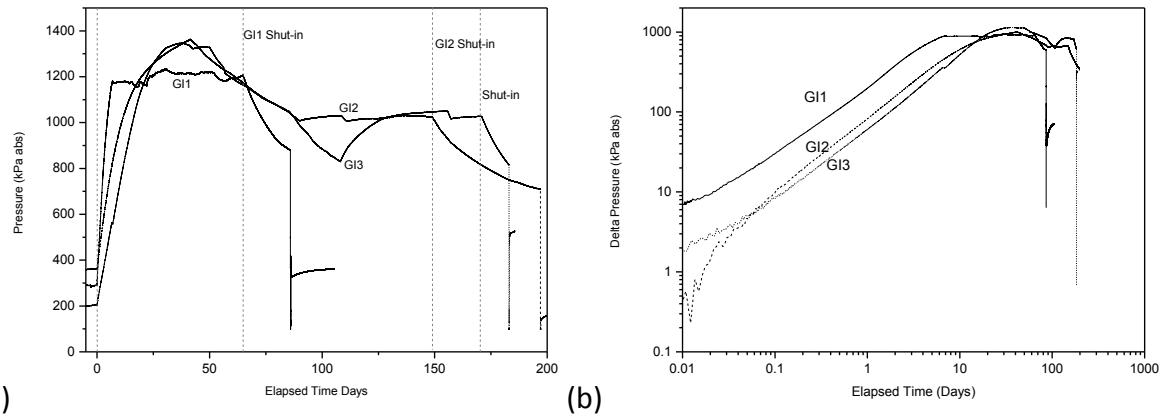

Figure 39 a) Linear and b) log-log plots of delta pressure from GI1-3.

During GI2 test section pressure rose more slowly than in GI1 and then peaked at 1363kPa on 12/07/10. After the pressure breakdown, the test section pressure drops over about a month by about 350 kPa to 975 kPa and then stabilises at about 1040kPa.

During GI3, test section pressure again peaks at 1347 kPa but with a broader peak than in GI2 and then drops to about 840 kPa due to an interruption in injection before recovering (after resumption of gas injection) and stabilizing at about 1040 kPa.

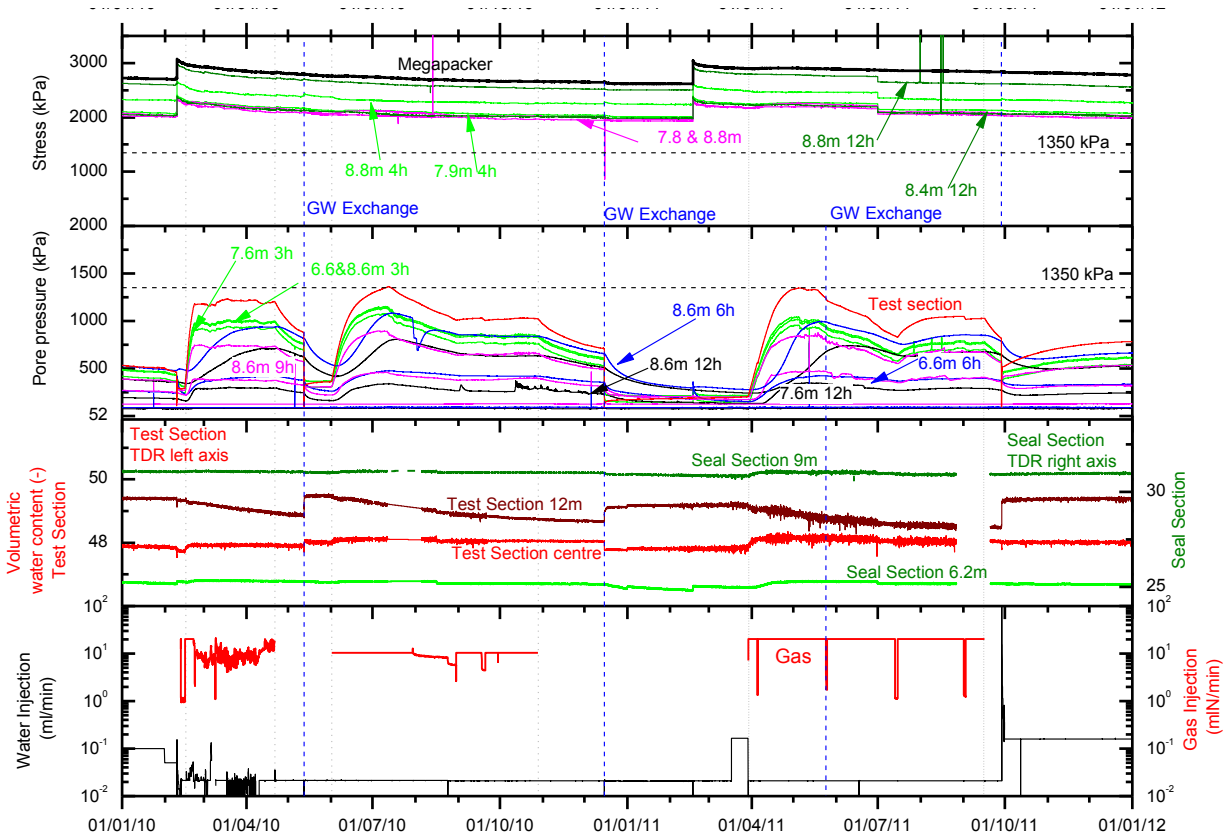

Figure 40 Microtunnel stress, pore pressure, water content and flowrate measurements during gas injection.

Pressures in the sealing section during gas injection were lower and lagged those in the test section as would be expected (Figure 40). Pressure response is highly heterogeneous. Pressure along the 3 o'clock sensors reacts most strongly and quickly to the test section suggesting a high diffusivity connection. However, the pressure at Section 1 in PES-S1-3h (sensor close to the rear of the sealing element) is high (in fact higher than PES-S2-3h a sensor in the centre of the seal section) and comparable to PES-S3-3h closest to the test section. This suggests that this piezometer is not well connected to the open tunnel. All other piezometers in Section 1 show no response to gas injection and remain at close to atmospheric pressure.

After shut-in and depressurisation remnant high pressures were observed at some piezometers in the sealing section indicating possible closure after gas injection or some other loss of connectivity, perhaps, due to water invasion and blocking.

So called "self-sealing" tests were performed during all stages of the experiment, including saturation phase, hydrotest phase and subsequent to each gas injection event. For this, a simple measure of the flow resistance across the seal section as the Sealing Index S (ml/min/kPa) was defined, based on the injection rate and test section pressure as:

$$S = \frac{Q}{P_{Test\,section} - 100}$$

where Q is the flow into the test section in ml/min and $P_{TestSection}$ is the absolute test section pressure in kPa. Assuming linear flow and a flowpath length of 3m (seal section), the sealing index can be converted into an EDZ conductance (m^3/s) by multiplying by a factor 5×10^{-7} (considering only resistance along the seal section). Sealing indices were calculated only for those test phases, when full water saturation was ensured in the backfilled test section. Figure 41 shows the calculated Sealing Index after filtering for flow rate changes to minimize storage effects.

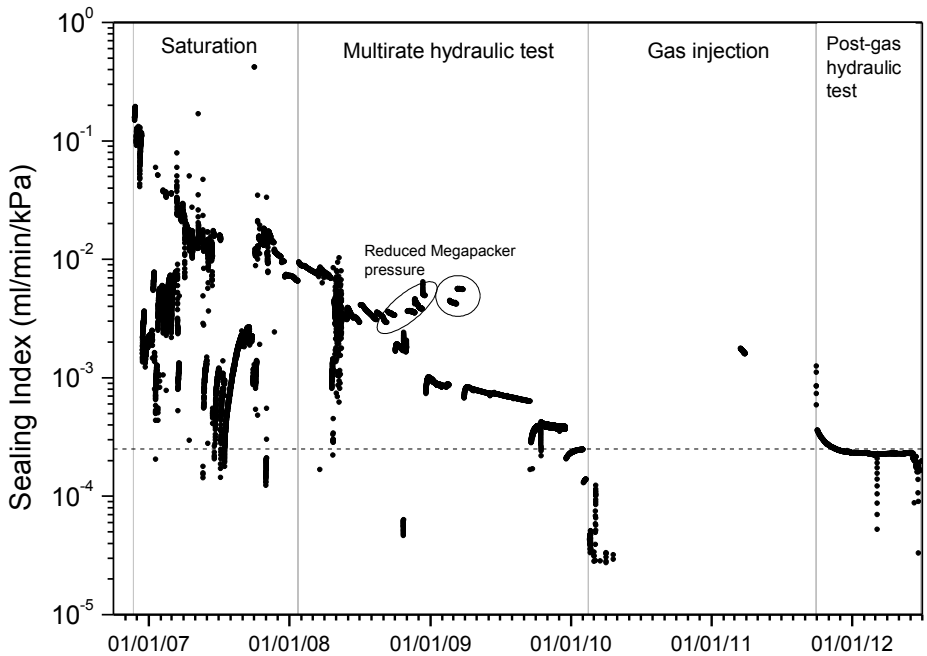

Figure 41 Sealing Index during water injection. Periods of reduced Megapacker pressure (low effective stress) are marked.

In the year prior to gas injection the sealing index reduced from 10^{-3} to less than 10^{-4} (ml/min/kPa) equivalent to a hydraulic conductance of 5×10^{-11} m^3/s. This corresponds to a

hydraulic conductivity of the EDZ of 5×10^{-11} m/s, assuming an EDZ with a cross sectional area of 1 m^2 (equivalent EDZ thickness: 0.26 m). The water injections following the gas injection sequence confirm a long-term sealing tendency of the EDZ. The effective conductance shows an ongoing reduction during the subsequent hydraulic testing. Following gas injection the effective conductance swiftly reduces to values in the order of 10^{-5} (ml/min/kPa).

3.1.4 Conclusions and outlook

The ongoing HG-A in-situ experiment has given valuable insight in the evolution of both gas leak-off rates and gas release paths from a sealed tunnel section in response to gas overpressures. Furthermore, the self-sealing capacity of the Opalinus Clay has been confirmed by repeated water injection tests, demonstrating an ongoing reduction of leakage rates along the EDZ around the pressurised megapacker system.

Overall, the following conclusions can be drawn about the hydro-mechanical evolution of the tunnel near-field of the HG-A experiment and the associated water and gas flow:

- The rock around a backfilled tunnel in the Opalinus Clay is characterised by a significant heterogeneity of the hydraulic and mechanical rock properties due to pre-existing and EDZ-induced flaws (see Figure 42a). The stress redistribution in the wallrock in response to the excavation of the tunnel may re-activate pre-existing fractures or create damage of the intact rock due to high shear stresses (incl. activation of bedding).
- Dissolution and diffusion of dissolved gas are important and well-understood processes, which delay the build-up of gas pressures in the backfilled test section (Figure 42b)
- Gas overpressures develop in the backfilled test section as soon as the solubility limit of the porewater in the backfill is exceeded. The gas overpressure starts to expel pore water from the backfill into the rock, increasing the gas storage capacity and lowering the water level in the test section (Figure 42c).
- Due to the spatial variability of the hydraulic and mechanical rock properties around the backfilled tunnel section, it is very likely that gas from the over-pressurised headspace will enter the wallrock at a local entry pressure, which is significantly lower than the entry pressure of intact Opalinus Clay (Figure 42d). The invading gas displaces the porewater along the pore networks of the EDZ until the gas breakthrough to the tunnel atmosphere / Gallery 04 is reached.
- The gas pressure build-up in the sealed tunnel section during GI1-GI3 was low (<1.4 MPa) even though the applied gas injection rates correspond approximately to the cumulative gas generation rate, inferred for a 500 m long SF/HLW emplacement tunnel (assumption: steel corrosion rates: 2 μm). This fact underlines the high gas transport capacity of the EDZ along the seal section of the megapacker.
- Significant deformation of the rock around the test section and the seal section (extensometers, inclinometers, deflectometers and stress cells) was not observed during the gas injection events, suggesting that simple porewater displacement along the EDZ-related pore network was the main gas transport process. Pathway dilation processes are only likely if the test section pressure approaches the local minimum stress.
- The slight increase in gas transport capacity in turn of the successive gas tests GI1 – GI3 may indicate an enhancement of the local permeability along the gas path from the test section towards the Gallery 04 niche; notably such phenomena are known from experiments on multiphase flow in granular materials. On the macroscopic scale,

however, the hydraulic conductance of the EDZ reduces successively, indicating an efficient self-sealing mechanism.

- No clear signs of gas transport into the intact Opalinus Clay around the test section were observed. Pressure signals of several piezometers in the wallrock are interpreted as a response on the porewater displacement due to gas injection in the backfill.

The existing hydraulic and mechanical data (pore pressures, flow rates, deformation, stress) have been forwarded to several modelling teams for detailed data analyses and simulations. The preliminary results indicate that the hydraulic tests and the gas injections can be simulated with plausible assumptions on boundary and initial conditions and consistent geotechnical parameters from laboratory testing. However, successful model discrimination is not possible with the existing data sets, because the knowledge about the spatial extension of the gas path along the EDZ is yet vague. For this reason, a new experimental phase of the HG-A experiment has been launched recently, aimed at visualising the propagation of the gas front during gas injection tests by means of seismic tomography. It is expected, that such information will improve the calibration and validation of coupled hydromechanical models for gas transport in deformable media.

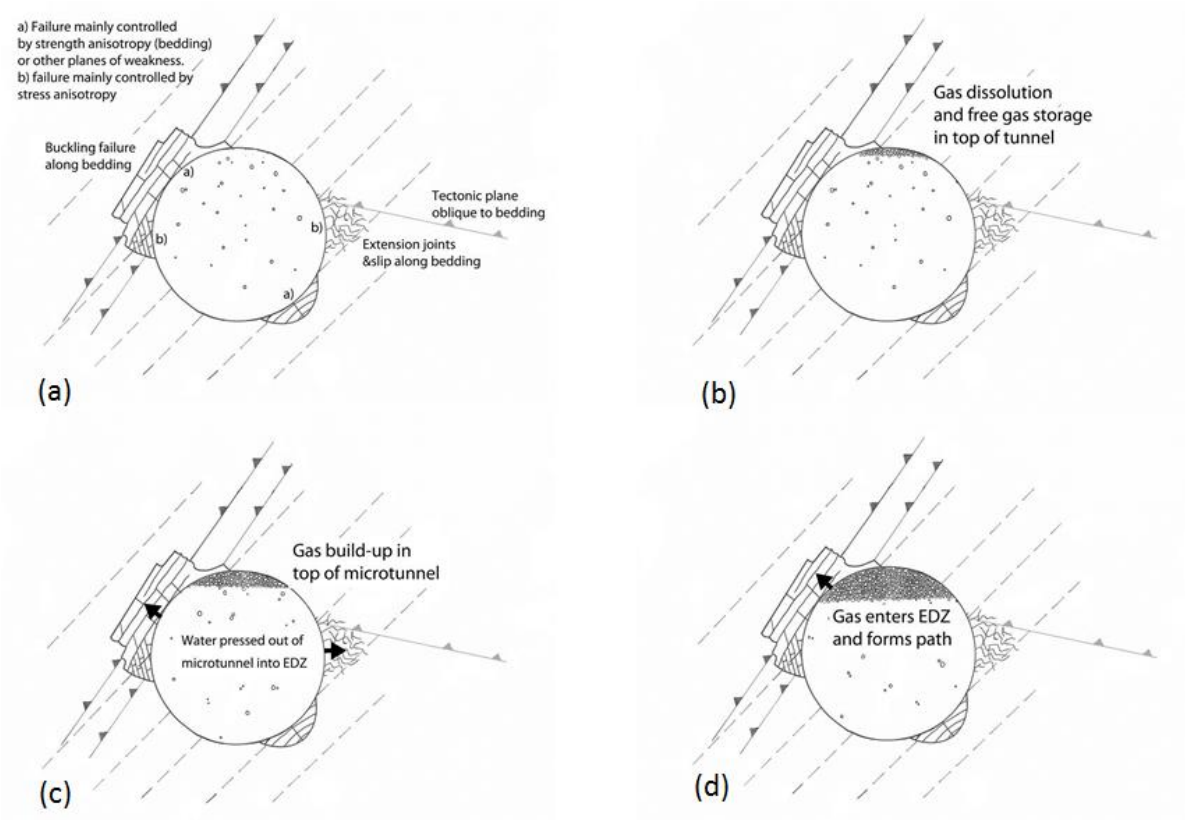

Figure 42 EDZ schematic (from Marschall et al. 2008) with stages of gas injection: a) EDZ structure, b) storage & dissolution, c) storage & leakage, d) breakdown and gas flow into the EDZ.

3.2 GAS TRANSPORT IN EDZ - IN SITU EXPERIMENT IN BOOM CLAY (SCK)

3.2.1 Objectives and background

This section reports the design and installation of two multi-filter monitoring boreholes and one large-diameter dual packer system carried out by SCK•CEN as part of the FORGE European

Commission FP7 project, under deliverables D4.4. The monitoring boreholes and packer system were installed in the Boom Clay at the Underground Research Facility (URF) of the High-Activity Disposal Experiment Site (HADES) located in Mol, Belgium. This work was completed in June 2011.

The packer system includes two large-diameter inflatable packers equipped with radial displacement sensors, pore pressure measurement filters and total pressure sensors. The sensors are embedded in the rubber membrane to measure the direct pressure and displacement at the interface between the clay and the packers. In addition, the packers contain both injection and detection filters to perform in-situ gas experiments. The objective of the gas experiments is to study the role played by the excavated disturbed zone (EDZ), the interface host rock/engineered barrier system (EBS) and the host formation on the release of gas overpressure and radionuclide (RN) transport in the Boom Clay..

The Forge packer system has been installed horizontally in the Boom Clay, at a depth of 225 m below surface, and opposite to the PRACLAY gallery, as shown in Figure 43. The installation consists of two multi-piezometer monitoring boreholes and one dual mega packer. The depth of the installation of the mega packers is 18.55 m while that of the two monitoring boreholes is 19.9 m.

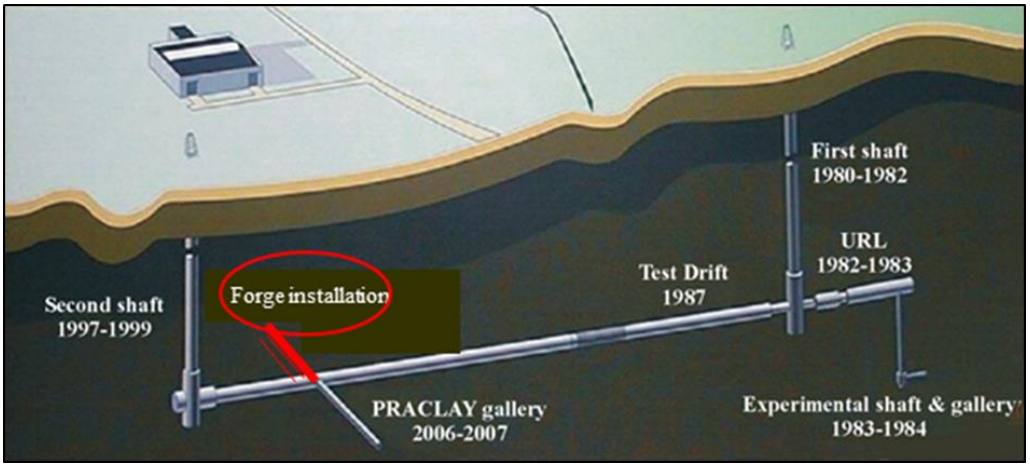

Figure 43 EDZ The URF in Mol showing the location of the Forge packer system installation.

3.2.2 Description of installation

3.2.2.1 Components

The installation includes a large-diameter dual packer and two multi-filter borehole monitoring piezometers. A summary of the principal components is given in the next paragraphs. More details are provided in D4.4/D4.11.

Mulit-filter monitoring piezometers

The multi-filter piezometers are located vertically underneath and to the left of the packers, as shown in Figure 44. The two multi-filter monitoring boreholes are installed parallel and at a distance of approximately 35 cm from the megapackers. The piezometers installed in these boreholes contain 8 filters. Each filter is designed with a small (42x64 mm), single screen to allow an accurate measurement of travel distance between the injection and detection filters.

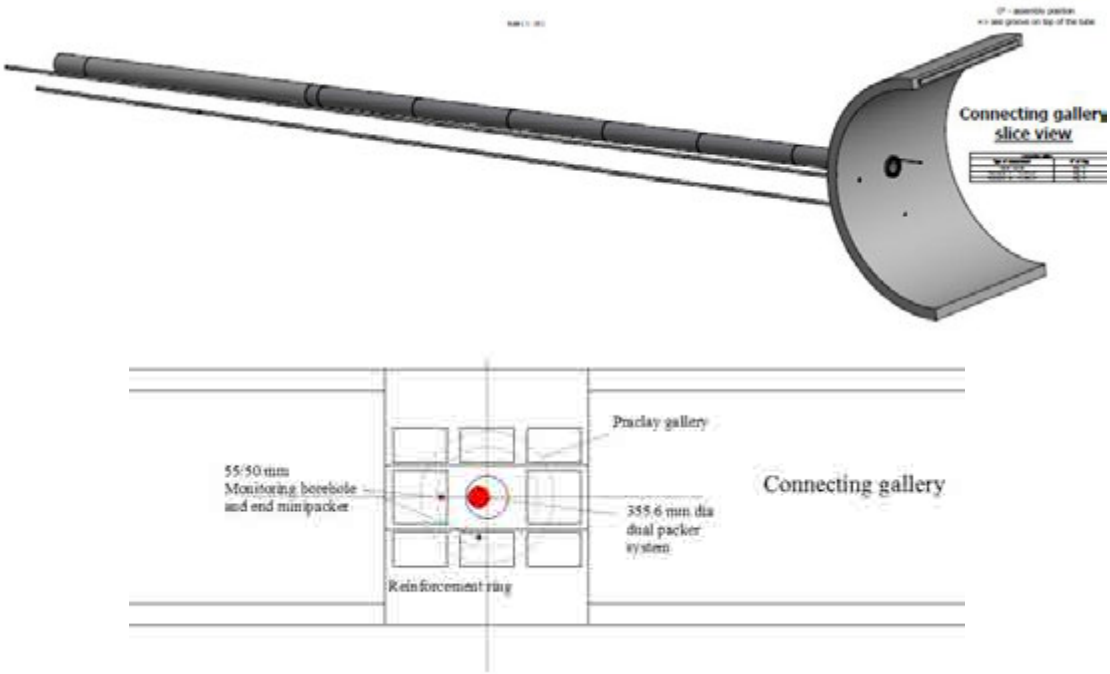

Figure 44 Layout [bottom] and overview [top] of packer system and multi-filter monitoring boreholes.

All filters have dual pressure tubes to allow for optimum flushing of the system. The pressure lines and casing are fabricated using AISI 316L stainless steel. The sintered steel Krebsöge filters have an aperture of 5 microns. The piezometer casings have a diameter of 55/45 mm and a total length of 19.9 m. The ends of both monitoring piezometer boreholes were installed with a mini packer to measure the total stress in the clay. The mini packer was damaged during installation of the megapackers and do not function anymore.

Megapackers

The mega packer system consists of two identical and inflatable large diameter packers manufactured by Solexperts in Switzerland. The packers have fixed ends to prevent axial displacement during inflation and deflation. They are inflated using Midel® synthetic ester oil, a synthetic and biodegradable oil. The inflatable rubber section contains an inner reinforced rubber layer of 1 cm in thickness and an outer non-reinforced layer of 3 cm in thickness. Both are made of Nitrile rubber, which is compatible with the Midel® oil used as inflating medium. The metal parts consist of stainless steel 316L for corrosion resistance against the Boom clay host formation.

The middle of each packer is instrumented at six hour-clock locations, labeled clockwise from 12:00 to 22:30. The following sensors are installed in the rubber sleeves of the packers:

- LVDT displacement transducers;
- Pore water pressure; and
- Total pressure.

The packer performance characteristic curve for confined inflation appears in Figure 45. The performance curve gives the maximum inflation pressure in function of inflated diameter.

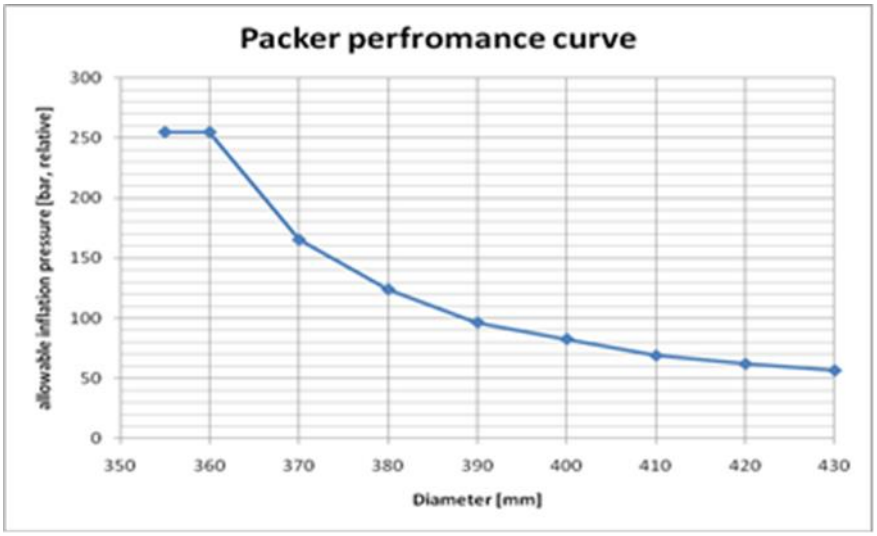

Figure 45 Layout Packer performance curve under confinement.

Interval injection- and detection filters

The packers are joined to three interval sections, as shown in Figure 46. The interval sections are labelled Interval 1, 2 and 3 and contain both injection and detection filters, as follows:

- Interval 1 is located at the end of packer 1 and contains four injection and four detection filters;
- Interval 2 separates the two packers and contains four injection and eight detection filters; and
- Interval 3 connects packer 2 to the casing and has four injection and four detection filters.

Both the injection and the detection filters have openings located at the four orthogonal clock positions of 12:00, 15:00, 18:00 and 21:00, as shown in Figure 46. The injection filters have openings of 60° while the detection filters have smaller 15° openings.

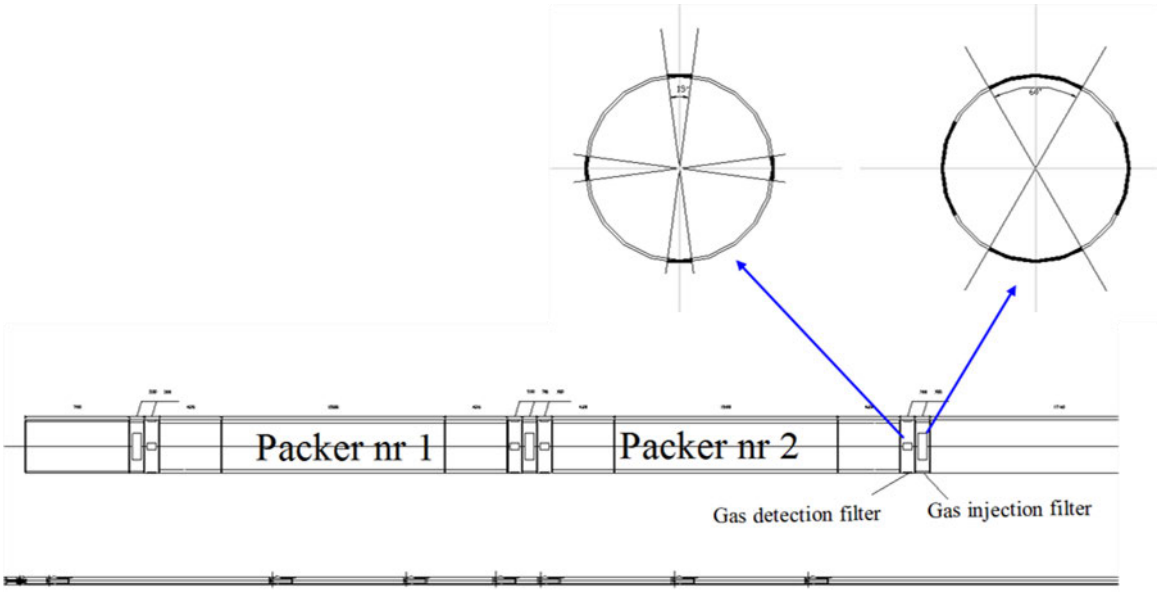

Figure 46 Detection and injection filters installed at Intervals 1, 2 and 3 of the packers [top] and one of the multi-filter monitoring boreholes showing minipacker and seven of the eight monitoring piezometer locations [bottom].

The end of Interval 1 is extended with an end tube of 700 mm in length in order to minimize the disturbance zone around the deepest packer. The length of the end tube was determined by

numerical simulations, which estimated the length of the end tube necessary to minimize the stress influence at the end of Packer 1 caused by the drilling operations.

Extension tubing

The design and fabrication of the extension (casing) tubing was carried out by SCK•CEN. In total, six extension tubes were fabricated using AISI 304 stainless steel. Due to the limited space in the URL, the extension tubes did not exceed 2.5 m in length.

Data acquisition

The data acquisition (DAQ) system consists of a computer-controlled measuring and recording system including a visual readout display. The DAQ system connects to a control unit consisting of manometer pressure readout gauges fitted with Swagelok® valves. The control unit connects to each pressure line in the packers for direct control of pressures during inflation and deflation of packers.

The DAQ system is accessible via an internet connection. The data is uploaded to an internal server accessible via the intranet network of SCK•CEN where the data is permanently stored and backed up on a daily basis. In total, the DAQ system has 80 channels.

Assemblage and performance control tests

After construction and assemblage, the packers and accessory components were fully tested at Solexperts before delivery to HADES. The performance control tests included testing the DAQ and control unit systems as well as the calibration of all sensors installed in the packer system.

The results of these tests are described in detail in D4.4/D4.11.

3.2.2.2 Installation

Installation of the multi-filter piezometer boreholes

The installation of the two multi-filter monitoring piezometers was performed approximately 6 months prior to the installation of the packers. They were installed in horizontal boreholes drilled with a diameter of 75 mm to a depth of 19.9 m.

Drilling of large-diameter borehole for packer installation

The large-diameter borehole was drilled horizontally in the Boom Clay with a final diameter of 402 mm. The borehole was drilled to a depth is 19.5 m, which is 0.95 meters longer than the length of the installed packer installation. The extra depth was necessary to provide storage space for the clay cuttings generated by the sliding action of the packers during installation. Drilling was performed by the ESV EURIDICE drilling crew with assistance from Smet Boring, a Belgian company that specializes in drilling operations. During drilling a survey crew from Geomodus was present to measure and record the orientation and depth of the borehole.

The drilling of the borehole was performed in two phases. The first phase consisted of drilling a pilot borehole. This borehole had a diameter of 160 mm and performed the following primary functions:

- Create unloading of the clay and allow partial convergence to reduce final convergence of the borehole;
- Provide guidance for drilling the final, large diameter borehole; and
- Reduce total amount of cuttings generated during final drilling.

The second phase consisted of drilling the large-diameter borehole with final diameter of 402 mm. The borehole was drilled using the pilot hole as orientation. The drilling used a custom-

made drilling head fabricated by ESV EURIDICE specifically for this project. The drill head consisted of a twin drill-head construction incorporating a small-diameter drill head at its end and a larger-diameter one placed behind it, as shown in Figure 47. Both had a conical construction and serrated teeth to cut and pulverize the clay, which facilitates the drilling and the removal of the cuttings. The small-diameter drill head had the same diameter as that of the pilot hole while the larger drill head had a diameter of 402 mm.

Figure 47 Custom-made twin drill head used to drill large diameter borehole for installation of the packers.

The Boom Clay is very sensitive when brought in direct contact with free water, which precluded the use of water for drilling. The standard practice at HADES, and the method used for the drilling to install the packers, is to use compressed air. The compressed air is forced inside the hollow drill casing providing cooling for the drill head. As it travels back along the outside of the casing it brings the cuttings along with it.

Installation of packer system

An open borehole in the Boom Clay converges relatively quickly when left unsupported. For this installation, the time allocated to install the packers was estimated at approximately 4 to 6 hours, after which the hole will have converged sufficiently to become too narrow for the packers to fit in. To shorten the installation time, the two packers and all the pressure lines were assembled and placed in the PRACLAY gallery before the start of drilling. The PRACLAY gallery is located opposite to and in the same axis as that of the borehole. For practical reasons, the extension tubes could not be pre-assembled and had to be assembled during installation of the packers.

At the start of the installation, the two pre-assembled packers were pushed into the borehole with the help of overhead pulleys and the hydraulic piston from the drill machine. The piston of the drill machine was coupled to a metal cover that fitted over the packers in order to prevent damage of the packers during installation. The drill machine wasremoved after the insertion of the two packers to create space for the installation of the pressure lines and extension tubes. The extension tubes and lines were installed using a separate thrust system specially adapted for the installation.

The system consisted of two 5 ton chain-driven electric hoist frames. The hoist frames were fixed on either side of the borehole. The extension tubes were assembled one by one using a table placed in front of the borehole,. Once the pressure lines had been fed through and the tubes were securely bolted together, they were pushed slowly into the borehole using the

electric hoist system. The reaction chains were coupled to the end of the tubes by means of a metal beam, which together with the hoist system provided the necessary thrust to push the tubes into the borehole.

More details on the drilling process and the installation are provided in D4.4/D4.11.

3.2.3 Results

3.2.3.1 Drilling and installation

The drilling of the small-diameter pilot borehole was accomplished without major difficulty. During this drilling, a relatively small septaria was encountered at 4.5 m depth and an equally small but highly abrasive pyrite zone was encountered at 14.5 m. The pyrite zone required over coring before proceeding further with the drilling. The pilot borehole was successfully completed to the depth of 19.5 m.

The drilling of the large-diameter borehole passed through the septaria depth of 4.5 m without major difficulty. At the depth of 14.5 m the borehole encountered the highly abrasive pyrite zone. This abrasive zone caused significant wear to the drill head requiring the complete rebuilding of the cutting blades. After resuming with drilling, the borehole encountered another highly abrasive pyrite zone between approximately 17.5 and 19.5 m. This zone had not been previously intercepted by the drilling of the same pilot hole.

During retrieval of the drill rods, the drill head became blocked at 18.5 m. The blockage was likely caused by the collapse of the borehole behind the drill after drilling. It is also possible that blocks of pyrite fell into the borehole further contributing to the blockage of the drill. Several attempts were made to free the rods and drill head, without success. During these attempts the drill rods were kept rotating in order to keep the hole open and prevent further collapse, which would result in the complete blockage of the drill and a total loss of the borehole.

In order to force the drill head through the blocked zone, the rods were operated in a continuous cycle of advance-and-retreat movements until the rods and head were finally freed. It required approximately six hours to finally free the rods and head. During this operation, a large cavity was created at the end of the borehole. The size of the cavity was sufficiently large enough to hit both of the nearby installed multi-filter monitoring piezometers. In the process, it destroyed the two mini packers installed at the end of the multi-filter piezometers and caused a large deviation of the borehole in the last 3 to 4 meters of its depth.

After removal of the drill from the borehole, the packers were successfully installed to a depth of 18.55 m. This is approximately 0.49 m short of the originally planned installation depth but was necessary in order to avoid placing the packers directly in the highly abrasive pyrite zone.

3.2.3.2 Monitoring and follow-up

After installation, the packers were filled with Midel® 7131 Oil and pressurized just enough to establish contact with the borehole opening and without exceeding the maximum designed packer diameter of 430mm. The initial inflating pressure required to establish contact with the borehole opening for both packers was approximately 250 kPa. After this pressure was reached, the inflation pressure was closed off. Since then, the packers have been operated on a passive mode, allowing the inflation pressure to change only due to the convergence of the clay.

Packer 1 developed a small leak on the 7th of August 2011, as seen in Figure 48, showing the inflation pressure of the packers with time. Since then, the inflating pressure has continued to recover, as observed. Packer 2 experienced pressure losses on 18th August, 2011 and on 2nd

February, 5th April and 19th June in 2012, as observed. Since then, no pressure loss has been observed in this packer. The inflating pressure of both packers continues to increase but has not yet stabilized, as shown.

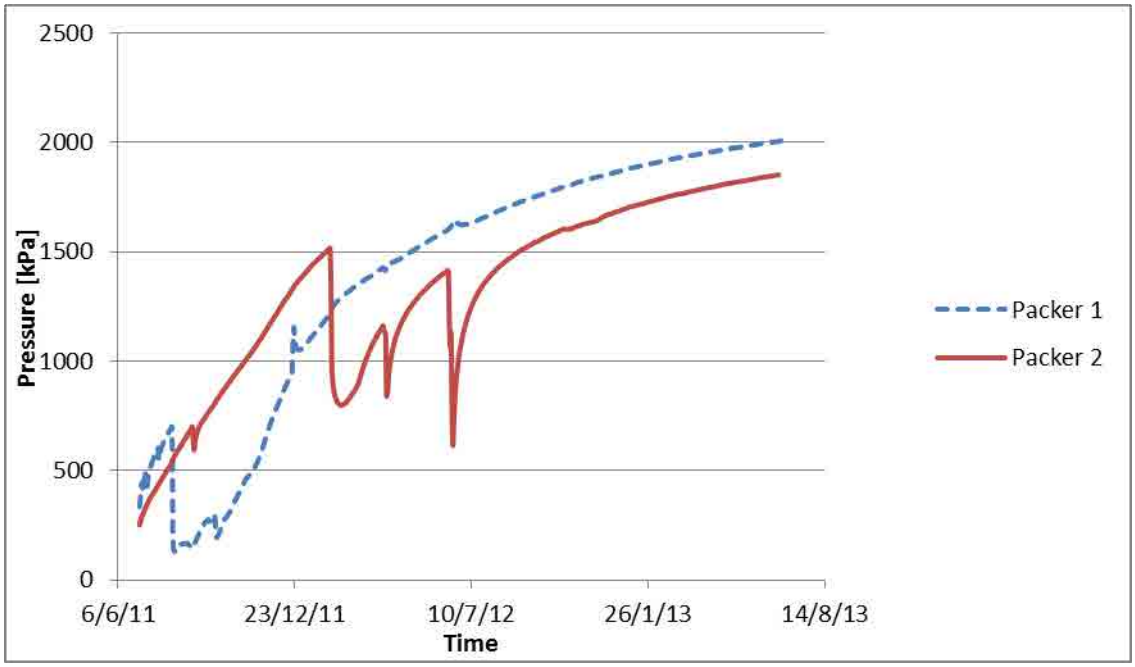

Figure 48 Evolution of inflation pressure of packers.

The evolution of the pore pressures in the multi-filter piezometers shows a similar trend as that observed for the packers, as seen in Figure 49 and Figure 50 for monitoring piezometer 1 and 2, respectively. The sudden changes in pressure in filter 7 of monitoring borehole 1 and in filters 6 & 7 in borehole 2 are due to manual intervention performed to de air the pressure lines in these filters. Like the inflating pressures of the packers, the pore pressures have also not yet stabilized, suggesting that the disturbed area around the packers created during installation has not yet fully recovered.

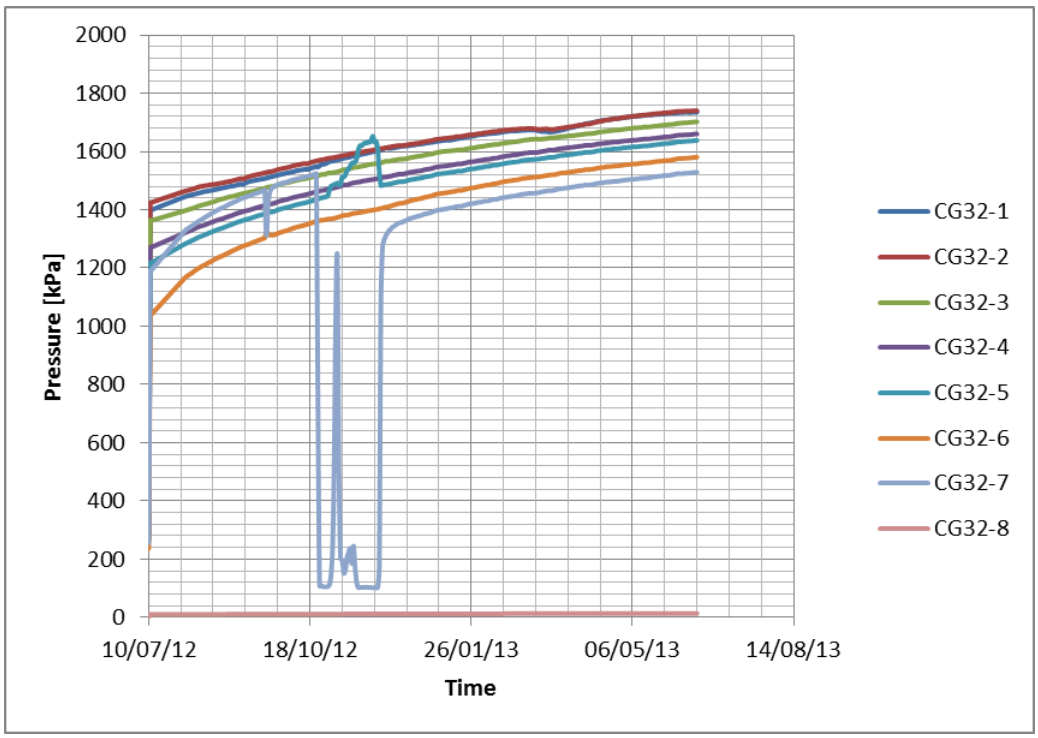

Figure 49 Evolution of pore water pressures in monitoring piezometer 1.

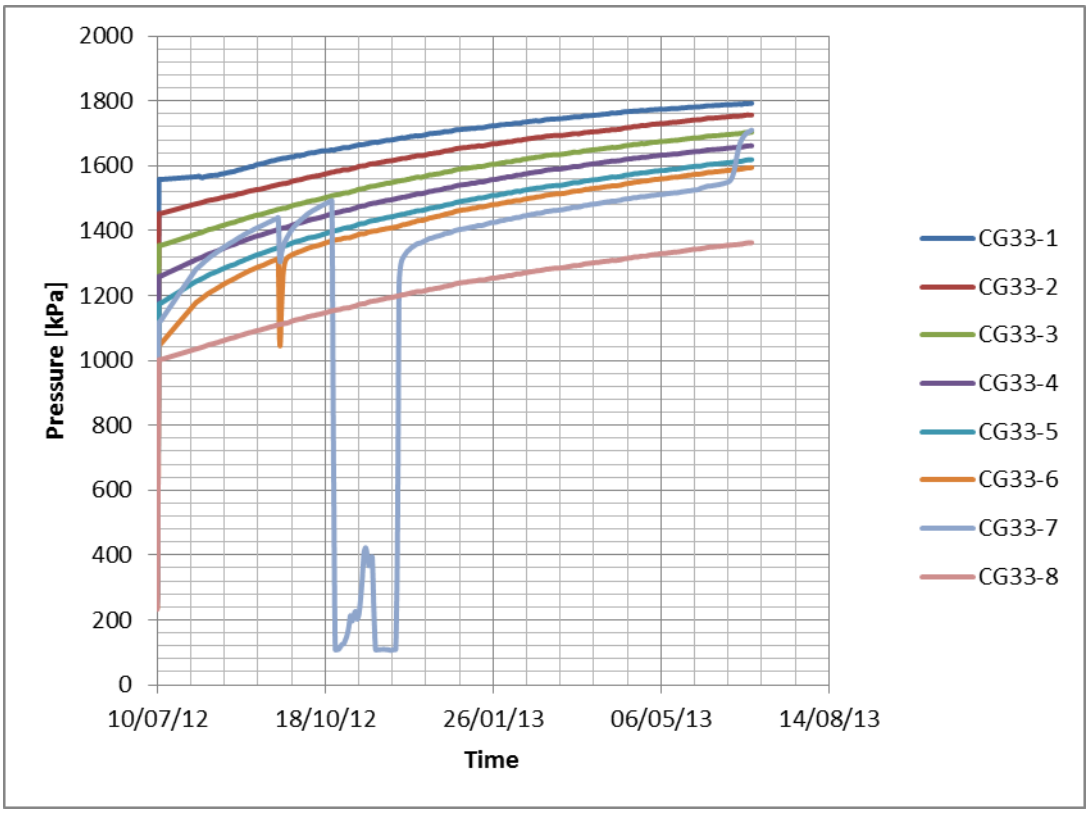

Figure 50 Evolution of pore water pressures in monitoring piezometer 2.

On the 20th of December 2011 a special Conax feed-through adaptor was installed at the end of the multi-detection piezometer number 1, located to the left of the packers, in order to close off the pressure tube leading to the damaged mini packer previously hit during the rescue operations performed to free up the drill. The damaged tube created a flow pathway to the Connecting Gallery affecting the buildup of pore water pressure in the clay around the packers. After installation of the Conax adaptor, the casing was filled with Midel oil in order to further resist the flow of water from the clay along the casing and to prevent the clay from entering it, which both affect the normal stress build up in the clay around the packers. There is a noticeable improvement in the buildup of pore water pressures around the packers since installing the Conax adaptor.

More detailed information on the monitoring results are provided in D4.4/D4.11.

3.2.3.3 Remedial action for leakage of packers

The inflation pressure losses observed in packers 1 and 2 appear to be due to leakage of the packers. This is supported by observations made during de-airing of some of the pressure lines in both the monitoring piezometers and the packers, which confirmed the presence of oil in the filters. The progressive increase in inflation pressure measured in the packers since the leakage was detected suggests that the leakage is small and that it seals itself when the contact pressure with the clay is sufficiently high and uniform around the packer.

However, a leakage will affect the working of the packers and needs to be addressed before performing gas tests. SCK•CEN has taken contact with Solexperts to seek a solution for the leakage of the packers. Following this, a trial test was completed in February 2012 at Solexperts to test the effectiveness of a sealing compound which, if successful, could be used to inject into the packers in an effort to stop the leakage. The first test results were not successful and Solexperts is pursuing contacts with the manufacturer to try to improve the product.

3.2.3.4 Planned gas tests

A series of gas tests have been planned for the mega packer system. These tests will be carried out when the condition of the packers has been fully evaluated to determine the impact of the observed leakage and the hydro mechanical conditions around the packers have stabilized. The time required for the hydro mechanical conditions to stabilize is much longer than initially anticipated due to the problems encountered during drilling and installation of the packers, as explained earlier in this report. The gas tests will use the various injection [IF] and detection [DF] filters installed in the packer sleeve (Figure 51) to inject and detect the gas flow.

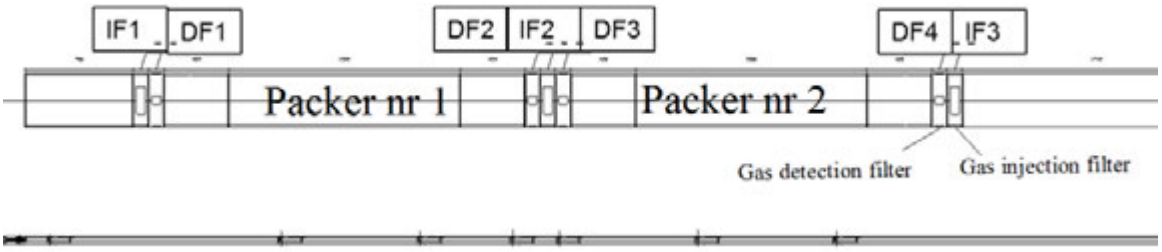

Figure 51 Planned future in-situ gas test set-up.

As mentioned earlier, before the gas tests are carried out, the packers need first to be tested to assess the nature and influence of the observed leakage on the ability of the packers to sustain internal inflation pressure. These tests will be carried out as soon as the convergence of the clay around the packers has stabilized.

3.2.4 Conclusions and remarks

The drilling of the large-diameter borehole encountered a highly abrasive pyrite zone at the depth of 14.5 m and again between 17.5 and 19.5 m. These abrasive zones caused significant wear to the drill head requiring the complete rebuilding of the cutting blades. Eventually, the drill head became blocked at 18.5 m requiring significant efforts to remove it from the borehole. The blockage was likely caused by the collapse of the borehole behind the head in the pyrite zone. It is also possible that blocks of pyrite fell into the borehole further contributing to the blockage.

During the attempts performed to free the drill head, the drill rods were kept rotating in order to prevent further collapse of the borehole. This created a large cavity around the borehole and resulted in a significant deviation of its alignment. These events have seriously affected the quality of the installation and the recovery of the clay.

The inflation pressure losses observed in packers 1 and 2 appear to be due to leakage of the packers. This is supported by observations made during de-airing of some of the pressure lines in both the monitoring piezometers and the packers, which confirmed the presence of oil in the filters. The increase in inflation pressure measured in the packers suggests that the leakage is small and that it seals itself when the contact pressure with the clay is sufficiently high and uniform around the area of the leakage. However, a leakage will affect the working of the packers and needs to be addressed before the gas tests can be carried out. Plans are underway to address these issues as soon as the clay has converged sufficiently around the packers and hydro-mechanical properties of the clay stabilize.

3.3 GAS TRANSPORT IN CRYSTALLINE ROCK (CTU)

3.3.1 Scope and objectives

One of a number of deep RAW repository construction concepts considers crystalline structures as the host rock environment. The CEG's role in the FORGE-WP4 project was to study the behaviour of disturbed crystalline rock formations. The Josef Underground Laboratory was used for in-situ testing, principally the granodiorite section of the underground complex. The main objective of the research was to study the various roles played by the EDZ as a provider of preferential routes for gas transport.

The research focused on two main areas the first of which was to study the differences between the EDZ and the undisturbed host rock and the second to study pathway dilation processes. In order to obtain experimental data for the study of these processes a series of tests was conducted at the Josef Underground Laboratory. The testing methodology was based on the large-scale in-situ gas injection technique the principle of which is to inject compressed air into boreholes which have been sealed using the packer system and the subsequent monitoring of the behaviour of the injected air. A mobile measuring device was designed especially for this purpose.

The permeability of the rock is greater and the associated sealing function less effective within the disturbed/damaged rock environment of the EDZ than elsewhere in the rock mass. Therefore it was considered important to study permeability within the EDZ as well as the more distant intact host rock. Since it was expected that there would be an extensive EDZ in the vicinity of the borehole openings, it was also expected that gas permeability would decrease with distance from the gallery. Therefore, in order to confirm the hypothesis, a testing method was employed which involved the gradual deepening of a vertical borehole. The borehole was gradually extended and the gas permeability of individual sections of the borehole measured using pressure test techniques and the single packer system.

The typical behaviour of crystalline rocks containing discontinuity networks of various origin involves the opening of preferential pathways (pathway dilation) following the injection of any media. Once injection pressure exceeds the corresponding *in situ* stress level, existing fractures are opened further and new fractures created which typically leads to a local increase in rock permeability. One of the objectives of the experiment was to verify the expectation that higher injection pressure levels lead to the opening of preferential pathways allowing the escape of gas which, in turn, leads to an increase in gas permeability. A series of gas injection tests was performed at various pressure levels in order to examine the trend of increasing permeability with increasing gas pressure. Testing was conducted at various pressure levels both above and below the expected rock mass primary stress value and employing a range of injected air flow rates.

3.3.2 Description of the experiment

The experiment consisted of three stages: site characterisation, pilot testing and main field testing. During the site characterisation stage a total of four sites, with differing geological conditions, were selected for pilot testing purposes. A detailed geological description of the sites was carried out and a horizontal borehole was drilled at each location at which pilot gas injection testing was subsequently conducted. The objective of the pilot testing stage was to verify the characteristics of the rock mass in-situ, to test and confirm the instrumentation setup and to finalise the design of the testing methodology.

Based on the results of these initial tests a vertical borehole was then drilled into the granodiorite rock area of the Josef facility for the purposes of taking field measurements. The method used for the research consisted of the gradual deepening of the borehole and the measurement of gas permeability using gas injection methods.

3.3.2.1 Site characterisation

The Josef facility is an underground laboratory complex created by means of the reconstruction of the former Josef exploratory gold mine galleries. The underground complex consists of the main exploration gallery which is connected to the two main sections (Celina and Mokrsko). Both sections consist of a number of drifts (galleries) with a cross-section of around 15m^2 which can be used for in-situ experiments. Celina and the eastern part of Mokrsko are situated in tuffs and vulcanites of the Jilovske belt. Most of the western section of Mokrsko lies in granodiorite rock of the Central Bohemian Pluton. The overlying rock thickness ranges from between 90m and 150m and most of the galleries are unlined.

The area was mapped in detail during the conducting of exploratory work in the 1980s. The objective of the exploration was to come up with an estimate of the gold reserves in the area. The gold mineralisation zones are made up of a network of steep parallel veins and veinlets. Therefore mapping also focused on the documentation of tectonic features and the mining maps include information on discontinuities (joints). The rock environment is characterised by a high level of jointing and, in the vertical direction, is traversed by venous rocks. In addition to natural jointing, the rock massif was disturbed in areas surrounding the open underground spaces as a result of construction work. The technology employed during construction and exploration consisted of drilling and blasting which led to the formation of an extensive EDZ. Detailed geological mapping was carried out as part of the project at those locations selected for gas injection testing (Svoboda and Smutek, 2010). Detailed geological investigation included the study of rock petrography, hydrogeology and tectonic characteristics. Rock mass classification systems were also employed in order to assess the quality of the rock mass.

Horizontal boreholes, with a diameter of 57mm, were drilled at each of the four locations for the purpose of pilot testing. The length of the boreholes ranged between fifteen and twenty-two meters. In the second phase a new site was selected in the Mokrsko- West area in granitic rock (Svoboda and Smutek, 2011). A new vertical borehole (MW-SP67-3V) also with a diameter of 57mm directed beneath the water table was drilled at this site. The local water table is at the level of the bottom of the tunnel; the gallery serves for the drainage of underground water. In the first phase the borehole was sunk to a depth of 19.69m, following the conducting of pressure tests it was extended to a depth of 30.10m and in the final stage to 40.50m. The petrography of the Mokrsko-West area is relatively monotonous i.e. grey and green-grey biotitic-amphibolic granodiorite (Sázava type - Upper Devonian) with fine to intermediate crystallisation. The host rock is traversed by a nearly vertical (steep) system of quartz (calcite, barite) veins. The height of the overburden (MW-SP67 drift) is approximately 100m, therefore, based on the known material characteristics of the rock, the *in situ* stress level was estimated at between 2.5 and 3.0MPa.

3.3.2.2 Experimental equipment

The principle of in-situ testing is based on injecting air into a sealed borehole in the rock mass and monitoring changes of air properties over time. The custom-made measuring instrumentation consists of a packer, measuring apparatus, a cylinder and a compressor (Figure 52). The injected air is supplied by means of the compressor and the cylinder serves as a compressed air reservoir which helps to reduce compressor running time.

The measuring apparatus is equipped with a pressure controller and a flow meter which allows for the recording of the instantaneous flow rate and the total amount of air injected. The device is controlled by software running on a connected laptop computer. The device is also equipped with pressure and temperature sensors. The maximum operating pressure of the measuring device is 15Mpa and the volume of measurable airflow is between 1 and 40 normal litres per minute. The maximum injection pressure is, however, limited by the type of packer used. The flow rate of air into the borehole is directly dependent on the pressure at the point of input of the measuring apparatus. A reducing valve is used for the regulation of input pressure to values of between 0 and 16Mpa.

Packers with a diameter of 42mm were used and the maximum operating pressure in the 57mm diameter borehole was around 8Mpa. The pressure inside the packer must always be higher, taking into account a certain safety margin, than the pressure of the injected medium; therefore the maximum injection pressure level was limited to 5Mpa. The length of the rubber seal component of the single packer was 1m. The double packer consists of two rubber sealing components with lengths of 0.5m which separate an injection zone also of 0.5.

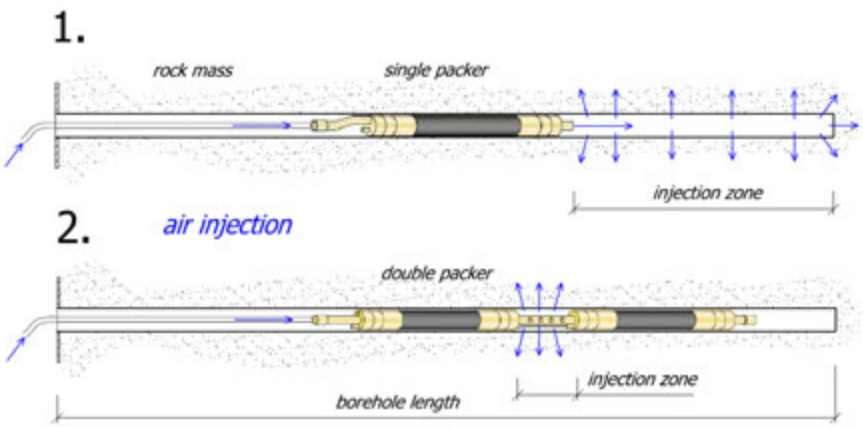

Figure 52 Experimental equipment

3.3.2.3 Testing methodology

Several types of test were designed based on the results of the pilot testing stage. Two types of test can be used to obtain the data required to calculate gas permeability. The testing methodology of the first type of test (the Constant Head Injection Test - CHIT or Constant Flow Injection test - CFIT) is based on pressurizing the borehole to a prescribed pressure/flow level and then waiting until a steady flow state is attained. The second type of test, the pressure

drop test (PDT), commences immediately following the CHIT and is based on ceasing injection once the air flow has been stabilized and subsequently observing the pressure drop curve.

During the CHIT test the prescribed pressure level is maintained under varying air flow conditions. The CHIT test is suitable for testing in environments with very low permeability and it is advisable to perform the test in a number of pressure stages. The CFIT test is suitable for testing in more permeable environments. At the beginning of the test a constant flow of air is set and the test ends when steady pressure is achieved in the borehole. It is also useful to perform the test employing multiple flow rates.

3.3.3 Injection tests

Initially a series of pilot tests was performed in order to verify the characteristics of the rock mass in-situ, to test the overall setup of the apparatus and to finalise the design and provide for the debugging of the testing methodology. Various types of tests, both short- and long-term, were performed on different injection sections in a total of four boreholes. Baseline permeability measurements of the rock in the vicinity of the injection boreholes were obtained by means principally of the constant head injection test and pressure drop test techniques.

Following pilot testing in the horizontal boreholes, detailed testing was performed in the vertical borehole in the granodiorite rock environment of the Mokrsko area. The tests were necessarily of a long-term nature since it took a considerable period of time to stabilize injected air flow conditions. Long-term testing lasted from several days to a number of weeks. Long-term testing also had the advantage of better replicating deep repository conditions since final waste disposal will be of a very long-term nature.

More than 20 long-term test series (each test consisting of several subtests at distinct injection pressure levels) were performed in the MW-SP-67-3V borehole. The levels of permeability of individual sections of the borehole were measured by placing the packer in different positions within the borehole (usually in 2.5m steps).

Multiple pressure levels and flow rates were used during the gas injection stage. It was possible to set the flow rate value within a range of between 0 and 40Nl/min (normal litres per minute). In addition, various flow rates were used in a number of borehole sections in order to study changes in permeability.

In the undisturbed part of the rock mass pressure levels of between 10 and 40 bar were applied (CHIT tests, Figure 53). In the most permeable rock of the upper part of the borehole, a maximum constant flow rate was applied and borehole pressure was subsequently measured (Figure 54). The maximum achieved pressure at a steady state in these upper sections was found to be lower than 25 bar which corresponded to the local primary stress level. Graphs of the measurement results show the relative injection pressure (the increase from the initial atmospheric pressure value). The difference in pressure levels which resulted from the necessity to maintain injection pressure levels can be clearly seen in the graphs. In the disturbed rock (the upper packer positions) the maximum flow rate was applied (35Nl/min) but it was not possible to reach pressure levels as high as those attained in the lower sections. Conversely, in the lower sections of the borehole extremely low flow rates were observed which could not be measured by the flow meter. Indirectly calculated flow rates ranged from 0.01 to 0.40Nl/min in these sections.

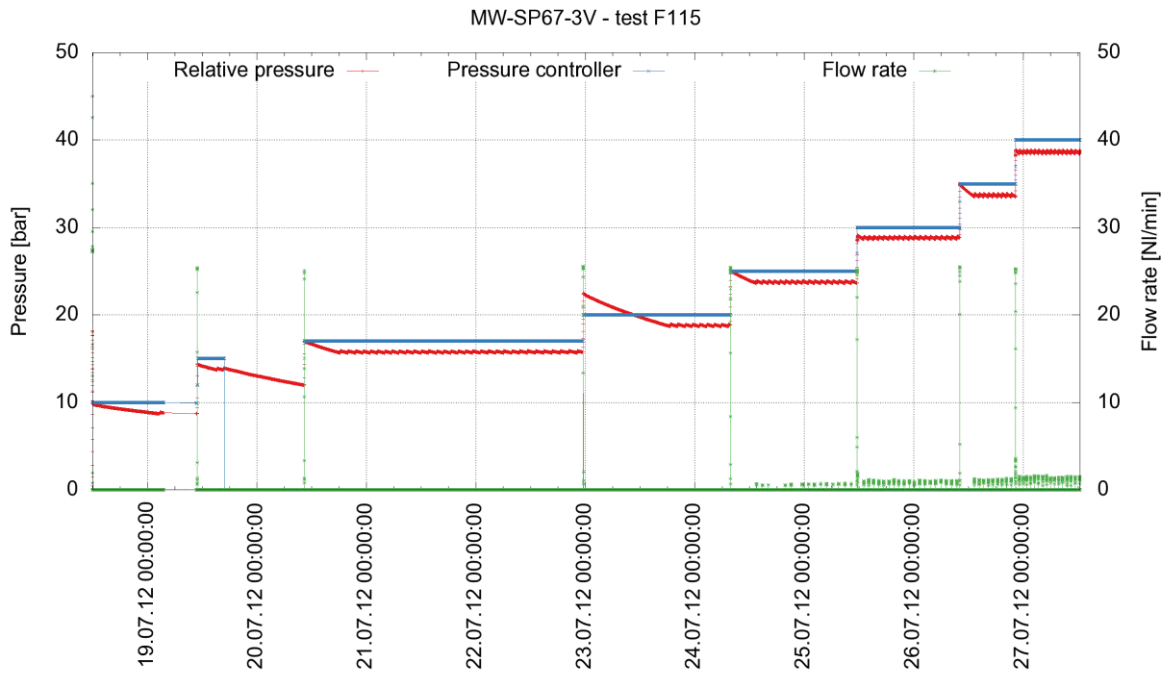

Figure 53 Example of CHIT tests in undisturbed rock

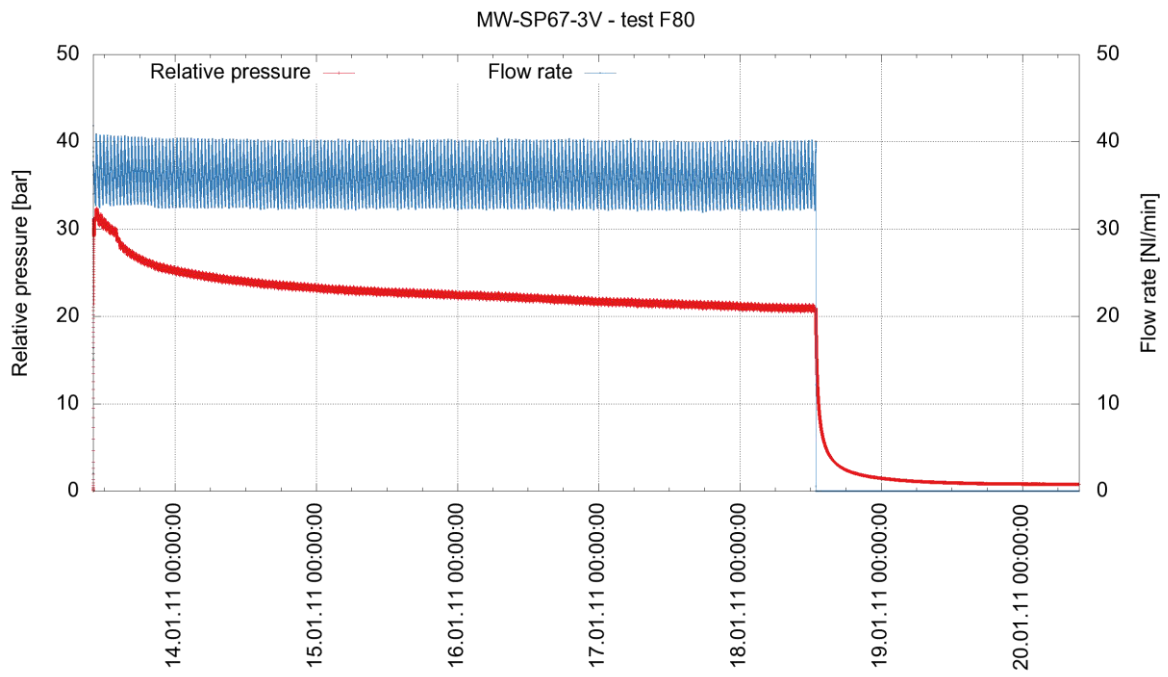

Figure 54 Example of CFIT test in disturbed rock with maximum flow rate

3.3.4 Test evaluation

The flow rate of the injected air was measured by a Coriolis flow meter which formed part of the measuring apparatus. In the case of the extremely low permeability of undisturbed rock environments, where flow rate values were below the measurement limits of the flow meter, the flow rate was calculated from pressure drops/losses based on the known volume of the borehole injection section.

The output of each test consisted of the intrinsic permeability and therefore gas conductivity of the respective rock mass section. Intrinsic permeability and gas conductivity were determined based on recorded values of injection pressure and the air flow rate in the steady flow state. The analytical calculation of these parameters depends upon the mathematical model of gas flow selected with regard to the geometrical arrangement (Svoboda and Smutek, 2011). A simplified analytical solution of the radial 2D model (cylindrical) of flow was considered for the calculation of permeability. The total flow rate is given by equation (1).

$$Q = \frac{\Delta(p^2)}{p_0 \ln(\frac{R}{r})} \pi L \frac{k}{\mu} \tag{1}$$

where:

Q flow rate [m^3s^{-1}]

k intrinsic permeability [m^2]

Δ p difference between pressures [Pa]

P_0 reference pressure (atmospheric) [Pa]

r radius of the borehole [m]

R effective radius (radius of influence) [m]

L length of the borehole section (injection zone) [m]

μ dynamic viscosity of the gas [$kgm^{-1}s^{-1}$]

Gas conductivity was then calculated using an equation describing the relationship between intrinsic permeability and gas conductivity (2).

$$K_g = \frac{k\rho\, g}{\mu} = \frac{kg}{\nu} \tag{2}$$

where:

K_g gas conductivity [ms^{-1}]

k intrinsic permeability of the rock [m^2]

ρ density of the gas [kgm^{-3}]

g gravity acceleration [ms^{-2}]

ν kinematic viscosity [m^2s^{-1}]

Such a simplified flow model cannot provide absolutely precise values of permeability/conductivity. The values obtained by the respective model are affected by the selected input parameters of effective radius (R) which represents the distance from areas theoretically unaffected by gas injection. It is impossible to practically determine this boundary condition; therefore the effective radius must be estimated. However, this parameter occurs in the calculation formula as a logarithm therefore the final value of permeability is not so sensitive to value changes. A constant value of effective radius of 10m was used for calculation purposes. In addition, the flow model considered only the single flow phase, i.e. it was assumed that once a steady flow state in the injection test had been achieved, all of the injection medium would have been pushed out from the flow field (which was observed). Nevertheless,

an absolutely accurate determination of permeability was not crucial; the aim of the project was to examine trends in relative changes of permeability, differences in values obtained between the EDZ and the undisturbed rock environment and changes in permeability under different pressure loads (pressure levels or flow rates).

3.3.5 Discussion of the results

The overall results of the experiment are shown in Figure 55. The cells highlighted in green contain values of intrinsic permeability and gas conductivity (in italics) calculated from measurement results; the yellow highlighted cells show the difference in values between two tests at different depth which are used to estimate the permeability/conductivity of borehole section. The latter type of calculation employed average values from all the tests performed in the same section and at all pressure levels (flow rates). Some parts of the borehole (the lower injection sections) displayed a higher flow rate (or lower pressure) than the upper (longer) part. This was probably the result of injected air escaping back into the borehole through interconnected longitudinal joints (along the packer); in such sections it was not possible to back-calculate permeability. The results of recalculated permeability are set out in Figure 56 which shows the dependence of permeability on distance from the mouth of the borehole (the gallery). If one ignores the non-standard results from sections at a depth of around 20m, a relatively good reliability coefficient of trend was obtained. The results of tests performed with the packer in the upper positions (long injection zones) revealed that final permeability is in the order of between 10E-16 and 10E-17m^2 and that deeper in the borehole, i.e. in undisturbed rock environments, values average approximately 10E-19m^2.

The results of tests using various pressure levels and flow rates are summarised in Figure 57 which reveals the dependence of calculated intrinsic permeability on injection pressure for different borehole sections. The less permeable rock deeper within the borehole allowed the performance of CHIT tests employing various pressure levels thereby allowing the examination of changes in permeability depending on injection pressure. In the borehole section 20-40.5m a series of CFIT tests was also carried out which revealed changes in permeability with varying levels of injection pressure.

The underground spaces were excavated using the drill and blast method and therefore featured a considerable EDZ. Gas permeability should therefore decrease with distance from the gallery. This decreasing trend has been confirmed to a surprisingly high degree. There is strong evidence of a large difference in this respect between the EDZ and the undisturbed rock; permeability differs by 3 orders of magnitude and decreases by one order of magnitude every ten metres. According to the results, the EDZ plays a major role in terms of gas transport due to its significantly higher permeability; therefore gases could more easily open fractures within the EDZ due to lower stress levels and damage caused by excavation. Conversely, sections further away survived excavation by blasting surprisingly well which suggests that it can be expected that the rock mass will seal the repository despite local damage.

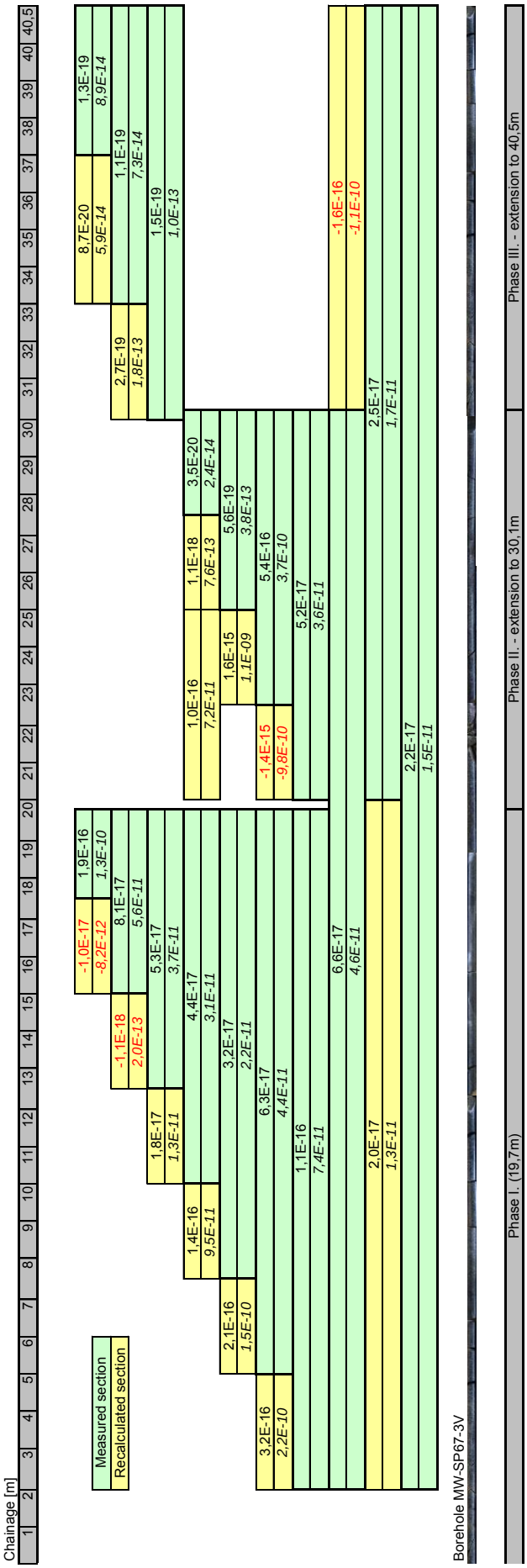

Figure 55 Results of the intrinsic permeability and gas conductivity testing of individual borehole sections.

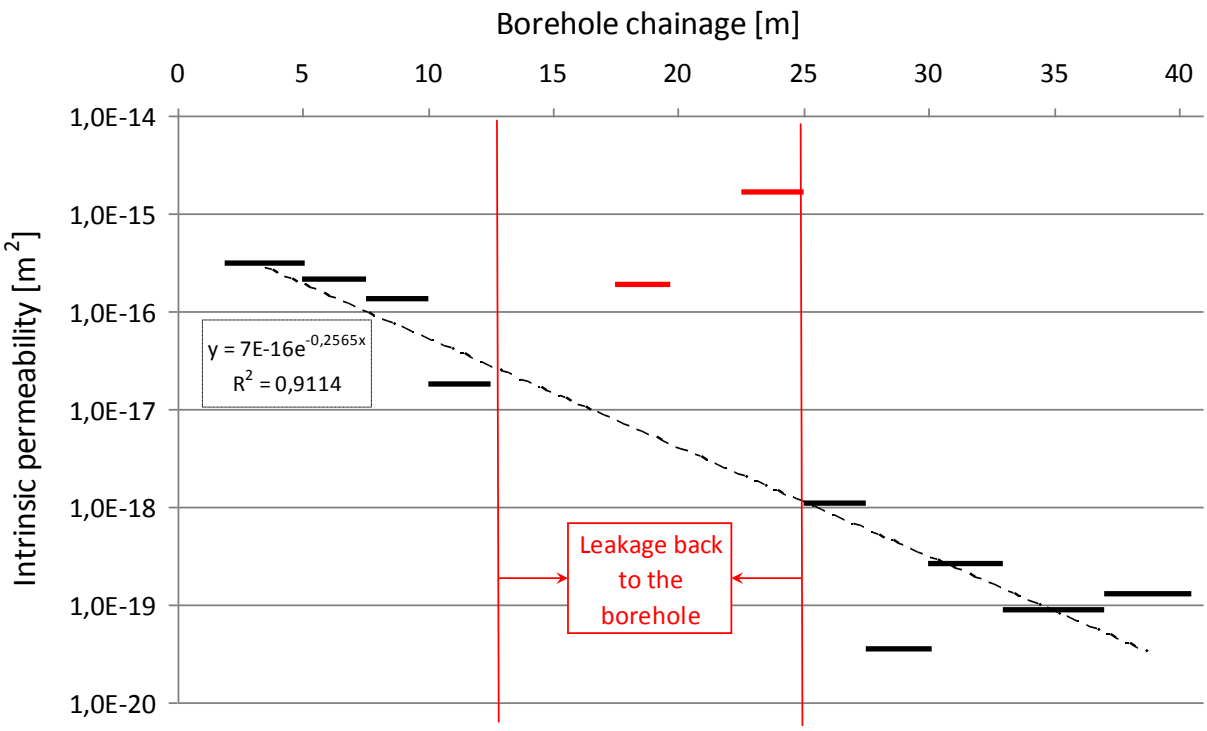

Figure 56 Dependence of intrinsic permeability (gas tests) on distance from the gallery.

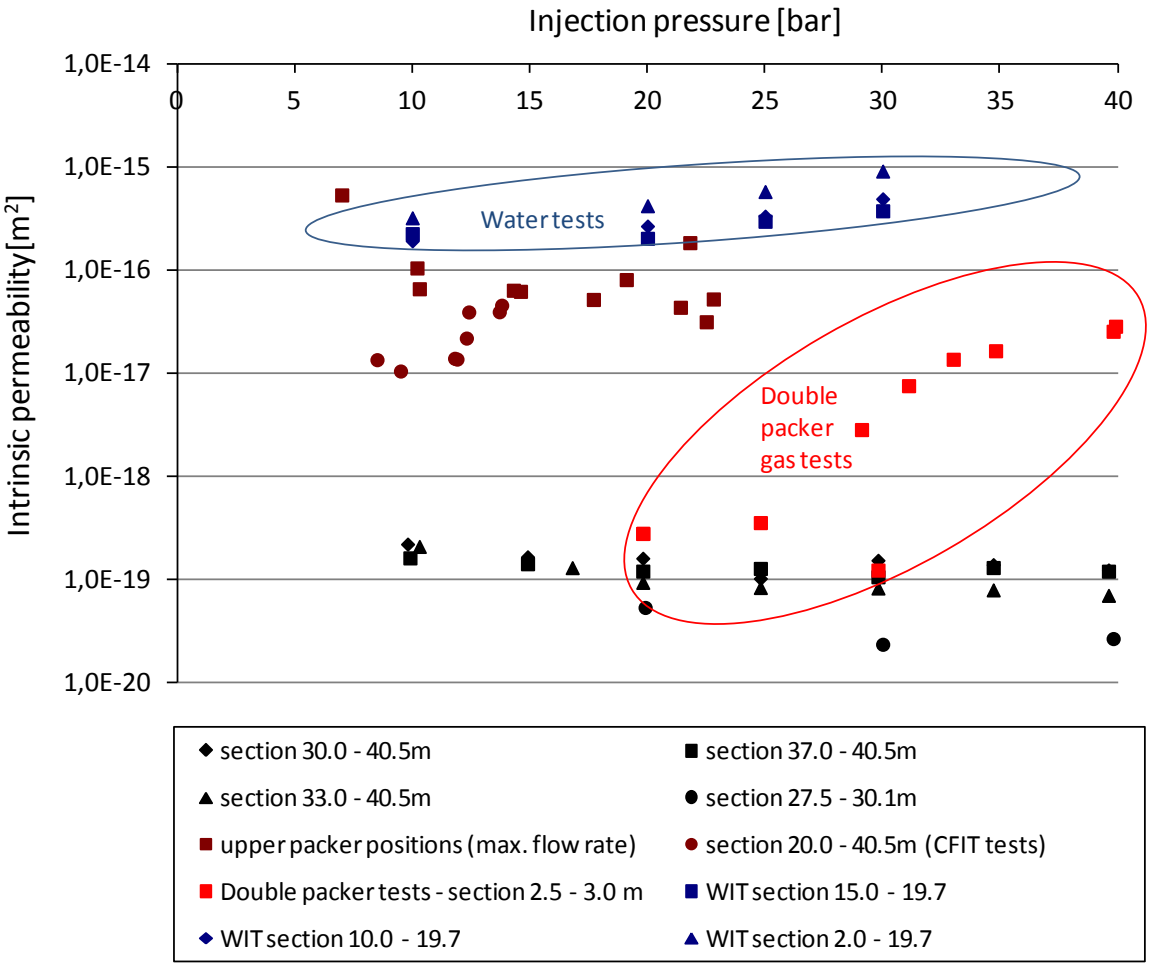

Figure 57 Dependence of intrinsic permeability on injection pressure (gas and water injection tests).

Discontinuity systems in crystalline rock often differ in terms of origin. Joints can be caused by natural processes or can be artificially created as a result of the excavation method employed during the construction of underground facilities. When gas is injected at pressures exceeding the primary stress level it is likely to lead to the opening of existing fractures or the creation of new ones which will cause a local increase in rock permeability. Therefore it can be expected that higher injection pressure levels will lead to the opening of preferential pathways for the escape of gas which will, in turn, lead to an increase in gas permeability.

The opening of fractures had already been observed during water pressure testing. Several water injection tests (WIT) using the single packer system were carried out in the MW-SP67-3V borehole. Three different borehole sections were used, each with 4 pressure levels. Figure 58 shows the results of intrinsic permeability measurement calculated on the basis of these tests. The estimated value of primary stress in the rock at a depth of 100m is between 25 and 30 bar; however the tested sections were located within a stress redistribution field around the gallery therefore stress levels could be expected to be lower. Nevertheless, a trend for permeability to increase (pathway dilation) is evident. It was observed that the closer the testing zone was to the gallery, the greater was the increase in permeability.

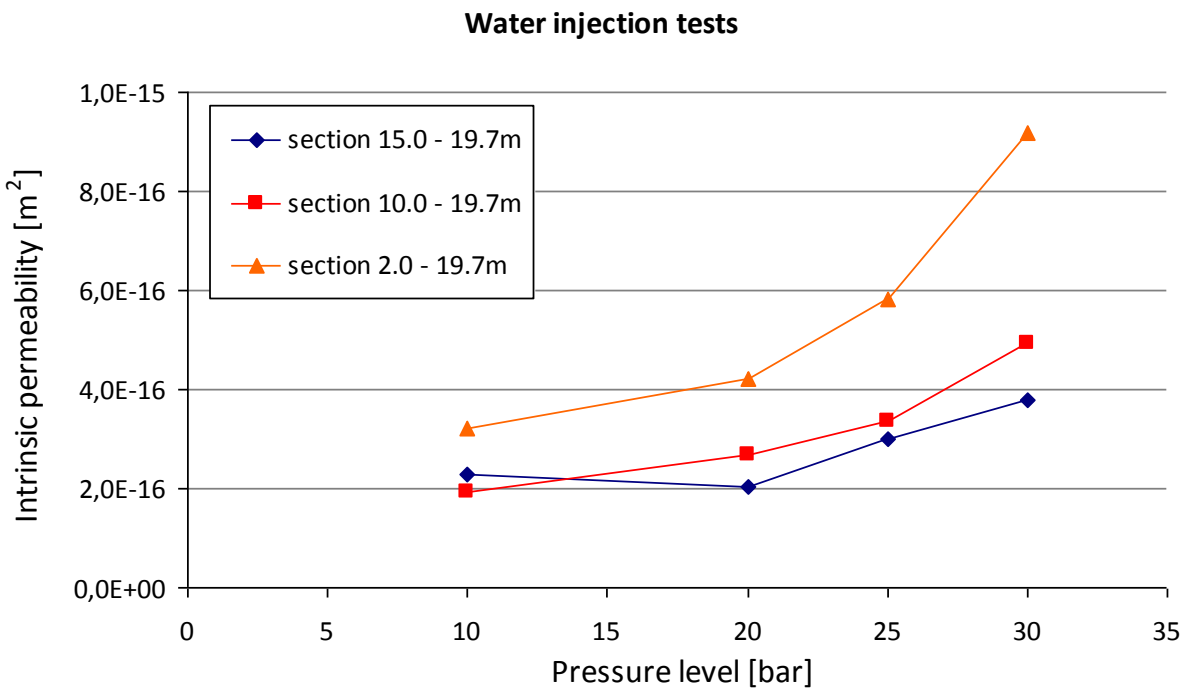

Figure 58 Dependence of intrinsic permeability (water injection tests) on injection pressure.

The trend for gas permeability to increase was observed only to a limited extent and usually during testing with the double packer. This was observed during the double packer testing of the 2.5 - 3.0m section. This section was tested at a number of pressure levels ranging between 20 and 40 bar. The observed change was rapid; intrinsic permeability increased by two orders of magnitude (Figure 57). Most single packer tests did not reveal this trend. Increasing permeability during single packer testing was observed only during CFIT testing in the EDZ where, admittedly, only low pressure levels were attained (all were below the primary stress level). Generally, in most places the results showed the opposite trend. Figure 59 shows the results of several series of CHIT tests from lower borehole sections where, even with high injection pressures (up to 40 bar) exceeding primary stress values, no break in the trend was observed; indeed the trend in this case was even slightly the reverse.

It seems therefore that permeability increases only when localised flow through the fracture takes place and not in the case of a more distributed flow through rock masses with more extensive fracture networks.

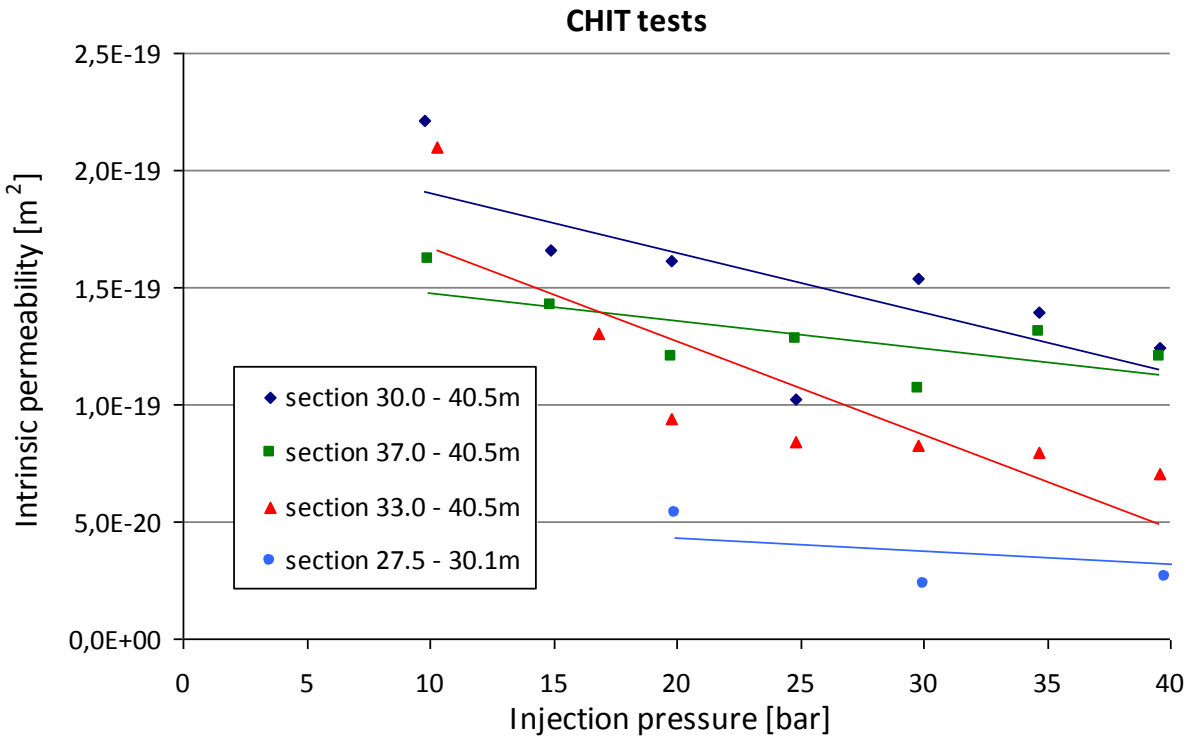

Figure 59 Dependence of intrinsic permeability (gas CFIT tests) on injection pressure.

3.3.6 Conclusions

A decrease in gas permeability with distance from the gallery has been confirmed. Strong evidence was detected of a difference in this respect between the disturbed (EDZ) and undisturbed rock formations. An extensive EDZ was identified in the vicinity of the drifts which affected the gas permeability of the rock mass even up to distances of 20 metres. The tests, which clearly demonstrate the greater level of permeability of the EDZ compared with the intact rock, highlight the importance of interfaces in crystalline host rock disposal concepts. The evolution of these features is likely to evolve both temporally and spatially, though no direct observations relevant to this assumption were recorded as part of the project. This effect might well lead to significant problems in the repository in that the EDZ, working as a “collector” within the undisturbed (“impermeable”) host rock, could allow a concentration of gases in certain locations (the equivalent of a stratigraphic trap). Effective sealing around the access shafts/tunnels is crucial therefore so as to prevent the EDZ working as a conduit to the surface.

The opening up of fractures observed during water pressure and double packer gas injection testing was not observed in the more distant undamaged sections of the rock mass even when gas injection pressure exceeded the primary stress level. This was, however, only observed for localised gas injection. The phenomenon of the opening up of localised fractures versus the non-opening up of the fracture network will have to be examined more closely since this could have a significant impact on gas migration within the repository.

4. Modelling

4.1 GAS MIGRATION IN OPALINUS (UPC)

The main features and results of the modelling of the HG-A in situ test are presented below. Details can be found in the FORGE progress and final reports by Alcoverro et al. (2012a, 2012b).

4.1.1 The HG-A in situ test

The HG-A in situ test is located in the Mont Terri URL (Jura, Switzerland). It consists of a horizontal (micro-) tunnel 13.0 m long and 1.0 m in diameter excavated in the ultra low permeable Opalinus clay. From its end to its mouth, the tunnel is divided into 3 sections: the test section (4.0 m long, backfilled with gravel), the megapacker section (3.0 m long, where a megapacker 3.0 m long and 1.0 m in diameter is installed) and the liner section (6.0 m long, where a steel liner is installed). After saturation of the test section and application of an initial pressure to the megapacker, liquid or gas was injected into the test section and forced to flow back through the EDZ generated around the tunnel during its excavation, while the megapacker pressure was varied.

4.1.2 General modelling approach

The HG-A Test has been modelled within the framework of multiphase porous deformable media. The porous material is assumed to consist of 3 phases: solid (made of species mineral), liquid (made of species water and species air) and gas (made of species water and species air). Species mineral is assumed to remain in the solid phase, but both species water and species air are assumed to be exchangeable between the liquid and gas phases.

Using the continuum mechanics approach, the porous medium has been idealized as 5 interacting continua: species mineral in the solid phase (solid skeleton), species water in the liquid phase (liquid water), species air in the liquid phase (dissolved air), species water in the gas phase (water vapour) and species air in the gas phase (dry air). Following this approach, equations establishing the balances of mass, momentum and energy have been postulated for each of the interacting continua. For each balanced property (mass, momentum and energy), the balance equation for each interacting continuum includes a term representing the exchange of the balanced property with the other continua, and are such that their sum for all interacting continua vanishes.

It has been assumed that motions are slow, so that there is mechanical equilibrium (inertial terms and terms involving products with velocities are neglected), phase change equilibrium (species water and species air are in equilibrium with respect to phase changes between the liquid and gas phases) and thermal equilibrium (at a given space point and time instant, all interacting continua have the same temperature). We have used the psychrometric and Henry's laws for stating the phase change equilibrium of species water and species air between the liquid and gas phases, extensions of Darcy's law appropriate to unsaturated conditions for the motions of the liquid and gas phases, and extensions of Fick's law appropriate to porous media for the motions of species air in the liquid phase and of species water in the gas phase. Details of this formulation may be found in Olivella et al. (1994).

Constitutive assumptions define the material properties for the interacting continua, whereby a generalized form of Terzaghi's effective stress principle appropriate to unsaturated conditions has been used. Deformations of the solid phase depend on the effective stress tensor σ', defined as

$$\boldsymbol{\sigma}' = \boldsymbol{\sigma} + p^* \boldsymbol{I}$$

where, using the continuum mechanics sign convention (compressions are negative), $\boldsymbol{\sigma}$ is the (total) stress tensor of the porous medium, $p^* = \max(p_l, p_g)$ is the effective fluid pressure and $\boldsymbol{I}$ is the identity tensor.

Using the equilibrium restrictions and the constitutive assumptions in the balance equations, we get the field equations, a system of partial differential equations (balance of mass of species water, balance of mass of species air, balance of momentum of the porous medium, and balance of energy of the porous medium) in terms of unknown fields, functions of space position and time (p_l pressure of the liquid phase, p_g pressure of the gas phase, $\boldsymbol{u}_s$ displacement vector of the solid phase, and T temperature). Consideration of appropriate initial and boundary conditions allows determining the aforementioned unknown fields.

For the HG-A test, isothermal conditions have been assumed, thereby dropping the balance of energy for the porous medium from the system of partial differential equations and setting temperature to the fixed constant temperature in the remaining equations. In this case, the field equations read

$$\phi \frac{\partial}{\partial t}(\omega_l^w \rho_l S_l + \omega_g^w \rho_g S_g) + (\omega_l^w \rho_l S_l + \omega_g^w \rho_g S_g)\frac{\partial \varepsilon_{s,vol}}{\partial t} + div(\boldsymbol{i}_l^w + \omega_l^w \rho_l \boldsymbol{q}_l + \boldsymbol{i}_g^w + \omega_g^w \rho_g \boldsymbol{q}_g) = 0$$

$$\phi \frac{\partial}{\partial t}(\omega_l^a \rho_l S_l + \omega_g^a \rho_g S_g) + (\omega_l^a \rho_l S_l + \omega_g^a \rho_g S_g)\frac{\partial \varepsilon_{s,vol}}{\partial t} + div(\boldsymbol{i}_l^a + \omega_l^a \rho_l \boldsymbol{q}_l + \boldsymbol{i}_g^a + \omega_g^a \rho_g \boldsymbol{q}_g) = 0$$

$$div(\boldsymbol{\sigma}' - p^* \boldsymbol{I}) + ((1-\phi)\rho_s + \phi S_l \rho_l + \phi S_g \rho_g)\boldsymbol{g} = \boldsymbol{0}$$

In these equations, ρ_s, ρ_l and ρ_g are the densities of the solid, liquid and gas phases, ϕ is the void ratio, S_l and S_g are the degrees of saturation of the liquid and gas phases ($S_l + S_g = 1$), $\boldsymbol{v}_s$ is the velocity of the solid phase, ω_l^w and ω_l^a are the mass fractions of species water and species air in the liquid phase ($\omega_l^w + \omega_l^a = 1$), ω_g^w and ω_g^a are the mass fractions of species water and species air in the gas phase ($\omega_g^w + \omega_g^a = 1$), $\varepsilon_{s,vol}$ is the volumetric deformation of the solid phase skeleton, $\boldsymbol{q}_l$ and $\boldsymbol{q}_g$ are the volume fluxes of the liquid and gas phases with respect of the solid phase ($\boldsymbol{q}_l = \phi S_l(\boldsymbol{v}_l - \boldsymbol{v}_s)$ and $\boldsymbol{q}_g = \phi S_g(\boldsymbol{v}_g - \boldsymbol{v}_s)$, where $\boldsymbol{v}_l$ and $\boldsymbol{v}_g$ are the velocities of the liquid and gas phases), $\boldsymbol{i}_l^w$ and $\boldsymbol{i}_l^a$ are the mass fluxes with respect to the liquid phase of species water and species air in the liquid phase ($\boldsymbol{i}_l^w = \rho_l \omega_l^w \phi S_l(\boldsymbol{v}_l^w - \boldsymbol{v}_l)$ and $\boldsymbol{i}_l^a = \rho_l \omega_l^a \phi S_l(\boldsymbol{v}_l^a - \boldsymbol{v}_l)$, where $\boldsymbol{v}_l^w$ and $\boldsymbol{v}_l^a$ are the velocities of species water and species air in the liquid phase; since $\omega_l^w \boldsymbol{v}_l^w + \omega_l^w \boldsymbol{v}_l^a = \boldsymbol{v}_l$, it follows $\boldsymbol{i}_l^w + \boldsymbol{i}_l^a = \boldsymbol{0}$), $\boldsymbol{i}_g^w$ and $\boldsymbol{i}_g^a$ are the mass fluxes with respect to the gas phase of species water and species air in the gas phase ($\boldsymbol{i}_g^w = \rho_g \omega_g^w \phi S_g(\boldsymbol{v}_g^w - \boldsymbol{v}_g)$ and $\boldsymbol{i}_g^a = \rho_g \omega_g^a \phi S_g(\boldsymbol{v}_g^a - \boldsymbol{v}_g)$, where $\boldsymbol{v}_g^w$ and $\boldsymbol{v}_g^a$ are the velocities of species water in the gas phase and of species air in the gas phase; since $\omega_g^w \boldsymbol{v}_g^w + \omega_g^w \boldsymbol{v}_g^a = \boldsymbol{v}_g$, it follows $\boldsymbol{i}_g^w + \boldsymbol{i}_g^a = \boldsymbol{0}$), and $\boldsymbol{g}$ is the gravity acceleration.

The volume fluxes $\boldsymbol{q}_l$ and $\boldsymbol{q}_g$ of the liquid and gas phases are given by extensions of Darcy's law appropriate to unsaturated conditions:

$$\boldsymbol{q}_l = -\frac{k_{rl}(S_l)\boldsymbol{k}(\varepsilon_{s,vol})}{\mu_l}\left[grad(p_l) - \rho_l \boldsymbol{g}\right] \quad \text{and} \quad \boldsymbol{q}_g = -\frac{k_{rg}(S_g)\boldsymbol{k}(\varepsilon_{s,vol})}{\mu_g}\left[grad(p_g) - \rho_g \boldsymbol{g}\right],$$

where $\boldsymbol{k}(\varepsilon_{s,vol})$ is the intrinsic permeability tensor, $k_{rl}(S_l)$ and $k_{rg}(S_g)$ are the relative permeabilities to the liquid and gas phases, and μ_l and μ_g are the viscosities of the liquid and gas phases. The mass fluxes $\boldsymbol{i}_l^a$ and $\boldsymbol{i}_g^w$ of species air in the liquid phase and of species water in the gas phase are given by extensions of Fick's law appropriate to porous media:

$$\boldsymbol{i}_l^a = -\rho_l(\phi S_l D_l^a \boldsymbol{I} + \boldsymbol{D}_l')grad(\omega_l^a) \quad \text{and} \quad \boldsymbol{i}_g^w = -\rho_g(\phi S_g D_g^w \boldsymbol{I} + \boldsymbol{D}_g')grad(\omega_g^w),$$

where D_l^a and D_g^w are the diffusion coefficients for species air in the liquid phase and species water in the gas phase, and $\boldsymbol{D}_l'$ and $\boldsymbol{D}_g'$ are the dispersion tensors for the liquid and gas phases.

The transition between saturated and unsaturated states was controlled by the water retention curve, relating the degree of saturation S_l with suction $p_g - p_l$, for which van Genuchten's model law was used. In saturated conditions, where no gas phase exists, p_g is the pressure that the gas phase would have if it were present, and in phase change equilibrium with the liquid phase.

4.1.3 Modelling of the tunnel excavation

In order to model the tunnel excavation, a 3D model using CODE_BRIGHT (a FEM code developed at the Geotechnical Engineering Department of UPC) was prepared, which took into account the anisotropy induced by the bedding planes of the Opalinus clay. The model assumed full saturation of the Opalinus clay, which was implemented by dropping the balance of mass for the air species from the field equations and setting $p_g = 0.10\,\text{MPa}$ (atmospheric pressure), $\omega_l^w = 1$, $\omega_l^a = 0$ (no dissolved air in the liquid phase; Fick's laws yield $\boldsymbol{i}_l^w = \boldsymbol{i}_l^a = \boldsymbol{0}$) and $\omega_g^w = 0$, $\omega_g^a = 1$ (no water vapour in the gas; Fick's laws yield $\boldsymbol{i}_l^w = \boldsymbol{i}_l^a = \boldsymbol{0}$) in the remaining field equations. For the solid skeleton of the Opalinus clay, a cross-anisotropic linear poroelastic constitutive law with cross-anisotropic (constant) intrinsic permeability was assumed, thereby introducing the anisotropy due to the bedding planes, with a strike line parallel to the tunnel axis and a dip angle of 45°. Though such an elastic material cannot reproduce the formation of the EDZ, which entails a change of material properties, it is believed that it might indicate the zones where the EDZ will form.

4.1.3.1 Tunnel excavation process

As shown in **Figure 60**, the excavation rate has been taken into account rather accurately, because of its influence in the evolution of the solid skeleton displacement and liquid phase pressure fields.

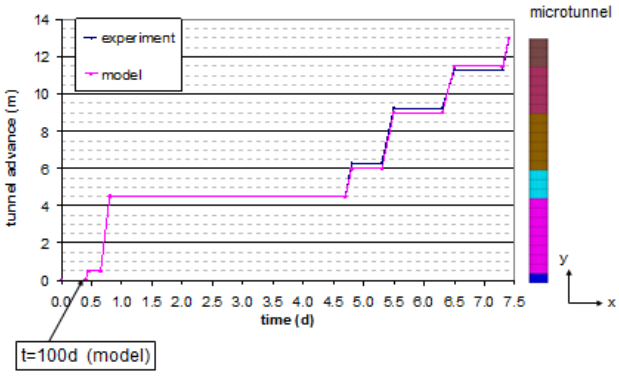

Figure 60 Real and modelled tunnel excavation rates.

4.1.3.2 3D MODEL

The modelled region was an orthogonal quadrangular prism 18 m × 10 m × 10 m, such that the tunnel axis passed through the centre of the square bases. This region was occupied by the (undamaged) Opalinus clay as shown in the following figure

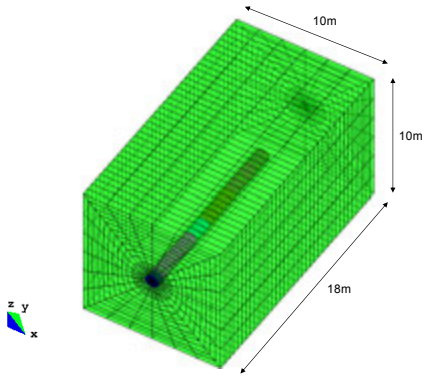

Figure 61 Modelled region and system of coordinates.

The boundary conditions applied to the mesh surfaces are schematized in the following figure, whereby the applied stresses and liquid phase pressures were based on in situ measurements at the Mont Terri URL.

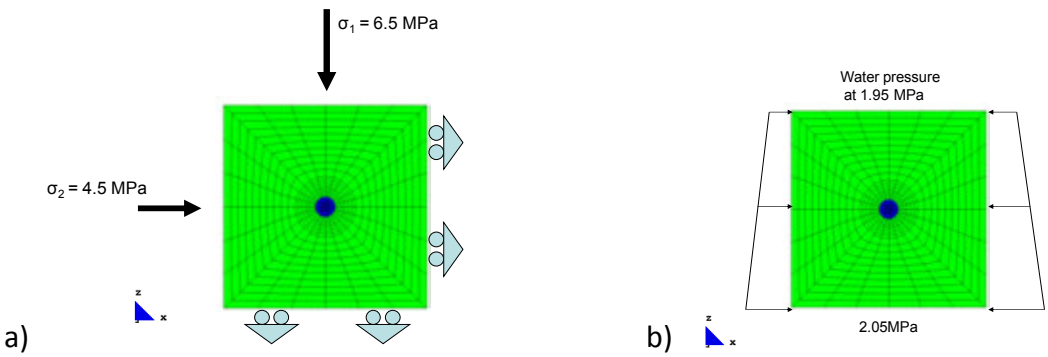

Figure 62 Boundary conditions: a) mechanical ($\sigma_1 = 6.5$ MPa, $\sigma_2 = 4.5$ MPa, $\sigma_3 = 2.5$ MPa compression is positive); b) hydraulic (upper face $p_l = 1.95$ MPa, lower face $p_l = 2.05$ MPa).

Three modeling phases were considered: (1) initialization (during 100 days, the initial stress field and liquid phase pressure field were generated); (2) tunnel excavation (during the next 7 days, the tunnel excavation was simulated, whereby elements were removed from the finite element mesh and, on the newly created surfaces, a total pressure of 0.1 MPa and a liquid phase pressure p_l of 0.1 MPa (atmospheric pressure) was applied); liquid phase excess pressure dissipation (during the additional period of 110 days, the evolution of the state of the Opalinus clay near the tunnel was determined).

The figure below shows the measured and computed evolutions of liquid phase pressure at the isolated intervals of boreholes HG-A2 and HG-A3, that are sub-parallel to the tunnel axis. The shapes of these evolutions are similar, but the corresponding values are quite different.

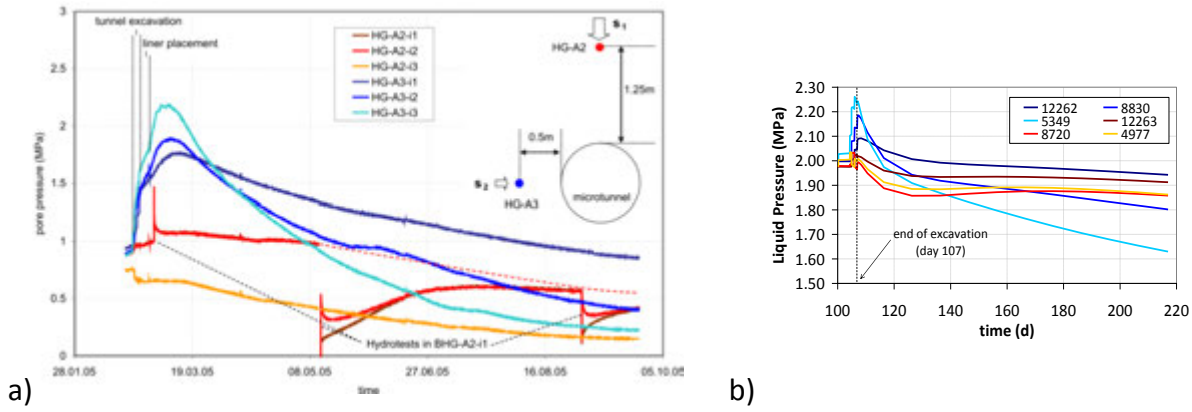

Figure 63 Evolutions of liquid pressure at the isolated intervals in boreholes HG-A2 (above the tunnel) and HG-A3 (at the left of the tunnel), that are subparallel to the tunnel; a) measured by the installed sensors, Marschall et al. (2006); b) computed using the model. Note that the same colours are used for corresponding evolutions in a) and b), but time and pressure scales used on b) double those used on a).

As shown in Figure 64, the evolution of liquid phase pressure at points located at 0.5 m from the tunnel is highly dependent on their position. The corresponding evolutions, which are symmetric with respect to the bedding planes, exhibit large variations at points 2, 6 (decrements), 4 and 8 (increments), but small variations at points 1, 5 (increments), 3 and 7 (decrements). Therefore, a change in the considered dip angle of the bedding planes would improve the predictions at the isolated intervals of boreholes HG-A2 and HG-A3.

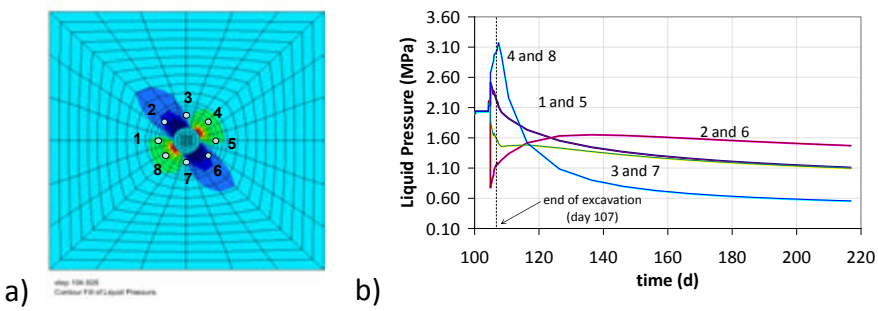

Figure 64 Evolution of the liquid phase pressure at 8 points on the vertical plane at y = 7 m and 0.5 m from the tunnel wall; a) location of points; b) computed evolutions.

The following figure shows the damaged zones around the excavated tunnel and the computed distributions of porosity on a vertical plane at y = 7 m just after finishing the tunnel excavation and 110 days thereafter. It may be seen that, due to the liquid phase pressure dissipation, porosity increases with time and is greater on the observed most damaged zones.

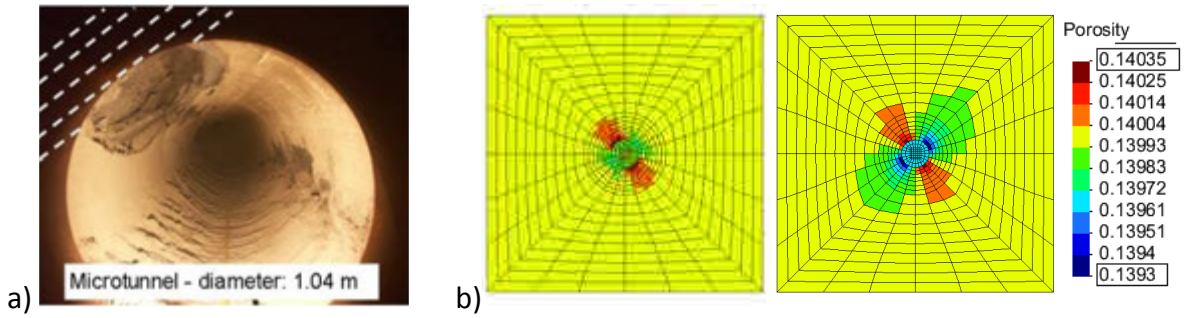

Figure 65 a) damage zones around de HG-A tunnel, Marschall et al. (2008); b) porosity distributions on a 10 m × 10 m square zone around the tunnel on a vertical plane at y = 7 m at 107 days (left) and 217days (right).

Finally, the following figure shows the liquid pressure distributions at the beginning of the tunnel excavation, at the end of the tunnel excavation and at 110 days after the end of the tunnel excavation. Large variations of liquid phase pressure are evident.

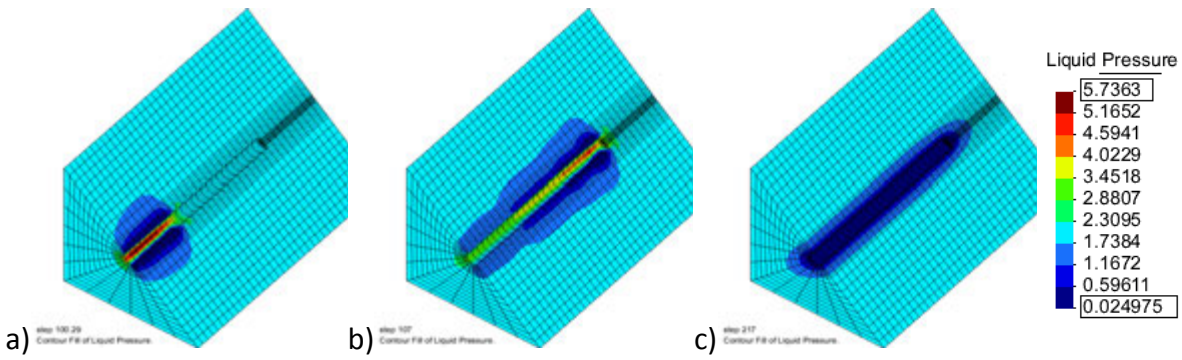

Figure 66 Liquid pressure distribution (in MPa) on a plane orthogonal to the Opalinus clay bedding planes and passing through the tunnel axis at several times: a) 100.29 days; b) 107 days; and c) 217 days.

4.1.4 Modelling of the liquid and gas injection tests

In an effort to keep the modelling as simple as possible, the anisotropy induced by the bedding planes of the Opalinus clay was not taken into account, and the effect of gravity was been neglected. This approach leads to a 2D axisymmetric model, which corresponds to an average behaviour of the EDZ. Indeed, there is evidence that the EDZ is anisotropic and inhomogeneous, whereby some zones were detached (and subsequently repaired) and localized zones of relatively high conductivity were observed. In the modelling of the liquid and gas injection tests, two models were prepared: a 2D axisymmetric model using CODE_BRIGHT and a 1D simplified model. In both models, the EDZ was assumed to have a uniform thickness of 0.20 m and the same constitutive laws were used.

In order to be able to model the variations of intrinsic permeability due to the variation of the aperture of the cracks on the EDZ, the deformation-dependent model presented in Olivella et al. (2008) was used, namely

$$\boldsymbol{k}(\varepsilon_{vol}) = \boldsymbol{k}_{matrix} + \frac{1}{12a}[b(\varepsilon_{vol})]^3 \boldsymbol{I}$$

where $\boldsymbol{k}_{matrix}$ is the matrix permeability tensor such that, at a given space point, remains constant, $\boldsymbol{I}$ is the identity tensor, a is the mean spacing between cracks and $b(\varepsilon_{vol})$ denotes the crack aperture as a function of ε_{vol} defined by

$$b(\varepsilon_{vol}) = \begin{cases} b_0 & \varepsilon_{vol} \le \varepsilon_{vol0} \\ b_0 + (\varepsilon_{vol} - \varepsilon_{vol0})a & \varepsilon_{vol0} \le \varepsilon_{vol} \le \varepsilon_{vol0} + (b_{max} - b_0)/a \\ b_{max} & \varepsilon_{vol0} + (b_{max} - b_0)/a \le \varepsilon_{vol} \end{cases}$$

where ε_{vol0} is the volumetric deformation at which the crack aperture starts increasing, b_0 is the minimum crack aperture, b_{max} is the maximum crack aperture and a is the mean spacing between cracks. The following figure shows the variations of crack aperture and intrinsic permeability with volumetric deformation, with the parameters used in the calculations. Note the large variations in intrinsic permeability induced by changes in volumetric deformation.

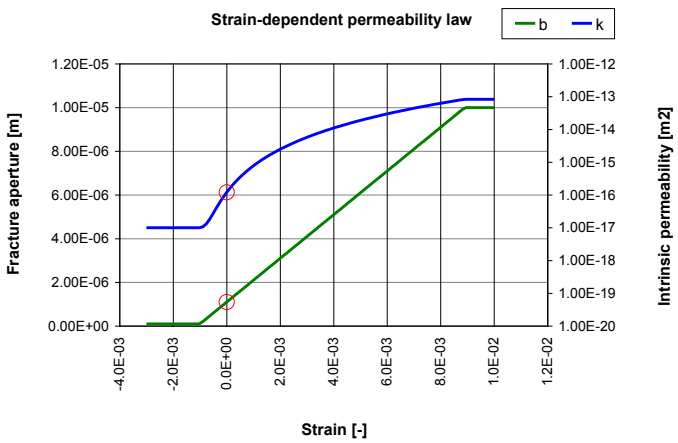

Figure 67 Evolution of the crack aperture (left axis) and of the intrinsic permeability (right axis, in logarithmic scale) as a function of volumetric deformation with the parameters used in the calculations (circles indicate the initial state, at $\varepsilon = 0$).

4.1.4.1 Test protocols

Using appropriate sensors, the evolution of the megapacker pressure, the liquid volume injection rate (liquid injection tests) and the gas volume injection rate (gas injection tests) were monitored. For modelling purposes, these evolutions were approximated by polygonal evolutions, as can be seen in the following figure.

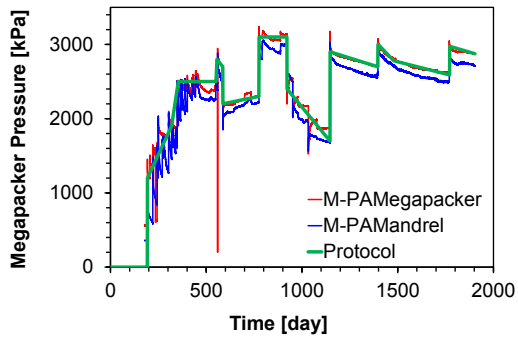

a)

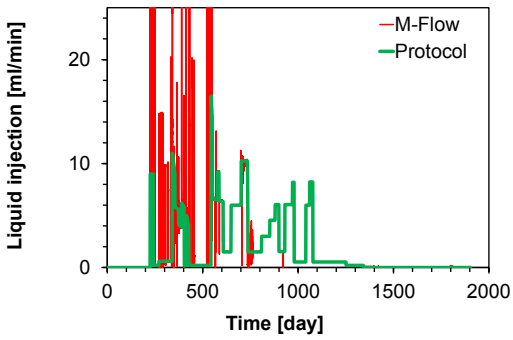

b)

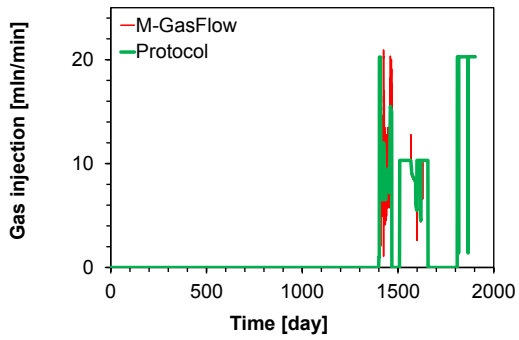

c)

Figure 68 Measured input evolutions and model polygonal approximations: a) megapacker pressure; b) liquid volume injection rate; and c) gas volume injection rate.

4.1.4.2 2D AXISYMMETRIC MODEL

The tunnel axis was considered to be the axisymmetry axis. The figure below shows the geometry around the megapacker section, the system of coordinates used and the modelled region, whose external dimensions are 18 m × 5 m. The EDZ has a thickness of 0.20 m.

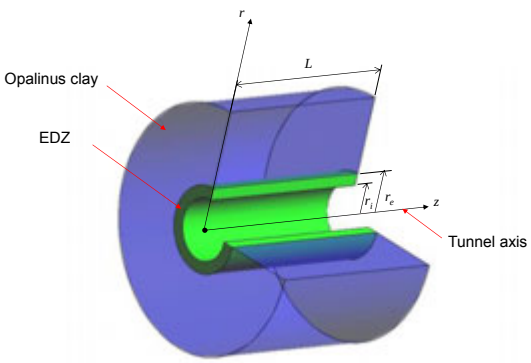

a)

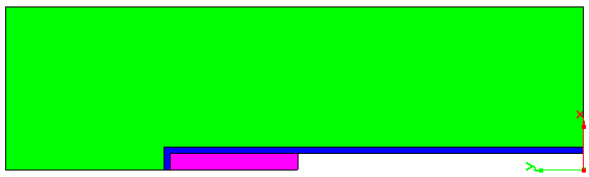

b)

Figure 69 a) Geometry around the megapacker section and system of coordinates; b) modelled region and materials: (undamaged) Opalinus clay (green), EDZ (blue) and gravel (pink). The tunnel axis is the axisymmetry axis.

The figure below shows the considered boundary conditions: mechanical (prescribed displacements and prescribed tractions) and hydraulic (prescribed liquid and gas phase pressures and prescribed species water and species air mass rates). At the injection point (as

explained later, two positions have been considered), the mass rates of species water and species air (obtained from the injected volume rates of liquid and gas phases) were imposed.

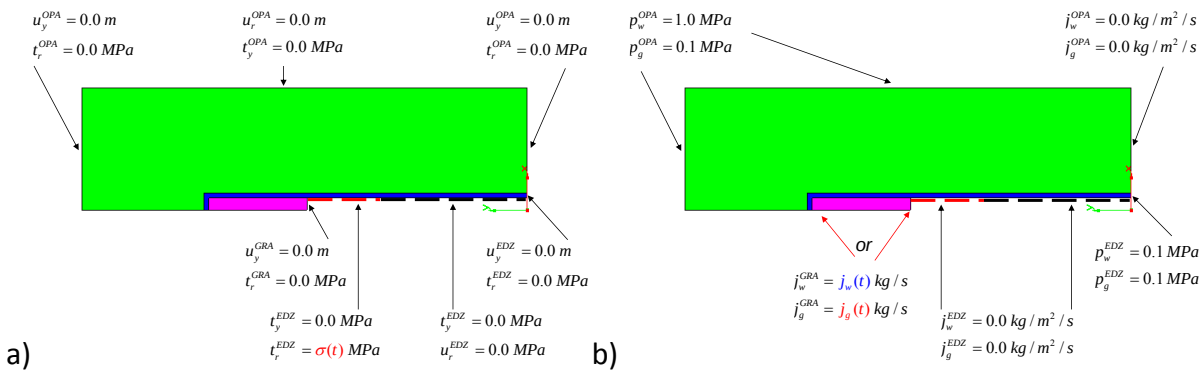

Figure 70 Boundary conditions: a) mechanical (u_y are and u_r are the components of the displacement; t_y are and t_r are the components of the (total) traction); b) hydraulic (j_w are and j_a are mass rates of species water and species air).

The 1D simplified model (see below) proved to be convenient for carrying out the pertinent sensitivity analyses. A number of cases were run. First, the gravel was considered to be saturated and the liquid injection tests were used to calibrate the parameters related to liquid flow and deformation. Afterwards, the gravel was changed from initially saturated to unsaturated to better capture the early liquid phase pressure variations induced by liquid injection. Finally, to improve the modeling results, additional cases were run changing the location of the injection point into the test section from close to the megapacker to close to the tunnel end (to eliminate the gas entrapped at the tunnel end) and incorporating venting before gas injection tests (before starting a gas injection test, liquid was circulated through the test section in order to eliminate entrapped gas). The figure below shows the best predictions of the liquid and gas phase pressures in the test section compared with the recorded evolution of the liquid phase pressure. The computed evolution of the intrinsic permeability in the EDZ close to the test section exhibits large variations, due to variations in crack apertures.

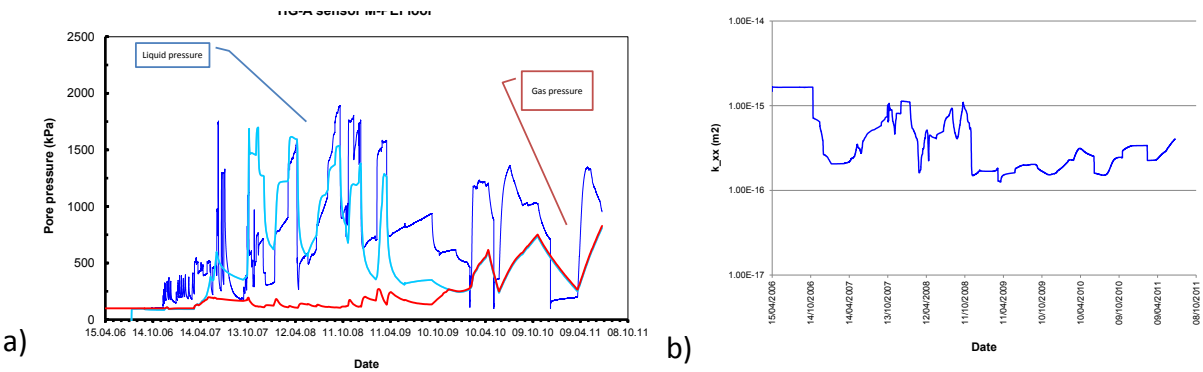

Figure 71 a) Evolution of the measured liquid phase pressure (dark blue), computed liquid phase pressure (light blue) and gas phase pressure (red) in the EDZ; b) evolution of the computed intrinsic permeability in the EDZ, close to the test section.

4.1.4.3 1D SIMPLIFIED MODEL

In addition to axisymmetry, we assumed the following simplifying assumptions: mechanical: slices $z = const$ move independently and in plane strain; hydraulic: in the EDZ, liquid phase and gas phase flows are longitudinal; in the Opalinus clay, there is neither gas phase nor dissolved air in the liquid phase, and the liquid phase flow vanishes. Additionally, it was assumed that the liquid phase density remained constant. In these conditions, the pressure of the liquid phase p_l and the pressure of the gas phase p_g depend only on the axial distance *z*, and time *t*, and the displacement vector of the solid phase $\boldsymbol{u}_s$ may be expressed in closed form in terms of p_l and p_g, that are found by solving a reduced system of differential equations (balance of mass of species water and balance of mass of species air) on a 1D geometric domain, representing the part of the EDZ in front of the megapacker. As schematized in the figure below, axisymmetric hydraulic boundary conditions were transformed into 1D boundary conditions using the dependence of p_l and p_g only on the axiall distance *z*, and time *t*, and axisymmetric mechanic boundary conditions were transformed into 1D body terms. At the end of the 1D domain in contact with the test section, the evolution of mass fluxes of species water and species air (obtained from the evolution of the injected volume fluxes of liquid and gas) was imposed. At the end of the 1D domain in contact with the liner section, the volume fluxes of liquid and gas were assumed to be proportional to the difference of the liquid or gas phase pressure at that point and the ones at the Mont Terri URL. In the FORGE progress report by Alcoverro et al. (2012a), the simplified 1D model and its numerical solution are presented in detail.

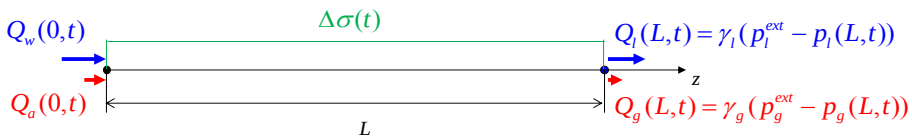

Figure 72 Transformation of 2D axisymmetric boundary conditions into 1D boundary conditions and body terms. The 1D domain represents the EDZ in front of the megapacker, which is bounded to the left by the test section and to the right by the liner section.

The results of the 2D axisymmetric CODE_BRIGHT model confirm the validity of the simplifying assumptions away from the megapacker ends, as shown in the figure below.

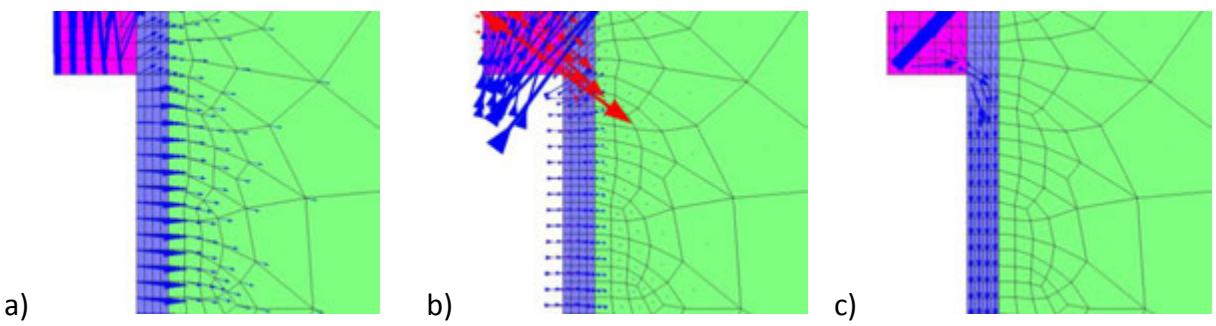

Figure 73 Results of the 2D axisymmetric model at day 900 (hydraulic tests) on the zone around the megapacker half close to the test section: a) displacements (radial); b) strains (plane strain); and c) volume flow of liquid phase (axial on EDZ, zero on Opalinus clay).

The system of differential equations was solved numerically using the finite element method, and was implemented on an Excel spreadsheet. As already mentioned, this tool was used to calibrate the model parameters for the 2D axisymmetric model, by performing a series of sensitivity analyses. It should be borne in mind that, due to the assumption that slices $z = const$ move independently and in plane strain, the 1D simplified model was restricted to the slices containing the megapacker. Thus, the test section was not modelled, so the aforementioned problems of the 2D axisymmetric model concerning the elimination of gas in the test section did not occur, and the response to liquid and gas injection was immediate.

The figure below summarizes the main results. The evolution of the effective fluid pressure in the test section (EDZ zone close to the test section) is compared with the evolution of pressure recorded by the pertinent sensor. It may be seen that the results are similar to the ones obtained using the 2D axisymmetric model, and that while they capture the main observed features, the observed increasing trend is not reproduced. The computed evolution of the intrinsic permeability is similar to the one obtained using the 2D axisymmetric model.

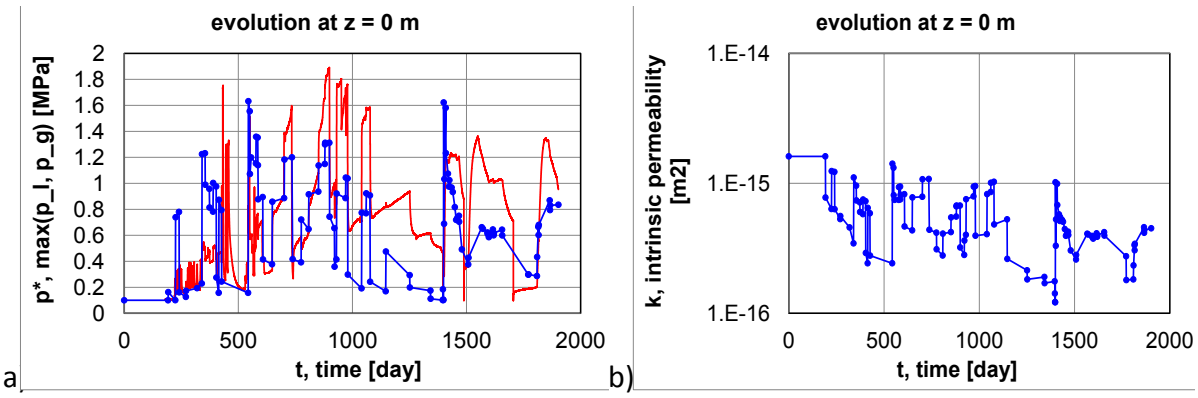

Figure 74 Results of the 1D simplified model (EDZ zone close to the test section): a) measured (red) and computed (blue) evolution of fluid pressure in the test section; b) computed evolution of intrinsic permeability in the EDZ.

4.1.5 Conclusions

The modelling of the HG-A in situ test has been able to reproduce the general features of the response recorded during the tunnel excavation and during the liquid and gas injection tests. Some features, however, have not been satisfactorily reproduced and would require a more detailed knowledge of the geometry and material behaviour of the EDZ. The 1D simplified model provided insight in the HG-A test and facilitated the parameter calibration.

4.2 GAS MIGRATION IN OPALINUS CLAY AND CALLOVO-OXFORDIAN CLAYSTONE (EDF)

This chapter is dedicated to numerical modelling of gas migration in clay. For Opalinus clay, only preliminary study has been conducted in order to have a first estimation of Damage Zone around borehole of HG-A experiment. Gas phase of this experiment has not been modelling. For Callovo-Oxfordien Claystone, a fully modelling of PGZ1 experiment (Gas injection in clay) has been conducted. All the modelling have been conducted with Code_Aster (www.code-aster.org).

4.2.1 Model used in this study

We consider an unsaturated biphasic Hydro-Mechanical model. Details of Hydro-Mechanical models available in *Code_Aster* are given in (Granet et al., 2012) generally in (Gerard et al., 2010). Hereafter, we recall main equations of the model.

We consider 2 components (N_2 and H_20), denoted by upper index *c* existing into 2 phases (liquid and gas), denoted by lower index *p*. In our study, we consider that there is no vapor; hence water does not exist in gaseous phase. Gaseous phase is composed of nitrogen, liquid phase is composed of water and dissolved nitrogen.

Mechanical unknowns are displacements $u = (u_x, u_y, u_z)$. Hydraulical unknowns are liquid pressure $p_l = p_l^{H_2O} + p_l^{N_2}$ and gas pressure $p_g = p_g^{N_2}$. They are related by capillary pressure $p_c = p_g - p_l$. Capillary pressure p_c is related to water saturation S_l by Van-Genuchten relation:

$$S_{we} = \frac{1}{\left(1+\left(\frac{p_c}{p_r}\right)^n\right)^m} \quad with \quad S_{we} = \frac{S_l - S_{wr}}{1 - S_{wr}}$$

where we have introduced S_{wr} the residual saturation, S_{we} the effective saturation, p_r, n and m Van-Genuchten parameters such as: $m = 1 - 1/n$.Liquid relative permeability is also given by Mualem Van-Genuchten model, such that :

$$k_r^l = \sqrt{S_{we}}\left[1-\left(1-S_{we}^{1/m}\right)^m\right]^2$$

Gas relative permeability is given by a cubic law ponderated by a coefficient C_k:

$$k_r^g = C_k\left(1-S_l\right)^3$$

Nitrogen N_2 obeys to perfect gases law:

$$p_g^{N_2} = \frac{\rho_g^{N_2}}{M_{N_2}} RT$$

Where we introduce ρ the density, M_{N_2} the Nitrogen molar mass, R the perfect gas constant and T the temperature. Water is slightly compressible, hence we have the relation

$$\frac{d\rho_l}{\rho_l} = \frac{dp_l}{K_l}$$

where coefficient K_l denotes water compressibility. Nitrogen dissolution obeys to Henry's law

$$\frac{\rho_l^{H_2}}{M_{N_2}^{ol}} = \frac{p_g^{H_2}}{K_H}$$

where K_H designates Henry's constant and $M_{N_2}^{ol}$ nitrogen molar mass.

Two main equations govern system's evolution: balance momentum and fluid mass conservation. Balance momentum equation is

$$\nabla \cdot \sigma(u, p_c, p_g) = 0$$

Stress tensor is decomposed in effective stress tensor σ' and pressure stress tensor σ_p

$$\sigma(u, p_c, p_g) = \sigma'(u) + \sigma_p(p_c, p_g)$$

Incremental form of pressure stress tensor reads:

$$d\sigma_p = -b(dp_g - S_l dp_c)$$

Where *b* designates Biot coefficient and S_l water saturation.

The variation of porosity $d\varphi$ is given by the classical eulerian representation

$$d\varphi = (b - \varphi)\left(d\varepsilon_v + \frac{S_g dp_g + S_l dp_l}{K_S} \right)$$

With ε_v is volumic strain and K_S the compressibility of the skeleton.

Mechanical behaviour obeys to Drucker-Prager's law. Material Young modulus and Poisson ratio are respectively denoted *E* and ν. Plasticity surface *F* reads

$$F = \sqrt{\frac{3}{2}} II_{\hat{\sigma}} + m\left(I_\sigma - \frac{3c}{\tan\phi} \right) = 0$$

where $II_{\hat{\sigma}} = \sqrt{\hat{\sigma}_{ij}\hat{\sigma}_{ij}}$ is second deviatoric stresses invariant, $\hat{\sigma}_{ij} = \sigma_{ij} - \frac{I_\sigma}{3}\delta_{ij}$ is deviatoric stresses tensor, $I_\sigma = \sigma_{ij}\delta_{ij}$ is first stresses invariant, coefficient *m* is given by relation $m = \frac{2\sin\phi}{3 - \sin\phi}$, ϕ is friction angle and *c* is cohesion. We notice that gravity effects are here neglected.

Mass conservation reads for component *c*:

$$\dot{m}_c + \nabla \cdot \left(F_l^c + F_g^c \right) = 0$$

where m_c (resp. F_l^c, F_g^c) designates mass inflow (resp. liquid, gaseous flux) of component *c*. For each phase p, hydraulic fluxes obey to Darcy's law :

$$F_p = -\frac{k.k_r^p(S_l)}{\mu_p} \nabla p_p$$

k stands for anisotropic intrinsic permeability $k = (k_x, k_y, k_z)$, k_r^p for relative permeability and μ_p for dynamic viscosity of phase *p*. Diffusion in liquid phase obey to Fick's law:

$$\frac{F_l^{H_2O}}{\rho_l^{H_2O}} + \frac{F_l^{N_2}}{\rho_l^{N_2}} = -D_l \nabla \rho_l^{N_2}$$

where D_l stands for Fick diffusion coefficient in liquid phase. In the sequel, we will express D_l as a linear function of tortuosity τ , saturation and porosity such that:

$$D_l = S_l.\tau.\varphi.D_{N2}^w$$

with D_{N2}^w the diffusion coefficient of nitrogen into water.

4.2.2 Brief Description of experiment

4.2.2.1 Opalinus (HG-A)

The HG-A experiment is a 4 years test in the laboratory of Mont-Terri described in chapter 3.1 and a complete description of the instrumentation of the rock with their responses is proposed by Marshall (Marshall et al., 2006). In this section, we will just emphasize on some packer systems placed around the borehole (before the excavation) to measure the evolution of pore pressure. These packers are separated into three monitoring intervals labeled as "-i1" (12.5 - 14 m along hole), "-i2" (12 – 9.5 m ah) and "-i3" (9 - 5.5 m ah).

Figure 75(a) shows the evolution of pore pressure in the different monitoring intervals. In the short monitoring period before tunnel excavation, pore pressure in the observation intervals ranges between 0.75 and 0.9 MPa and increases slightly towards the expected (pseudo-)static formation pressure of about 1.0 – 1.2 MPa. Immediately after starting the tunnel excavation, a significant rise in pore pressure is seen in borehole HG-A3, which is located at a distance of 0.5 m from the tunnel side wall. In borehole HG-A2, located at a distance of 1.5m above the microtunnel, the evolution of the pore pressure is quite different with an increase much more moderate. Instantaneous failure of the rock was caused by the combined effect of the anisotropy in far-field stress, the anisotropy in geomechanical rock properties and the heterogeneity of the rock mass. We can see in

Figure 75(b) a scan of the HG-A micro-tunnel with the failure observed after the excavation. The breakouts occur on the upper left side (named position 9: 00 to 11: 00 o'clock).

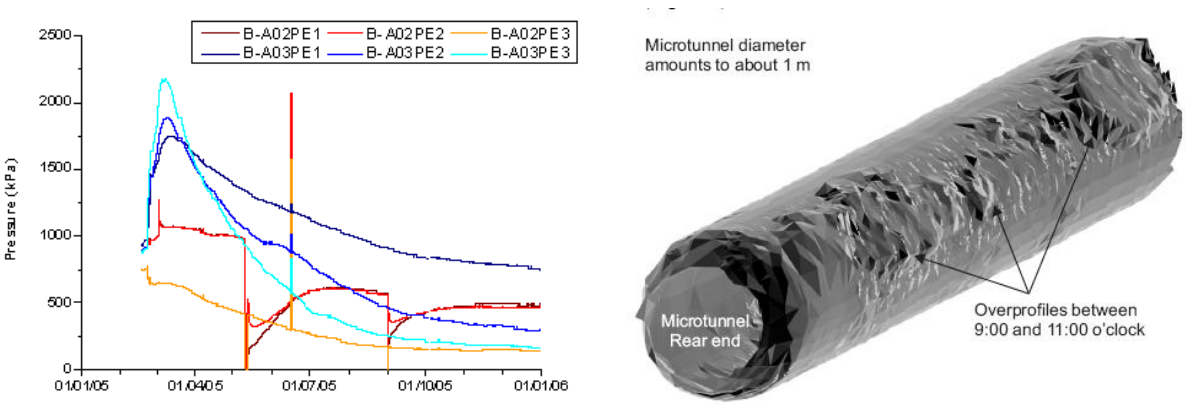

Figure 75: Experimental results. (a) on the left: The water pressure in triple packer HG-A02 and HG-A03. (b) on the right: 3D laser scan of the HG-A micro-tunnel with a tachymeter. Pictures ext from Marshall et al (2006).

4.2.2.2 Callovo-Oxfordien (PGZ1)

PGZ1 experiment (De La Vaissière et al., 2012) consists of 3 boreholes: one borehole for gas injection and measurement and two boreholes for strain and gas pressure measurements (*Figure 76*). Each borehole is composed of 3 intervals (for measurement or injection) separated by packers. Six various gas injection steps, with constant fluxes, followed by shut-in phases have been done in intact claystone. This experiment began in 2009 and is still in progress. Pressure measurements are made during injection. Pressure remains lower than 10 MPa which is less than minimum principal stress. At this height, fracing threshold is not reached. Main goal of this in situ experiment is therefore a better understanding and quantification of gas transfer mechanisms in claystone.

Different phases of experiment could be summarizing as following:

- Drilling of the borehole
- Equipment installation
- Hydraulic tests (HYDRO 1) composed of pulse and constant pressure test
- Gas injection (GAS1) composed of 6 steps of injection

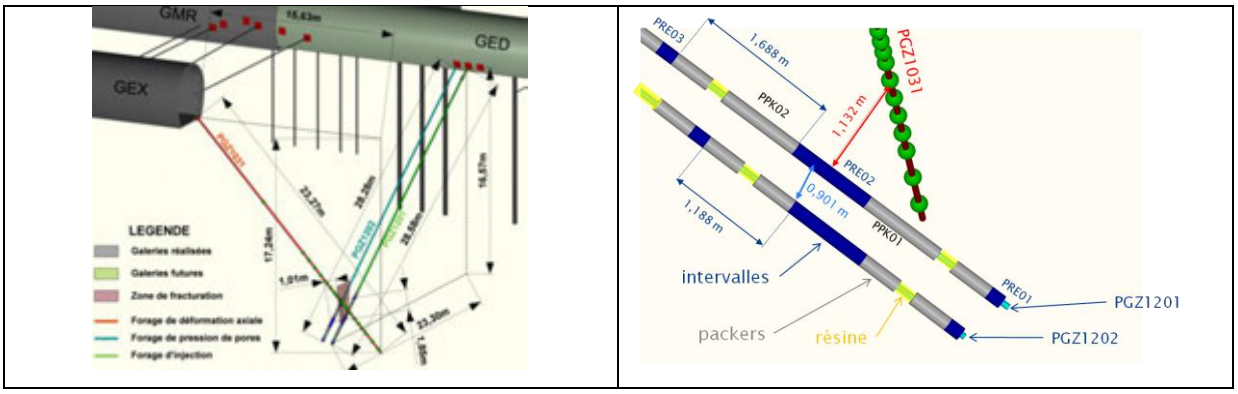

Figure 76 – PGZ1 experiment configuration.

Gas (Nitrogen) production begins on 02/01/10 in central chamber PRE02. This injection, with constant fluxes, followed by stopping phases, is illustrated in purple in *Figure 77* (a). This figure also shows measured pressure in the 3 chambers (PRE01, PRE02, PRE03) of PGZ1201 during the experiment. After HYDRO1 phase, there is a regular but unexplained decrease of water pressure mostly in PRE02. We expected pressure to be stable. Drainage by other borehole (PGZ1031) was suspected and has been confirmed by simulations of ULg. During the GAS1 phase we observe the different steps of pressure increase according to gas flow injection. The influence of gas injection in PRE02 into two chambers PRE01 and PRE03 seems to be negligible. Therefore, first supposition was that there is no significant Borehole Damage Zone due to drilling.

In PGZ1202, *Figure 77* (b), we observe in PRE02 chamber a slight influence of gas injection. Of course this evolution is smoother than those observed in PRE02 of PGZ1201.

We will mainly use pressure data from *Figure 77* (a) in PGZ1201 to assess quality of our numerical simulation and focus on pressure evolution in injection chamber PRE02. Details of experiments and modeling are given in deliverable D5.19.

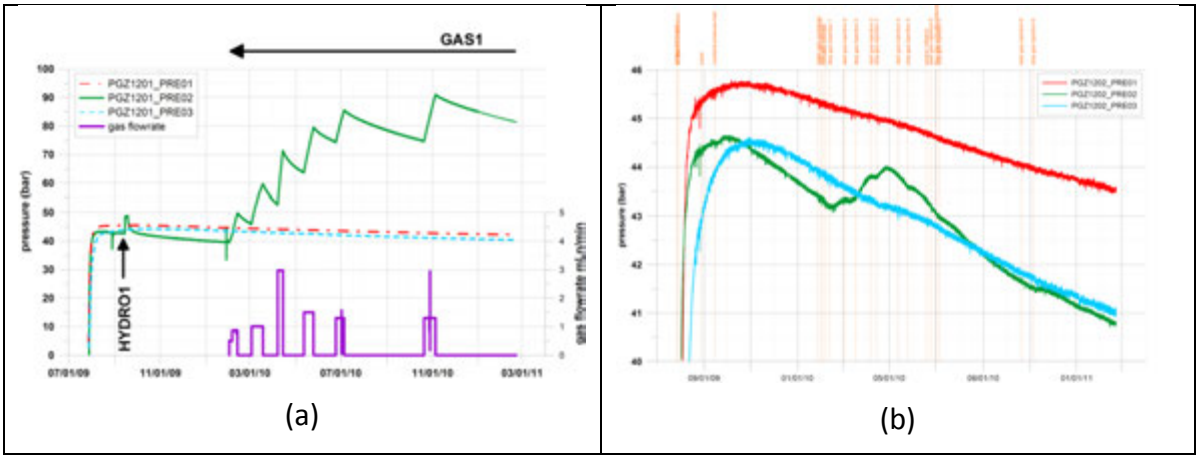

Figure 77 – Water pressure and gas fluxes in PGZ1201 (a) and Water pressure in PGZ1202 (b).

4.2.3 Characterisation of EDZ (HG-A and PGZ1)

4.2.3.1 Opalinus (HG-A)

For this 3D computation, we model the digging considering an excavation layer by layer with an elasto-viscoplastic model based on a Drucker-Prager behaviour law, with the same yield surface as the one presented in Section 4.2.1 (the reader can see Code Aster Documentation R7.01.22 for more details). We respect the real time of drilling as indicated on the Figure 78. The different steps are taken into account.

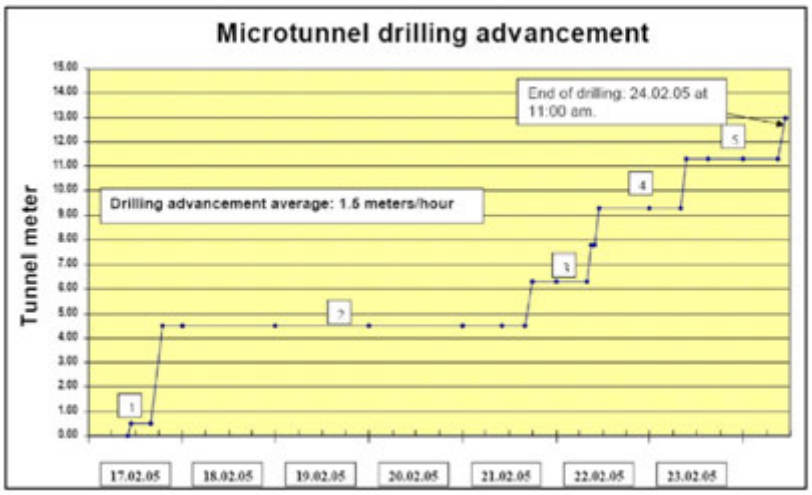

Figure 78 : time steps of excavation.

We consider the following geometry: 10m *10m *14 m (Figure 79) and a classical mesh composed of 45490 tetrahedra (Figure 79). The mesh is composed of 52 layers and the boundary conditions are described Figure 81.

We present on Figure 82 and Figure 83 the pressures obtained on HG-A3. Comparisons are done on those figures between experimental results and simulations (doted lines). As in 2D (see [4]), global appearance of the curves are quite similar. For the different steps of digging: the pressure builds up are equivalent. The more the drill is close to the packer, the more the pressure increase is important (5th day for i3, 6th for i2). On the other hand, we observe only on computation results, some pressure decrease. We notice that differences between

experimental and numerical results (for i2 and i3) are mainly due to the initial state. Indeed it seems that this state is not homogeneous along the packer.

Then, we present on Figure 84 the pressures obtained on HG-A2. In this case, the results are in better agreement with experimental results even if we observe differences due to initial state.

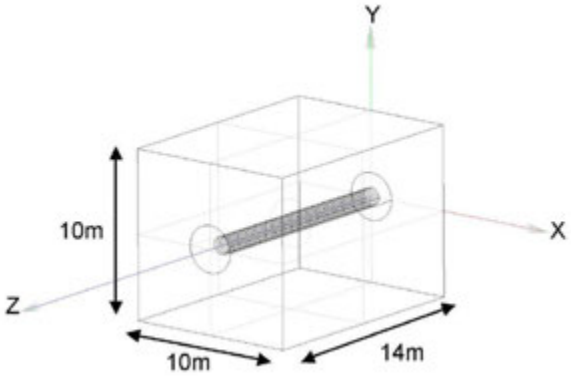

Figure 79 : 3D geometry.

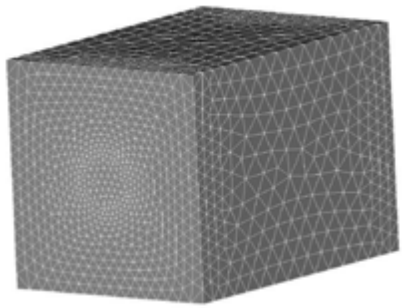

Figure 80 : 3D mesh.

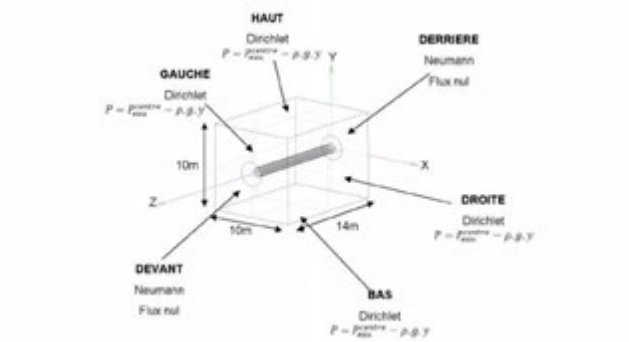

Figure 81 : Boundary conditions.

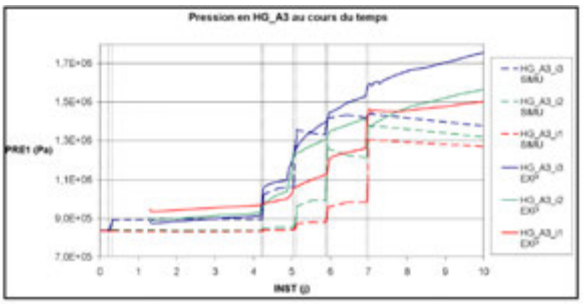

Figure 82 : Pressure on HG-A3 for the first 10 days.

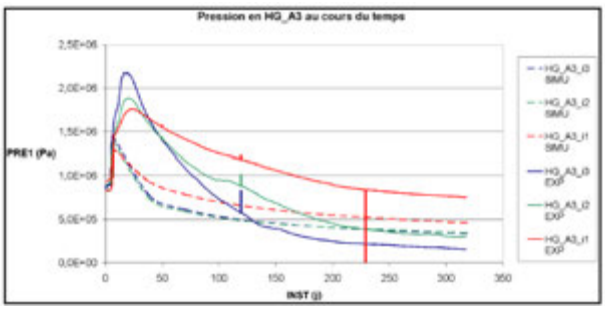

Figure 83: Pressure on HG-A3 for 45 weeks.

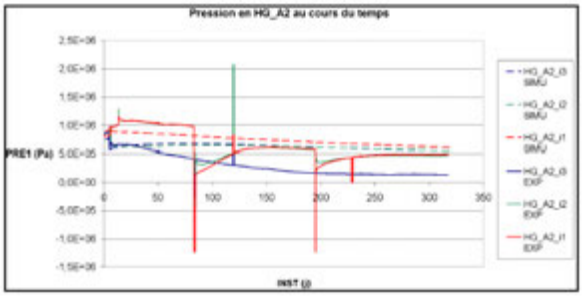

Figure 84 : Pressure on HG-A2 for 45 weeks.

In conclusion, we can consider that those results are quite convenient, if we take into account the weakness of the hypothesis to fit our model (only one experimental triaxial test), and according to the simplifications we made (isotropic calculation).

4.2.4 Callovo-Oxfordien (PGZ1)

Because anisotropy has no major effect in this test, axisymmetrical configuration is finally retained in all the computation (Figure 85). We first consider only injection chamber and argillite.

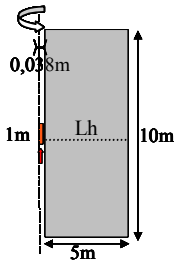

Figure 85 – 2D axisymmetrical geometry.

The materials data used for undisturbed Callovo-oxfordien and chamber are the following:

	Argilite	**Injection Chamber**
Intrinsic permeability	$k_x = k_y = k_z = 2.10^{-20} m^2$	$k_x = k_y = k_z = 10^{-12} m^2$
Initial porosity	$\varphi^0 = 0{,}18$	$\varphi^0 = 0{,}25$
Van Genuchten Parameters	Pr = 15MPa ; n= 1.49 ; Swr = 0.01	Pr = 0.05 MPa ; n= 1.5 ; Swr = 0.0
Gas perm. Coef.	$C_k = 250$	1
Tortuosity	$\tau = 0{,}25$	$\tau = 1$
Young Modulus	$E = 4000\ MPA$	$E = 1\ MPA$
Poisson's ratio	$\nu = 0{,}3$	$\nu = 0{,}1$
Biot coef.	$b = 0{,}6$	$b = 1$
Friction angle	$\phi = 15°$	-
Cohesion	$c = 3\ MPA$	-

Table 6 - Hydro-mechanical parameters for Argilite and Chamber.

In first computations, we modeled borehole excavation before gas injection and hydraulic phase during 181 days. Figure 86 shows plastic deformation along the cross section Lh

perpendicular to borehole: a small (2cm) plastic area appears after borehole digging but stays constant after that. The coupling from hydraulic to mechanic seems to be small.

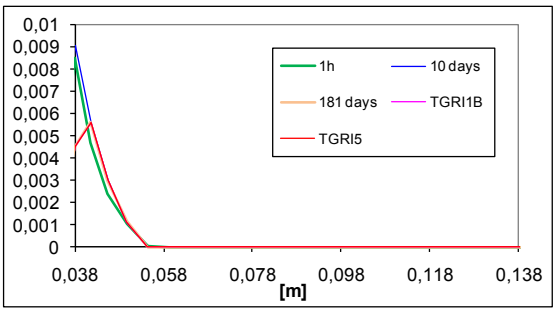

Figure 86 – Plastic deformation on Lh.

Knowing that, in the following we won't simulate excavation anymore. Damage Zone will be simulated by an "a priori zone". We call this area "Borehole Damage Zone" (BDZ) because we can imagine that this zone is composed of an area due to drilling (Figure 86), but also of a "transient zone" mixed of a damage zone and materials produced by injection gas (mud, gel, etc.). We take a radius equal to the radius of the hole (a little bit larger than the obtained results). Experimental observations show that the influence of the gas injection in other borehole intervals is negligible. For this reason, we can imagine that the damaged zone has been closed around the swollen packers (Figure 87). For that we consider two different damage zone. Only intrinsic permeabilities are modified.

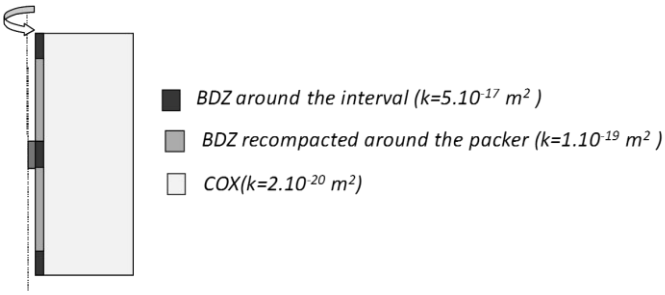

Figure 87 – Configuration and hypothesis of BDZ model.

4.2.5 Modelling of gas migration in Callovo-Oxfordian

4.2.5.1 Some elements concerning the volume of the injection's chamber

De La Vaissière et al (2012) and De La Vaissière (2013) show an analysis of the volume of vacuum Interval 2 (Figure 88) and give more precisions. This volume of void is composed of an "incompressible" volume (corresponding to the case of a full convergence around the filter) and of a part corresponding to a void around this filter. This void will be filled up during the convergence of the rock. Knowing that, the theoretical volume of vacuum in interval 2 ranges between two extremes:

- 804 cm^3 if the rock is fully converged
- 1540 cm^3 when there is no convergence

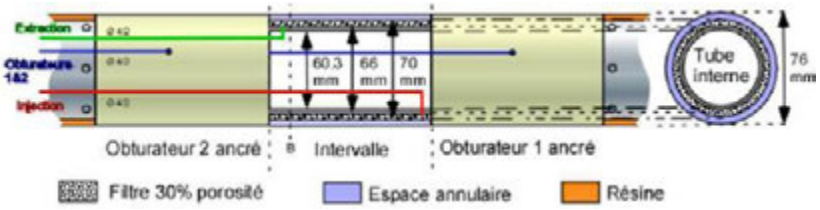

Figure 88 –injection chamber Interval 2 (or PRE02).

Moreover, the volume of water rejected by flushing in the interval during the water/gas exchange before GAS1 phase is equal to 810 cm^3. This volume corresponds to the initial volume of gas in the chamber before injection.

At least, in De La Vaissière (2013) the pressure differential is fitted by an analytical solution at constant volume using a Perfect Gas law. The best fitting before GAS1 is obtained with a volume of 1040 cm^3. This gives us an indication of the volume of interval at the beginning of injection. After that, the fitting is done for each injection steps: the gas volume increases and becomes more important than maximum theoretical value (1540 cm^3) of interval volume after GRI3. An interpretation of that is that residual water is first rejected, and then that gas penetrates in the rock but more and more hardly.

In a first set of hypothesis presented in (Granet et al., 2012) the chamber is fully saturated before gas injection due to hydraulic phase. This is not consistent with the hypothesis done before. In the following, computations are only done for Gas 1 phase considering a volume of 1040 cm^3 for the interval 2 instead of 1100 cm^3. Most of all, initial saturation of gas will be taken into account.

4.2.5.2 Hypothesis of computation

Volume of the chamber is equal to 1040 cm^3 ($\phi^0 = 0{,}23$). Only GAS1 phase is modelled. The 6 steps of injection are modelled.

- Initial condition in argillite:

As shown by De La Vaissière (2013) the argillite is initially fully saturated, and the gravity is neglected. The initial pressure is equal to 4,5MPa.

- Initial condition in injection chamber:

The saturation is such as:

$$S_l = 1 - \frac{810}{1040} = 0{,}22$$

According to the Van-Genuchten parameters indicated in Table 6, it provides an "artificial capillary pressure" $p_c^0 = 0{,}021 MPa$.

4.2.5.3 Reference computation (undisturbed Host rock)

In this section, we only consider undisturbed host rock (without BDZ). Gas pressure evolution with this hypothesis is presented in Figure 89 with the red curve. Until second injection step (≈230 days), experimental results are well reproduced, afterwards, differences are consequents.

The blue curve represents the same computation but with a chamber initially partially saturated (0.9). Logically, the pressure is much higher (and this, as the first step of injection). Looking at the profiles on the line L_h at several times of gas pressure and liquid saturation

respectively Figure 90 and Figure 91, we observe that penetration of gas remains located near the injection interval: influence area is less than 20cm. The saturation stays high (more than 0,495). Looking at the ratio between gas and liquid nitrogen volume on Figure 92, we confirm that even in this case, most of nitrogen is transported by dissolution/diffusion.

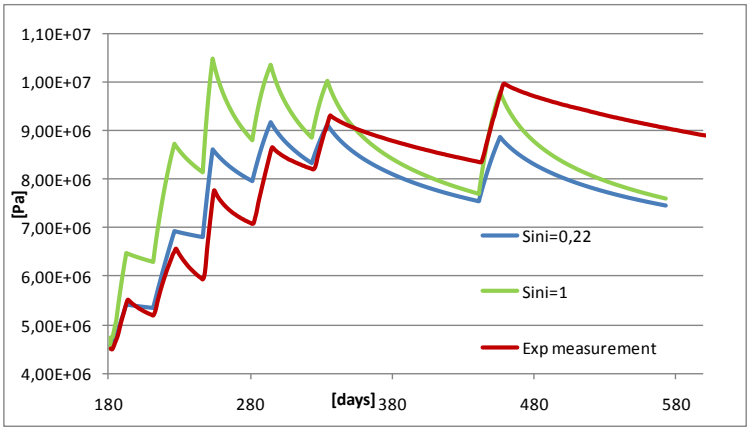

Figure 89 – Liquid pressure evolution in interval 2: goal of initial saturation.

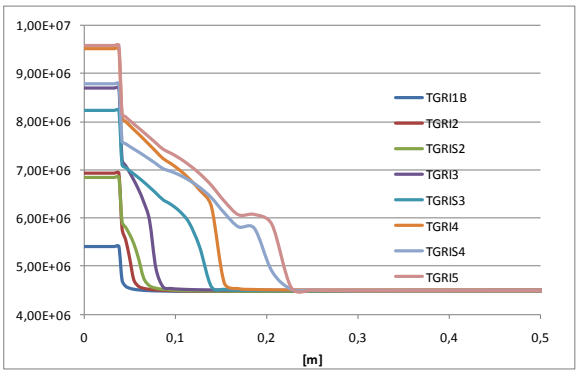

Figure 90 – Gas Pressure at several times along L_h.

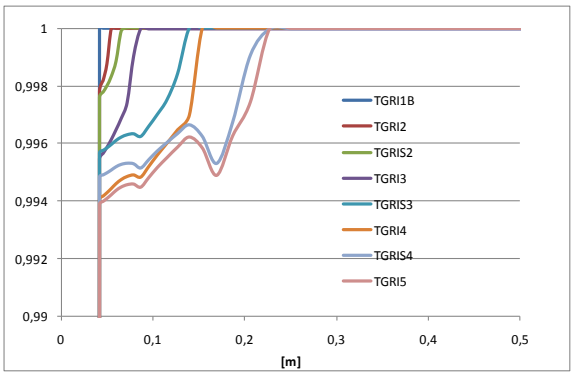

Figure 91 – Liquid Saturation at several times along L_h.

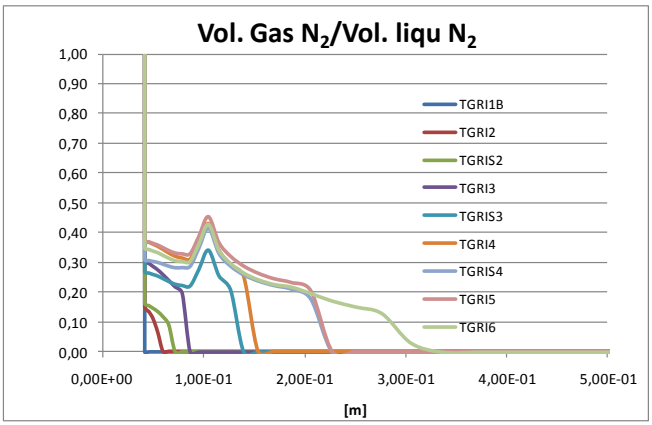

Figure 92 – Gas/liquid ratio of Nitrogen at several times along L_h.

4.2.6 Goal of the borehole damage zone

The BDZ is now introduced according to hypothesis defined in 4.2.4. Figure 93 shows pressure evolution in interval 2.

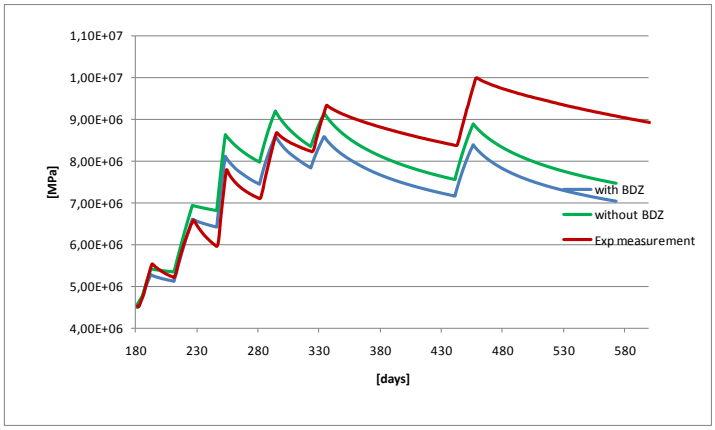

Figure 93 – Gas pressure evolution in interval 2 : goal of BDZ.

We can observe that results with or without BDZ differ very weakly until 230 days. In this part, we can suppose that injection chamber behavior plays the main role and that water removal is the major phenomena. After 230 days, the results obtained with BDZ are better than those without: this damage zone seems to play an important role. Results are in very good agreement with experimental results until the begin of third injection step, after they differ. Nevertheless, after this, differences between results with and without BDZ seem to remain more or less constant.

4.2.7 Goal of gas permeability in host rock

As written previously and according to several experimental results, we take for argillite a coefficient C_k for gas permeability law. This law is not precisely known and we propose here a sensitive For that, we change the cubic law in the undisturbed host rock by a quadratic law: $k_r^g = C_k(1-S_l)^4$.

In BDZ, the relative permeability remains a cubic law. All the other data are the same than previous.

According to Figure 94 we observe that this parameter is not influent for the 4 first steps of injection. After that differences are significant. We can interpret that, according with time, each material is successively predominant: Injection chamber then BDZ and finally undisturbed host rock.

4.2.8 Conclusions of PGZ1 modeling

This contribution proposes a numerical modeling of a field scale test with a classical coupled two-phase flow model. The major difficulty in experience modelling is finally to understand and capture what happens in the instrumentation process and not only as far as the undisturbed clay is concerned. Indeed, it seems that different materials successively play a role: injection chamber and water displacement, borehole damage zone and at least undisturbed host rock. In both simulations and experimental results, we observe that the gas influence zone is very small and close to injection chamber. PGZ1 test is still in process.

We can see that even for PGZ1 (expected as a test in a undisturbed host rock), damage zone plays an important goal. This zone is complex to estimate a priori because not only due to digging. A better characterization this of damage zone (succion, gas permeability, etc.) seems to be necessary to obtain a better fit of experimental results and predictive computations.

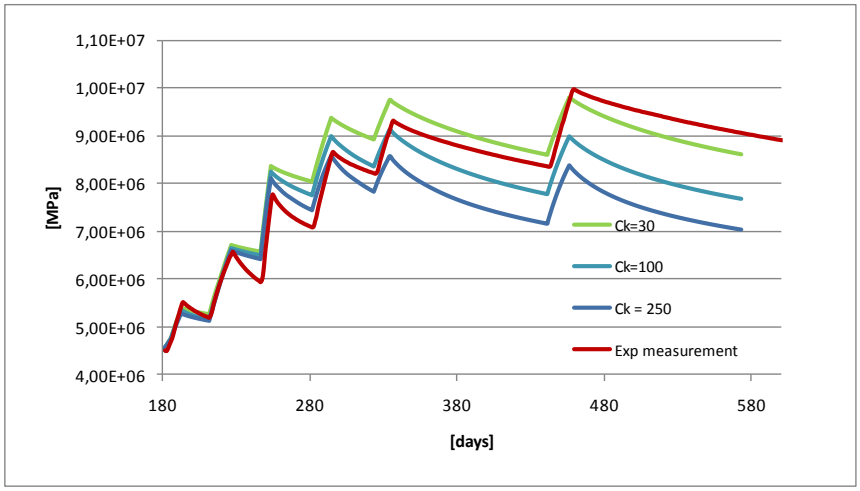

Figure 94 – Gas pressure evolution in interval 2: goal of relative permeability in host rock.

4.3 GAS MIGRATION IN OPALINUS/COX (ULG)

4.3.1 Mechanisms of gas transfers in clayey materials

In a clay-based material, four primary phenomenological models describing gas flow are considered (Marschall et al., 2005): (i) gas movement by diffusion and/or solution within interstitial fluids along prevailing hydraulic gradients; (ii) gas flow in the original porosity of the fabric, commonly referred to visco-capillary (or two-phase) flow; (iii) gas flow along localised dilatant pathways which may or may not interact with the continuum stress field; (iv) gas fracturing of the rock similar to that performed during hydrocarbon stimulation exercises.

The ULg contribution in the Forge project is mainly based on the hydro-mechanical modelling (with finite element code Lagamine) of laboratory and field scale experiments highlighting the first three mechanisms of gas transfers.

To reproduce gas movement by diffusion or by visco-capillary effects, a two-phase flow model is defined. This model consists of a liquid phase, composed of liquid water and dissolved gas and a gaseous phase, which is an ideal mixture of dry gas and water vapour. It takes into account the advection of each phase using the Darcy's law and the diffusion of the components within each phase (Fick's law). In the model a distinction between the water permeability in saturated conditions and the gas permeability in dried conditions is assumed, and permeability anisotropy can be defined (see Charlier et al., 2012 or Forge deliverables D4.5 and D5.5 for more details).

When gas pressure increases, gas migration can be associated with the development of gas preferential paths along existing or pressure-dependent discontinuities. A hydro-mechanical coupling between the pathways aperture, permeability and air entry pressure is proposed to explain the development of gas localised pathways. Such a model is based on the ideas of the "embedded fracture model" proposed by Olivella & Alonso (2008). More details about the model development can be obtained in the next section.

An anisotropic non-associated linear elastic-perfectly plastic model (with Drucker-Prager yield surface) is also assumed to reproduce the mechanical behaviour of the porous media. The extent to the anisotropy of a non-associated elasto-plastic model is also one of the model development proposed by ULg in the frame of the Forge project.

4.3.2 Model development

4.3.2.1 Mechanical model

The model uses elastic cross-anisotropy coupled with an extended Drucker-Prager hardening plasticity model. The plastic yield limit considers that the material cohesion depends on the angle between major principal stress and the bedding orientation.

The elasto-plasticity principle (concept of a loading surface f in the stress space which limits the region of elastic deformation) allows that the total strain rate $\dot{\varepsilon}_{ij}$ be split into elastic $\dot{\varepsilon}_{ij}^{e}$ and plastic $\dot{\varepsilon}_{ij}^{p}$ components:

$$\dot{\varepsilon}_{ij} = \dot{\varepsilon}_{ij}^{e} + \dot{\varepsilon}_{ij}^{p} \tag{1}$$

Because of elastic anisotropy, the elasto-plastic stress-strain relations are more convenient to be expressed in the anisotropic axis, as indicated by the star in exponent ($\sigma_{ij}'^{*}$ and ε_{ij}^{*})

$$\dot{\sigma}_{ij}'^{*} = C_{ijkl}\dot{\varepsilon}_{kl}^{*} \tag{2}$$

where C_{ijkl} is the elasto-plastic constitutive matrix.

In the more general situation, the reference axes do not coincide with the axes of anisotropy and the expression of $\sigma_{ij}'^{*}$ and ε_{ij}^{*} can be obtained from σ_{ij}' and ε_{ij} expressed in the system of reference through the following transformation:

$$\sigma_{ij}'^{*} = R_{ki}R_{lj}\sigma_{kl}' \quad ; \quad \varepsilon_{ij}^{*} = R_{ki}R_{lj}\varepsilon_{kl} \tag{3}$$

where R_{ij} is the ij component of the rotation matrix:

$$R = \begin{bmatrix} \cos\alpha\cos\varphi & \sin\alpha\cos\varphi & \sin\varphi \\ -\sin\alpha\cos\theta - \sin\theta\sin\varphi\cos\alpha & \cos\alpha\cos\theta - \sin\theta\sin\varphi\sin\alpha & \sin\theta\cos\varphi \\ \sin\theta\sin\alpha - \cos\alpha\sin\varphi\cos\theta & -\sin\varphi\sin\alpha\cos\theta - \sin\theta\cos\alpha & \cos\varphi\cos\theta \end{bmatrix} \tag{4}$$

in which α is the rotation angle around the axes $\underline{E}_3$ (rotation in the $(\underline{E}_1, \underline{E}_2)$) plane, the angles φ and θ define the rotation around the axes $\underline{e}'_2$ and $\underline{e}_1$, respectively (Figure 95). The positive direction of rotation is counter-clockwise. $(\underline{E}_1, \underline{E}_2, \underline{E}_3)$ and $(\underline{e}_1, \underline{e}_2, \underline{e}_3)$ are the reference axes and the anisotropic axes, respectively.

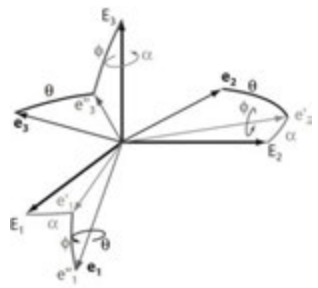

Figure 95: Transformation of the global axis $(\underline{E}_1, \underline{E}_2, \underline{E}_3)$ into anisotropic axes $(\underline{e}_1, \underline{e}_2, \underline{e}_3)$.

At the end of each step of computation, the stress and strain obtained in the anisotropic axes (σ'^{*}_{ij} and ε^{*}_{ij}) are re-transformed to be expressed in the global axes (σ'_{ij} and ε_{ij}):

$$\sigma'_{ij} = R_{ik} R_{jl} \sigma'^{*}_{kl} \quad ; \quad \varepsilon_{ij} = R_{ik} R_{jl} \varepsilon^{*}_{kl} \tag{5}$$

Elastic anisotropy

$\dot{\varepsilon}^{*e}_{ij}$ is the ij strain rate component that does not modify the hardening state of the material. $\dot{\varepsilon}^{*e}_{ij}$ is linked to stress rate through the Hooke law :

$$\dot{\varepsilon}^{*e}_{ij} = D^{e}_{ijkl} \dot{\sigma}'^{*}_{kl} \tag{6}$$

The D^{e}_{ijkl} matrix considers anisotropic elasticity. Considering the requirement of symmetry of the stiffness matrix, the anisotropic elasticity needs a maximum of 21 independent parameters to be fully described. However, axes of symmetry in the structure of many materials limit the number of independent parameters. Then, an anisotropy induced by three orthogonal structural directions, usually called *orthotropy,* requires 9 parameters to define the elastic matrix. It results that by inversing the matrix D^{e}_{ijkl} the elastic relation becomes:

$$\dot{\sigma}'^{*}_{ij} = C^{e}_{ijkl} \dot{\varepsilon}^{*e}_{kl} \tag{7}$$

with

$$C^{e}_{ijkl} = \begin{bmatrix} \frac{1-\nu_{23}\nu_{32}}{E_2 E_3 \det} & \frac{\nu_{21}+\nu_{31}\nu_{23}}{E_2 E_3 \det} & \frac{\nu_{21}\nu_{32}+\nu_{31}}{E_2 E_3 \det} & & & \\ \frac{\nu_{12}+\nu_{13}\nu_{32}}{E_1 E_3 \det} & \frac{1-\nu_{13}\nu_{31}}{E_1 E_3 \det} & \frac{\nu_{32}+\nu_{31}\nu_{12}}{E_1 E_3 \det} & & & \\ \frac{\nu_{13}+\nu_{23}\nu_{12}}{E_1 E_2 \det} & \frac{\nu_{23}+\nu_{21}\nu_{13}}{E_1 E_2 \det} & \frac{1-\nu_{21}\nu_{12}}{E_1 E_2 \det} & & & \\ & & & 2G_{12} & & \\ & & & & 2G_{13} & \\ & & & & & 2G_{23} \end{bmatrix} \tag{8}$$

and $\det = \frac{1-\nu_{31}\nu_{13}-\nu_{21}\nu_{12}-\nu_{32}\nu_{23}-2\nu_{31}\nu_{12}\nu_{23}}{E_1 E_2 E_3}$, assuming $\frac{\nu_{21}}{E_2} = \frac{\nu_{12}}{E_1}$; $\frac{\nu_{31}}{E_3} = \frac{\nu_{13}}{E_1}$; $\frac{\nu_{23}}{E_2} = \frac{\nu_{32}}{E_3}$.

Sedimentary rocks show usually a more limited form of anisotropy. The behaviour is isotropic in the plane of bedding and the unique direction of anisotropy is perpendicular to bedding. The properties of such materials are independent of rotation about an axis of symmetry normal to the bedding plane (Graham and Houlsby, 1982). This type of elastic anisotropy, called *transverse isotropy* or *cross-anisotropy*, requires 5 independent parameters and is a particular case of Equations (6) and (8) for which:

$$E_1 = E_2 = E_{//} \qquad \nu_{12} = \nu_{21} = \nu_{//,//} \qquad G_{13} = G_{23} = G_{//,\perp}$$
$$E_3 = E_{\perp} \qquad \nu_{13} = \nu_{23} = \nu_{//,\perp} \qquad G_{12} = G_{//,//} = \frac{E_{//}}{2\left(1+\nu_{//,//}\right)} \tag{9}$$

where the subscripts // and ⊥ indicate, respectively, the direction parallel to bedding (directions 1 and 2) and perpendicular to bedding (direction 3).

Plastic anisotropy

The limit between the elastic and the plastic domain is represented by a yield surface in the principal stress space. This surface corresponds to the Drucker-Prager yield surface f (Drucker and Prager, 1952):

$$f \equiv II_{\hat{\sigma}} - m\left(I_{\sigma} - \frac{3c}{\tan\phi}\right) = 0 \tag{10}$$

with $m = \dfrac{2\sin\phi}{\sqrt{3}\left(3-\sin\phi\right)}$. I_{σ} and $II_{\hat{\sigma}}$ are the first stress tensor invariant and the second deviatoric stress tensor invariant, respectively:

$$I_{\sigma} = \sigma'^{*}_{ii}\,,\; II_{\hat{\sigma}} = \sqrt{\frac{1}{2}\hat{\sigma}'^{*}_{ij}\hat{\sigma}'^{*}_{ij}} \quad ; \quad \hat{\sigma}'^{*}_{ij} = \sigma'^{*}_{ij} - \frac{I_{\sigma}}{3}\delta_{ij}\,.$$

The criterion assumes that the strength of materials varies according to the orientation of the principal compressive stress with respect to the bedding plane orientation. Anisotropy of material cohesion depends on the angle between major principal stress and the normal to the bedding plane following experimental observations of Niandou et al. (1997) or failure criteria proposed for sedimentary rocks by Duveau et al. (1998), Pietruszczak and Mroz (2001) and Pietruszczak et al. (2002). Then, three cohesion values are defined, for major principal stress parallel ($\alpha_{\sigma_1} = 0°$), perpendicular ($\alpha_{\sigma_1} = 90°$) and with an angle of 45° ($\alpha_{\sigma_1} = 45°$) with respect to the normal to bedding plane. Between those values, cohesion varies linearly with α_{σ_1}. The mathematical expression of the cohesion is as follows (Figure 96):

$$c = \max\left[\left(\frac{c_{45°} - c_{0°}}{45°}\right)\alpha_{\sigma_1} + c_{0°}\;;\;\left(\frac{c_{45°} - c_{0°}}{45°}\right)\left(\alpha_{\sigma_1} - 45°\right) + c_{45°}\right] \tag{11}$$

with α_{σ_1} being the angle between the normal to the bedding plane $\vec{n}$ and the major principal stress $\vec{\sigma}_1$: $\alpha_{\sigma_1} = \arccos\left(\dfrac{\vec{n}.\vec{\sigma}'_1}{\|\vec{n}\|\|\vec{\sigma}'_1\|}\right)$.

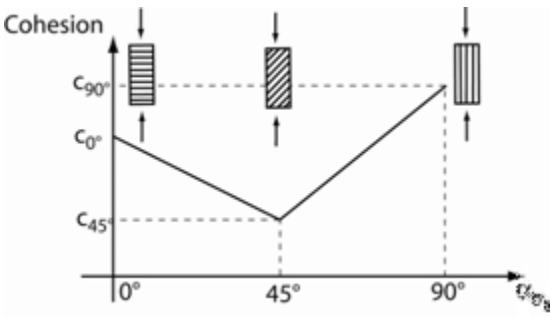

Figure 96: Schematic view of the cohesion evolution as a function of the angle between the normal vector to bedding plane and the direction of major principal stress.

In addition, a general non-associated plasticity framework is considered and the model allows hardening/softening processes during plastic flow as described in (Barnichon 1998).

4.3.2.2 EMBEDDED FRACTURE MODEL

To reproduce the development of conductive gas pathways in argillite when gas pressure increases, an additional hydro-mechanical coupling is introduced in the model. An evolution of the permeability as well as the air entry pressure with the strain is proposed on the basis of the "embedded fracture model" (Olivella & Alonso, 2008). The basic idea of this model is based on the appropriate representation of single fractures embedded in a continuous finite element matrix. These fractures are generated on tensile stress paths and are characterized by their aperture *b*. Permeability along the fracture K_{ij} increases with the opening of these features, whilst the air entry pressure P_r decreases.

A threshold strain corresponding to a maximal opening of the fracture is nevertheless added in comparison with the original model proposed by Olivella & Alonso (2008). In the finite element code, this aperture is linked with the strains in the discontinuities. The permeability-strain and air entry pressure-strain relationships can thus be written:

$$K_{ij} = K_{matrix} + K_0 \left(1 + \lambda \left(\langle \varepsilon_n - \varepsilon_0 \rangle\right)\right)^3 \left(\delta_{ij} - n_j n_i\right) \tag{12}$$

$$P_r = P_{r,0} \frac{1}{1 + \lambda \left(\langle \varepsilon_n - \varepsilon_0 \rangle\right)} \tag{13}$$

with $\langle \varepsilon_n - \varepsilon_0 \rangle = \begin{cases} 0 & \text{si } \varepsilon_n < \varepsilon_0 \\ \varepsilon_n - \varepsilon_0 & \text{si } \varepsilon_0 \le \varepsilon_n \le \varepsilon_1 \\ \varepsilon_1 - \varepsilon_0 & \text{si } \varepsilon_n > \varepsilon_1 \end{cases}$

and with ε_n the normal strain to the fracture, ε_0 the threshold strain required to initiate fracture opening, ε_1 a "maximal opening" threshold strain, λ a parameter reflecting the density of fractures and the rugosity, K_{matrix} the permeability of the undisturbed argillite, K_0 the initial permeability along the fracture and $\underline{n}$ the normal to the fracture (considered parallel to the maximum principal strain ε_1).

Two cases have to be considered according to the sign of the threshold strain:

- No fracture exists initially in the sample (b_0 = 0). Fracture opening is associated with stress paths reaching the tensile strength of the material. The "opening" threshold strain ε_0 is thus a tensile strain ($\varepsilon_0 < 0$) (Figure 97 (a)).
- Fracture opening can be also explained by the re-opening of pre-existing fractures ($b_0 > 0$). Considering the entire history of the test, these fractures could be closed by the confining pressure ($\Delta\varepsilon > 0$) which the sample is submitted to. Increasing the gas pressure involves extension of the sample ($\Delta\varepsilon < 0$). Strain state can thus reach a compressive "opening" threshold strain ($\varepsilon_0 > 0$) and provokes the re-opening of pre-existing fractures, without necessarily developing tension stresses in the sample (Figure 97(b)).

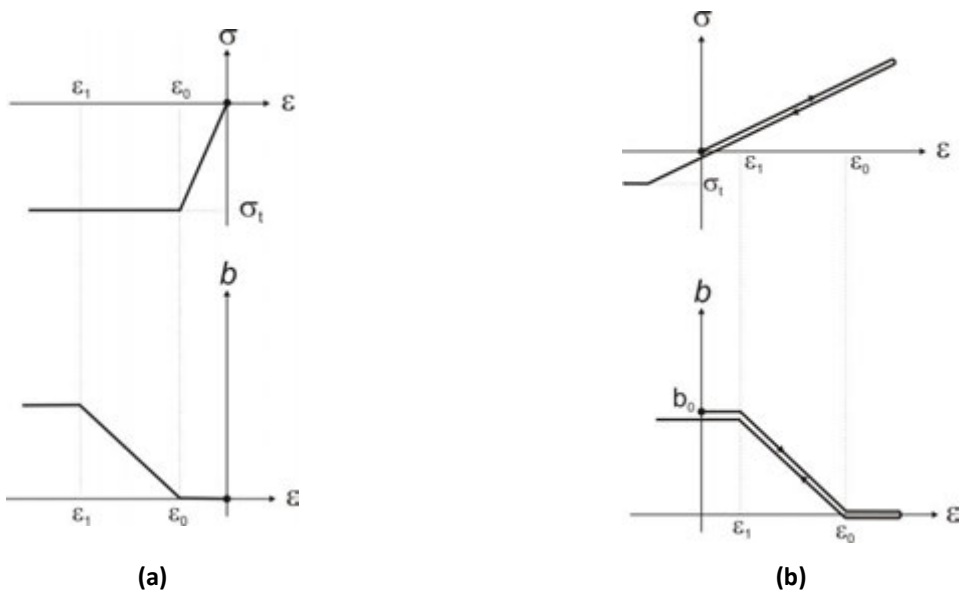

Figure 97: Evolution of fracture aperture with strains (a) in a potentially fractured rock and (b) in an initially fractured rock.

Initially this model has been applied successfully in the modelling of gas injection tests where the samples are submitted to triaxial conditions. Such a simulation highlights the sudden increase in gas permeability induced by sample shearing (Olivella & Alonso 2008). Moreover the embedded fracture model offers also good capabilities to reproduce the permeability evolution at the interfaces between two materials as a response to stress and strain changes (see Lasgit experiment modelling, Olivella & Alonso 2008). In Forge project, this model is used by ULg to reproduce numerically the development of gas pathways in laboratory experiments where the boundary conditions avoid the development of tensile or shear stresses in the sample. The model developments proposed above allow the gas migration through conductive pathways if the threshold strain ε_0 is assumed as a compressive strain.

4.3.3 Modellings results

ULg is involved in the modelling of several experiments, from the laboratory to field scale. The experiments are also performed in the frame of the Forge project. Three modelling results are presented in this document:

- The 2D hydro-mechanical modelling of the drilling and the ventilation of a cavity in Opalinus Clay (HGA experiment in Mont-Terri URL performed by Nagra). This modelling highlights the key roles played by anisotropy on Opalinus Clay behaviour.
- The 1D and 3D hydraulic modelling of a field scale gas injection test in Callovo-Oxfordian argillite (PGZ1 experiment in Meuse/Haute-Marne URL performed by Andra). This modelling highlights how a predictive two-phase flow model could reproduce successfully a large scale gas injection experiment.
- The 2D hydro-mechanical modelling of a laboratory gas injection test, performed by the British Geological Survey (BGS). This modelling highlights how hydro-mechanical couplings are necessary to reproduce the development of conductive gas pathways in claystone.

4.3.3.1 Opalinus Clay: HGA – Drilling and ventilation modelling

HGA experiment is a tunnel of 13m in length and 1.035m in diameter drilled in Opalinus Clay in Mont-Terri URL to investigate the hydro-mechanical evolution of a backfilled and sealed tunnel section (Trick et al. 2007). In particular, the goals concern (1) the understanding of the Excavated Damaged Zone (EDZ) generation and evolution in Opalinus Clay, (2) the upscaling of hydraulic conductivity determination from the lab test to the tunnel scale, (3) the investigation of self-sealing processes and (4) the estimation of gas leakage rates.

To model the hydro-mechanical behaviour of Opalinus Clay observed around the gallery during the drilling and the ventilation phases, a 2D plane strain approach has been developed in the finite element code Lagamine from Université de Liège. It consists in one week of excavation followed by 10 months of ventilation. Ventilation is put in place with a relative humidity RH = 83% and a temperature T = 13°C in average. To reproduce gallery ventilation, pore water pressure is linearly decreased from 0 to a given suction in 7 days and then a constant pressure is maintained at -23.8 MPa. In this model, four sources of anisotropy govern OPA behaviour: in-situ stress, elastic modulus, failure criterion and water permeability. The dependency of the shear strength with the bedding orientation is considered through an extended Drucker-Prager model with an anisotropic cohesion.

The modelling of HGA microtunnel excavation and ventilation has shown that the hydro-mechanical response of the Opalinus Clay around excavation is fully governed by the four sources of anisotropy, keeping quite complex its global response. Nevertheless, good agreements with available in-situ measurements in term of displacement and water pressure evolutions can be obtained by also considering a damaged zone (EDZ) around HGA microtunnel in numerical analysis. Based on plastic indicator PI field around the tunnel, an elliptic EDZ is expected (defined by PI > 0.5 or half-larger axis equals to 1.05m and half-smaller axis equals 0.6m). This EDZ amplifies hydro-mechanical effects: tunnel convergence is higher and water pressure and suction fields increase after ventilation phase (Figure 98). Model calibration on available in-situ measurements indicates that parameters have to be significantly modified in EDZ because of strong damage effects in Opalinus Clay: Young moduli have to be divided by 10, permeabilities have to be multiplied by 10^5 (Figure 99). However, these modifications are not unrealistic for Opalinus Clay if we refer to what has been observed on SELFRAC experiment (Bernier et al. 2007).

Furthermore, the presence of EDZ combined with clay anisotropies permits to justify the observed damage (Figure 100). Horizontally, damage can be related to stress concentration providing plasticity and larger water pressures evolutions. At 45°, damage results from hydraulic effects during ventilation when the gradient of saturation degree strongly decreases. Moreover, on the top of the microtunnel, the presence of a tectonic fault provides additional stress concentrations that amplify the damage.

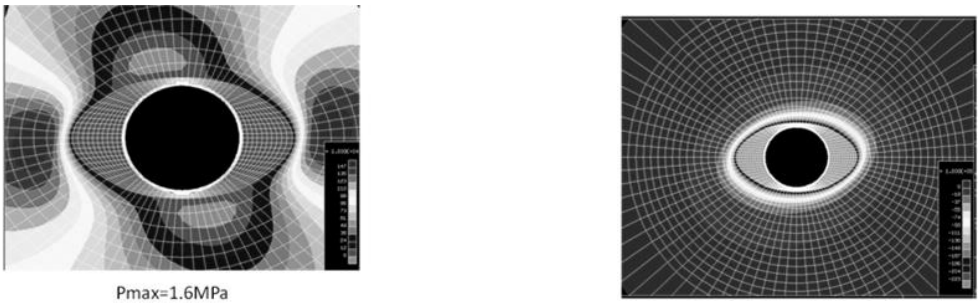

(a) water pressure **(b) suction**

Figure 98: Water pressure and suction fields after ventilation phase.

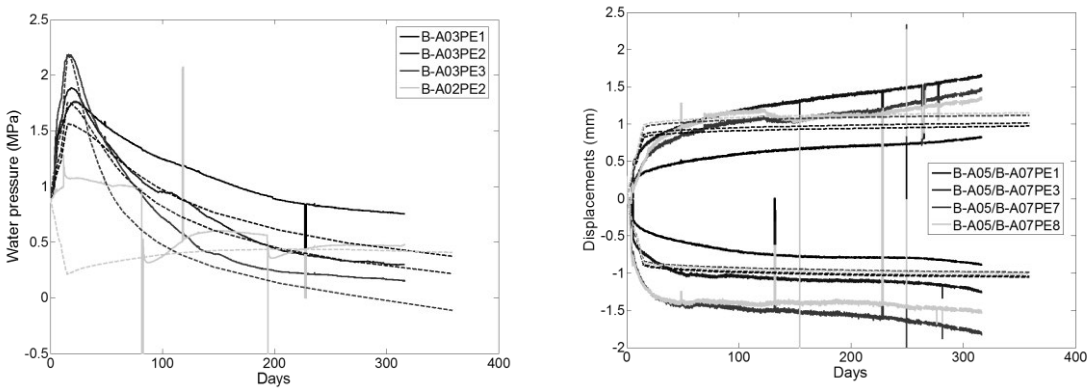

Figure 99: Water pressure and displacement evolutions with time.

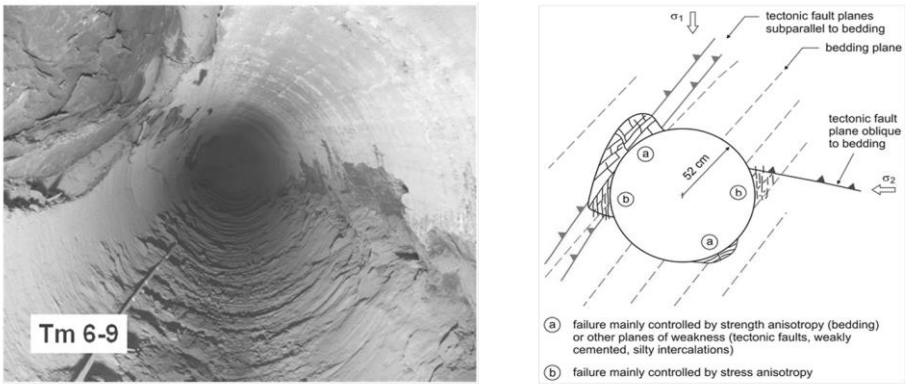

Figure 100: Damage observed in situ in HGA microtunnel.

Then, the modelling of HGA field-scale experiment has shown that hydro-mechanical response of the Opalinus Clay around excavation is strongly governed by 4 sources of anisotropy: in-situ stress, elastic modulus, failure criterion and water permeability. But these anisotropies are not sufficient to explain in situ observations. Displacements and water pressure fields are affected by a damaged zone that develops around HGA borehole. An EDZ yields to larger overpressures at the interface between EDZ and undamaged zone and a realistic delay in water pressure evolution after excavation. Then, the proposed 2D modelling is very relevant on Opalinus Clay hydro-mechanical behaviour characterization.

4.3.3.2 COX: PGZ1 – LARGE SCALE GAS INJECTION TEST MODELLING

To address the issues of gas transfer mechanisms in claystone, the French national Agency for the management of radioactive waste (Andra) has directed a field scale experiment examining the mechanisms controlling gas entry and gas migration in the Callovo-Oxfordian (COx) clay, the proposed host rock of the French deep geological repository project. This experiment, called PGZ1, studies the migration of nitrogen in the host rock. Nitrogen is injected at different flow rates from an injection interval, interrupted by shut-in phases. Different sensors provide the temporal evolution of pore pressures in the injection interval and in the rock mass (see deliverables D5.4 and D5.9 or de La Vaissière et al., 2012 for more details about the experiment description).

A field data analysis has been first achieved by Andra, emphasizing the influence on the results of some parameters for which some uncertainties remain, as the injection interval volume or the volume of remaining water in the interval (de La Vaissière et al., 2012).

ULg is involved in the modelling of this field scale gas injection experiment. The geometry of the problem and the permeability anisotropy lead to perform 3D modelling. But in order to highlight clearly the influence of each component of the system without time-consuming approaches, 1D hydraulic modelling is first proposed. It focuses on the numerical results obtained in the injection interval where the increase of the pore pressures is the most significant. In agreement with the hydraulic data analysis, the numerical predictions show the importance to know and to take into account accurately each component of the experiment system, as the volume and the initial conditions in the injection interval (Figure 101(a)).

Nevertheless the knowledge of the interval characteristics is not sufficient to obtain satisfactory long-term numerical predictions. The presence of a disturbed zone around the boreholes could thus be defined in our numerical problem. The extent of the EDZ is assumed close to the radius of the borehole (4 cm), which corresponds to previous experimental observations (Bossart et al., 2002). In this damaged zone, a high permeability and a low air entry pressure are considered, which improves strongly the numerical results in the injection interval (Figure 101(b)). Finally, a modification of Callovo-Oxfordian argillite transfer parameters is proposed to avoid the underestimation of the long-term pore pressures. Even if the hydraulic characteristics of COx have been already determined in numerous laboratory or field experimental studies, few of them investigate the gas transfer properties close to the saturation, owing to the experimental difficulties to impose accurately high degree of saturation and to detect and measure very low gas permeability. Cubic law is thus usually considered as gas relative permeability function even if we could not verify its relevance in the quasi saturated domain, but other relationships exist as the Parker's one:

$$K_g = K_g^{dry} k_{r,g} = K_g^{dry} \sqrt{1 - S_{r,w}} \left(1 - S_{r,w}^{1/\lambda}\right)^{2\lambda} \tag{14}$$

With the Parker relationship (Figure 102(b)), a better reproduction of the experimental data is obtained, as shown on Figure 102(a).

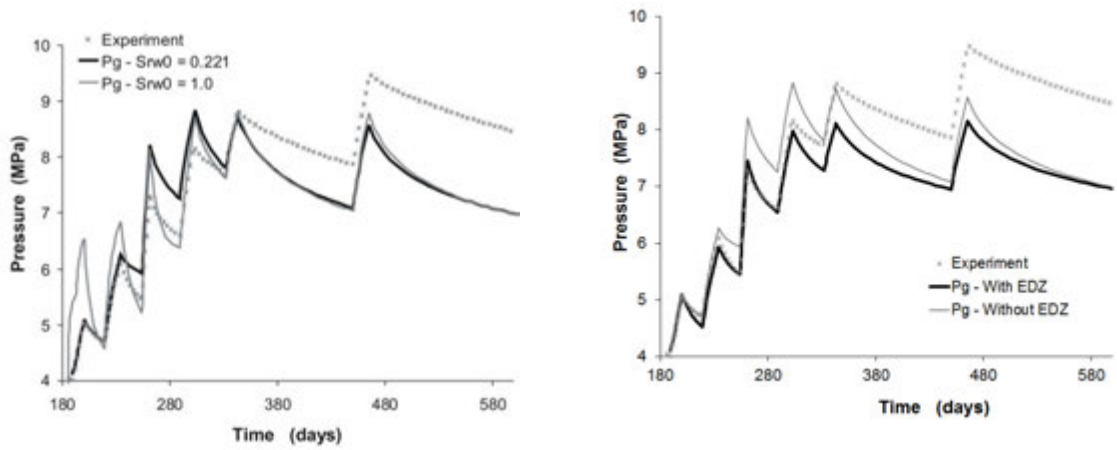

(a) (b)

Figure 101: Influence (a) of the initial degree of saturation in the injection interval and (b) of the presence of an excavated damaged zone around the borehole on the numerical results of the gas pressures in the injection interval.

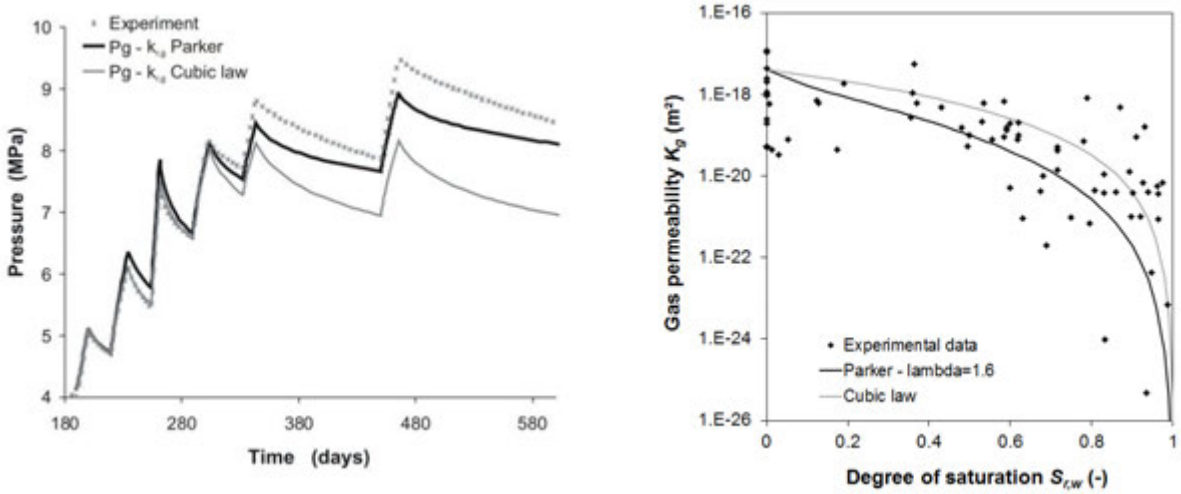

(a) (b)

Figure 102: (a) Influence of the gas relative permeability function of the undisturbed host rock on the numerical results of the gas pressures in the injection interval and (b) Gas permeability vs. Degree of saturation relationship tested.

From the successful 1D modelling, a set of parameters characterizing the behaviour of the injection interval, the excavated damaged zone and the undisturbed rock is used. These parameters are used in a 3D modelling of the problem, highlighting the role of the permeability anisotropy, the axial extent of the damaged zone along the borehole and the role of the axial flows. The numerical results show that the swelling of the packers (located between the measuring intervals) allows probably recovering the initial characteristics of the host rock in front of the measuring intervals. An EDZ must be thus considered only in front of the injection and measuring intervals. With these assumptions, the results in the injection interval are quite similar to those obtained in the 1D modelling (Figure 103), whereas the pore pressures evolution in the other sensors remain limited as observed experimentally (see Deliverable or de La Vaissière et al., 2013 for more details).

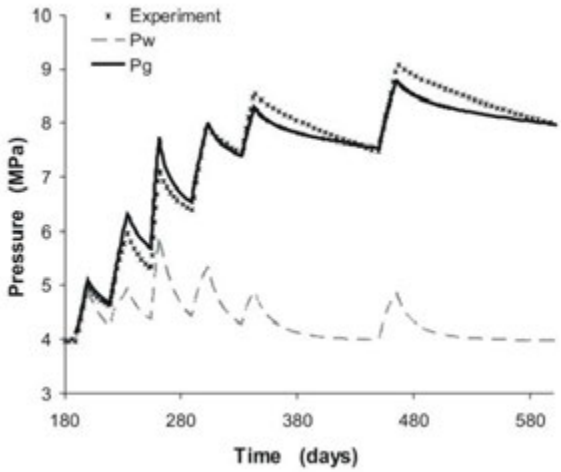

Figure 103: Time evolution of pore pressures in the injection interval – Comparisons between experimental and 3D numerical results.

In conclusion, this modelling task has shown that the experimental response does not characterize the rock mass behaviour at the beginning of the nitrogen injection, even though the experiment has been initially designed in order to study the gas transfers in a potential host rock for radioactive waste disposal. As confirmed by the gas flows profiles obtained from the best 1D modelling in a domain where the gaseous transfers are predominant (Figure 104), the first injection phase tests only the behaviour of the injection interval, whilst the response of the second and the third injection stages are also influenced by the excavated damaged zone. It is only from the fourth peak that nitrogen reaches the undisturbed claystone and the pore pressures measurements characterize thus its behaviour.

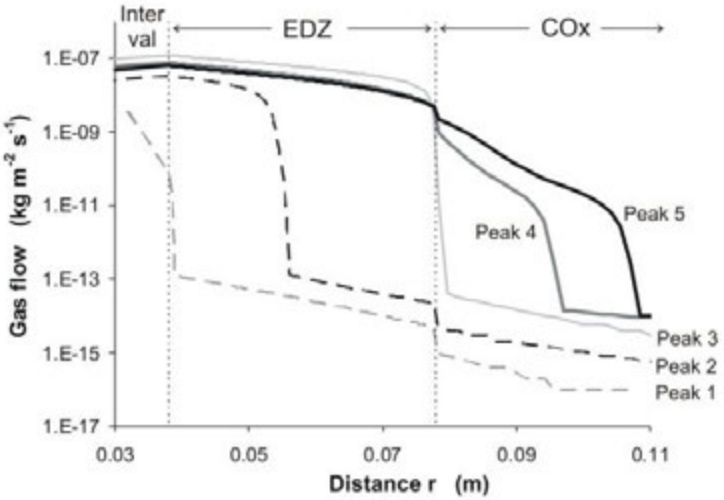

Figure 104: Gas flows profiles at different gas injection peak – 1D modelling.

Finally, such results show that a predictive model as two-phase flow approach is able to reproduce experimental observations in large scale system, as far as the injection flow rate and the gas pressures remain moderate. The influence of the gas permeability close to the saturation on the numerical predictions is also emphasized. Taking into account the development of gas preferential pathways is certainly a crucial issue in the description of laboratory experiment (see next section), but seems to be neglected for this part of the test. More generally, the PGZ1 experiment has shown that gas would remain mainly confined in the borehole disturbed zone. Even though gas penetrates in the undisturbed claystone, the quantities remain low and located near the injection interval with such gas injection conditions.

4.3.3.3 COX: LABORATORY GAS INJECTION TEST MODELLING

Long-term gas migration tests have been performed by the British Geological Survey on the COx, the proposed host rock for the French repository. Helium injection occurs through the base of the sample by slowly increasing gas pressure in a series of steps (from 6.5 to 12 MPa) and then decreasing stages (from 12 to 7 MPa), while outflow evolution is measured at the top. A backpressure of 4.5 MPa is continuously imposed at the top of the sample through the central filter and an isotropic confining stress of 12.5 MPa is maintained during the entire experiment. The argillite specimen has an initial diameter of 54.4 mm and a height of 53.9 mm. The orientation of the sample is perpendicular to the bedding plan. More details about the experiment conditions can be found in Harrington et al. (2012).

Results show first a small emergent flux during the early stages of testing, before a spontaneous increase of discharge rate after 170 days, which is interpreted as evidences of

major breakthrough. The movement of gas is then probably through a localised network of pathways, whose properties vary temporarily and spatially within the claystone (Harrington et al., 2012). In their entirety, these observations are difficult to explain with standard porous medium flow models and suggest that a strong hydro-mechanical coupling is therefore needed to adequately explain the formation and subsequent behaviour of gas conductive pathways within the Callovo-Oxfordian argillite.

A 2D axisymetrical model of the gas injection test is proposed with the extension of the "embedded fracture model" defined above. Evolution of permeability and air entry pressure is induced along a pre-existing fracture by changes in fracture aperture and its coupling with strain. This fracture is initially closed due to the high confining stress, but will be allowed to open as gas pressure in the sample increases (Figure 105).

The numerical results show the need for such hydro-mechanical models, in order to better reproduce the development of localised gas pathways in claystone. The main results of this study are:

- Two-phase flow model allows the reproduction of the small gas outflow noted during the first stages of testing, but is not sufficient to model the strong raise of the measured outflow during the breakthrough (Figure 106(a)).
- The spontaneous gas outflow observed after 170 days can be then reproduced with the proposed hydro-mechanical couplings. Pathway permeability increases and air entry pressure decreases with the extension induced by the experimental data, until the injection and backpressure platen are "gas connected". When this "gas connection" is reached, the numerical results show that it is necessary to consider that the aperture does not evolve any more despite the strain evolution in the discontinuities with the increase of the gas pressure. The "modified permeability" of the sample allows the reproduction of discharge rate observed during the last gas injection stages (Figure 107 (a) and (b)).
- In the "embedded fracture model", it is necessary to take into account the evolution of both permeability and air entry pressure with the strains when only permeability evolution is taken into account (Figure 106(b)).
- During the decreasing injection stages, the conductive pathways are progressively closed, but such calculations are subject to numerical difficulties and it is necessary to decrease the value of λ parameter (Figure 108(b)).
- The definition of the pre-existing fracture geometry is based on experimental evidences, but remains arbitrary. Modelling with other geometry of the pre-existing fracture have shown the ability of the model to reproduce localised pathways, but the set of parameters used must be adapted (Figure 108).

In conclusion, considering hydro-mechanical couplings has shown its relevance to interpret and explain gas migration mechanisms in claystone, but it does not consist in predictive modelling.

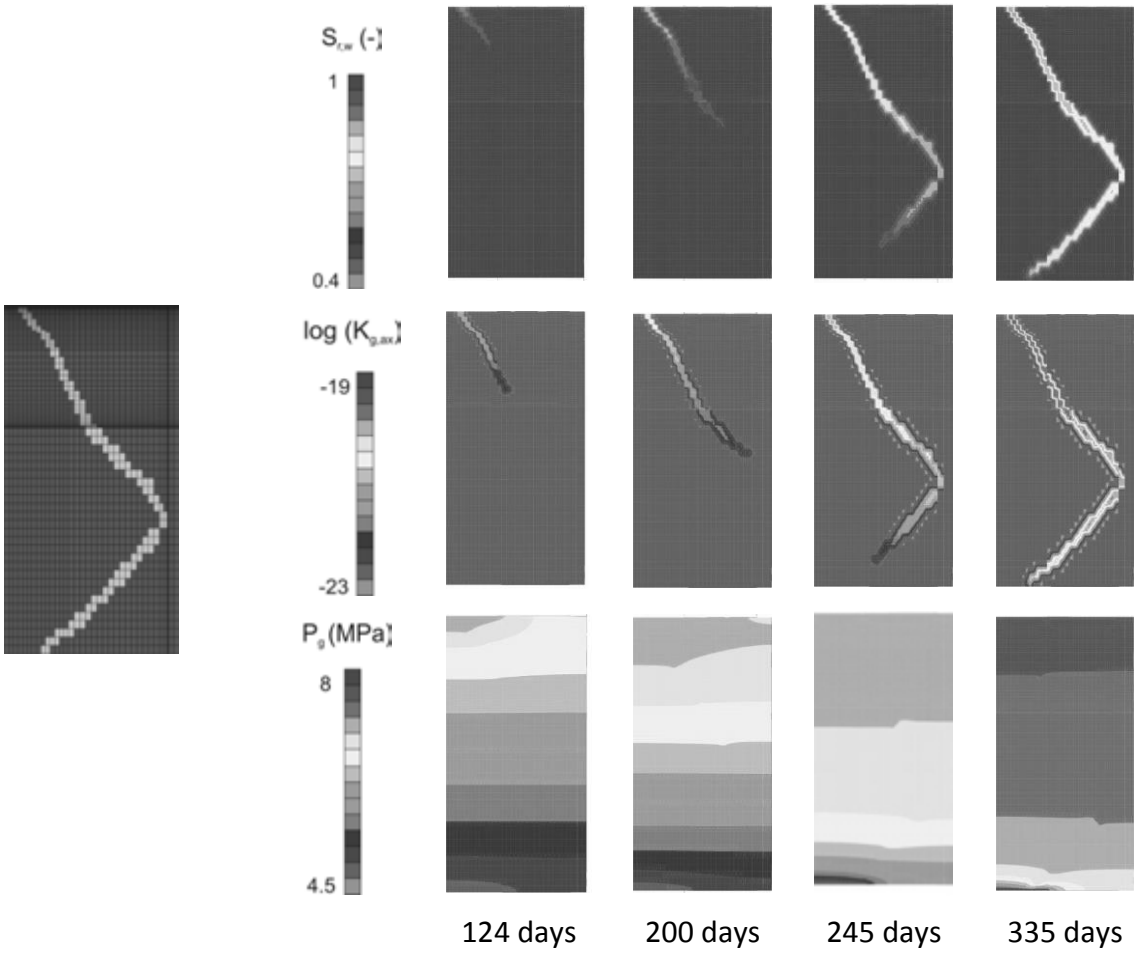

Figure 105: Pre-existing fracture and distribution of the degree of saturation, gas permeability and gas pressure at different increasing gas injection stages.

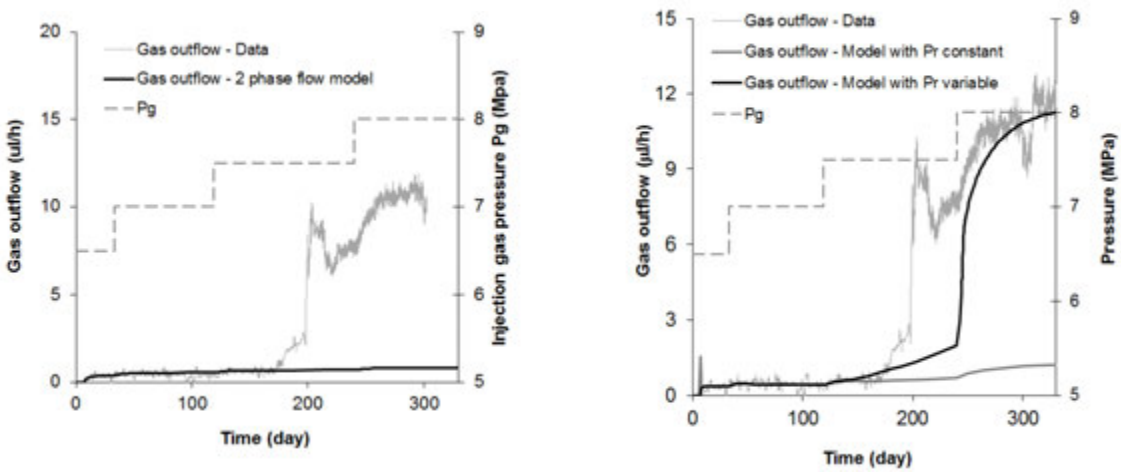

(a) (b)

Figure 106: Gas outflow: comparison between experimental and numerical results (a) with two-phase flow model and (b) with embedded fracture model with and without considering the evolution of air entry pressure.

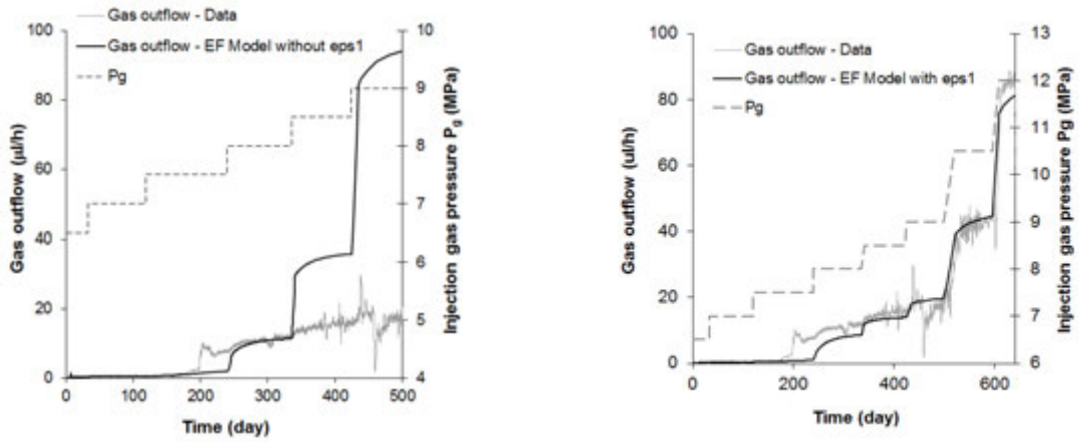

(a) (b)

Figure 107: Gas outflow: comparison between experimental and numerical results with embedded fracture model (a) without and (b) with considering the maximal opening threshold strain ε1 (ε0=6.4 10^{-4} - ε1=4.9 10^{-4} – Pr,0=5 MPa – λ=6700).

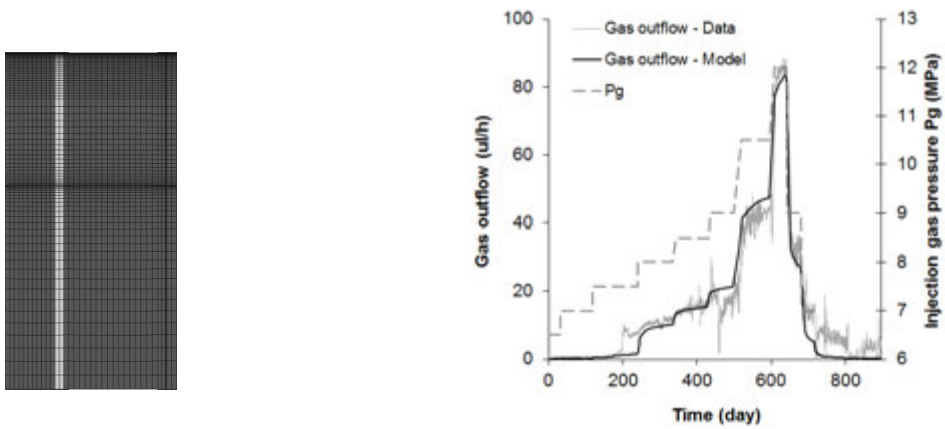

(a) (b)

Figure 108: (a) New pre-existing fracture geometry and (b) Gas outflow: comparison between experimental and numerical results with embedded fracture model for this new geometry (ε0=6.4 10^{-4} - ε1=4.9 10^{-4} – Pr,0=4MPa – λ=7000 for increasing stages and λ=4200 for decreasing stages).

4.3.4 Conclusions

An anisotropic hydro-mechanical model has been developed in the framework of FORGE project to take into account of couplings between the pathways aperture, permeability and air entry pressure and to explain the development of gas localised pathways. Following the idea of the "embedded fracture model" of Olivella & Alonso (2008), permeability and air entry pressure evolve in this model with strain in order to give an appropriate representation of single fractures embedded in a continuous finite element matrix.

Initially this model has been applied successfully in the modelling of gas injection tests where the samples are submitted to triaxial conditions. Such a simulation highlights the sudden increase in gas permeability induced by sample shearing (Olivella & Alonso 2008). Moreover the embedded fracture model offers good capabilities to reproduce the permeability evolution at the interfaces between two materials as a response to stress and strain changes (see Lasgit experiment modelling, Olivella & Alonso 2008). In Forge project, this model is used by ULg to reproduce numerically the development of gas pathways in laboratory experiments where the

boundary conditions avoid the development of tensile or shear stresses in the sample. The model developments proposed above allows the gas migration through conductive pathways if the threshold strain ε_0 is assumed as a compressive strain.

The modelling of laboratory tests or large scale experiments show that a predictive model as two-phase flow approach is able to reproduce experimental observations, as far as the injection flow rate and the gas pressures remain moderate. For laboratory experiment, gas probably progresses through a localised network of pathways, whose properties vary temporarily and spatially within the claystone. If these observations are difficult to explain with standard porous medium flow models, it is possible to well reproduce the development of localised gas pathways in claystone by introducing evolution of permeability and air entry pressure along a pre-existing fracture through changes in fracture aperture and its coupling with strain. Then, from fracture initially closed due to the high confining stress, they are allowed to open as gas pressure in the sample increases to form gas conductive pathways within argillite. On contrary, for large scale experiments, gas seems mainly confined in the borehole disturbed zone and even though gas penetrates in the undisturbed claystone, the quantities remain low and located near the injection interval with such gas injection conditions. Then, even if the hydraulic characteristics of COx can be determined in numerous laboratory or field experimental studies, few of them investigate the gas transfer properties close to the saturation, owing to the experimental difficulties to impose accurately high degree of saturation and to detect and measure very low gas permeability. Then, it is often necessary to re-calibrate parameters to avoid underestimation of the long-term pore pressures.

To conclude, anisotropic behaviour of argillite appears to be essential to well characterize hydromechanical couplings and to explain the formation and subsequent behaviour of gas conductive pathways within argillite. However, if taking into account the development of gas preferential pathways is certainly a crucial issue at laboratory scale, it seems to be negligible for the description of large scale test. Moreover, if the definition of the pre-existing fracture geometry at lab scale is based on experimental evidences, it remains arbitrary. Modelling with other geometries of the pre-existing fracture have shown the ability of the model to reproduce localised pathways, but the set of parameters used must be adapted. Finally, considering hydro-mechanical couplings has shown its relevance to interpret and explain gas migration mechanisms in claystone, but it has to be taken carefully in predictive modelling.

5. Discussion

5.1 GAS DIFFUSION

The movement of gas by diffusion will occur in all porous media as soon as gas is produced. Dedicated experiments focussing on the evaluation of gas diffusion coefficients in disturbed host rock formations were beyond the scope of FORGE, which was originally designed to address key issues associated with advective gas flow. While WP4 experiments were not specifically configured to measure gas diffusion behaviour, certain observations within the test programme can be attributed to the diffusion of gas. However, such phenomena are only relevant in long-duration tests and are invariably concept and material specific. For example, the EDZ in a fractured crystalline host rock may have a stronger influence on the direction and magnitude of diffusive gas flow than in clay-based repository systems exhibiting temporal self-sealing.

Outside of FORGE, a large number of experiments defining gas diffusion coefficients have been under taken. Nagra has commissioned many laboratory experiments on Opalinus Clay samples

with emphasis on the evaluation of gas diffusion processes (e.g. transient gas pressure decay experiments at RWTH Aachen [Poller et al. 2007], Mont Terri FM-C [Nagra 2002]; Mont Terri HT-experiment [Vinsot et al. 2012; NEA-Claytrac Project [Mazurek et al. 2009]). In addition, the gas diffusion properties of Boom Clay have also been extensively investigated. SCK•CEN have determined diffusion coefficients for both perpendicular (Jacops et al., 2012) and parrellel to bedding, defining an anisotropy ratio of between 0.62 and 0.58, depending on the type of gas used.

However, all of these measurements have been performed on intact (undamaged) samples. In the absence of direct experimental data, the role of the disturbed zone could be modelled using diffusion coefficients for the intact material and 'free' water in conjunction with an appropriate description of the 'fractured' medium.

5.2 TWO-PHASE FLOW (WP4)

Two-phase flow conditions are encountered when gas invades a porous medium as a separate phase. This process is associated with the drainage of interstitial fluid as the non-wetting phase (gas) displaces the wetting phase (pore water). Flow is within the original inter-granular porosity resulting in an isovolumetric boundary condition[5]. In reviewing the data from this section, it should be acknowledged that the majority of tests were performed on intact rock specimens, reflecting the difficulties in obtaining representative 'damaged' material and the large matrix of tests that would be required to cover all 'disturbed' scenarios.

In Opalinus Clay, gas permeability tests performed on isostatic/triaxially stressed specimens provide evidence for the displacement of water by a gas phase (NTB 02-03, Marschall et al. 2005, Romero et al. 2012). Indirect evidence from microstructural analyses (Keller 2011), suggesting that (sparsely) connected systems of macro- and meso-pores exist in Opalinus Clay, which can be invaded by a gas phase. These observations support the hypothesis of classical two-phase flow.

Interpretation of the data from the PGZ field experiment performed by Andra at the Bure URL, indicates gas flow is initially focussed within the excavation damaged zone, which acts as a preferential pathway for gas. Numerical interpretation of PGZ appears to confirm the hypothesis of classical two-phase flow in the undisturbed host rock. However, the question of gas flow in disturbed host rock (EDZ) is very complex due to the difficulties of characterising this zone. To adequately model such behaviour, parameterisation of the EDZ (permeability/suction/damage) is necessary but likely to remain an unknown for most borehole scale field tests.

In contrast, experiments performed on undisturbed samples of Boom Clay by SCK•CEN have not yielded, as yet, evidence for the movement of gas by classical two-phase flow. SCK•CEN cite high gas entry pressures, no desaturation and the prevailing stress regime around a repository as arguments against classical two-phase flow. Similar observations were made for the gas injection phase of the HG-C experiment (WP5). Significant gas injection was only possible by exceeding a pressure threshold which probably corresponds to the minimum principle stress at the location. This is a strong indication that gas flow is accomplished by deformational effects.

[5] A coupled flow of a liquid and a gas phase can also take place in deformable media without an isovolumetric boundary condition. Thus, the term "two-phase flow" is sometimes used to describe this behaviour. However, in a strict sense, the term "two-phase flow" applies to the two-phase flow theory for porous media which is based on the assumption of a non-deformable medium used in the context report.

While considerable effort has been placed on examining the fundamental controls governing the advective movement of gas, definitive interpretation of the data to identify the underlying physics controlling gas flow, currently remains elusive. In part, this may stem from differences in experimental procedures, types of material, control of boundary conditions and terminology.

5.3 PATHWAY DILATANCY

Dilatant gas flow is taken to relate to the expansion/disruption of the inter-granular pores, where permeability is now a dependent function, related to the number of pathways in the plane normal to flow, together with the width and aperture distributions of these features. Evidence for the existence of dilatant flow stems from volume change of the sample at the onset of gas movement. This change in sample volume is in stark contrast to classical two-phase flow, which assumes an isovolumetric boundary condition. As in Section 4.3.3.3, the majority of laboratory tests have been performed on initially undisturbed samples.

Nagra has commissioned various laboratory tests aimed at exploring the regime of pathway dilation. However, as yet, clear evidence for dilatancy controlled gas flow has not been observed in the laboratory experiments (Romero et al. 2012). Additional laboratory tests have been commissioned outside of FORGE to further investigate this phenomenon. In contrast, recent field experiments (Mont Terri HG-C/HG-D) have provided indications for pathway dilation and self-sealing during gas testing (Marschall et al. 2005). Under these conditions, numerical simulations by GRS using TOUGH2, are not able to capture important aspects of transport in the pathway dilation regime. Under these conditions intrinsic permeability (assumed to be a material constant) is unable to fully describe gas flow where pathway aperture varies spatially and temporally. As such, GRS have found it necessary to include dilation in existing codes in order to model experimental data.

Laboratory experiments performed on samples of COx clearly demonstrate localised mechanical dilatancy at the onset of gas flow. This behaviour cannot be explained by the mechanical response of the sample to changes in effective stress alone. The clear correlation between dilation and outflow, along with no measureable desaturation of the sample after testing, provides strong evidence that dilatancy is a key process in the movement of gas in COx. Experimental observations indicate that these pathways are temporal in nature, evolve over time, are unstable, may heal, which can make re-initiation of flow difficult. A separate and independent study performed by LAEGO-ENSG (Cuss *et al.*,2013) observed similar behaviour with dilatancy occurring at the onset of gas flow.

Experiments undertaken by SCK•CEN on undisturbed and pre-fissured Boom Clay samples suggest dilatancy occurs during gas flow. Experiments injecting nano particles (Harrington et al., 2012) in a carrier gas (performed at BGS) provide direct evidence for the formation of dilatant pathways during gas flow. As with COx, dilatant pathways were very unstable after breakthrough (Jacops et al. 2013). While gas breakthrough occurred at a lower pressure in artificially fissured cores, there was no indication for gas flow along the plane of the pre-existing fracture. Further experiments will continue beyond FORGE investigating these processes further, including the influence of micro-fracture orientation to bedding. Unfortunately, at the time of writing, the field-scale experiment had yet to yield supportive evidence.

Analogue tests performed by BGS investigating the onset of gas flow in an EDZ also show the formation of localised dilatant pathways. The geometry of the features appears to vary between tests, suggesting the direction of gas flow in clay-filled (kaolinite) fractures is difficult to spatially predict. In loading and unloading cycles fracture transmissivity exhibits a high

degree of hysteresis, which suggests the complex stress history observed in the EDZ during the full life cycle of a repository is of fundamental importance.

Gas injection tests into disturbed host rock were analysed by GRS using numerical models. In the GS, HG-C, and HG-D experiments, gas entered the disturbed rock at pressures significantly below the expected minimum stress (gas entry around 1 – 2 MPa above atmospheric). Gas injection tests at elevated pressures indicated a marked permeability increase, when gas pressure exceeded the magnitude of normal stress on the bedding planes (around 4 MPa). The analysis showed no significant interaction between the liquid and gas phase indicating that the dilatant gas pathways were highly localised. The observed injection flows were described numerically by single-phase flow of gas. It was shown that the dilatant flow paths were not accessible to water during the following water injection phases. Possibly, the pore sizes of the gas pathways were very small so that water adsorption at mineral surfaces became significant and advective flow was impeded.

While there is clear evidence to support pathway dilation, a definitive description of flow processes has yet to be realised due to the paucity of available data.

5.4 GAS FRACTURING

This process is associated with the rapid build-up of gas pressures significantly above the minimum principle stress. In reality, the likelihood of gas pressure build-up to such high values is unlikely as the gas moves by diffusion and advection. Hydraulic frac tests have been performed by Nagra (GP-A experiment) though the focus of these was on the determination of *in situ* stress fields.

5.5 ROLE OF INTERFACES

5.5.1 EBS/host rock interfaces

Laboratory and in-situ experiments in clay-based systems support the hypothesis that interfaces within a repository are regions of stress redistribution and fabric disruption. Interfaces are likely to represent favourable pathways for gas flow when there is either a continuous pathway/plane of weakness along the interface or when the contact pressure (created by swelling and convergence) is less than the minimal principal stress. The HG-A experiment at Mont Terri is a typical example for the inter-dependence of the leakage rate and radial stress distribution around a sealed tunnel. However, such interfaces are not stable with time as also demonstrated in laboratory experiments performed on Boom Clay. In analogue tests (BGS), gas pathways along clay-filled interfaces continue to evolve after initial breakthrough with decreasing peak pressure with subsequent breakthrough events. A multitude of mechanisms may affect the gas transport capacity of an interface including stress and pore pressure conditions, stress history, orientation of the interface to the stress field, strains and hydro-chemical porewater-rock interactions (e.g. swelling, precipitation, filtration, erosion). Dedicated experiments have been conducted in the past to address the issue of interface opening/closure (within Bock et al., 2010).

The importance of interfaces is also recognised in crystalline host rock disposal concepts with experiments performed by CTU clearly demonstrating an increase in permeability of the EDZ in contrast to intact rock. The evolution of these features is likely to evolve temporally and spatially, though no direct observations were recorded as part of FORGE.

5.5.2 Treatment of interfaces in experiments

Considerable care and attention is taken by all experimentalists, either in the laboratory or field, to minimise/negate experimental interfaces. This includes elements in the design of experiments, methodologies, sample preparation, interpretation of data etc. Unless stated to the contrary, tests are designed to reflect realistic in situ conditions, with separate detailed bespoke tests specifically designed to interrogate the interfaces in water and gas flow.

5.6 SPATIAL UPSCALING

5.6.1 Upscaling of experimental results and understanding

Rigorous upscaling approaches for immiscible flow have been proposed in various geoscientific disciplines (Artus & Noetinger 2004, Hilfer & Helmig 2004, Jacobs & Gelhar 2004, Niessner & Helmig 2006, Stauffer et al. 2009, Neuweiler et al. 2010). All approaches are based on stochastic assessments of the spatial variability of an appropriate porosity/connectivity indicator. These approaches provide a solid theoretical framework, defining the model assumptions and the range of validity of the presented numerical/analytical solutions and the data generated in WP4 will help in this process.

For a given gas transport problem, the following methodology may be followed to provide the basis for process and parameterisation upscaling: (i) analysis of the relevant structural elements of the rock fabric along the composite gas flow path (identification of the scales of heterogeneity); (ii) characterisation of the multi-phase flow properties of the relevant structural elements of the composite flow path; (iii) perform, if possible, gas transport experiments on the scale of the composite gas flow path (e.g. laboratory tests, mock up experiments, *in-situ* tests).

However, in practice this may not be practical and system components may need to be reduced to individual elements and a phenomenological approach adopted[6]. Only with a full knowledge of the stress and gas flow boundary conditions (including temporal and spatial evolution/influence) will it be possible to understand and predict the real behaviour of gas at a repository scale. Either way, validation of model predictions to repository scales can be achieved using the following steps: (i) blind predictions based on lab tests; (ii) calibrated predictions from field data; (iii) final predictions and evaluation of results (based on all appropriate data).

This approach, once complete, can be scaled to natural flow boundary conditions based on a detailed characterisation and knowledge of the initial and boundary conditions at the appropriate repository scale. However, the validity of any theoretical framework has to be demonstrated explicitly (e.g. assumption of weak disorder, separation of scales, etc.).

5.6.2 Numerical upscaling

Experiments often show that “reality” is too complex to be fully captured by the available models. Upscaling in geological systems often requires ‘homogenisation’ which needs to be validated to have confidence in the output of the model. However, it is also important to recognise that models may not need to capture all observed behaviour, but only those directly relevant to the safety of a repository.

[6] Even for large-scale *in situ* experiments it is difficult to characterise, for example, local stress states due to on-going hydromechanical transients, which complicates interpretation of results.

5.6.3 Time upscaling

Assuming the approach outlined in 5.6 has been followed, simulations should be reliable for a wide range of gas source terms, with uncertainly analysis performed to provide additional confidence where required.

6. Conclusions

At the onset of FORGE the rationale of WP4 was to examine the evolution of the EDZ around the backfilled underground structures of a disposal/storage facility as a potential escape route for gases (and dissolved radionuclides). After repository closure, the evolution of the EDZ as a gas transport path is controlled by a variety of features, events and processes, such as the connectedness of EDZ fracture network, the resaturation of the repository nearfield, pore pressure recovery, build-up of swelling pressures in the clay-bearing EBS, rock creep in response to the local stress field and last, but not least, by the nature of the actual gas source term (gas generation rates, gas species). While previous EU projects such as SELFRAC, TIMODAZ and NF-PRO improved basic understanding of EDZ creation and evolution along selected stress paths, a paucity of data defining key HM responses remained, in particular those associated with unsaturated and saturated conditions. WP4 identified a number of issues including the evolution of sealing and gas migration during complex stress paths, fracture self-sealing, tunnel convergence, radionuclide displacement and possible repository over-pressuring. As common with other WP's, a combination of focussed laboratory, field and numerical simulation techniques were employed to develop process models in support of repository performance assessment (WP1). All experiments followed a similar approach, resaturating the sample/borehole before the injection of gas. It is important to acknowledge that obtaining representative 'damaged' material (both laboratory and field) is technically challenging and would require a large matrix of tests in order to cover all 'disturbed' scenarios. Within the timeframe of FORGE this ambition could never be fully realised, but our understanding of processes governing gas flow in the EDZ has significantly improved as a result of the project.

The movement of dissolved gas by diffusion in the liquid phase will occur in all porous media as soon as gas is produced. Gas diffusion occurs predominantly in the connected micro-, meso- and macropores of the intact host rock, whereas the contribution of the EDZ fractures to enhance diffusive gas transport capacity is limited. For this reason, dedicated experiments focussing on the evaluation of gas diffusion coefficients in disturbed host rock formations were not in the scope of FORGE, which was instead designed to address key issues associated with advective gas flow. Gas diffusion in the liquid phase is omnipresent in the WP4 experiments. Such phenomena are only relevant in small rock samples, because the Peclet number (ratio between advective and diffusive flow) is proportional to the travel distance through the specimen. Outside of FORGE, a large number of experiments defining gas diffusion coefficients in intact rock have been undertaken for a range of candidate repository materials.

Data from WP4 clearly demonstrates that gas flow is initially focussed within the excavation damaged zone (EDZ), the network of discrete EDZ fractures acting as a preferential pathway for gas migration. Within the EDZ, flow is seen to be highly localised along the largest EDZ fractures, exhibiting a complex inter-dependence between flow rate and the distribution of radial stress around tunnel. This zone is not stable over time, as demonstrated in laboratory experiments. Analogue tests with clay-filled interfaces (representing fractures) clearly demonstrate temporal evolution of the flow behaviour. A multitude of mechanisms may affect gas transport properties including stress and pore pressure conditions, stress history,

orientation of EDZ fractures to the stress field, strains and hydro-chemical porewater-rock interactions (e.g. swelling, precipitation, filtration, erosion).

However, interpretation of the data to elicit the fundamental processes governing gas flow in the EDZ is complex, due to the difficulties of characterising this zone. For laboratory experiments it has been difficult to reproduce EDZ damage and fully represent its behaviour (i.e. the anisotropic distribution of fractures around a tunnel). In the field, it has also been difficult to characterise the evolution in properties of the EDZ following closure (i.e. limited instrumentation in respect to localised phenomena; monitoring boreholes intersecting the EDZ will have their own corresponding damaged zone). Despite these challenges, significant progress has been made on understanding gas flow in the EDZ. However, incomplete descriptions of hydro-mechanical processes exist and can lead to non-unique interpretations of the data resulting in a limited predictive capability of the models.

In light of these observations, identification of the appropriate theoretical framework to describe gas flow in the EDZ is far from trivial. Numerical simulations based on two phase concepts are able to represent elements of the data by homogenisation and simplification of the system. However, the validity of such an approach to forward prediction of repository performance is restricted, because these concepts have a limited capability to mimic hydromechanical coupling evident in the data (e.g. pressure-dependence of porosity, permeability, entry pressure). Models have been developed that mimic dilatancy using a number of different approaches in order to better represent the data and to improve simulations. While current modelling approaches do not capture all the elements observed in the experimental data, they provide a powerful tool with which to test and verify conceptual models and theoretical frameworks used to describe these systems.

Upscaling of the EDZ related features and processes in time and space is another challenge. In practice, modelling the evolution of entire system may not be practical. Instead, it may be necessary to reduce the system to individual simplified elements and a phenomenological approach adopted. Only with a detailed knowledge of the stress state and gas flow boundary conditions together with a detailed description of the initial EDZ fracture network in terms of geometry and hydraulic characteristics will it be possible to understand and predict the real behaviour of gas at the repository scale. Partial validation of model predictions to repository scales can be achieved using the following steps: (i) blind predictions based on lab tests; (ii) calibrated predictions from field data; (iii) final predictions and evaluation of results (based on all appropriate data).

To improve our knowledge base and support model development, further testing and modeling validation are required. In particular additional laboratory and *in situ* tests should be undertaken to better characterise material behavior at a range of scales before, during and after the formation of the EDZ, providing additional data on the temporal evolution of system. In this regard, models should assist in the design of these tests and the data thereafter used to improve the constitutive models facilitating the inclusion, where appropriate, of additional relevant physical processes.

While considerable progress has been made on examining the fundamental controls governing the advective movement of gas in the EDZ, definitive interpretation of the data to identify the underlying physics controlling gas flow, remains elusive.

7. References

ADAMS, B.A., AND WULFSOHN, D. (1997) Variation of the critical-state boundaries of an agricultural soil. *European Journal of Soil Science*, **48**, pp.739-748.

ALCOVERRO, J., OLIVELLA, S., ALONSO, E.E. (2012a) Basic formulation for modelling water and gas flow through the EDZ. Application to HG-A in situ test. D4.12 Progress report – definition of constitutive laws and initial simulations. FORGE EU-FP7 PROJECT.

ALCOVERRO, J., ARNEDO, D., OLIVELLA, S., ALONSO, E.E. (2012b) Simulation results of the HG-A test D4.23 Final report – simulation results (HG-A). FORGE EU-FP7 PROJECT.

ANGELI, M., SOLDAL, M., SKURTVEIT, E., AND AKER, E. (2009) Experimental percolation of supercritical CO_2 through a caprock, *Energy Procedia*, 1, pp.3351-3358.

ASKARIEH, M.M., CHAMBERS, A.V., DABNIEL, F.B.D., FITZGERALD, P.L., HOLTOM, G.J., PILKINGTON, N.J. AND REES, J.H. (2000) The chemical and microbial degradation of cellulose in the near field of a repository for radioactive wastes. *Waste Management*, 20, 93-106.

AUTIO, J., GRIBI, P., JOHNSON, L. AND MARSCHALL, P. (2006) Effect of excavation damage zone on gas migration in a KBS-3H type repository at Olkiluotu. *Physics and Chemistry of the Earth*, 31, 649-653.

AZIZ, K. AND SETTARI, A. (1979) *Petroleum Reservoir Simulation*. Applied Science, London

BARNICHON, J.D. (1998) *Finite element modelling in structural and petroleum geology*. PhD Thesis, Université de Liège.

BARTON, C.A., ZOBACK, M.D. , MOOSE, D .(1995) Fluid flow along potentially active faults in crystalline rock. *Geology*, 23, no. 8, pp. 683-686.

Bernier F., Li X.L., Bastiaens W., Ortiz L., Van Geet M., Wouters L., et al. (2007) Fractures and self-healing within the excavation disturbed zone in clays (Selfrac). *Final report*, 5th EURATOM Framework Programme (1998 – 2002).

BLOCK, H, DEHANDSCHUTTER, B., MARTIN, C.D., MAZUREK, M., DE HALLER, A., SKOCZYLAS, F. AND DAVY, C. (2010) SELF-SEALING OF FRACTURES IN ARGILLACEOUS FORMATIONS IN THE CONTEXT OF GEOLOGICAL DISPOSAL OF RADIOACTIVE WASTE: REVIEW AND SYNTHESIS. NEA NO. 6184, OECD 2010. ISBN 978-92-64-99095-1.

BOSSART, P., MEIER, P.M., MOERI, A., TRICK, T., AND MAYOR, J-C. (2002) Geological and hydraulic characterisation of the excavation disturbed zone in the Opalinus Clay of the Mont Terri Rock Laboratory. *Engineering Geology*, 66, no. 1-2, p. 19-38.

BRUDY, M., ZOBACK, M.D., FUCHS, K., RUMMEL, F., AND BAUMGÄRTNER, J. (1997) Estimation of the complete stress tensor to 8 km depth in the KTB scientific drill holes: Implications for crustal strength. *Journal of Geophysical Research-Solid Earth*, 102, no. B8, p. 18453-18475.

BYERLEE, J.D. (1967) Frictional characteristics of granite under high confining pressure. *Journal of Geophysical Research*, 72, pp. 3639-3648.

COTECCHIA, F., AND CHANDLER, R.J. (2000) A general framework for the mechanical behaviour of clays. *Géotechnique*, 50, pp. 431-447.

CUSS, R.J. (1999) An experimental investigation of the mechanical behaviour of sandstones with reference to borehole stability. Ph.D. thesis, Manchester, UK, University of Manchester.

CUSS, R.J., HARRINGTON, J.F., GIOT, R., AND AUVRAY, C. (2013) Experimental observations of mechanical dilation at the onset of gas flow in Callovo-Oxfordian claystone. *Clays in Natural and Engineered Barriers for Radioactive Waste Confinement*. Geological Society Special Publications: London, United Kingdom, Geological Society of London.

CUSS, R.J., RUTTER, E.H., AND HOLLOWAY, R.F. (2003) The Application of Critical State Soil Mechanics to the Mechanical Behaviour of Sandstone. *International Journal of Rock Mechanics and Mining Sciences*, 40, pp. 847-862.

CUSS, R.J., SATHAR, S. AND HARRINGTON, J.F. (2012) Validation of critical stress theory applied to repository concepts. *British Geological Survey Commissioned Report*, CR/12/133. 59pp.

CUSS, R.J., MILODOWSKI, A., AND HARRINGTON, J.F. (2011) Fracture transmissivity as a function of normal and shear stress: first results in Opalinus clay. *Physics and Chemistry of the Earth*. 36, pp.1960-1971.

CUSS, R.J., SATHAR, S. AND HARRINGTON, J.F. (2012) Fracture transmissivity test in Opalinus Clay. *British Geological Survey Commissioned Report*, CR/12/132. 63pp.

CUSS, R.J., SATHAR, S., and HARRINGTON, J.F. (2013) Final Report of FORGE WP4.1.2: Validation of critical stress theory applied to repository concepts. *British Geological Survey Commissioned Report*, CR/13/001. 116pp.

DAVID, C., WONG, T.F., ZHU, W., AND ZHANG, J. (1994) Laboratory measurement of compaction-induced permeability change in porous rocks; implications for the generation and maintenance of pore pressure excess in the crust. *Pure and Applied Geophysics,* 143, pp. 425-456.

DE CRAEN, M., WANG, L., VAN GEET, M., MOORS, H. (2004) *"Geochemistry of Boom Clay pore water at the Mol site"* SCK•CEN Report (BLG 990)

DE LA VAISSIERE, R. TALANDIER, J. Gas entry pressure in Callovo/oxfordian claystone : in situ expermiment PGZ1. Acte du colloque national Transfert 2012, ECL/LML 2012.

DE LA VAISSIERE, R., GERARD, P., RADU, J., CHARLIER, R., COLLIN, F., GRANET, S., TALANDIER, J., PIEDEVACHE, M., & HELMLINGER, B. (2013). GAS INJECTION TEST IN THE CALLOVO-OXFORDIAN CLAYSTONE : DATA ANALYSIS AND NUMERICAL MODELLING. GEOLOGICAL SOCIETY SPECIAL PUBLICATION, 400.

DEWHURST, D.N., APLIN, A.C., AND SARDA, J.-P. (1999[A]) Influence of clay fraction on pore-scale properties and hydraulic conductivity of experimentally compacted mudstones. *Journal of Geophysical Research*, 104, pp. 29,261-29,274.

DEWHURST, D.N., YANG, Y., AND APLIN, A.C. (1999[B]) Permeability and fluid flow in natural mudstones. In: Aplin, A.C., Fleet, A.J., and Macquaker, J.H.S., eds., *Mud and Mudstones: Physical and Fluid Flow Properties*, Geological Society of London, Special Publications, 158, pp. 23-43.

DIAZ-RODRIGUEZ, J.A., LEROUEIL, S., AND ALEMAN, J.D. (1992) On yielding of Mexico City clay and other natural clays. *Journal of Geotechnical Engineering American Society of Civil Engineers*, 118, pp. 481-495.

DRUCKER, D.C., PRAGER, W. (1952) Solid mechanics and plastic analysis for limit design. *Quarterly of Applied Mathematics*, vol. 10(2), 157-165.

DUVEAU, G., SHAO, J.F. AND HENRY, J.P. (1998) Assessment of some failure criteria for strongly anisotropic geomaterials. *Mechanics of cohesive-frictional materials*, vol. 3, 1-26.

EKEROTH, E., ROTH, O. AND JONSSON, M. (2006) The relative impact of radiolysis products in radiation-induced oxidative dissolution of UO2. *Journal of Nuclear Materials*, 355, 38-46.

ENGELDER, T. (1992) *Stress regimes in the lithosphere*. Princeton University Press

FINKBEINER, T., BARTON, C.A. AND ZOBACK, M.D. (1997) Relationships Among In-Situ Stress, Fractures and Faults, and Fluid Flow, Monterey, Formation, Santa Maria Basin, California. *AAPG Bulletin*, 81, p. 1975-1999.

GALLÉ, C., AND TANAI, K. (1998) Evaluation of gas transport properties of backfill materials for waste disposal: H2 migration experiments in compacted Fo-Ca clay. *Clays and Clay Minerals*, 46, 5, 498-508.

GERARD, P., CHARLIER, R., COLLIN, F., FERNANDES, R., GRANET, S., ARNEDO, D., OLIVELLA, S. (2010) Description of initial numerical codes and conceptual model (undisturbed and disturbed host rocks). Forge Project – Deliverables 4.5 and 5.5

GRAHAM, J., HOULSBY, G.T. (1982) Anisotropic elasticity of a natural clay. *Géotechnique*, vol. 33(2), 165-180.

GRANET, S., MEUNIER, S., (2012) Numerical Modeling of in situ-experience of Gas Injection : PGZ1 Acte du colloque national Transfert 2012, ECL/LML

HARRINGTON, J.F. AND HORSEMAN, S.T. (1997) Projects on the effects of gas in underground storage facilities for radioactive waste (Pegasus project): Gas Migration in Clay. Proceedings of a progress meeting held in Mol, Belgium, 28 and 29 May, 1997, *European Science and Technology Series* (1998) EUR 18167 EN, pp153-173, ISBN 92-828-2757-7.

HARRINGTON, J.F. AND HORSEMAN, S.T. (1999) Gas transport properties of clays and mudrocks. In. Aplin, A.C., Fleet, A.J. and Macquaker, J.H.S. (eds) *Muds and Mudstones: Physical and Fluid Flow Properties. Geol. Soc. London, Spec. Pub.* 158, 107-124.

HARRINGTON, J.F., NOY, D.J., HORSEMAN, S.T., BIRCHALL, J.D. AND CHADWICK, R.A. (2009) Laboratory study of gas and water flow in the Nordland Shale, Sleipner, North Sea. in M. Grobe, J. C. Pashin, and R. L. Dodge, eds., c*arbon dioxide sequestration in geological media—State of the science: AAPG Studies in Geology* 59, p. 521– 543.

HARRINGTON, J.F., DE LA VAISSIÈRE, R., NOY, D.J., CUSS, R.J. AND TALANDIER, J. (2012[A]) Gas flow in Callovo-Oxfordian Clay (COx): Results from laboratory and field-scale measurements. Mineralogical Magazine, Vol. 76(8), pp. 3303-3318.

HARRINGTON, J.F. MILODOWSKI, A.E., GRAHAM, C.C., RUSHTON, J.C. AND CUSS, R.J. (2012[B]) Evidence for gas-induced pathways in clay using a nanoparticle injection technique. Mineralogical Magazine, Vol. 76(8), pp3327-3336.

HEFFER, K. AND LEAN, J. (1993) Earth stress orientation - a control on, and guide to, flooding directionality in a majority of reservoirs, Tulsa, PennWell Books, *Reservoir Characterization III*, 799-822 p.

HORSEMAN, S.T., HARRINGTON, J.F. AND SELLIN, P. (1996) Gas migration in Mx80 buffer bentonite. In: Symposium on the Scientific Basis for Nuclear Waste Management XX (Boston), Materials Research Society, Vol. 465. 1003-1010.

HORSEMAN, S.T., HARRINGTON, J.F. AND SELLIN, P. (1999) Gas migration in clay barriers. In: Pusch, R. and Yong, R.N. (eds) Microstructural Modelling of Natural and Artificially Prepared Clay Soils with Special Emphasis on the Use of Clays for Waste Isolation (1999 Special Edition), Engineering Geology, Vol 54, pp139-149, Elsevier, Amsterdam.

HORSEMAN, S.T., HARRINGTON, J.F. AND SELLIN, P. (2004) Water and gas flow in Mx80 bentonite buffer clay. In: Symposium on the Scientific Basis for Nuclear Waste Management XXVII (Kalmar), Materials Research Society, Vol. 807. 715-720.

HORSEMAN, S.T., HARRINGTON, J.F., BIRCHALL, D.J., NOY, D.J. AND CUSS, R.J. (2005) Consolidation and rebound properties of Opalinus clay: A long-term, fully-drained test. *British Geological Survey Commissioned Report.* CR/05/128. 60 pp (Commercial - In Confidence).

HUDSON, J.A., AND HARRISON, J.P. (1997) *Enginerring rock mechanics: an introduction to the principles*. Oxford, Elsevier Science Ltd.

JACOPS, E., VOLCKAERT, G., MAES, N., GOVAERTS, J., WEETJIENS, E. (2012) Determination of gas diffusion coefficients in undisturbed Boom Clay. 5th International Meeting on Clays in natural and engineerd barriers for radioactive waste confinement, Montpellier (France), 2012.

JACOPS E., MAES N., MAES T., VOLCKAERT G., WEETJENS E. (2013) *Gas induced tracer transport in undisturbed & disturbed Boom Clay and Boom Clay – bentonite interfaces,* SCK•CEN Report (ER-222).

JAEGER, J.C., COOK, N.G.W., AND ZIMMERMAN, R.W. (2007) *Fundamentals of rock mechanics*, Wiley-Blackwell.

KATSUBE, T.J., BOITNOTT, G.N., LINDSAY, P.J., AND WILLIAMSON, M. (1996[A]) Pore structure evolution of compacting muds from the seafloor, offshore Nova Scotia. In: Anonymous, ed., Eastern Canada and national and general programs. *Current Research - Geological Survey of Canada,* pp. 17-26.

KATSUBE, T.J., ISSLER, D.R., AND COYNER, K. (1996[B]) Petrophysical characteristics of shale from the Beaufort-Mackenzie Basin, northern Canada; permeability, formation factor, and porosity versus pressure, Interior plains and Arctic Canada. *Current Research - Geological Survey of Canada*. pp. 45-50.

KATSUBE, T.J. (2000) Shale permeability and pore-structure evolution characteristics. *Geological Survey of Canada*. Ottawa, ON, Canada. Pages: 9.

KIRBY, J.M. (1994) Simulating soil deformation using a critical-state model; I, Laboratory tests. *European Journal of Soil Science*, 45, pp. 239-248.

KIRBY, J.M., AND O'SULLIVAN, M.F. (1997) Critical state soil mechanics analysis of the constant cell volume triaxial test. *European Journal of Soil Science*, 48, pp. 71-78.

KRESIS, P. (1991) Hydrogen evolution from corrosion of iron and steel in low/intermediate level waste repositories. *Nagra Technical Report*, NTB 91-21.

KWON, O., KRONENBERG, A.K., GANGI, A.F., AND JOHNSON, B. (2001) Permeability of Wilcox Shale and its effective pressure law. *Journal of Geophysical Research, B, Solid Earth and Planets,* 106, pp. 19,339-19,353.

LAUBACH, S.E., OLSON, J.E. AND GALE, J.F.W. (2004) Are open fractures necessarily aligned with maximum horizontal stress? *Earth and Planetary Science Letters*, 222, no. 1, p. 191-195.

MAÂTOUK, A., LEROUEIL, S., AND LA ROCHELLE, P. (1995) Yielding and critical state of a collapsible unsaturated silty soil. *Géotechnique*, 45, pp. 465-477.

MALTMAN, A. (1994) *The geological deformation of sediments*. London, United Kingdom, Chapman and Hall, 362 pp.

MARSCHALL, P., DISTINGUIN, M., SHAO, H., BOSSART, P., ENACHESCU, C. AND TRICK, T. (2006) Creation and Evolution of Damage Zones Around a Microtunnel in a Claystone Formation of the Swiss Jura Mountains. SPE-98537-PP.

MARSCHALL, P., HORSEMAN, S.T., AND GIMMI, T. (2005) Characterisation of Gas Transport Properties of the Opalinus Clay, a Potential Host Rock Formation for Radioactive Waste Disposal. *Oil & Gas Science Technology*. 60, n°1, 121-139.

MARSCHALL, P., TRICK, T., LANYON, G.W., DELAY, J., SHAO, H. (2008) Hydro-Mechanical Evolution of Damaged Zones around a Microtunnel in a Claystone Formation of the Swiss Jura Mountains. ARMA 08-193 (American Rock Mechanics Association).

MAZUREK, M., ALT-EPPING, P., BATH, A., GIMMI, T., WABER, N. (2009) Natural Tracer Profiles Across Argillaceous Formations: The CLAYTRAC Project. *Nuclear Energy Agency Organisation for economic co-operation and development, NEA Report No. 6253.*
MITCHELL, R.J. (1970) On the yielding and mechanical strength of Leda clays. *Canadian Geotechnical Journal*, 7, pp. 297-312.

MORROW, C., SHI, L.Q., AND BYERLEE, J.D. (1984) Permeability of fault gouge under confining pressure and shear stress. *Journal of Geophysics Research*, 89, pp. 3193-3200.

NERETNIEKS, I. (1984) Impact of alpha-radiolysis on the release of radionuclides from spent fuel in a geologic repository. *Materials Research Society Symposium* (Boston, USA, 14 November 1983), Volume: 26, 1009-1022.

NAGRA (2002): Projekt Opalinuston - Synthese der geowissenschaftlichen Untersuchungsergebnisse. Entsorgungsnachweis für abgebrannte Brennelemente, verglaste hochaktive sowie langlebige mittelaktive Abfälle. *Nagra Tech. Rep. NTB 02-03. Nagra, Wettingen, Switzerland.*

NEUZIL, C.E., BREDEHOEFT, J.D. AND WOLFF, R.G. (1984) Leakage and fracture permeability in the Cretaceous shales confining the Dakota aquifer in South Dakota. In: *Proceedings of First C.V. Theis Conference on Geohydrology* in Dublin, Ohio. Jorgensen, D.G. and Signor, D.C. (eds.). National Water Well Association. pp.113-120.

NIANDOU, H., SHAO, J.F., HENRY, J.P. FOURMAINTRAUX, D. (1997) Laboratory investigations of the mechanical behaviour of Tournemire shale, *Int. J. Rock Mech. Min. Sci.*, vol. 34, 3-16.

NORRIS, S., LEMY, F., DEL HONEUX, C.-A., VOLCKAERT, G., WEETJENS, E., WOUTERS, K., WENDLING, J.,DYMITROWSKI, M., PELLEGRINI, D., SELLIN, P., JOHNSON, L., SENTIS, M. AND HARRINGTON, J., (2013) Synthesis Report: Updated Treatment of Gas Generation and Migration in the Safety Case, EC FORGE Project, Milestone M68, 2013.

OLIVELLA, S., CARRERA, J., GENS, A., ALONSO, E.E. (1994) Nonisothermal Multiphase Flow of Brine and Gas through Saline Media. Transport in Porous Media 15, 271-293.

OHNAKA, M. (1973) The quantitive effect of hydrostatic confining pressure on the compressive strength of crystalline rocks. *J. Phys. Earth*, 21, pp. 125-140.

OLIVELLA, S., ALONSO, E.E. (2008) Gas flow through clay barriers. Géotechnique 58, No. 3, 157-176.

ORTIZ, L., VOLCHARET, G., DE CANNIERE, P., AERTSENS, M., HORSEMAN, S.T., HARRINGTON, J.F., IMPEY, M., AND EINCHCOMB, S. (1996). MEGAS - Modelling and Experiments on Gas Migration in Repository Host-rocks. Proc. EU PEGASUS Meeting at Rapolina-Terme, Italy, 14-15 June 1995. *Nuclear Science and Technology Series*, EUR 16746 EN, Luxembourg, 127-147.

ORTIZ, L., VOLCKAERT, G. AND MALLANTS, D. (2002) Gas generation and migration in Boom Clay, a potential host rock formation for nuclear waste storage. *Engineering Geology*, 64, 287-296.

PETLEY, D.N. (1999) Failure envelopes of mudrocks at high confining pressures, in Macquaker Joe, H.S., ed., *Muds and mudstone; physical and fluid-flow properties*, 158: Geological Society Special Publications London, United Kingdom, Geological Society of London, pp. 61-71.

PIETRUSZCZAK, S., MROZ, Z. (2001) On failure criteria for anisotropic cohesive-frictional materials. *Int. J. Numer. Anal. Meth. Geomech.*, vol. 25, 509-524.

PIETRUSZCZAK, S., LYDZBA, D., SHAO, J.F. (2002) Modelling of inherent anisotropy in sedimentary rocks. *Int. J. Solids and Structures*, vol. 39, 637-648.

POLLER, A., MAYER, G., CROISÉ, J. (2007) Hydrogeologic Analyses and Synthesis (HA Experiment) - Two-phase Flow Analysis of Gas Tests in Opalinus Clay Core Specimen: Complementary Analysis. *Mont Terri TN 2007-01.*

REEVES, H. J. (2002) *The effect of stress and fractures on fluid flow in crystalline rocks, Cumbria*, PhD Thesis, University of Durham, 239 p.

ROOGERS, S.F., (2003) Critical stress-related permeability in fractured rocks. *Fracture and in-Situ Stress Characterization of Hydrocarbon Reservoirs*, 209, p. 7-16.

ROGERS, S.F. AND EVANS, C.J. (2002) Stress-dependent Flow in Fractured Rocks at Sellafield, United Kingdom. *AAPG Special Volumes, v. AAPG Methods in Exploration No. 13: Geological Applications of Well Logs*, p. 241-250.

ROMERO, E., SENGER, R., MARSCHALL, P., GÓMEZ, R. (2013) Air tests on low-permeability claystone formations. Experimental results and simulations. In: *Laloui L, Ferrari A, editors. Multiphysical Testing of Soils and Shales.Springer; 2012, p.57-68.*

ROSCOE, K.H. AND BURLAND, J.B. (1968) On the generalised stress-strain behaviour of "wet" clay. In: *Engineering Plasticity*. Heyman, J. and Leckie, F.A. (eds.). Cambridge University Press. pp.535-609.

ROSCOE, K.H., SCHOFIELD, A., AND WROTH, C.P. (1958) On the yielding of soils. *Géotechnique*, 8, pp. 22-53.

RUTQVIST, J., BÖGESSON, L., CHIIMATSU, M., HERNELIND, J., JING, L., KOBAYASHI, A., AND NGUYEN, S. (2009) Modeling of damage, permeability changes and pressure responses during excavation of the TSX tunnel in granitic rock at URL, Canada. *Environmental Geology*, 57, no. 6, p. 1263-1274.

SATHAR, S., REEVES, H.J., CUSS, R.J. AND HARRINGTON, H.J. (2012) Critical stress theory applied to repository concepts; the importance of stress tensor and stress history in fracture flow. *Mineralogical Magazine*.

SCHOFIELD, A., AND WROTH, C.P. (1968) *Critical State Soil Mechanics.* London, McGraw-Hill, 310 pp.

SCHOFIELD, A. (1998) Mohr Coulomb error correction. *Ground Engineering*, 31, pp. 30-32.

SMART, N.R., CARLSON, L., HUNTER, F.M.I., KARNLAND, O., PRITCHARD, A.M., RANCE, A.P. AND WERME, L.O. (2006) Interactions between iron corrosion products and bentonite. *Serco Assurance Report,* SA/EIG/12156/C001.

SVOBODA, J, and SMUTEK, J. (2010) *Field Installation and Rock Characterisation*, FORGE Report D4.9. 35pp.

SVOBODA, J, and SMUTEK, J. (2011) *Baseline Hydraulic Measurements (crystalline rocks)*, FORGE Report D4.14. 72pp.

SWAN, G., J. COOK, S. BRUCE, and MEEHAN, R. (1989) Strain rate effects in Kimmeridge bay shale. *International Journal of Rock Mechanics and Mining Sciences & Geomechanics Abstracts*, 26(2), 135–149, doi:10.1016/0148-9062(89)90002-8.

TAVENAS, F., AND LEROUEIL, S. (1977) Effects of stresses and time on yielding of clays . *Proceedings of the 9th International Conference on Soil Mechanics*, Tokyo, 1977.

TRICK T., MARSCHALL P., RÖSLI U., LETTRY Y., BOSSART P., ENACHESCU C. (2007) Instrumentation for a gas path through host rock and along sealing experiment. *7th International Symposium on Field Measurements in Geomechanics*.

VINSOT, A., APPELLO, C.A.J., LUNDY, M., WECHNER, S., LETTRY, Y., SCHWYN, B., MCKELVIE, J., DEWONCK, S., BOSSART, P., DELAY, J (2012) In situ diffusion test of hydrogen gas in the Opalinus Clay. *International meeting "Clays in Natural and Engineered Barriers for Radioactive Waste Confinement". Abstracts, Montpellier, France, Oct. 22-25, 2012.*

VAN GEET M., BASTIAENS W., ORTIZ L. (2008) *"Self-sealing capacity of argillaceous rocks: Review of laboratory results obtained from the SELFRAC project."* PHYSICS AND CHEMISTRY OF THE EARTH, Volume: 33 Pages: S396-S406

VOLCKAERT G., ORTIZ L., DE CANNIÈRE P., PUT M., HORSEMAN S.T., HARRINGTON J.F., FIORAVANTE V. IMPEY M. (1994) *MEGAS Modelling and Experiments on Gas Migration in Repository Host Rocks. Final Report Phase 1*. EUR16235 EN, Luxembourg.

WALSH, J.B., AND BRACE, W.F. (1984) The effect of pressure on porosity and the transport properties of rock*. Journal of Geophysical Research. B*, 89, pp. 9425-9431.

WEETJENS, E. AND SILLEN, X. (2006) Gas Generation and Migration in the Near Field of a Supercontainer-Based Disposal System for Vitrified High-Level Radioactive Waste, *Proc. 11th Int. High-Level Radioactive Waste Management Conf.* (IHLRWM), Las Vegas, Nevada, April 30–May 4, 2006.

WENK, H.-R., VOLTOLINI, M., MAZUREK, M., VAN LOON, L.R. AND VINSOT, A. (2008) Preferred Orientations and Anisotropy in Shales: Callovo-Oxfordian Shale (France) and Opalinus Caly (Switzerland), *Clays and Clay Minerals*, 56, pp 285-306.

WHEELER, S.J., AND SIVAKUMAR, V. (1995) An elasto-plastic critical state framework for unsaturated soil. *Géotechnique*, 45, pp. 35-53.

WIKRAMARATNA, R.S., GOODFIELD, M., RODWELL, W.R, NASH, P.J. AND AGG, P.J. (1993) A preliminary assessment of gas migration from the Copper/Steel Canister. *SKB Technical report* TR93-31.

WONG, T.-F., DAVID, C., AND ZHU, W. (1997) The transition from brittle faulting to cataclastic flow in porous sandstones; mechanical deformation. *Journal of Geophysical Research, B, Solid Earth and Planets*, 102, pp. 3009-3025.

ZHANG, C-L, ROTHFUCHS, T., SU, K., AND HOTEIT, N. (2007) Experimental study of the thermo-hydro-mechanical behaviour of indurated clays. *Physics and Chemistry of the Earth*, 32, 957–965.

ZHU, W., AND WONG, T.-F. (1997[a]) The transition from brittle faulting to cataclastic flow; permeability evolution. *Journal of Geophysical Research*, *B, Solid Earth and Planets*, 102, pp. 3027-3041.

ZHU, W., MONTESI, L.G.J., AND WONG, T.-F. (1997[b]) Shear-enhanced compaction and permeability reduction: Triaxial extension tests on porous sandstone. *Mechanics of Materials*, 25, pp. 199-214.

ZOBACK, M.D., AND BYERLEE, J.D. (1975) The effect of microcrack dilatancy on the permeability of Westerly Granite. *Journal of Geophysics Research*, 80, pp. 752-755.

ZOBACK, M. D., MOOS, D., MASTIN, L., AND ANDERSON, R.N. (1985) Well bore breakouts and in situ stress. *Journal of Geophysical Research-Solid Earth*, 90(B7), p. 5523-5530.

www.code-aster.org and www.code-aster.org Documentation R7.01.22. Loi de comportement VISC_DRUC_PRAG